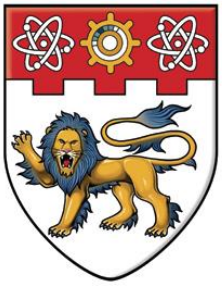

NANYANG TECHNOLOGICAL UNIVERSITY

Miniature Gas Turbines: Numerical Study of the Effects of Miniaturization on the Performance of Compressor

Xiang Junting

School of Mechanical and Aerospace Engineering

2015

Miniature Gas Turbines: Numerical Study of the Effects of Miniaturization on the Performance of Compressor

Xiang Junting

School of Mechanical and Aerospace Engineering

A thesis submitted to the Nanyang Technological University
in fulfillment of the requirement for the degree of
Doctor of Philosophy

2015

Acknowledgements

First and foremost, I'd like to express my sincere gratitude to my supervisor, Dr Jörg Schlüter. His constant support and guidance are essential for carrying out this research. I've really benefited from numerous discussions with him, from which I've gained the ability of independent thinking and the confidence to solve problems confronted. His warm personality has also won my appreciation.

I'd also like to express my gratitude to my co-supervisor, Dr Fei Duan. His continuous support and caring are highly appreciated. Frequent conversations with him have always encouraged me to move forward. Special thanks extend to Dr Randy Chue, from whom I've received helpful suggestions and his dedication to research has won my respect.

I'd like to thank my colleagues and friends in Aerodynamics Lab, Dr Zhang Xiaoqin, Dr Ji Xiaona, Dr John Wang, Dr Vincent Chai, Dr Imran H Ibrahim, Dr Abhishek Sarkar, Dr. Earnest Goh, Mr. Tan Hong Huat, Mr. Arne Reinecke, Mr. Kian Poshtiban, Mr. Dushyant Parkhi and Mr. Chen Song, who have made my stay so special and memorable.

I'd like to thank Defense Science Organization for funding the current project, Nanyang Technological University for providing research facilities and opportunities to interact with talents from different fields and backgrounds. This experience is really treasurable.

Last but not least, I wish to express my love and deepest gratitude to my family, for their dedication and love for me during all these years.

Table of Contents

Acknowledgements i

Abstract v

Nomenclature vi

List of Tables ix

List of Figures ix

Chapter 1 1

Introduction 1

1.1 Literature Review 4

1.1.1 Reynolds Number Effect 4

1.1.2 Heat Transfer Effect 5

1.1.3 Tip Clearance Effect 7

1.1.4 Micro Gas Turbines 9

1.2 Layout of Dissertation 9

Chapter 2 12

Theory & Fundamentals 12

2.1 Fundamentals of Fluid Dynamics 12

2.1.1 Conservation Laws 13

2.1.2 Compressible Flow 14

2.1.3 Viscous Flow 15

2.1.4 Turbulent Flow 16

2.1.5 Fundamentals of Aerodynamics 17

2.2 Theory of Gas Turbine 19

2.3 Fundamentals of Numerical Approach 22

2.3.1 Discretization Method 22

2.3.2 Flow Solvers 23

2.3.3 Turbulence Models 26

2.3.4 Rotating Machinery Interface Treatment Approach 32

Chapter 3 36

Validation & Simulation Setup 36
3.1 Geometry & Design Parameters 36
3.2 Mesh Generation 40
3.3 Grid Independence Study 42
3.4 Boundary Condition & Numerical Scheme 44
3.5 Interface Method Comparison 45
3.6 Turbulence Model Comparison 48
3.7 Flow Field Analysis 56
3.7.1 Flow Field Analysis at 100% Design Speed 57
3.7.2 Flow Field Analysis at 70% Design Speed 63
Chapter 4 71
Reynolds Number Effect 71
4.1 Reynolds Number Effect in Rotor Zone 78
4.2 Reynolds Number Effect in Stator Zone 90
Chapter 5 99
Heat Transfer Effect 99
5.1 Effect of Heat Flux 103
5.2 Effect of Isothermal Wall 109
Chapter 6 118
Tip Clearance Effect 118
6.1 Effect of Constant Tip Clearance 119
6.2 Effect of Varying Tip Clearance 129
6.3 Effect of Reynolds Number with Constant TC 146
Chapter 7 152
Conclusions and Recommendations 152
7.1 Conclusions 152
7.2 Recommendations 154
APPENDIX I 155
KJ-66 Micro Gas Turbines Compressor Test 155
A-I.1 Design Details of KJ-66 MGT Compressor 155
A-I.2 Numerical Approach Setup 157

A-I.3 Numerical Results for KJ-66 MGT Compressor 160
APPENDIX II 168
Bibliography 174

Abstract

Micro Gas Turbines (MGT) are an attractive choice for Unmanned Aerial Vehicles (UAV) and small-scale power generation. Compared with other propulsion systems, MGT have several advantages including high power-to-weight ratio, availability for various fuels, endurance and others. However, the direct miniaturization of conventional gas turbines designed at large scales may induce performance loss. Therefore, the effects of miniaturization on gas turbines need to be investigated. In this research, an axial compressor in a gas turbine is studied, to understand the effects of the miniaturizing process. Using a numerical approach, parameter studies are conducted on three of the most important parameters during the miniaturizing process: the Reynolds number effect, the increased heat transfer and the tip clearance.

The NASA Stage35 compressor is selected as the configuration in this study. Firstly, a thorough validation of the computational tools and methods is conducted, suggesting the suitability of the numerical methods for follow-up study. Then, the effect of Reynolds number is investigated, in the range of *Re* 2.14×10^5 to *Re* 8.54×10^5. Our results indicate a drop of performance with the decrease of Reynolds number, due to the increased viscous effect in boundary layer when compressor is miniaturized. Thereafter, the effect of heat transfer is investigated due to thermal conduction; adiabatic wall conditions, constant heat transfer coefficient conditions and isothermal conditions are applied, respectively. The results indicate that the increased heat transfer from internal flow to the ambient air will actually benefit compressor performance, but the heat transfer from the downstream combustor to the compressor has an adverse effect on compressor overall performance. Subsequently, the effect of tip clearance (TC) is investigated, with varying TC value and varying Reynolds number. Our results indicate that the existence of TC has an adverse effect on compressor performance, and the loss of performance amplifies during the miniaturization process.

Nomenclature

D_H	Hydraulic Diameter
Exp	Experimental Data
Mach	Mach Number
Mfr	Mass Flow Rate
MGT	Micro Gas Turbine
MRF	Multiple Reference Frame
MP	Mixing Plane
Pt	Total Pressure
RPM	Round per Minute
R_{LE}	Rotor Leading Edge
R_{TE}	Rotor Trailing Edge
R_{ss}	Rotor Suction Surface
R_{ps}	Rotor Pressure Surface
S_{LE}	Stator Leading Edge
S_{TE}	Stator Trailing Edge
S_{ss}	Stator Suction Surface
S_{ps}	Stator Pressure Surface
SF	Scaling Factor
ΔS	Entropy Change $\Delta S = \int \frac{dQ_{rev}}{T}$
TC	Tip Clearance
Tt	Total Temperature
ΔT	Temperature Difference
∇T	Temperature Gradient
UAV	Unmanned Aerial Vehicle
Ω	Finite Control Volume

$\partial\Omega$	Boundary of a Control Volume
dS	Element Surface Area
S_{ij}	Components of Strain-Rate Tensor
Q	Source Term
U	General Flow Variables
$\vec{U}$	Vector of General Flow Variables
Re	Reynolds Number
Pr	Total Pressure Ratio $Pr = \overline{P_{out}}/\overline{P_{in}}$
Tr	Total Temperature Ratio $Tr = \overline{T_{out}}/\overline{T_{in}}$
η_{ad}	Adiabatic Efficiency $\eta_{ad} = ((\overline{P_{out}}/\overline{P_{in}})^{(\gamma-1)/\gamma} - 1)/((\overline{T_{out}}/\overline{T_{in}}) - 1)$
y^+	Non-dimensional Wall Distance $y^+ = \frac{yu_\tau}{\upsilon}$
u_τ	Wall Friction Velocity $u_\tau = \sqrt{\tau_w/\rho}$
h	Heat Transfer Coefficient
γ	Ratio of Specific Heat (1.4)
ῡ	Turbulent Viscosity
υ	Kinematic Viscosity
μ	Dynamic Viscosity Coefficient
ϰ	Thermal Diffusivity Coefficient
k	Turbulent Kinetic Energy
ϵ	Turbulent Dissipation Rate
ω	Specific Dissipation
$\vec{n}$	Unit Normal Vector
τ	Viscous Stress
$\bar{\bar{\tau}}$	Viscous Stress Tensor
τ_{ij}	Components of Viscous Stress Tensor
τ_{ij}^R	Components of Reynolds Stress Tensor

E	Total Energy
e	Internal Energy per Unit Mass
H	Total Enthalpy
h'	Enthalpy per Unit Mass
Δt	Time Step
$\dot{q}_h$	Heat Flux due to Radiation, Chemical Reactions, etc
$\vec{q}$	Local Heat Flux Density
$\vec{v}$	Velocity Vector with the Components u, v, w
u, v, w	Cartesian Velocity Components
ρ	Density
d	Distance
$\vec{\omega}$	Angular Velocity
$\underset{\omega}{\rightarrow}$	Vorticity
w/	With
w/o	Without
in	Rotor Inlet Surface
out	Stator Outlet Surface
ref	Reference Point
rev	Reversible Process

List of Tables

Table 2.1 Types of Mixing Plane Pairs 34
Table 3.1 Design Parameters of NASA Stage35 Compressor 36
Table 3.2 Grid Details of NASA Stage35 Compressor for Grid Independence Study 43
Table 3.3 Combinations of Rotor and Stator Boundary Conditions at Interface 45
Table 4.1 Relations between Reynolds Number and SF Applied 72
Table 5.1 Specifications of Wall Thermal Conditions 99
Table 5.2 Comparison of Results from Different Thermal Conditions 106
Table 6.1 Specification of Three Tip Clearance (TC) Approaches 118
Table 6.2 Specification of TC Value and TC Ratio 130
Table 6.3 Specification of Tip Clearance and Reynolds Number 146
Table A-i.1 Design Parameters and Performance Characteristics of KJ-66 MGT 156
Table A-i.2 Details of Boundary Conditions and Mfr at Various Operation Speed 160

List of Figures

Fig 1.1 MQ-9 Reaper (Left) [4] & RQ-11 Raven (Right) [5] 2
Fig 2.1 Forces on an airfoil 18
Fig 2.2 Cutaway view of an axial gas turbine [64] 19
Fig 2.3 An idealized Brayton cycle [65] 20
Fig 2.4 (a) Cycle efficiency changes with an increase in pressure ratio & (b) Specific power output changes with an increase in gas turbine inlet temperature for two different pressure ratios [68] 22
Fig 2.5 Conservation of flux in a finite volume based on 2D example 23
Fig 2.6 The stencil for a common implicit method based equation 24
Fig 2.7 The stencil for a common explicit method based equation 25
Fig 2.8 Zones formed by non-periodic intersection 35
Fig 3.1 NASA Stage35 compressor geometry 37
Fig 3.2 Alignment of rotor blade and stator blade 38
Fig 3.3a Blade profile at rotor hub section 39
Fig 3.3b Blade profile at rotor 50% spanwise section 39
Fig 3.3c Blade profile at rotor tip section 40
Fig 3.4 Locations of three rotor profile sections along blade radial direction 40
Fig 3.5 Computational grid of rotor & stator domain 41
Fig 3.6a NASA 35 compressor rotor mesh quality examination for Grid 3 42
Fig 3.6b NASA 35 compressor stator mesh quality examination for Grid 3 42
Fig 3.7 Changes of Pr & η_{ad} with the increase of mesh size, with design Mfr at 100% design speed 43
Fig 3.8a Distribution of Pr in radial direction for different interface methods, with design Mfr at 100% design speed 47

Fig 3.8b Distribution of *Tr* in radial direction for different interface methods, with design Mfr at 100% design speed..... 47
Fig 3.8c Distribution of η_{ad} in radial direction for different interface methods, with design Mfr at 100% design speed..... 48
Fig 3.8d Distribution of Mach number in radial direction on compressor outlet surface, with design Mfr at 100% design speed..... 48
Fig 3.9a Distribution of *Pr* in radial direction for different turbulence models, with design Mfr at 100% design speed..... 50
Fig 3.9b Distribution of *Tr* in radial direction for different turbulence models, with design Mfr at 100% design speed..... 50
Fig 3.9c Distribution of η_{ad} in radial direction for different turbulence models, with design Mfr at 100% design speed..... 51
Fig 3.9d Distribution of Mach in radial direction on compressor outlet surface for different turbulence models, with design Mfr at 100% design speed..... 51
Fig 3.10a Distribution of *Pr* for different turbulence models, with varying Mfr at 70% design speed..... 52
Fig 3.10b Distribution of *Tr* for different turbulence models, with varying Mfr at 70% design speed..... 53
Fig 3.10c Distribution of η_{ad} for different turbulence models, with varying Mfr at 70% design speed..... 53
Fig 3.11a Distribution of *Pr* for different turbulence models, with varying Mfr at 100% design speed..... 54
Fig 3.11b Distribution of *Tr* for different turbulence models, with varying Mfr at 100% design speed..... 55
Fig 3.11c Distribution of η_{ad} for different turbulence models, with varying Mfr at 100% design speed..... 55
Fig 3.12 Distribution of Pt in the rotor & stator fluid zone, with design Mfr at 100% design speed..... 57
Fig 3.13 Distribution of Pt at 50% spanwise, with design Mfr at 100% design speed..... 58
Fig 3.14 Distribution of Mach at 50% spanwise of rotor and at $R_{ss,}$ with design Mfr at 100% design speed..... 58
Fig 3.15 Distribution of Mach at 50% spanwise of stator and at $S_{ss,}$ with design Mfr at 100% design speed..... 59
Fig 3.16 Distribution of Mach on different spanwise of stator, with design Mfr at 100% design speed..... 59
Fig 3.17a Distribution of turbulent viscosity, Strain Rate and Reynolds Stress at 30% spanwise of stator, with design Mfr at 100% design speed..... 60
Fig 3.17b Distribution of turbulent viscosity on different spanwise of stator, with design Mfr at 100% design speed..... 61
Fig 3.18 Distributions of entropy on R_{ss} and $S_{ss,}$ with design Mfr at 100% design speed 62
Fig 3.19 Distribution of entropy on different spanwise of rotor, with design Mfr at 100% design speed..... 62
Fig 3.20 Distribution of entropy on different spanwise of stator, with design Mfr at 100% design speed..... 62

Fig 3.21 Distribution of Pt on different spanwise of rotor, with optimal Mfr at 70% design speed 63
Fig 3.22 Distribution of Mach at 50% spanwise of rotor and at $R_{ss,}$ with optimal Mfr at 70% design speed 64
Fig 3.23 Distribution of entropy at 50% spanwise of rotor and at $R_{ss,}$ with optimal Mfr at 70% design speed 64
Fig 3.24 Distribution of Mach along the stator flow path, with optimal Mfr at 70% design speed 65
Fig 3.25 Distribution of entropy along the stator flow path, with optimal Mfr at 70% design speed 66
Fig 3.26 Development of turbulent viscosity in the stator fluid zone 67
Fig 3.27 Development of turbulent viscosity in the outlet vane fluid zone 67
Fig 3.28 Streamline in rotor at 100% and 70% design speed respectively 68
Fig 3.29 Streamline in stator at 100% and 70% design speeds respectively (View from Z axis) 69
Fig 3.30 Streamline in stator at 100% and 70% design speeds respectively (View from X axis) 70
Fig 4.1 Variation of rotor blade height for different SF applied 71
Fig 4.2 Adjustment of RPM at different SF conditions 72
Fig 4.3 Comparison of η_{ad} at different *Re* condition, with design Mfr at 100% design speed 73
Fig 4.4 Distribution of *Pr* at different *Re* condition, with design Mfr at 100% design speed 74
Fig 4.5 Distribution of *Tr* at different *Re* condition, with design Mfr at 100% design speed 75
Fig 4.6 Variations of η_{ad} with varying Mfr, at 100% design speed 76
Fig 4.7 Variations of *Pr* with varying Mfr, at 100% design speed 77
Fig 4.8 Variations of *Tr* with varying Mfr, at 100% design speed 77
Fig. 4.9 Comparison of entropy distributions on R_{ss} during its miniaturization process, with design Mfr at 100% design speed 78
Fig 4.10 Comparison of entropy distributions on 30% spanwise of rotor, with design Mfr at 100% design speed 79
Fig 4.11 Locations of data extraction points on the primary surface in rotor zone 79
Fig 4.12 Distribution of entropy at 5% span and 20% span from R_{ss} based on the primary surface, with design Mfr at different *Re* condition 81
Fig 4.13 Distribution of Mach at 5% span and 20% span from R_{ss} based on the primary surface, with design Mfr at different *Re* condition 81
Fig 4.14 Distribution of turbulent viscosity at 5% span and 20% span from R_{ss} based on the primary surface, with design Mfr at different *Re* condition 82
Fig 4.15 Comparison of turbulent viscosity at 50% span from rotor hub, with design Mfr at different *Re* condition 83
Fig 4.16 Comparison of turbulent viscosity at 80% streamwise, with design Mfr at different *Re* condition 83

Fig 4.17 Expansion of flow separation near R_{TE}, with design Mfr at *Re* 2.14×10^5 condition 84
Fig 4.18 Expansion of Mach contour near R_{TE}, with design Mfr at *Re* 2.14×10^5 condition 84
Fig 4.19 Locations of data extraction points on R_{ps} 86
Fig 4.20 Distribution of entropy on R_{ps}, at 20%, 50%, 80%, 90% and 95% spanwise of rotor, with design Mfr at *Re* 5.34×10^5 condition 86
Fig 4.21 Distribution of Mach on R_{ps}, at 20%, 50%, 80%, 90% and 95% spanwise of rotor, with design Mfr at *Re* 5.34×10^5 condition 87
Fig 4.22 Distribution of turbulent viscosity on R_{ps}, at 20%, 50%, 80%, 90% and 95% spanwise of rotor, with design Mfr at *Re* 5.34×10^5 condition 87
Fig 4.23 Distribution of entropy at 5%, 20% and 40% span from R_{ss}, with design Mfr at *Re* 5.34×10^5 condition 89
Fig 4.24 Distribution of Mach at 5%, 20% and 40% span from R_{ss}, with design Mfr at *Re* 5.34×10^5 condition 89
Fig 4.25 Distribution of turbulent viscosity at 5%, 20% and 40% span from R_{ss}, with design Mfr at *Re* 5.34×10^5 condition 90
Fig 4.26 Comparison of entropy distribution on S_{ss} at different *Re* condition, with design Mfr 91
Fig 4.27 Comparison of entropy distribution on 30% spanwise of stator at different *Re* condition, with design Mfr 91
Fig 4.28 Locations of data extraction points on the primary surface in stator zone 92
Fig 4.29 Distribution of entropy at 5% and 20% span from S_{ss} based on the primary surface, with design Mfr at different *Re* condition 93
Fig 4.30 Distribution of Mach at 5% and 20% span from S_{ss} based on the primary surface, with design Mfr at different *Re* condition 94
Fig 4.31 Distribution of turbulent viscosity at 5% and 20% span from S_{ss} based on the primary surface, with design Mfr at different *Re* condition 95
Fig 4.32 Comparison of turbulent viscosity on 30% spanwise of stator, with design Mfr at different *Re* condition 95
Fig 4.33 Distribution of entropy at 5%, 20% and 40% span from S_{ss}, with design Mfr at *Re* 5.34×10^5 condition 97
Fig 4.34 Distribution of Mach at 5%, 20% and 40% span from S_{ss}, with design Mfr at *Re* 5.34×10^5 condition 97
Fig 4.35 Distribution of turbulent viscosity at 5%, 20% and 40% span from S_{ss}, with design Mfr at *Re* 5.34×10^5 condition 98
Fig 5.1 Locations of data extraction points on rotor inlet surface 100
Fig 5.2 Locations of data extraction points on stator outlet surface 100
Fig 5.3 Distribution of *Pr* at different blade radial spans 101
Fig 5.4 Distribution of *Tr* at different blade radial spans 102
Fig 5.5 Distribution of η_{ad} at different blade radial spans 103
Fig 5.6a Distribution of *Pr* and η_{ad} with the increase of heat transfer coefficient 105
Fig 5.6b Distribution of *Tr* with the increase of heat transfer coefficient 105
Fig 5.7 Comparison of *Pr* for Wall Q=0 & Wall *h*=200 $W/m^2\cdot k$ 107

Fig 5.8 Comparison of η_{ad} for Wall Q=0 & Wall h=200 W/m^2·k 107
Fig 5.9 Comparison of entropy distribution on R_{ss} for Case1 & Case 2, with design Mfr at *Re* 5.34×10^5 condition 108
Fig 5.10 Comparison of temperature distribution on R_{ss} for Case 1 & Case 2, with design Mfr at *Re* 5.34×10^5 condition 108
Fig 5.11 Comparison of entropy distribution Variation on R_{ss} for Case2, with design Mfr at varying *Re* condition 109
Fig 5.12 Comparison of temperature distribution Variation on R_{ss} for Case2, with design Mfr at varying *Re* condition 109
Fig 5.13 Distribution of *Pr* with the change of isothermal wall temperature, with design Mfr at *Re* 5.34×10^5 condition 111
Fig 5.14 Distribution of *Tr* with the change of isothermal wall temperature, with design Mfr at *Re* 5.34×10^5 condition 111
Fig 5.15 Distribution of η_{ad} with the change of isothermal wall temperature, with design Mfr at *Re* 5.34×10^5 condition 112
Fig 5.16 Comparison of temperature distribution on R_{ss} with different isothermal wall conditions, with design Mfr at *Re* 5.34×10^5 condition 113
Fig 5.17 Comparison of entropy distribution on R_{ss} with different isothermal wall conditions, with design Mfr at *Re* 5.34×10^5 condition 113
Fig 5.18 Comparison of temperature distribution at 30% spanwise of rotor with different isothermal wall conditions, with design Mfr at *Re* 5.34×10^5 condition 113
Fig 5.19 Comparison of entropy distribution at 30% spanwise of rotor with different isothermal wall conditions, with design Mfr at *Re* 5.34×10^5 condition 114
Fig 5.20 Comparison of turbulent viscosity distribution at 30% spanwise of rotor with different isothermal wall conditions, with design Mfr at *Re* 5.34×10^5 condition 114
Fig 5.21 Comparison of spanwise *Pr* distribution at different wall thermal conditions, with design Mfr at *Re* 5.34×10^5 condition 116
Fig 5.22 Comparison of spanwise *Tr* distribution at different wall thermal conditions, with design Mfr at *Re* 5.34×10^5 condition 116
Fig 5.23 Comparison of spanwise η_{ad} distribution at different wall thermal conditions, with design Mfr at *Re* 5.34×10^5 condition 117
Fig 6.1 Tip clearance mesh 119
Fig 6.2 Specification of spanwise planes (Left) and streamwise data points (right) 120
Fig 6.3 Comparison of Mach distribution on 95% spanwise plane 121
Fig 6.4 Comparison of Pt distribution on 95% spanwise plane 121
Fig 6.5 Comparison of turbulent viscosity distribution on 95% spanwise plane 123
Fig 6.6a Comparison of turbulent viscosity distribution on 100% streamwise span 123
Fig 6.6b Distribution of turbulent viscosity, strain rate field and Reynolds stress at rotor exit plane, for TC=0.5mm 123
Fig 6.7 Comparison of entropy distribution on 95% spanwise plane 124
Fig 6.8 Comparison of Mach distribution along rotor streamwise direction, with TC=0 and TC=0.5mm 126
Fig 6.9 Comparison of Pt distribution along rotor streamwise direction, with TC=0 and TC=0.5mm 126

Fig 6.10 Comparison of turbulent visocisty distribution along rotor streamwise direction, with TC=0 and TC=0.5mm 128
Fig 6.11 Comparison of entropy distribution along rotor streamwise direction, with TC=0 and TC=0.5mm 128
Fig 6.12 Comparison of Tt distribution along rotor streamwise direction, with TC=0 and TC=0.5mm 129
Fig 6.13 Specification of streamwise data planes (Left) and span width data points (right) 130
Fig 6.14 Change of *Pr* and η_{ad} with varying TC ratio 131
Fig 6.15 Percentage of loss of *Pr* and η_{ad} with varying TC ratio 131
Fig 6.16 Variation of Mach at 95% span line, on 60%, 80% and 100% streamline planes, with TC=1.25mm 133
Fig 6.17 Variation of turbulent viscosity at 95% span line, on 60%, 80% and 100% streamline planes, with TC=1.25mm 134
Fig 6.18 Variation of vorticity at 95% span line, on 60%, 80% and 100% streamline planes, with TC=1.25mm 134
Fig 6.19 Distribution of vorticity on 100% streamwise plane, with TC=1.25mm 135
Fig 6.20 Distribution of Mach on 100% streamwise plane, at TC=0.3125mm, TC=0.75mm and TC=1.25mm 136
Fig 6.21a Distribution of turbulent viscosity on 100% streamwise plane, at TC=0.3125mm, TC=0.75mm and TC=1.25mm 137
Fig 6.21b Distribution of turbulent viscosity on 120% streamwise plane, at TC=0.3125mm, TC=0.75mm and TC=1.25mm 137
Fig 6.21c Distribution of turbulent viscosity on 140% streamwise plane, at TC=0.3125mm, TC=0.75mm and TC=1.25mm 137
Fig 6.22 Distribution of Mach at 90% span line on 100% streamwise plane, at TC=0.3125mm, TC=0.75mm and TC=1.25mm 139
Fig 6.23 Distribution of Pt at 90% span line on 100% streamwise plane, at TC=0.3125mm, TC=0.75mm and TC=1.25mm 139
Fig 6.24 Distribution of turbulent viscosity at 90% span line on 100% streamwise plane, at TC=0.3125mm, TC=0.75mm and TC=1.25mm 140
Fig 6.25 Distribution of vorticity at 90% span line on 100% streamwise plane, at TC=0.3125mm, TC=0.75mm and TC=1.25mm 140
Fig 6.26 Distribution of Mach at 50% span line on 100% streamwise plane, at TC=0.3125mm, TC=0.75mm and TC=1.25mm 142
Fig 6.27 Distribution of Pt at 50% span line on 100% streamwise plane, at TC=0.3125mm, TC=0.75mm and TC=1.25mm 143
Fig 6.28 Distribution of turbulent viscosity at 50% span line on 100% streamwise plane, at TC=0.3125mm, TC=0.75mm and TC=1.25mm 143
Fig 6.29 Distribution of vorticity at 50% span line on 100% streamwise plane, at TC=0.3125mm, TC=0.75mm and TC=1.25mm 144
Fig 6.30 Distribution of Mach at 10% span line on 100% streamwise plane, at TC=0.3125mm, TC=0.75mm and TC=1.25mm 145

Fig 6.31 Distribution of vorticity at 10% span line on 100% streamwise plane, at TC=0.3125mm, TC=0.75mm and TC=1.25mm 145
Fig 6.32 Comparison of *Pr* for w/ and w/o TC cases, at varying *Re* condition 147
Fig 6.33 Comparison of η_{ad} for w/ and w/o TC cases, at varying *Re* condition 147
Fig 6.34 Distribution of *Pr* and η_{ad} with varying TC ratio 148
Fig 6.35 Streamline at rotor TC with top view, at large and small *Re* condition 149
Fig 6.36 Streamline at rotor TC with front view, at large and small *Re* condition 149
Fig 6.37 Streamline at stator TC with downstream view, at large and small *Re* condition 150
Fig 6.38 Streamline at stator TC with top view, at large and small *Re* condition 150
Fig A-i.1 Layout of KJ-66 micro gas turbine 156
Fig A-i.2 3D model of KJ-66 MGT compressor, w/ and w/o shroud 157
Fig A-i.3 3D view of the computational domain 158
Fig A-i.4 Structured mesh for KJ-66 MGT compressor 158
Fig A-i.5 Specification of boundary conditions for KJ-66 MGT compressor 159
Fig A-i.6 Distribution of *Pr* with varying Mfr, at different operation speed 161
Fig A-i.7 Distribution of experiment *Pr* with varying Mfr at different operation speed 161
Fig A-i.8 Distribution of η_{ad} with varying Mfr, at different operation speed 162
Fig A-i.9 Distribution of experiment[92] η_{ad} with varying Mfr at different operation speed 163
Fig A-i.10 Distribution of Pt within compressor (Left) and on rotor blade (Right) 164
Fig A-i.11 Distribution of Pt on R_{ps} and R_{ss} along rotor meridional length, at different operation speed 164
Fig A-i.12 Distribution of radial velocity (Left) and Entropy (Right) along impeller streamwise, with design Mfr at 117k rpm 165
Fig A-i.13 Distribution of entropy on rotor blade with design Mfr at 117k rpm and over impeller meridional length at different operation speed 166
Fig A-i.14 Streamline along impeller streamwise (Left) and diffuser streamwise (right), with design Mfr at 117k rpm 167
Fig A-i.15 Velocity vectors on 50% spanwise in diffuser, normal view (Left) and zoom-in view, with design Mfr at 117k rpm 167

Chapter 1

Introduction

The first concepts of drones date back to mid-1800s, when unmanned balloons were used for the attack of Venice by Austrians. However, the earliest attempt for drones commonly referred to today was carried out in early 1900s, and the first trial of powered unmanned aerial vehicle was in 1916, when A. M. Low's "Aerial Target" project was requisitioned during WWI. Numerous advances of remote-controlled airplanes were made during and after WWI and continued development was made during WWII. These planes were used for target practice as well as fly attack missions. Jet engines were incorporated in after the wars years and gained popularity since then[1].

With its first Unmanned Aerial Vehicle (UAV) built in 1959, the United States has developed into a dominant UAV user during decades. Concerned about losing pilots in hostile situations, the UAVs were first deployed for combat missions during the Vietnam War [2]. Intelligence gathering operations were intensely carried out in Afghanistan, Pakistan and Yemen, after the terrorist attacks. According to the USA department of defense [3], as of October 2008, UAVs have flown around 500,000 flight mission hours. Troops or soldier lives are at less risk since more information is obtained by surveillance and dangerous job could be done by UAV or other unmanned vehicles.

Two types of UAVs are shown in Figure 1.1, which are mainly operated by U.S. military nowadays. Operated as a combat UAV, the turboprop-engine-powered General Atomics MQ-9 Reaper is shown on the left; the right figure shows the launching of the battery-powered AeroVironment RQ-11 Raven, which is a small hand-launched and remote-controlled UAV. The flight of UAV is either autonomously controlled by computers mounted on the vehicle, or under remote navigational control, or piloted from ground workstation. Due to its versatility and endurance, UAV has gained its importance for civilian use as well. By performing

tasks such as surveillance, precision target designation, signal intelligence, mineral exploration, and transportation, it has demonstrated its potential in utilization in more areas.

Fig 1.1 MQ-9 Reaper (Left) [4] & RQ-11 Raven (Right) [5]

The world's first true gas turbine was built in 1791, when John Barber received a patent for his breakthrough [6]. It was the first time that details of gas turbine principles were described and all the important features of modern gas turbines were included in his work. The first steam turbine-powered vessel, Turbinia, was built in 1894, as a milestone for turbine powered steamships. In the following year, 1895, three 4-ton 100kw radial flow generators were installed to power the first electric street lighting in Cambridge, UK. A Norwegian, Ægidius Elling, successfully developed the first self-powered gas turbine which produced sufficient energy to run its own components in 1903. His work utilized rotary components and achieved 11 hp. The design of a centrifugal gas turbine for jet propulsion was patented by Frank Whittle in 1930, but it was not until 1937 that the first successful power jet engine runs was recorded. Continued efforts were made for the advances of gas turbines and it has extended its utility to several applications during decades. Nowadays, gas turbines are applied for powering aircraft, naval and civilian marines, electrical generators, trains, etc [7]. The application of gas turbines is unlimited and its potential is continued to be explored.

Apart from using Micro Gas Turbine (MGT) in UAV, the use of MGT is attractive for small-scale localized power generation. Miniaturized power generation system has become popular in recent years. Motivated by the idea of providing power to meet an individual person's electric needs, Alan Epstein has made efforts to build millimeter size turbine at MIT, to deliver 1200-1500 W·h/kg in the longer term[8]. The German company Lichtblick and Volkswagen have joined forces to develop miniature power stations for home usage [9]. Jan Peirs has made efforts to build ultra MGT generator in Belgium, expecting to produce a power output of 1000 W [10]. Researchers from ETH Zurich have also tried to develop MGT as a portable power device [11]. The mini-jet group in NTU Singapore has investigated the performance of MGT for UAV application [12-15].

The increasing demand for knowledge about MGT leads to the initial motivation of current study. How compressor performance will change if the MGT is scaled down from current large conventional gas turbines is our main concern. Therefore, the primary objective of the current PhD study is to perform numerical investigations of the effects of miniaturization on compressor performance based on conventional gas turbines. We focus on three of the most important factors,

a) The Reynolds Number Effect,

b) The Heat Transfer Effect

c) The Tip Clearance Effect

to understand the effects of these parameters during the miniaturization process of a conventional axial compressor. These factors are selected based on literature review about main concerns during compressor operation, coupled with our expectations of their impact on compressor performance when miniaturization is applied. The hope is to understand the performance of miniaturized gas turbines, and to provide optimization recommendations for UAV applications.

The Mach number effect is not considered in this thesis. The rotor tip speed is kept constant at different scales as clarifies in Chapter 4. Also, the incoming specific mass flow rate at different scales is also kept constant, i.e., the incoming flow velocity is unchanged. The Mach number would then be only affected by the

local temperature. Our simulations show that the temperature variations are small. Therefore, the local Mach number at different scales can be considered unchanged. The changing Mach number issue is beyond our scope as the scaling effect is our main concern. Besides that, Mach number is still referred and used throughout the thesis to aid our analysis.

1.1 Literature Review

Documents and literatures are collected and referred to aid our understanding of gas turbine performance. Various investigations have been conducted regarding different impact factors on gas turbine compressor operation, based on both experimental and numerical approach.

1.1.1 Reynolds Number Effect

The Reynolds number is an important factor in determining compressor performance. The change of Reynolds number leads to variations of inertial effect as well as viscous effect, further results in compressor performance change when miniaturized gas turbines are built. Thus parametric studies on the effect of Reynolds number are conducted in this study. Previous endeavors have been made to enlighten this issue, which lay the foundation of the current work. Wang and Hu [16] have studied the stability and performance of axial fans and compressors with regards to the effects of the Reynolds number. They have experimentally validated the performance variation and stability of compressors, indicating that both of these criteria deteriorate with decreasing Reynolds number. Hobson and Hansen [17] have experimentally investigated the Reynolds number effect on separation bubbles on compressor stator blades based on wind tunnel testing using Laser Doppler Velocimetry (LDV).The experiment Reynold number ranges from 2.1×10^5 to 6.4×10^5, quantifying the separation bubbles and flow reversal at low, intermediate and high Reynolds number conditions by LDV. The experimental data, especially the low Reynolds number data, are claimed to be excellent test case for LES and DNS of cascade flow field. Zhao and Lu [18]focused their research on the low Reynolds number effects on flow stability.

Both steady and unsteady simulations are carried out under different conditions, representing operations at sea level and at high altitude (Low Reynolds number condition). Their results showed that tip clearance flow is the dominant factor affecting flow stability under either high or low Reynolds number conditions. Choi and Baek [19] have considered the loss characteristics in an axial compressor due to the effects of low Reynolds numbers. Their study indicated that hub boundary layer and suction surface separation, caused by the low Reynolds number, reduced the static pressure and compressor performance. Back and Hobson [20] have focused on the relation between surface roughness and Reynolds number in compressor cascade performance. They found that the rough surface area, roughness location and Reynolds number interactively contributed to the loss coefficient. Besides that, Casey and Robinson [21] have endeavored to derive a correction equation, which related changes in compressor efficiency with Reynolds number to changes in surface roughness. Based on that, Dietmann and Casey [22] have further endeavored to provide improved correlations for the effect of Reynolds number and roughness on compressor performance. Two theoretical approaches and the modification of the friction factor in the original equation are proposed, with suggestions for an improved correlation provided. Recently, Zheng and Lin [23] have investigated the Reynolds number effect on a high pressure ratio turbocharger compressor. Their results showed that compressor efficiency and pressure ratio decreased by 6.9% and 7.9%, respectively, when Reynolds number dropped from 9.86×10^5 to 2.96×10^5, based on their experimental and numerical results. Although extensive endeavors have been made regarding Reynolds number effect, the understanding of it on miniaturized gas turbines is still limited.

1.1.2 Heat Transfer Effect

The effect of heat transfer is another concern during the miniaturization of compressor. Due to increased surface-to-volume ratio, the heat transfer between internal flow within compressor and external ambient air intensifies. In addition, the heating effect from downstream combustor on the upstream compressor

should also be of concern, especially for miniaturized gas turbines. Previous investigations regarding compressor heat transfer have been referred to deepen our understanding. Schiele and Wittig [24] have summarized the current techniques regarding gas turbine heat transfer and introduced the new design concept for ceramic gas turbine components. Their research suggested that cooling in gas turbine was essential and will pose challenges in the years to come. Romagnoli and Martines-Botas [25] have investigated the performance of turbocharger under non-adiabatic conditions. Experiments were conducted to assess the impact of engine on temperature distribution and a 1-D heat transfer model was developed with validation from experimental data. The test results indicated that the surface temperature of both turbine and compressor was largely impacted by the engine and they linearly varied with the temperature of the exhaust gases. Chen and Sun [26] have examined the effect of heat resistance on the performance of a closed gas turbine cycle. The results indicated that the power output of the cycle was dependent on the effectiveness of the three heat exchangers discussed. They concluded that for the maximum power production, an optimal temperature matching in the working fluid of the cycle and of the surrounding heat reservoirs existed. Maffulli and He [27] have focused their research on the effects of wall temperature on heat transfer coefficient for high-pressure turbines. Computational investigation suggested strong dependence of heat transfer coefficient on wall temperature, therefore, a three-point nonlinear method was proposed. The new method considered the heat transfer to vary with wall temperature, rather than being independent of it as commonly assumed, and its effectiveness was demonstrated. Ma and Xi [28] have studied the heat transfer and Reynolds number effect on scaling of a centrifugal compressor impeller, but more thorough study on wall heat flux effects was still required for engineering guidance. Although extensive investigations regarding heat transfer effect on gas turbine engine cycle or turbine have been conducted, the study of the heat transfer effect on compressor, especially for miniaturized gas turbine compressor, is still limited.

1.1.3 Tip Clearance Effect

The effect of tip clearance is a critical issue in determining compressor performance. For miniature gas turbines, the effect of tip clearance is amplified due to the increased tip clearance ratio, as a result of manufacturing tolerances. Both experimental and numerical investigations have been widely conducted regarding conventional gas turbines or linear cascade, which provided assistance in the analysis of tip clearance effect for miniaturized models. Domercq and Escuret [29] have studied the effects of tip clearance variations on the matching of compressor stages. Their research illustrated the effect of increased rear block clearance on performance and stability based on available experimental data and then a numerical tool was introduced with its validity demonstrated. The validated numerical tool was demonstrated to be capable in allowing the adjustment of aerodynamic design to the range of in-service clearances. Puterbaugh and Brende [30] have investigated the interaction of shock and tip clearance flow in a transonic compressor rotor. A combination of experimental, computational and analytical efforts was used and their results suggested that the change of momentum was attributed to the shock-induced pressure rise and it should be accounted as the reason for interaction of tip clearance flow and shock. Williams and Gregory-Smith [31] have utilized a linear cascade to assess large tip clearance effects, based on both experiments and computations. Their results suggested the loss did not further increase with clearance greater than 4% and the blade loading increased toward the tip when clearance was larger than 2%, which was unexpected. Van Zante and Strazisar [32] compared numerical results with Laser-Doppler Velocimeter (LDV) measurement, proving recommendations for achieving accurate numerical simulation of tip clearance flows, based on a transonic compressor rotor. Chen and Greitzer [33] have proposed a similarity method for analyzing compressor tip clearance flow. The clearance velocity field was decomposed into independent throughflow and crossflow, due to the much smaller chordwise pressure gradients in the clearance region. Their method emphasized on the vortical structure associated to tip clearance as it was the dominant feature of the end wall flow. Wang and Xi [34] have considered the

deformation of impeller for the investigation of tip clearance variation effect on centrifugal compressor performance. The deformation of impeller geometry was due to the thermal loads and mechanical loads, and it was taken into account by fluid/solid interaction method in their work. The impeller deformation and adjusted tip clearance was claimed to influence the aerodynamic performance and structure reliability of the compressor system. Kunte and Schwarz [35] have investigated the tip clearance and bleed effect, based on a centrifugal compressor stage. Experimental data were gathered and compared with CFD results from TRACE, which was developed by DLR. Their results contributed to the understanding of the flow phenomena in the pipe diffusor of a centrifugal compressor. Besides that, TRACE was also used to investigate the tip clearance effects in an axial transonic compressor by Ciorciari and Lesser[36]. Kwak and Zhang and Deng [37] have investigated the operating conditions, tip clearance sizes and external unsteady excitations on the tip clearance flow in an isolated axial compressor. The results showed that the unsteady tip clearance vortex was in a periodic manner and the frequency of the unsteady tip clearance vortex was independent of the external excitations with different frequencies. Han [38] have also studied the heat transfer coefficient near tip clearance regions and their results showed that the heat transfer coefficient on the tip increased with the increase of tip clearance. Kato and Taniguchi [39] have experimentally and numerically investigated the compressor cascade flows with tip clearance, at a low Reynolds number condition. The low Reynolds number condition represents compressor operating at high altitude missions or compressor in a compact engine core with reduced blade size. Their research highlighted the importance of casing wall relative motion in analyzing leakage flow. Although many endeavors have been made regarding the tip clearance flows in compressor, the tip clearance effect on compressor performance and efficiency for miniaturized gas turbines is still limited.

1.1.4 Micro Gas Turbines

Considerable endeavors have been made to understand the performance of Micro Gas Turbines (MGT). Gong and Sirakov [40] explained that MGT differed from conventional gas turbines because it had a low operating Reynolds number, hence a relatively higher skin friction and heat transfer rate. Ferrari and Pascenti [41] have built MGT for educational purpose and their tests provided suggestions about the MGT performance and control strategy development. Mizuki [42] has discussed the problems for developing ultra MGT system, from the internal flow and performance characteristics point of view. Following that, the design and manufacturing processes of ultra MGT centrifugal compression system was explained, with measured results also presented. Zanger and Widenhorn [43] have experimentally investigated the pressure losses on the performance of a MGT system. Both steady-state and transient conditions were considered in their study to aid the understanding of pressure loss. Verstraete and Alsalihi [44] have numerically studied the heat transfer in MGT. Their research considered the turbine and compressor of MGT and tried to quantify the heat transfer and to reveal the different mechanisms that contributed to it for both components. Steele and Baldwin [45] have considered the insertion of shock wave compression into MGT, for the purpose of increasing efficiency and reducing costs. Their proposed technology offered potential advantages for greater efficiency, fewer parts, lower weight, etc. Chen and Zhang [46] have investigated the correlation of adjusting mass flow rate and optimization of thermodynamic performance. Although extensive researches have been conducted regarding MGT, more thorough understanding of MGT performance characteristic is still required.

1.2 Layout of Dissertation

In this study, the effects of miniaturization of gas turbine compressor are studied computationally. Parameter studies are conducted regarding aforementioned factors. Numerical results are validated with available experimental data to generate confidence of the computational tools and methods applied. The overall

performance and flow structure are analyzed, to understand the behavior of fluid properties during operation, for both conventional and miniaturized gas turbine compressor.

Chapter 1 presents the background and motivation for this study. In addition, a literature review is presented, regarding the follow-up parameter studies to be discussed.

Chapter 2 presents the theory and fundamentals applied in this study. Fundamentals of fluid dynamics, numerical approach and the theory of gas turbines are introduced to aid the understanding of compressor operation and discussions addressed in follow-up chapters.

Chapter 3 presents the validation of the computational tools and methods. Numerical results are validated with available experimental data, providing confidence of applying adopted operation conditions in later study. Mesh generation techniques and grid independence study are discussed, as they are essential for generating reliable results. Numerical techniques, such as rotor-stator interaction treatment and turbulence model selection, are also discussed. Flow field analysis based on the benchmark case is conducted to aid understanding of the behavior of fluid properties.

Chapter 4 presents the study of the Reynolds number effect, i.e. when compressor is miniaturized. Varying scaling factors are applied on the original compressor model, to rescale the compressor size. Operation conditions are kept identical with validation case, with similitude principle fulfilled. This is conducted to maintain Reynolds number the only varying parameter in this study.

Chapter 5 presents the study of the heat transfer effect, when varying thermal conditions are applied. Results from adiabatic wall condition, predefined heat flux condition and isothermal wall condition are compared as well as with available experimental data. Compressor size is also changed, to understand the effect of different thermal conditions when engine size changes, i.e., at different Reynolds number conditions.

Chapter 6 presents the study of the tip clearance effect, with three different methods adopted. The effect of tip clearance at constant Reynolds number condition and at varying Reynolds number condition are both investigated. The analysis of tip clearance impact on flow field has helped explain the change of compressor performance when clearance gap is considered.

Chapter 7 presents the conclusions and remarks of this research. Recommendations for future work based on current study are also provided.

The Appendix I presents a case study of the KJ-66 MGT compressor, to further understand the performance of MGT. Comparison of numerical results and experimental data is conducted and CFD well captures the experimental output. Analysis of flow structure and irreversibility within the compressor is also carried out.

The Appendix II presents some of the experimental data from NASA Lewis Research Center[47, 48], which is used for the validation of the current numerical study.

Chapter 2

Theory & Fundamentals

In this chapter, the fundamentals of fluid dynamics and gas turbine engine will be discussed in section 2.1 and section 2.2, respectively. In addition, details of the numerical approach related to this work will also be introduced in section 2.3. The solid understand of the subject and the techniques, is beneficial for the implement of practical and reliable approach to solve the problems.

2.1 Fundamentals of Fluid Dynamics

Fluid dynamics is a sub-discipline of fluid mechanics, dealing with the motion of fluids. Fluid dynamics principles and theories are widely applied in different applications, including weather forecasting, subsea pipeline design, drag reduction of aircraft and offshore wind turbines, etc. The theory of fluid dynamics is based on the continuum assumption, whether for liquids or gases, fluids are assumed to be continuous rather than discrete molecules. On the foundation of that, fluid properties including density, pressure, temperature and so forth, are defined at infinitesimally small points and assumed to vary continuously.

The Navier-Stokes equations are usually used to describe fluid motion, where stress linearly depends on velocity gradient and pressure. Equation 2.1 shows the general compressible form of Navier-Stokes equation.

$$\rho\left(\frac{\partial \vec{v}}{\partial t} + \vec{v}\cdot\nabla\vec{v}\right) = -\nabla p + \mu\nabla^2\vec{v} + \left(\frac{\mu}{3}\right)\nabla(\nabla\cdot\vec{v}) + \rho\vec{g} \qquad (2.1)$$

where $\vec{v}$ is the flow velocity, ρ is the fluid density, p is the pressure, μ is the dynamic viscosity, $\vec{g}$ is the body accelerations per unit mass, and ∇ is the gradient operator.

2.1.1 Conservation Laws

Three conservation laws are used for solving fluid dynamics problems. The mathematical formulation of these principles in an Eulerian System is based on the concept of a control volume, which is a specified volume air flows through. The integral formulation of the conservation laws includes the change of mass, momentum and energy within the control volume. The conservation of these properties is further illustrated in details, respectively.

Conservation of Mass

The conservation of mass principle states that mass is neither created nor destroyed in the control volume [49]. In another word, the rate of change of fluid mass within a control volume equals to the net rate of mass flux into the volume. Equation 2.2 shows the integral form of the continuity equation[50].

$$\frac{\partial}{\partial t}\int_{\Omega} \rho d\Omega + \oint_{\partial\Omega} \rho(\vec{v}\cdot\vec{n})dS = 0 \qquad (2.2)$$

where Ω is the defined control volume, $\partial\Omega$ is the closed surface of the control volume. We introduce a surface element dS its associated, outward pointing unit normal vector$\vec{n}$. ρ is the fluid density, $\vec{v}$ is a velocity vector and t is time.

Conservation of Momentum

The conservation of momentum principle indicates that any change of momentum of the air within a control volume is occurred by the net flow of air into the volume and the action of external forces on the air within the volume. Equation 2.3 shows the integral form of the equation of the momentum conservation law[50].

$$\frac{\partial}{\partial t}\int_{\Omega} \rho\vec{v}d\Omega + \oint_{\partial\Omega} \rho\vec{v}(\vec{v}\cdot\vec{n})dS = \int_{\Omega} \rho\vec{f_e}d\Omega - \oint_{\partial\Omega} p\vec{n}dS + \oint_{\partial\Omega}(\bar{\bar{\tau}}\cdot\vec{n})dS \qquad (2.3)$$

where $\rho\vec{f_e}$ is the body force per unit mass, $\bar{\bar{\tau}}$ is a viscous stress tensor, such as viscos forces.

Conservation of Energy

The conservation of energy principle indicates that, in an isolated system, the total energy remains constant. Although energy can be converted from one form to another, it cannot be created nor destroyed. Equation 2.4 shows the integral form of energy conservation equation in fluid dynamics[50].

$$\frac{\partial}{\partial t}\int_{\Omega} \rho E d\Omega + \oint_{\partial\Omega} \rho H(\vec{v}\cdot\vec{n})dS = \oint_{\partial\Omega} \kappa(\nabla T\cdot\vec{n})dS + \int_{\Omega}\left(\rho\vec{f_e}\cdot\vec{v} + \dot{q}_h\right)d\Omega + \oint_{\partial\Omega}(\bar{\bar{\tau}}\cdot\vec{v})\cdot\vec{n}dS \quad (2.4)$$

where E is the total energy per unit mass of a fluid which is written as $E = e + \frac{|\vec{v}|^2}{2} = e + \frac{u^2+v^2+w^2}{2}$,with e the internal energy per unit mass and u, v, w the velocity components. H is the total enthalpy which is written as $H = h' + \frac{|\vec{v}|^2}{2} = E + \frac{p}{\rho}$, with h' the enthalpy per unit mass. κ is the thermal diffusivity coefficient, T is the temperature, $\dot{q}_h$ is the time rate of heat transfer per unit mass.

2.1.2 Compressible Flow

The compressibility of flow is classified by the fluid density. The change in pressure and temperature results in changes in density, though it is more common for gases. The determination of compressible or incompressible fluid dynamics is evaluated by the Mach number (the ratio of the flow speed to the sound speed) of the flow. Generally, significant compressibility occurs when the Mach number is great than 0.3, and the compressible fluid dynamics is supposed to be used in this situation [51]. The study of jet engines, high-speed aircraft and gas pipelines are all counted as compressible flow problems.

For situations where compressibility is essential, such as shock waves and sound propagation, more general description of the Navier-Stokes equation is required, as the fluid compressibility is taken into account. Equation 2.1 has previously shown the compressible form of Navier-Stokes equation. Although for many fluids, the dynamic viscosity μ depends significantly on the temperature and μ is

regarded as a function of spatial location. However, it happens often that the differences in temperature are small enough for μ to be assumed uniform over the fluid[52].

2.1.3 Viscous Flow

As a measurement of fluid resistance to gradual deformation, Due to shear stress or tensile stress, viscosity usually refers to the resistance of fluid deformation. For fluid dynamics applications, the viscous problem is induced by effects of fluid friction on the fluid motion. For evaluating whether viscous or inviscid equations should be applied for the problem, Reynolds number (*Re*) is often referred to. Equation 2.5 shows the definition of Reynolds number [53, 54].

$$Re = \frac{\rho v L}{\mu} \tag{2.5}$$

where L is a reference length, v is the reference velocity of the fluid, μ is the dynamic viscosity of the fluid, ρ is the density of the fluid. As a dimensionless quantity, the Reynolds number is defined as the ratio of inertial forces to viscous forces, as indicated in its definition equation, which quantifies the importance of these two types of forces for certain flow condition. Therefore, for high Reynolds number problems, the inertial forces are more prominent than the viscous force, and for very high Reynolds number the flow can be assumed to be inviscid in bulk of the flow region, although this assumption does not apply to the thin boundary layer at the wall and viscosity should always be taken into consideration. On the contrary, for very low Reynolds numbers, for example, when Re<<1, the inertial forces should be neglected and the viscous forces dominant, which is usually known as creeping flow.

Special attention should be paid to the flow near solid boundaries, where boundary layer is generated due to non-slip condition, even when Reynolds number is high. A thin region of large strain rate near solid boundaries enhances the effect of viscosity, and induces vorticity. Therefore, viscous flow equations should be used, if the calculation of net forces on bodies is required. In

computational fluid dynamics which will be discussed in details shortly, the combination of solving Euler equations, which is valid for the inviscid flow away from wall, and solving of boundary layer equations, which is valid in the near wall region involving viscosity, is feasible.

2.1.4 Turbulent Flow

Turbulent flow is usually characterized by a high irregular, stochastic, fluctuating motion, including recirculation or eddy generation. Flow without the exhibition of turbulence is called laminar flow, where the kinetic energy of fluctuation dies out because of the action of fluid molecular viscosity. Mathematically, Reynolds decomposition is often used to represent turbulent flow, in which the flow is decomposed into an average component and a perturbation component. Usually, Reynolds number is referred for the determination of turbulence. Turbulence will first be sustained when Reynolds number larger than a critical value of about 2040 in a pipe [55], and flows at Reynolds number larger than 5000 are typically turbulent. The appearance and interaction of different scales of unsteady vortices are often observed for turbulent flow.

The irregularity and randomness of flow makes it "The most important unsolved problem of classical physics", as described by Nobel Laureate Richard Feynman[56]. However, it is believed that turbulent flow can be well described by the Navier-Stokes equations. For most flows of interest, for example, the flow over aircraft wings or flow in jet engine, etc., the Reynolds number is beyond 1×10^6, turbulent models are required to solve these real-life problems. Typically, the large scale turbomachines operates at high Reynolds numbers and exhibit turbulent flow[57]. The typical operation Reynolds number range is 4.5×10^5 to 8.5×10^5 for gas turbine engine blades[58]. The MGT to date are mostly in the low Reynolds number range from 1×10^2 to 1×10^5, indicating mainly laminar flow and high viscous losses [57, 59, 60]. In the current study, the operating Reynolds number ranges from 2.14×10^5 to 8.54×10^5, therefore the flow remains fully turbulent. The Reynolds-averaged Navier-Stokes equations (RANS) together with additional turbulence modelling, is an approach to model turbulent flow effects.

Other approaches such as large eddy simulation (LES) are also promising methodology to model turbulent flow [61].

Turbulent flow is of interest for various researches, as it induces many effect, either beneficial or adverse for certain applications. The boundary layer skin friction often increases because of the interaction of fluid and solid surface, which results in the increase of drag. Furthermore, the laminar-turbulent transition in the boundary layer is often affected by the Reynolds number, the pressure distribution of the outer flow, the wall roughness, etc.[62], which will have impact on the drag generation. In addition, turbulent flow enhances the heat and mass transfer, when fluid particles exhibit additional transverse motion. Because of the difficulty to predict and control of turbulent flow, endeavors to better understand the issue is always required.

2.1.5 Fundamentals of Aerodynamics

The Aerodynamics is a sub-field of fluid dynamics, specifically concerned with studying the motion of air. Therefore, many aspects of aerodynamics theory follow those of the fluid dynamics. The recent work of aerodynamics focuses on issues related to compressible flow, turbulence and boundary layers, which are discussed previously. The wind tunnel experimentation, empirical approximation, mathematical analysis and computer simulations have developed into the scientific basis for the development of heavier-than-air flight, since the first achievement of it in 1903 by the Wright brothers.

In addition to the equations of conservation of mass, momentum and energy, which are used for solving the fluid dynamics problems, the ideal gas law is often required to completely specify the problem of aerodynamics. Equation 2.6 illustrates the common form of the ideal gas law, which approximates the state of a hypothetical ideal gas [63].

$$PV = nRT \tag{2.6}$$

where P is the absolute pressure of the gas, V is the volume of the gas, n is the substance of gas in moles, R is the gas constant ($R = 8.314j \cdot k^{-1}mol^{-1}$), and T is the absolute temperature of the gas. This thermodynamic equation of state relates the pressure as a function of other thermodynamic variables for the fluid. The continuum assumption is also applied, during the study of air motion around an object. The continuum flow field is characterized by properties including velocity, pressure, density and temperature, based on the spatial position and time. The fundamental forces of interest in aerodynamics problems are lift, drag, thrust and weight. Figure 2.1 shows forces on an airfoil, where the lift and drug are aerodynamics forces occurred by flow over a solid body.

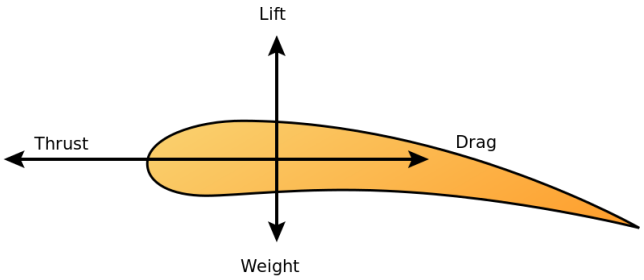

Fig 2.1 Forces on an airfoil

As mentioned earlier, the compressibility of flow should also be addressed, especially for aerodynamics problems where high Mach number flow is often involved. According to the speed of the fluid motion, or the value of Mach number of flow, aerodynamics problems are classified into several branches. Usually, when the motion of airflow is much lower than the speed of sound, i.e., Mach number is less than 1, the flow is classified to be subsonic flow. For subsonic flow problems, the effect of compressibility is considered small when Mach number is smaller than 0.3 as discussed earlier, while the compressible aerodynamics should be applied when Mach number is larger than that value. When the airflow speed falls in the range of Mach 0.8-1.2, the flow is considered as transonic problem. This definition is applicable when some parts of the airflow are subsonic which other parts become supersonic, and generally fall between the critical Mach number ranges. When the airflow speed is greater than the speed of

sound, or Mach 1, the flow is classified as supersonic aerodynamic problems. In contrast with subsonic aerodynamic problems, the presence of shock waves and the compressibility effects of high-velocity, make supersonic aerodynamics problems behave differently. Both transonic and supersonic problems should be considered as compressible aerodynamics problems.

2.2 Theory of Gas Turbine

Gas turbine is a type of internal combustion engine. It is composed of an upstream rotating compressor, a downstream turbine, and a combustion chamber in-between. Figure 2.2 shows the cutaway view of an axial gas turbine. The compressor pressurizes air flows through it, providing higher pressure when it enters the combustion chamber which follows. Higher energy density is achieved when the mixture of pressurized air and fuel ignites in the combustion chamber, and high-temperature flow is thus generated. The gas flow with high pressure high temperature expands in the turbine, producing the shaft work output in the process. The shaft work is used to drive the compressor as it shares the same shaft with turbine. The exhausted gases comes after the turbine produce thrust for the jet engines, and additional thrust is generated by the ducted fan located in front of the compressor, which can also be observed in Figure 2.2.

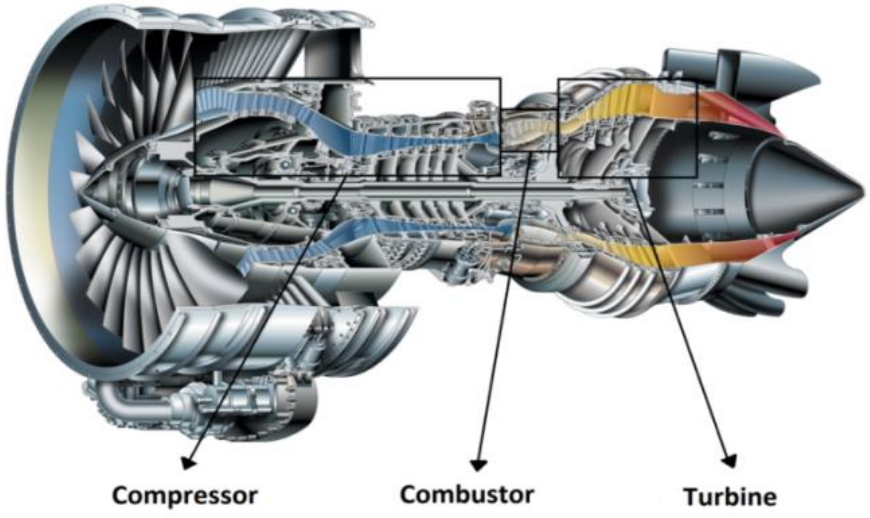

Fig 2.2 Cutaway view of an axial gas turbine [64]

As illustrated in Figure 2.2, atmosphere air enters the frontal ducted fan which is also driven by the shaft, some of the air enters compressor and flows through the gas turbine from left to right, while the rest of the air bypasses the turbine, also contributing to thrust. Both compressors and turbine parts are composed of many small rows of airfoil shaped blades, with some rows connected to the inner shaft and rotate at high speed while others remain stationary. The spinning rows are defined rotors and the fixed rows are defined stators.

For a typical gas turbine engine, it follows the thermodynamic Brayton cycle. The Brayton cycle is composed of three thermodynamic processes, including the isentropic compression, isobaric combustion and the isentropic expansion. Conventionally, it is assumed that the exhausted gases are reused in the intake, for the purpose of thermodynamic analysis as a closed system. Figure 2.3 shows the process of an idealized open Brayton cycle.

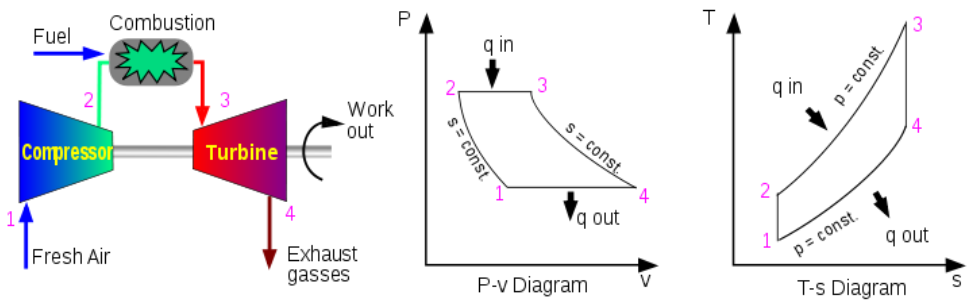

Fig 2.3 An idealized Brayton cycle [65]

As illustrated in Figure 2.3, ambient air is drawn into compressors and pressurized during the isentropic process, which is process from point 1 to point 2 in the P-V diagram; from point 2 to point 3, a constant pressure process, due to the chamber open to flow in and out, is existing, heat is added as compressed air runs through a combustion chamber and burns with fuel; The pressurized and heated air gives up its energy and expands through turbines during another isentropic process from point 3 to point 4, while simultaneously, some work extracted by turbine powers

the compressor in return; From point 4 to point 1, pressure is maintained constant as exhausted gases are reused as assumed.

However, ideally isentropic compression or expansion cannot be realistically achieved, thus losses of work efficiencies is inevitable. Therefore, the efficiency of the ideal Brayton cycle is defined in Equation 2.7[66].

$$\eta = 1 - \frac{T_1}{T_2} = 1 - (\frac{P_1}{P_2})^{(\gamma-1)/\gamma} \tag{2.7}$$

where γ is the heat capacity ratio. According the previous research, the increase of the compression ratio generally increases the overall power output of a Brayton cycle [67]. Figure 2.4 further illustrates how the conclusion is drawn.

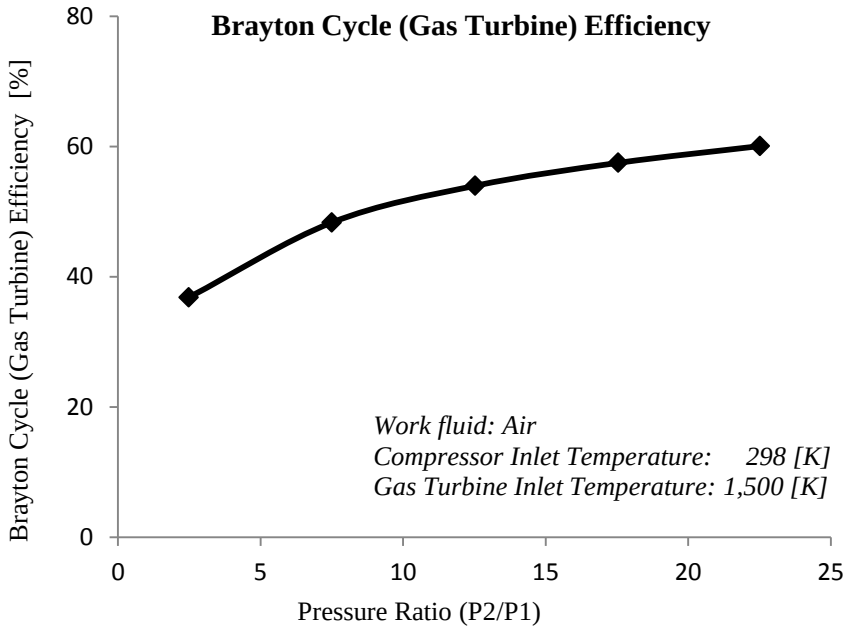

(a)

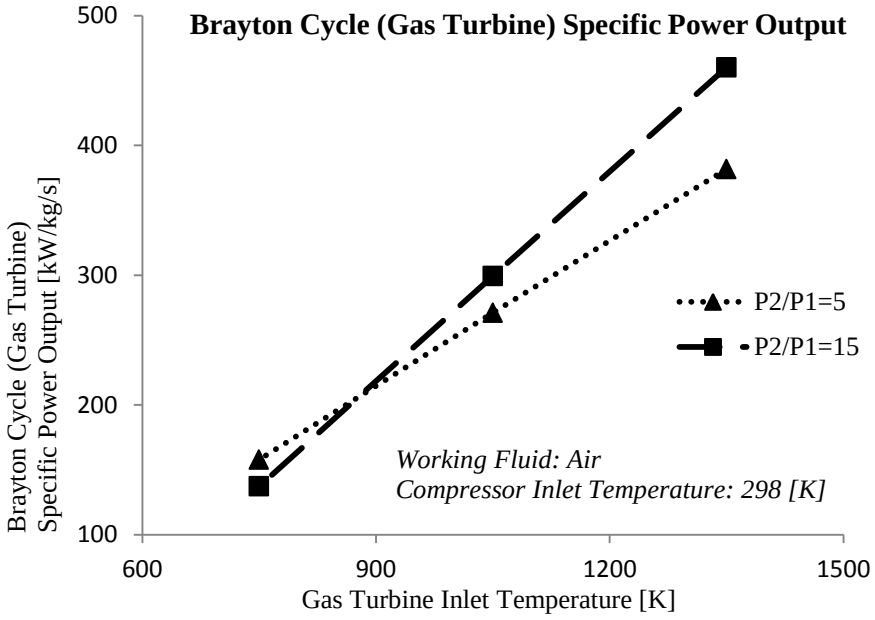

(b)

Fig 2.4 (a) Cycle efficiency changes with an increase in pressure ratio & (b) Specific power output changes with an increase in gas turbine inlet temperature for two different pressure ratios [68]

2.3 Fundamentals of Numerical Approach

The development of computer power and resources, has promoted the utilization of computational fluid dynamics, abbreviated as CFD, in solving and analyzing fluid flow related problems. In this section, the fundamentals of numerical approach, which are closely related in this work, will be discussed in details.

2.3.1 Discretization Method

Most CFD solvers use the finite volume method (FVM) to discretize and solve the Navier-Stokes equation. The FVM evaluates and calculates the values of partial differential equations at discrete places on a meshed geometry [69, 70]. In FVM, the small volume surrounding each mesh node point is considered. The divergence terms in a partial differential equation are evaluated as fluxes at the surface of each finite volume, where flux entering a defined volume is identical to those leave the volume, makes FVM a conservative method. Equation 2.8

illustrates the integral formulation of the conservation law for a general vector quantity $\vec{U}$ as[50],

$$\frac{\partial}{\partial t}\int_{\Omega} \vec{U} d\Omega + \oint_{\partial\Omega}\left[(\bar{\bar{F}}_C - \bar{\bar{F}}_D)\cdot\vec{n}\right]dS = \int_{\Omega} \vec{Q}_V d\Omega + \oint_{\partial\Omega}(\bar{\bar{Q}}_S\cdot\vec{n})dS \tag{2.8}$$

where $\vec{U}$ is a general vector quantity, $\bar{\bar{F}}_C$ is the convective flux tensor and $\bar{\bar{F}}_D$ is the diffusive flux tensor. Vector $\vec{Q}_V$ is the volume sources, and the surface sources are a tensor$\bar{\bar{Q}}_S$. As mentioned previously, Ω is the element of control volume and dS is the element surface. Figure 2.5 shows how the conservation of variables is achieved in FVM, based on a 2D example[50].

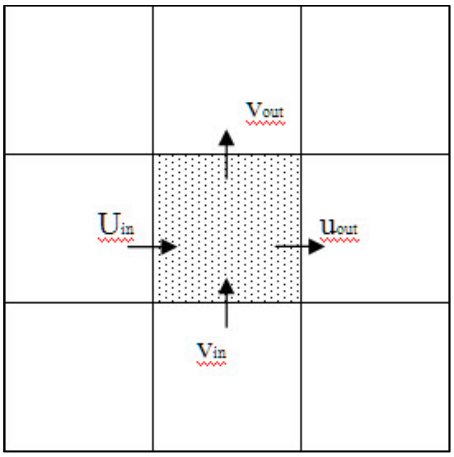

Fig 2.5 Conservation of flux in a finite volume based on 2D example

The FVM is commonly used in CFD codes, due to its advantages in memory usage and solution speed. Especially for large fluid dynamics problems, where high Reynolds number and turbulent flow is involved, FVM is considered a reliable approach. In addition, FVM is easily formulated to allow both structured and unstructured meshes, which makes it a suitable choice for many CFD packages.

2.3.2 Flow Solvers

Within this study, the commercial CFD package ANSYS Fluent is adopted, as it is robust and well-validated software and is widely used in turbo-machinery community [71-73]. Compared with other solvers, such as the ANSYS embedded

CFX, Fluent is superior in its capability in density-based coupled solver which is not feasible in CFX, as specified in the ANSYS 14.0 capability brochure[74]. For flow problems where strong coupling or interdependence between density, energy, and momentum exist, density-based coupled solver is a more appropriate option[75]. Besides that, both Fluent and CFX are capable and reliable for rotating equipment. Due to the control-volume-based technique adopted in Fluent, the governing equations are converted to algebraic equations which can be numerically solved. Mentioned previously, the control volume technique consists of integrating the governing equations about each control volume, yielding discrete equations that conserve each quantity on a control-volume basis.

For the purpose of obtaining solutions of time-dependent ordinary differential equations and partial differential equations in numerical analysis, implicit and explicit methods are considered.

Implicit Method

Implicit method solves an equation involving both current and the later state of the system. Equation 2.9 mathematically illustrates the equation to be implicitly solved,

$$G\big(Y(t), Y(t+\Delta t)\big) = 0 \tag{2.9}$$

where $Y(t)$ is the state of current system, Δt is a small time step applied, $Y(t+\Delta t)$ is the state at the later time which is supposed to be solved. Figure 2.6 shows the stencil for a common implicit method based equation[76], where the point of interest is geometrically arranged by a numerical approximation routine.

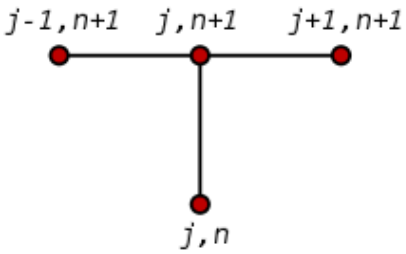

Fig 2.6 The stencil for a common implicit method based equation

where t_n is the current time, t_{n+1} is the next time step, the special locations of the finite volume used for calculation are indicated as j-1, j, j+1. Therefore, the state of the system at t_{n+1} is also involved in the calculation. Compared with explicit method, extra computation is required for an implicit approach. However, the ability to maintain numerical stability for computations with larger time steps, making implicit method a time efficient approach for certain cases.

Explicit Method

Different from the implicit method, where both the state of current and the later state of the system is considered during computation, explicit method obtains the state of the system at a later time simply based on the current state of the system. Equation 2.10 illustrates the equation to be explicitly solved,

$$Y(t + \Delta t) = F(Y(t)) \tag{2.10}$$

where $Y(t + \Delta t)$ is explicitly expressed by a formula of $Y(t)$, rather than considered an unknown in an equation. In comparison with the implicit method stencil, Figure 2.7 shows the stencil for explicit method based equation[76].

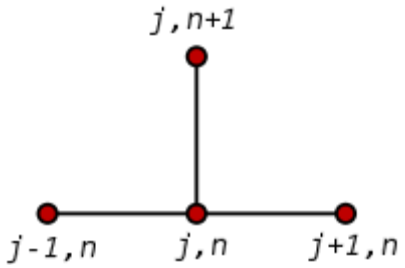

Fig 2.7 The stencil for a common explicit method based equation

where only the state of the system at t_n is involved for obtaining the state of the system at t_{n+1}, the values at location j-1, j, j+1 at t_n is used for the calculation, as illustrated in the geometric arrangement. Explicit method is easier to implement compared with the implicit approach. However, for cases which impractical small time steps Δt is required to maintain numerical stability, the explicit approach is not feasible anymore. The selection of implicit or explicit approach depends on the problem to be solved, i.e., time step size required to ensure convergence. In

addition, the computational resource available and computational cost should also be concerned, though it may not be the key issue with today's computing power.

2.3.3 Turbulence Models

For turbulent flows, the complexity of flow phenomena and range of length scales involved in turbulence has made most modeling approach either computationally too expensive or computationally impossible for resolving all scales involved in turbulence. Therefore, numerical model is required to approximate the unresolved phenomena. The computational cost highly depends on the resolution of the simulation, or how much the turbulent scales are resolved.

The Reynolds-averaged Navier-Stokes (RANS) equations are extensively discussed, as it is the turbulence modeling approach utilized in this work. RANS equations approximate the motion of fluid flow, where decomposition of instantaneous quantity into time-averaged and fluctuating quantities is performed. Time-averaged solution to the Navier-Stokes equations is achieved by approximation, based on knowledge of the properties of flow turbulence. Equation 2.11 shows the expression of RANS equations for incompressible Newtonian fluid[50].

$$\frac{\partial \bar{v}_i}{\partial x_i} = 0$$

$$\rho \frac{\partial \bar{v}_i}{\partial t} + \rho \bar{v}_j \frac{\partial \bar{v}_i}{\partial x_j} = -\frac{\partial \bar{p}}{\partial x_i} + \frac{\partial}{\partial x_j}(\bar{\tau}_{ij} - \rho \overline{v_i' v_j'}) \tag{2.11}$$

Where $\frac{\partial \bar{v}_i}{\partial x_i} = 0$ indicates the mass conservation. $\rho \bar{v}_j \frac{\partial \bar{v}_i}{\partial x_j}$ represents the change of mean momentum caused by the unsteadiness and convection of the mean flow, $\rho \frac{\partial \bar{v}_i}{\partial t}$ is the mean body force, $-\frac{\partial \bar{p}}{\partial x_i}$ is the isentropic owing to the mean pressure field, $\bar{\tau}_{ij} = \mu\left(\frac{\partial \bar{v}_i}{\partial x_j} + \frac{\partial \bar{v}_j}{\partial x_i}\right)$ is the laminar viscous stresses, and $\tau_{ij}^R = -\rho \overline{v_i' v_j'} = -\rho(\overline{v_i v_j} - \bar{v}_i \bar{v}_j)$ is the Reynolds stress tensor which represents the transfer of momentum due to turbulent fluctuations.

However, for compressible free shear layers, e.g., hypersonic flows, combustion and flames, density fluctuations need to in some cases be taken into account. Therefore, the density (mass) weighted or Favre decomposition to certain quantities in RANS equations should be applied, which is known as Favre- and Reynolds-Averaged Navier-Stokes equations as described in Equation 2.12 below,

$$\frac{\partial \bar{\rho}}{\partial t} + \frac{\partial}{\partial x_i}(\bar{\rho}\tilde{v}_i) = 0$$

$$\frac{\partial}{\partial t}(\bar{\rho}\tilde{v}_i) + \frac{\partial}{\partial x_j}\left(\bar{\rho}\tilde{v}_i\tilde{v}_j\right) = -\frac{\partial \bar{p}}{\partial x_i} + \frac{\partial}{\partial x_j}(\tilde{\tau}_{ij} - \bar{\rho}\widetilde{v_i^{"}v_j^{"}})$$

$$\frac{\partial}{\partial t}\left(\bar{\rho}\tilde{E}\right) + \frac{\partial}{\partial x_j}\left(\bar{\rho}\tilde{v}_j\tilde{H}\right) = \frac{\partial}{\partial x_j}\left(k\frac{\partial \tilde{T}}{\partial x_j} - \bar{\rho}\widetilde{v_j^{"}h^{"}} + \widetilde{\tau_{ij}v_i^{"}} - \bar{\rho}\widetilde{v_j^{"}K}\right)$$

$$+\frac{\partial}{\partial x_j}\left[\tilde{v}_i\left(\tilde{\tau}_{ij} - \bar{\rho}\widetilde{v_i^{"}v_j^{"}}\right)\right] \qquad (2.12)$$

Similar with the Reynolds averaging, the viscous stress tensor in the momentum (and energy) equation is extended by the Favre-averaged Reynolds-stress tensor $\tau_{ij}^{F} = -\bar{\rho}\widetilde{v_i^{"}v_j^{"}}$.

The current study, however, solves the RANS equations as the Morkovin's hypothesis[77] is assumed to be valid, where state that for wall-bounded flows up to a Mach number of about five, the turbulent structure of a boundary layer is not notably influenced by density fluctuations if $\rho' \ll \bar{\rho}$. The problems addressed in thesis falls into this category. The utilization of RANS computation for compressor study in similar range of Reynolds number is well justified [78-80]. In order to close the RANS equations, the nonlinear Reynolds stress, which is arisen by the convective acceleration, require additional modeling. Different turbulence models are developed to represent scales of the unresolved flow. The selection of reliable turbulence model is essentially important, for the purpose of obtaining satisfactory simulation results and shortening computational time. However, many factors should be taken into consideration for the decision of turbulence models, e.g., the required accuracy level, the physics encompassed in the flow, the

available computational resources and the simulation time requirement, etc. In this section, three main turbulence models will be further discussed in details.

Spalart-Allmaras Turbulence Model

The Spalart-Allmaras turbulence model is a one equation model, which solves a transport equation for the kinematic eddy (turbulent) viscosity, without calculating the length scale related to the shear layer thickness [81]. The Spalart-Allmaras model is specifically designed for aerospace applications involving wall-bounded flows and is gaining popularity for turbo-machinery applications as well. The transport equation of SA model is illustrated in Equation 2.13.

$$\frac{\partial \tilde{\upsilon}}{\partial t} + \frac{\partial}{\partial x_j}\left(\tilde{\upsilon} v_j\right) = C_{b1}(1 - f_{t2})\tilde{S}\tilde{\upsilon} + \frac{1}{\sigma}\left\{\frac{\partial}{\partial x_j}\left[(\upsilon_L + \tilde{\upsilon})\frac{\partial \tilde{\upsilon}}{\partial x_j}\right] + C_{b2}\frac{\partial \tilde{\upsilon}}{\partial x_j}\frac{\partial \tilde{\upsilon}}{\partial x_j}\right\} - \left[C_{w1} f_w - \frac{C_{b1}}{\kappa^2} f_{t2}\right]\left(\frac{\tilde{\upsilon}}{d}\right)^2 + f_{t1}\|\Delta\tilde{\upsilon}\|_2^2 \tag{2.13}$$

where $\tilde{\upsilon}$ is eddy-viscosity variable, $C_{b1}(1 - f_{t2})\tilde{S}\tilde{\upsilon}$ is the turbulent viscosity production term, $\frac{1}{\sigma}\left\{\frac{\partial}{\partial x_j}\left[(\upsilon_L + \tilde{\upsilon})\frac{\partial \tilde{\upsilon}}{\partial x_j}\right] + C_{b2}\frac{\partial \tilde{\upsilon}}{\partial x_j}\frac{\partial \tilde{\upsilon}}{\partial x_j}\right\}$ is conservative and non-conservative diffusion, $-\left[C_{w1} f_w - \frac{C_{b1}}{\kappa^2} f_{t2}\right]\left(\frac{\tilde{\upsilon}}{d}\right)^2$ is the near-wall turbulence destruction, $f_{t1}\|\Delta\tilde{\upsilon}\|_2^2$ is the transition source of turbulence. The destruction of turbulence occurs in the near wall regions, where dominant viscous damping and wall blocking effects exist. Furthermore, $\upsilon_L = \mu_L/\rho$ denotes that laminar kinetic viscosity and *d* is the distance to the closest wall. The other terms or factors are calibrated constants for each modelled physical effect.

The initial and boundary conditions in the Spalart-Allmaras model have to be specially addressed[50]. The initial value of $\tilde{\upsilon}$ is usually defined as $\tilde{\upsilon} = 0.1\upsilon_L$ and the same value is also specified at inflow boundaries. The $\tilde{\upsilon}$ value at outflow boundaries is extrapolated from the interior of the computational domain. At solid walls, it is appropriate to set $\tilde{\upsilon} = 0$ and therefore $\mu_T = 0$.

Realizable K-epsilon Turbulence Model

The realizable k-epsilon ($k-\epsilon$) turbulence model is a more recently developed model which generally describes the turbulence by two transport equations. Different from the standard $k-\epsilon$ turbulence model, the realizable $k-\epsilon$ model contains a new formation for the turbulent viscosity. In addition, the realizable $k-\epsilon$ model includes a new transport equation for the dissipation rate ϵ, derived from an exact equation for the transport of the mean-square vortices fluctuation. Equation 2.14 illustrates the modelled transport equations for the turbulent kinetic energy (k), which determines the energy in the turbulence, and the turbulent dissipation (ϵ), which determines the rate of dissipation of the turbulent kinetic energy.

$$\frac{\partial}{\partial t}(\rho k)+\frac{\partial}{\partial x_j}(\rho k v_j)=\frac{\partial}{\partial x_j}\left[\left(\mu_L+\frac{\mu_T}{\sigma_k}\right)\frac{\partial k}{\partial x_j}\right]+G_k+G_b-\rho\epsilon-Y_M+S_k \tag{2.14a}$$

And

$$\frac{\partial}{\partial t}(\rho\epsilon^*)+\frac{\partial}{\partial x_j}(\rho v_j\epsilon^*)=\frac{\partial}{\partial x_j}\left[\left(\mu_L+\frac{u_T}{\sigma_\epsilon}\right)\frac{\partial\epsilon^*}{\partial x_j}\right]+\rho C_1 S\epsilon-\rho C_2\frac{\epsilon^2}{k+\sqrt{\nu\epsilon}}+C_{1\epsilon}\frac{\epsilon}{k}C_{3\epsilon}G_b+S_\epsilon \tag{2.14b}$$

where $$C_1=\max\left[0.43,\frac{\eta}{\eta+5}\right],\eta=S\frac{k}{\varepsilon},S=\sqrt{2S_{ij}S_{ij}}$$

In these equations, $G_k=-\rho\overline{v_i'v_j'}\frac{\partial v_j}{\partial x_i}$ is the generation of turbulence kinetic energy due to the mean velocity gradient. $G_b=\beta g_i\frac{\mu_t}{Pr_t}\frac{\partial T}{\partial x_i}$ is the generation of turbulence kinetic energy due to buoyancy, with Pr_t the turbulent Prandtl number for energy, $g_i$the component of the gravitational vector in the ith direction, $\beta=-\frac{1}{\rho}(\frac{\partial\rho}{\partial T})_p$ the coefficient of thermal expansion. $Y_M=2\rho\epsilon M_t^2$ is the contribution of the fluctuating dilatation in compressible turbulence to the overall dissipation rate, with $M_t=\sqrt{\frac{k}{a^2}}$ the turbulent Mach number and $a=\sqrt{\gamma RT}$the speed of sound.

$C_2 = 1.9$ and $C_{1\epsilon} = 1.44$ are constants, $\sigma_k = 1.0$ and $\sigma_\epsilon = 1.2$ are the turbulent Prandtl numbers for k and ϵ, S_k and $S\epsilon$ are user-defined source terms. Furthermore,$\epsilon = \epsilon_w + \epsilon^*$, with ϵ_w the value of the dissipation rate at the wall. The realizable $k-\epsilon$ turbulence model satisfies certain mathematical constraints on the Reynolds stresses and it is consistent with the physics of turbulent flows. In addition, it is superior in performance for flows involving with separation, recirculation, rotation, and boundary layer under strong adverse pressure gradient, which is not reliable or feasible with the standard $k-\epsilon$ turbulence model.

The initial and boundary conditions in the Realizable $k-\epsilon$ model have to be specially addressed[50]. At solid walls, the proper boundary conditions are $k = 0$ and $\epsilon^* = 0$. This also indicates that $\mu_T = 0$ at walls. At inflow boundaries, the values of k and ϵ^* are computed based on turbulent intensity and length scale,

$$(T_u)_\infty = \frac{\sqrt{\frac{2}{3}k_\infty}}{\|\vec{v}_\infty\|_2}, \quad (l_T)_\infty = \frac{C_\mu k_\infty^{3/2}}{\epsilon_\infty^*} \tag{2.15}$$

where we assume $\epsilon_\infty^* = \epsilon_\infty$. The value of $(l_T)_\infty$ is chosen between 10^{-3} and 10^{-2} times the mean radial blade spacing for turbomachinery application. At outflow boundaries, the values of k and ϵ^* are extrapolated from the interior of the computational domain. In addition, wall functions [82-86] are usually used to deliver the values of k and ϵ^* at the node adjacent to the wall, as the realization $k-\epsilon$ equations are not solved at the wall and at the first layer of nodes.

SST K-omega Turbulence Model

The shear-stress transport (SST) k-omega ($k-\omega$) turbulence model is a two-equation eddy-viscosity model, which can effectively blend the robust and accurate formulation of the $k-\omega$ model in the near-wall region with the free-stream independence of the $k-\omega$ model in the far field [87]. The formulation of $k-\omega$ model makes it directly usable from the free-stream towards the wall through the viscous sub-layer, while it switches to $k-\epsilon$ behavior in the free-stream. Equation 2.16 illustrates the transport equations for the SST $k-\omega$ model.

k is the turbulent kinetic energy, which also determines the energy in the turbulence as mentioned shortly previously for the realizable $k-\epsilon$ model, and ω is the specific dissipation, which determines the scale of the turbulence[50].

$$\frac{\partial}{\partial t}(\rho k)+\frac{\partial}{\partial x_j}\left(\rho k v_j\right)=\frac{\partial}{\partial x_j}\left[(\mu_L+\sigma_k\mu_T)\frac{\partial k}{\partial x_j}\right]+\tau_{ij}^F S_{ij}-\beta^*\rho\omega k \qquad (2.16a)$$

And

$$\frac{\partial}{\partial t}(\rho\omega)+\frac{\partial}{\partial x_j}\left(\rho\omega v_j\right)=\frac{\partial}{\partial x_j}\left[(\mu_L+\sigma_\omega\mu_T)\frac{\partial\omega}{\partial x_j}\right]+\frac{C_\omega\rho}{\mu_T}\tau_{ij}^F S_{ij}-\beta\rho\omega^2+2(1-f_1)\frac{\rho\sigma_{\omega 2}}{\omega}\frac{\partial k}{\partial x_j}\frac{\partial\omega}{\partial x_j} \qquad (2.16b)$$

The terms on the right-hand side for both equations represent conservative diffusion, eddy-viscosity production and dissipation, respectively. Furthermore, $2(1-f_1)\frac{\rho\sigma_{\omega 2}}{\omega}\frac{\partial k}{\partial x_j}\frac{\partial\omega}{\partial x_j}$ in the ω-equation describes the cross diffusion. The strain rate tensor S_{ij} follows the form$S_{ij}=\frac{1}{2}(\frac{\partial v_i}{\partial x_j}+\frac{\partial v_j}{\partial x_i})$, the Favre-averaged turbulent stressτ_{ij}^F follows the form$\tau_{ij}^F=-\bar{\rho}\widetilde{v_i''v_j''}$. Compared with the standard $k-\omega$ model, SST $k-\omega$ model has made several refinements. Firstly, the blending function is designed to be one in the near-wall region to activate the standard $k-\omega$ and to be zero away from the surface to activate transformed $k-\epsilon$ model, since both models are added together. Secondly, a damped cross-diffusion derivative term is incorporated in the ω equation for SST $k-\omega$ model. Thirdly, modification of the definition of the turbulent viscosity is conducted to account for the transport of the turbulent shear stress. In addition, the modeling constants are different. Based on the refinement, SST $k-\omega$ is more reliable and accurate than the standard $k-\omega$ model for extensive flow problems, including transonic shock waves, airfoils, and adverse pressure gradient flow, etc.

The initial and boundary conditions in the SST $k-\omega$ model have to be specially addressed[50]. At solid walls, the values of the kinetic turbulent energy and the specific dissipation are $k=0$ and $\omega=10\frac{6\mu_L}{\rho\beta_1(d_1)^2}$, with d_1 the distance of the

first node (cell centroid) from the wall. Special attention should be drawn that the refined grid should has y^+<3. For the inflow boundaries, the recommended freestream values are,

$$\omega_\infty = C_1 \frac{\|\vec{v}_\infty\|_2}{L},\ (\mu_T)_\infty = (\mu_L)_\infty 10^{-C_2},\ k_\infty = \frac{(\mu_T)_\infty}{\rho_\infty}\omega_\infty \qquad (2.17)$$

Where L is the length of the computational domain, $1 \leq C_1 \leq 10$ and $2 \leq C_2 \leq 5$, respectively. At outflow boundaries, the values of k and ω are extrapolated from the interior of the computational domain.

2.3.4 Rotating Machinery Interface Treatment Approach

The scope of this work demands special treatment for rotor-stator interaction. Therefore, multiple fluid zones and rotating zones are involved, with interface boundaries applied to separate the zones. For rotating machinery problems, there are three approaches for interface treatment which are supported by ANSYS Fluent.

a) The Multiple Reference Frame Model (MRF)

b) The Mixing Plane Model

c) The sliding Mesh Model

Flow field is assumed to be steady for both MRF and mixing plane models since approximate means are utilized for rotor and stator effects. The sliding mesh model is used when the flow field is assumed to be unsteady and rotor-stator interaction is considerably intensive. More accurate simulation can be obtained by using sliding mesh method but much more computational cost is demanded.

The Multiple Reference Frame Model

For the MRF model, the calculation domain is divided into several subdomains. With respect to the laboratory frame, each subdomain might be rotating or translating at different speeds. The governing equations in each subdomain are written with respect to the subdomain's reference frame. Therefore, the moving

reference frame equation is activated for solving flow in each moving cell zone, and the stationary equation is activated if the zone is stationary ($\vec{\omega}$=0), i.e. angular velocity equals to zero. Differs from the mixing plane approach, ANSYS Fluent enforces the continuity of the absolute velocity for the MRF model, providing the correct neighbor value of velocity for the subdomain under consideration. The diffusion and other terms in the governing equations in one subdomain require values for the velocity in the adjacent subdomain at the boundary of them.

The relative motion of a moving zone with respect to adjacent zone is not counted in the MRF approach. Therefore, the MRF is often referred as the frozen rotor approach. Generally, the MRF model is able to provide reasonable approximations for uncomplicated flow between the moving and stationary zones, such as for the turbo-machinery application when rotor-stator interaction is relatively weak.

The Mixing Plane Model

The mixing plane concept is based on the assumption that each fluid zone is solved as a steady-state problem. Circumferentially Area-weighted average ($\overline{U} = \frac{1}{A}\int_A UdA$, where A is the interface area and U is the flow variables) of flow data at mixing plane interface is exchanged on both the rotor outlet and stator inlet boundaries, i.e., profiles of average total pressure, total temperature, turbulence kinetic energy and turbulence dissipation rate and so on are computed at rotor exit and used to update boundary conditions at the stator inlet. Vice versa, similar properties are computed at the stator inlet and used as a boundary condition on the rotor exit. A mixing plane pair is formed by coupling the upstream outlet boundary and a downstream inlet boundary zone, which must be of the following types described in Table 2.1.

Table 2.1 Types of Mixing Plane Pairs

Upstream Boundary	Downstream Boundary
Pressure Outlet	Pressure Inlet
Pressure Outlet	Velocity Inlet
Pressure Outlet	Mass Flow Inlet

Any unsteadiness arising from the circumferential variations is removed in the mixing plane model, such as wakes, separated flow, shock waves, when the flow is passed from upstream boundary to the adjacent downstream zone. However, the mixing plane approach is able to provide reasonable approximations of time-averaged flow field, despite its inherent simplification. The mixing plane model is a cost-effective alternative when it is not feasible to apply sliding mesh model, in the situation that the MRF is not physically meaningful when the flow at the boundary between adjacent zones is not uniform.

The Sliding Mesh Model

Rather than a time-averaged solution, the sliding mesh model provides a time-accurate solution for rotor-stator interaction, which is a necessity when computing unsteady flow field. Although it is the most computationally expensive method in dealing with flows in multiple reference frames, the sliding mesh model provides the most accurate results. Grid interface is formed by associating two adjacent zones, thus the two zones will move relative to each other along the interface. Flux across the interface is computed for each zone and the intersection is determined at each new time step. The intersection of two zones produces an interior zone, and a pair of wall zones for non-periodic problems, as illustrated in Figure 2.8, and the fluxes across the grid interface is principally computed using the time-dependently formed interior zone.

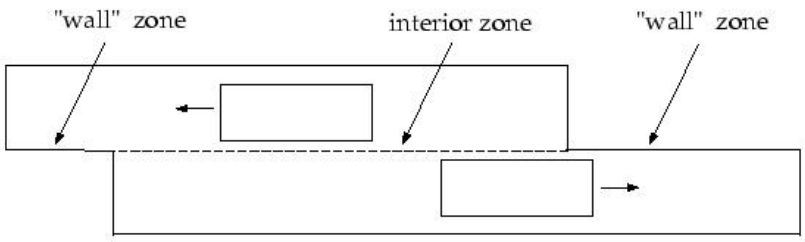

Fig 2.8 Zones formed by non-periodic intersection

The sliding mesh model is reliable for both translating sliding problems, such as trains passing through a tunnel, and time-periodic problems, such as for turbo-machinery application, where rotor-stator interaction is severe. Because of the principles applied in sliding mesh model, transient behaviors is well captured and maintained during the calculation, with relative motion between each zones also counted.

Chapter 3

Validation & Simulation Setup

3.1 Geometry & Design Parameters

Computational methods have taken great steps in the prediction of gas turbine performance [88, 89]. For the purpose of verifying the reliability of the current CFD approach, a validation study is conducted. The NASA Stage35 compressor is chosen as the configuration, as it is well-documented[47, 48]. The design parameters and compressor geometry are shown in Table 3.1 and Figure 3.1 respectively. In total, 36 rotor blades and 46 stator blades compose the full circular of the compressor.

Table 3.1 Design Parameters of NASA Stage35 Compressor

Total Pressure Ratio	1.82
Total Temperature Ratio	1.225
Adiabatic Efficiency	0.828
Polytropic Efficiency	0.842
Flow Coefficient	0.451
Airflow (kg/s)	20.188
RPM at 100% Design Speed	17188.7
Tip Speed (m/s)	454.456
Hub-Tip Radius Ratio	0.7
Rotor Aspect Ratio	1.19
Stator Aspect Ratio	1.26
Number of Rotor Blades	36
Number of Stator Blades	46

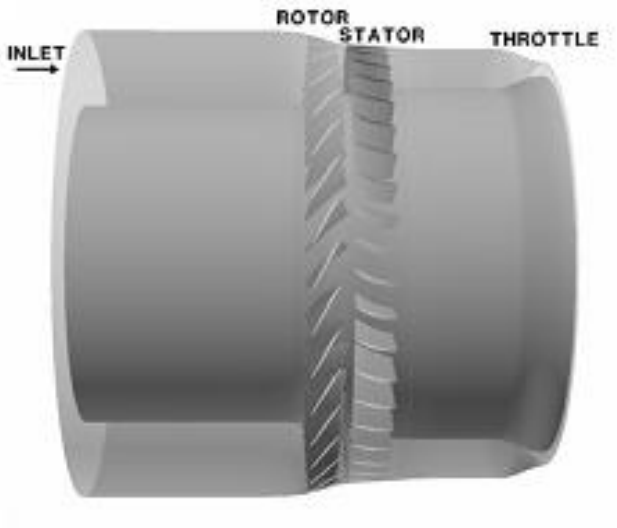

Fig 3.1 NASA Stage35 compressor geometry

The NASA Stage35 compressor is an eight normal stage compressor, in this study, only the first stage is considered. In addition, only one blade passage is meshed to represent the full circular during this numerical study, due to concerns about computational time and resources. Therefore, the rotor fluid passage is built with 10 degrees (circumferential length of 0.044m based on outer radius) and the stator fluid passage is built with 7.83 degrees (circumferential length of 0.033m based on outer radius), with periodic boundary condition applied in azimuthally direction. The geometry of the first stage blade is shown in Figure 3.2, where the alignment of rotor and stator blade is described. The contraction of flow path from rotor entrance towards stator exit is observed, indicating the compression of incoming flow.

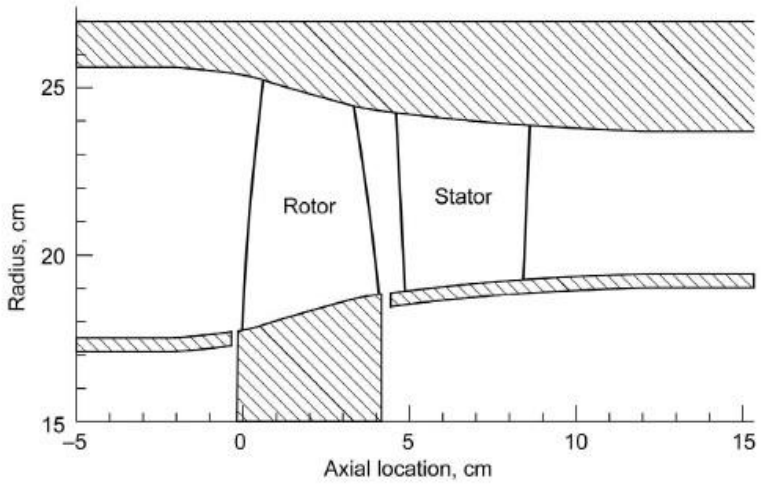

Fig 3.2 Alignment of rotor blade and stator blade

Multiple circular arc (MCA) blade profiles are built, according to the design requirement of NASA Stage35 compressor, aiming to produce the desired velocity diagrams with a minimum relative total pressure loss across the blade row. The blade elements are defined on an up-wrapped conical surface, approximating a surface of revolution generated by revolving the flow streamline about the compressor axis. After that, these elements are stacked about their center of area along a prescribed stacking line. Blade section coordinates are provided on a plane x-y coordinate system normal to a radial line. Three sections of rotor airfoil profiles are presented in Figure 3.3 as an example, which are hub section (radius=7.0000 inches), 50% spanwise section (radius=8.2500 inches), Tip section (radius=9.5520 inches). Figure 3.4 points out the locations of the mentioned three rotor blade sections along the radial direction.

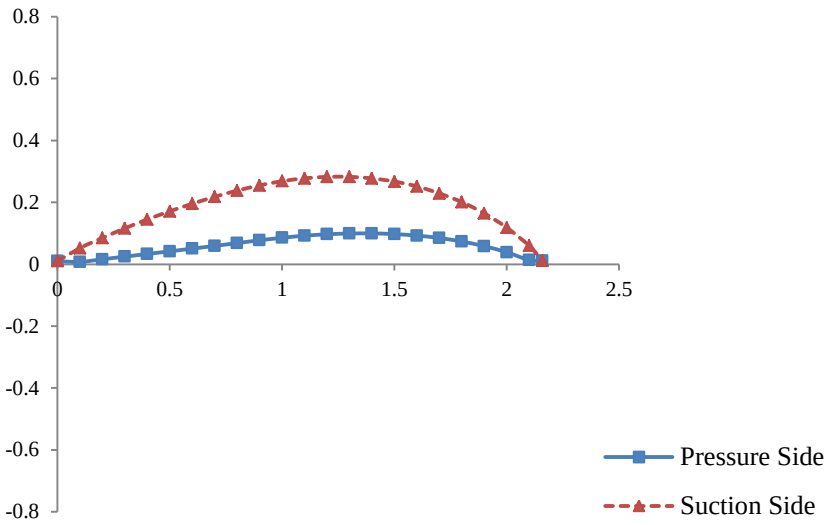

Fig 3.3a Blade profile at rotor hub section

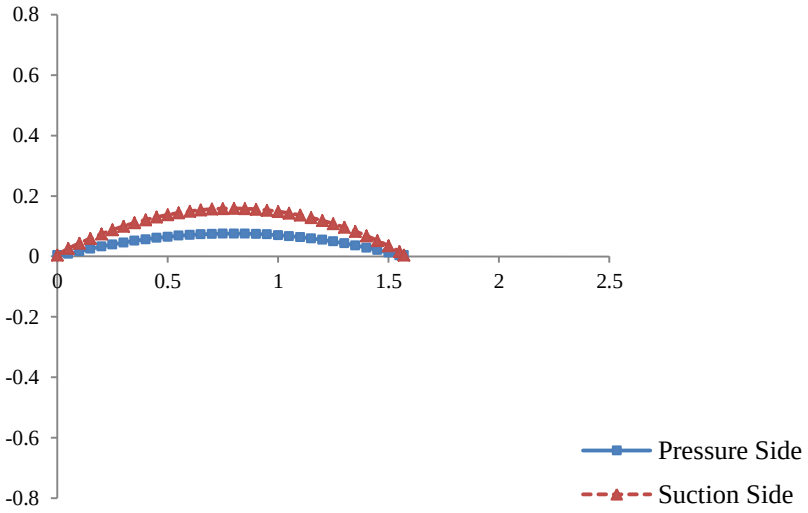

Fig 3.3b Blade profile at rotor 50% spanwise section

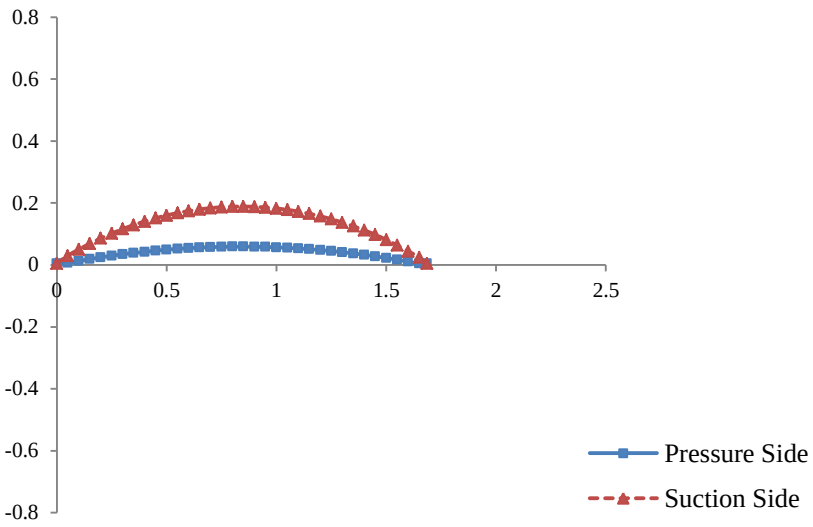

Fig 3.3c Blade profile at rotor tip section

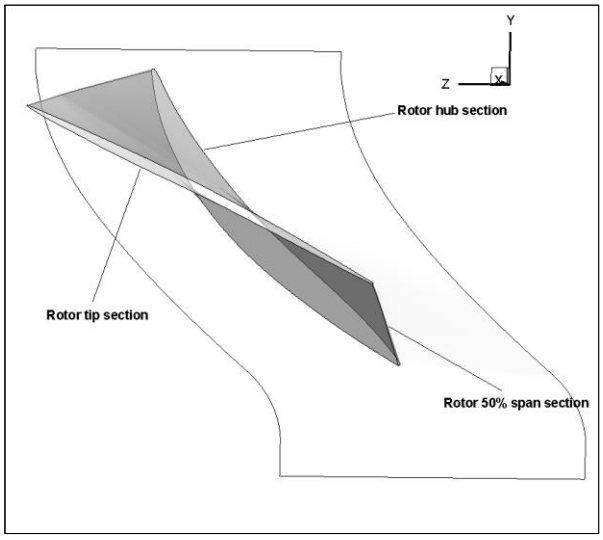

Fig 3.4 Locations of three rotor profile sections along blade radial direction

3.2 Mesh Generation

The best practice from CFD-online is followed and a multi-block structured mesh is generated for the computational domain using the software Gambit 2.4. The tip clearance is not applied currently, though specific research about it is presented shortly. The grid is formed separately for the rotor and stator fluid domain. Mesh refinements are conducted near blade leading and trailing edge regions. Near wall treatment is also employed and a y^+ (a non-dimensional wall distance, $y^+ = \frac{yu_\tau}{v}$, where u_τ is the wall friction velocity, y is the distance to the nearest wall and v is

the kinematic viscosity of the fluid) [62]value is adapted to 1. Figure 3.5 shows the computational grid of rotor and stator domain, for benchmark case.

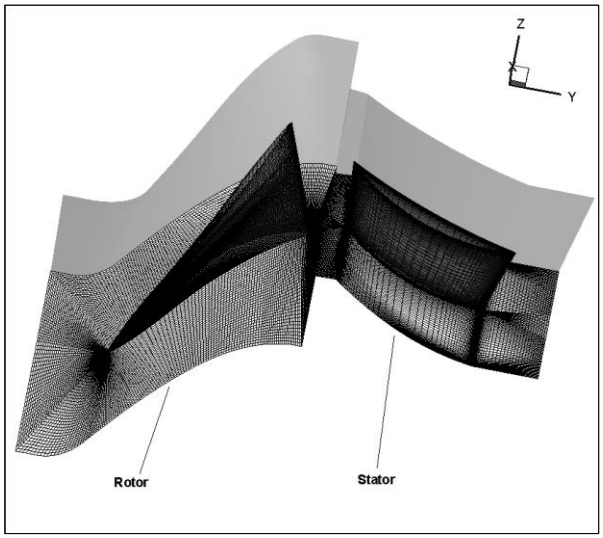

Fig 3.5 Computational grid of rotor & stator domain

Cell skewness is chosen as the criteria for mesh quality guarantee. It is one key measurement in determining cell quality, as it measures the difference between the shape of the cell and the shape of an equilateral cell of equivalent volume. Highly skewed cells can decrease accuracy and destabilize the solution. Although the common academic acceptable limit for skewness of structured meshes is 0.8, our mesh quality examination considers the current mesh acceptable, as the percentage of high skewness cells is negligible. Figure 3.6 presents the quality examination for Grid 3 as an example, where rotor blade with 0.77 million cells and stator blade with 0.58 million cells are coupled to form the continuous flow passage.

From value	To value	Count in range	% of total count (766360)
0	0.1	55027	7.18
0.1	0.2	158217	20.65
0.2	0.3	129972	16.96
0.3	0.4	141369	18.45
0.4	0.5	107984	14.09
0.5	0.6	70064	9.14
0.6	0.7	57558	7.51
0.7	0.8	39918	5.21
0.8	0.9	6248	0.82
0.9	1	3	0.00
0	1	766360	100.00

Measured minimum value: 0.012744
Measured maximum value: 0.900216

Fig 3.6a NASA 35 compressor rotor mesh quality examination for Grid 3

From value	To value	Count in range	% of total count (580400)
0	0.1	138945	23.94
0.1	0.2	198747	34.24
0.2	0.3	78542	13.53
0.3	0.4	74826	12.89
0.4	0.5	59495	10.25
0.5	0.6	29014	5.00
0.6	0.7	700	0.12
0.7	0.8	91	0.02
0.8	0.9	40	0.01
0.9	1	0	0.00
0	1	580400	100.00

Measured minimum value: 0.0674862
Measured maximum value: 0.866205

Fig 3.6b NASA 35 compressor stator mesh quality examination for Grid 3

3.3 Grid Independence Study

Due to concerns about the influence of mesh quality on the computational results, grid independence study is conducted, to determine the sufficient mesh size which guarantees sufficiently accurate results for our further study. Four different mesh cases are considered. As mentioned in section 3.2, Grid 3 is the benchmark case with a dimensionless spacing counts of h_3=1, two coarser Grid 1 and Grid 2 with an additional finer Grid 4 are constructed for comparison purpose. A constant interval of dimensionless spacing counts, Δh=1/5, is applied between two consecutive grids. Table 3.2 illustrates the grid details of four different mesh cases.

According to Table 3.2, a gradual increase of mesh size is achieved, with an interval of about 0.4 million for two consecutive grids.

Table 3.2 Grid Details of NASA Stage35 Compressor for Grid Independence Study

	Dimensionless Spacing Counts h	Total Cells
Grid 1	3/5	0.54 million
Grid 2	4/5	0.94 million
Grid 3	1	1.35 million
Grid 4	6/5	1.93 million

Simulations are conducted based on the commercial code ANSYS Fluent 13.0 for this validation study. The boundary conditions are specified as in section 3.4, with 100% design speed applied. Computational results suggest that 1.35 million mesh cells are sufficient in producing sufficiently accurate results, as indicated in Figure 3.7, when values of total pressure ratio, defined as $Pr = \overline{P_{out}}/\overline{P_{in}}$, and adiabatic efficiency, defined as $\eta_{ad} = ((\overline{P_{out}}/\overline{P_{in}})^{(\gamma-1)/\gamma} - 1)/((\overline{T_{out}}/\overline{T_{in}}) - 1$, are stabilized with further increase of mesh size. Therefore, Grid 3 is considered suitable and will be adopted for follow-up validation studies.

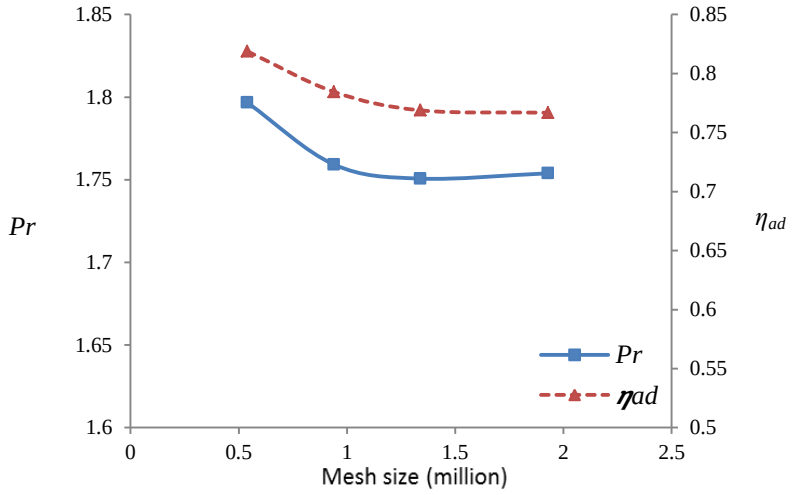

Fig 3.7 Changes of Pr & η_{ad} with the increase of mesh size, with design Mfr at 100% design speed

3.4 Boundary Condition & Numerical Scheme

The designed operation parameter and available experiment results are referred for the boundary condition definition. The definition of suitable initial and boundary conditions are essential, as it determines the state of the fluid at the time t=0. The better initial guess will be, the faster the final solution will be obtained. Furthermore, the probability of divergence during simulation will be reduced correspondingly. At least, the initial solutions should satisfy the governing equations and the additional thermodynamic relations[50].

The mass flow inlet boundary is applied on the rotor frontal surface and the pressure outlet boundary is applied on the stator exit surface. A specific mass flow rate (Mfr) of 172.6kg/m^2×s, corresponding to an Mfr of 0.56kg/s is used, by a conversion of 1/36 of the design total Mfr for this case. The initial gauge pressure values are specifically defined at inlet and outlet boundaries, based on experimental data.

The periodic boundary conditions are implemented to both rotor and stator domain in the azimuthal direction and it represents the full circular by allowing fluid variables across the boundary continuously. All wall boundaries are defined as non-slip ($u = v = w = 0$ at the surface) and adiabatic (Q=0, i.e., heat transfer through wall is not allowed) for the initial case setup, though detailed investigations about heat transfer effect will be discussed in Chapter 5.

The rotor operating speed is defined as 100% and 70% of design speed respectively, depending on validation purpose. While the stator domain remains stationary. The mixing plane method is chosen to address the rotor-stator interaction, where flow data is circumferentially averaged. Discussions about interface method comparison will be addressed in section 3.5. The Spalart-Allmaras turbulence model is selected, based on the validation study in section 3.6 and engineering experience.

In the study presented in this thesis, steady state density based algorithm is used, which produces time-averaged solutions by solving the continuity equation and momentum, energy, species transport as a coupled set of equations using an ideal gas. An implicit formulation is used for numerical solutions and 1st order upwind scheme is utilized to discretize both flow and turbulent viscosity. Small values of under relaxation factor are specified to initiate the simulation and aid convergence. Each computation takes approximately 12 hours to reach the final convergence on 16 processors. Although unsteady RANS or Large Eddy Simulation are also available, which capture the transient phenomenon in more details and may generate more accurate results, the current work is still merited as the compressor general performance change is our main concern and RANS is sufficient in predicting the compressor performance. In addition, transient simulations require more computational time and resources, which would render the parametric studies prohibitively expensive.

3.5 Interface Method Comparison

Because of the intensive rotor-stator interaction during compressor operation, the selection of a reliable interface treatment method is essential. In this section, the comparison of two rotor-stator interaction treatment methods, Mixing Plane (MP) and Multiple Reference Frame (MRF), which are developed for steady state simulations, are conducted. Table 3.3 illustrates the pairs of rotor and stator boundary conditions for two treatment methods.

Table 3.3 Combinations of Rotor and Stator Boundary Conditions at Interface

	Rotor Outlet	Stator Inlet
Mixing Plane	Pressure Outlet	Mass Flow Inlet
Multiple Reference Frame	Interface	Interface

Boundary conditions are specified as mentioned in section 3.4, except for interface method, which are defined in Table 3.3, respectively. Grid 3 is adopted and 100% design speed is applied for both cases. The experimental data from NASA is adopted to validate the simulation results. For this case, the reading

4004 from experiments[47] at 100% design is used. In total, 9 sectional locations from tip to hub are defined, on both rotor inlet and stator outlet boundaries. The values of total pressure and total temperature at these sections are collected. These locations are specified to correspond to the experimental measuring points. The collected data at each section are then averaged respectively, representing the value at that spanwise location.

Figure 3.8 presents the comparison of experiment data, MP results and MRF results for four main bulk properties: *Pr*, *Tr*, η_{ad} and Mach number. Here, the four properties represent sectional quantities, which are in contrast with those in Figure 3.7, where stage quantities are discussed. This definition applies for subsequent discussion, where distributions of bulk properties in spanwise direction refer to sectional quantities while distributions of bulk properties with mass flow rate refer to stage quantities. Figure 3.8a shows the distribution of total pressure ratio. More deviation is observed near the tip region, i.e. at 5% span. The best match of results from the three methods is identified at 85% span. Generally, the numerical results underestimate the experiment results for the value of *Pr*, but MP results show better consistence with the experiment results, compared with results from MRF method. Figure 3.8b shows the distribution of total temperature ratio. Both of the numerical methods produce satisfactory consistence with experimental results. The best prediction of experimental data is identified at 15% span from tip. Figure 3.8c shows the distribution of adiabatic efficiency. Discrepancies among three data sets are obvious, but the trend of efficiency is captured. The largest deviation is observed near tip region, though MP still produces better accuracy compared with MRF method. Despite the extremely large deviation region near tip, MP generally underestimates experimental data by 11% to 20% in the 30% to 95% spanwise region. The friction loss near tip and hub region and especially the tip clearance flow effect near tip region might have contributed to the deviation of η_{ad}. Figure 3.8d shows the distribution of Mach number in radial direction on compressor outlet surface. The MP generally captures the trend of experiment for Mach number, with more deviations observed near shroud, while the MRF doesn't present a correct trend for Mach number distribution. In general, the

validation study for interface method comparison suggests that MP method is more suitable in predicting rotor-stator interaction, and it will be adopted for follow up studies.

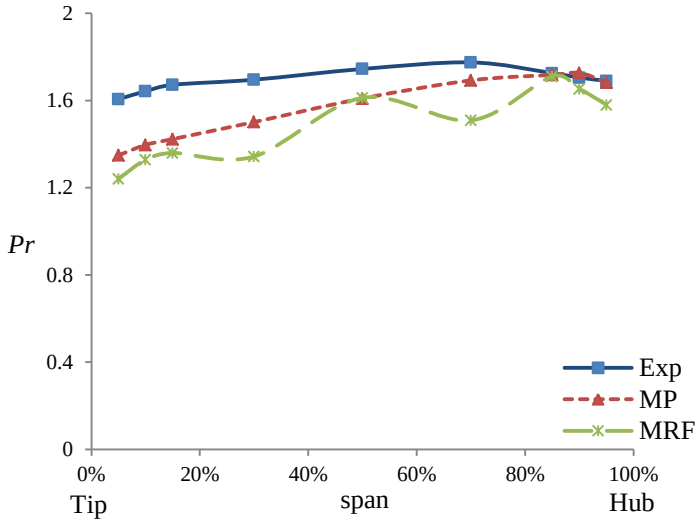

Fig 3.8a Distribution of *Pr* in radial direction for different interface methods, with design Mfr at 100% design speed

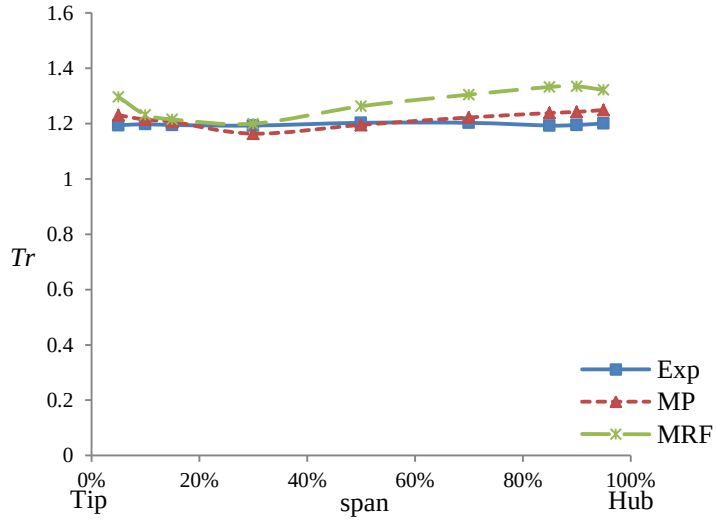

Fig 3.8b Distribution of *Tr* in radial direction for different interface methods, with design Mfr at 100% design speed

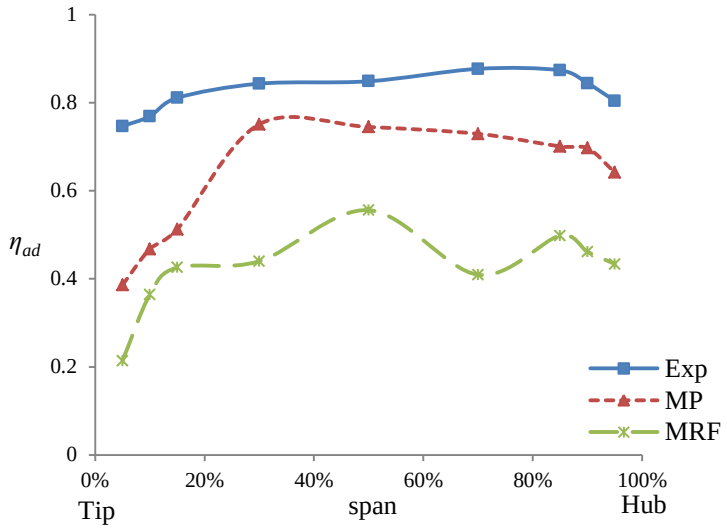

Fig 3.8c Distribution of η_{ad} in radial direction for different interface methods, with design Mfr at 100% design speed

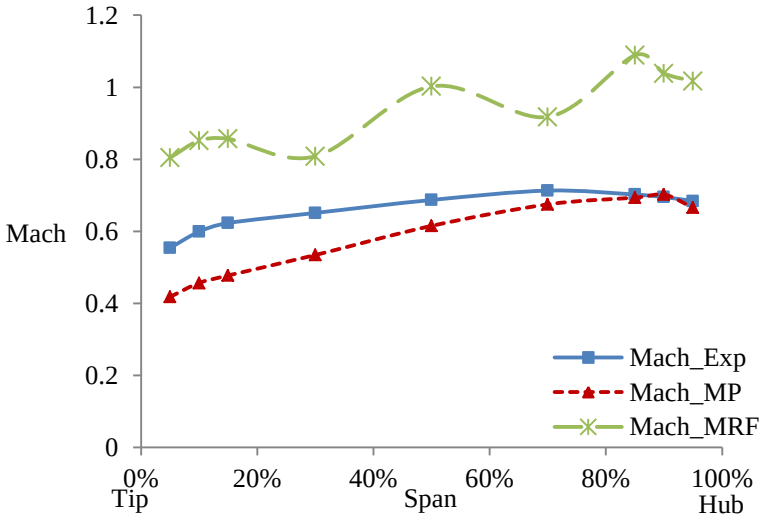

Fig 3.8d Distribution of Mach number in radial direction on compressor outlet surface, with design Mfr at 100% design speed

3.6 Turbulence Model Comparison

For the purpose of closing the Reynolds-averaged Navier-Stokes (RANS) equation, Turbulence models have been created to provide additional modelling of the nonlinear Reynolds stress. In this section, the comparison of three different most commonly employed turbulence models, Spalart-Allmaras, Realizable $k-\epsilon$ and SST $k-\omega$ models, are conducted. These models provide approaches to

compute the turbulence viscosity ῡ, with relatively low cost. Different turbulence models possess their own superiority in dealing with different problems, and that's why this validation study is conducted to determine the most suitable turbulence model in handling our problems.

In this section, the mentioned three different turbulence models are applied for comparison purpose, while all the other boundary conditions follow the same specification given in section 3.4. 100% design speed is initially applied, with a fixed value of designed Mfr. The experimental data from corresponding operation conditions are adopted for validation purpose. As mentioned in section 3.5 previously, 9 locations are specified from tip to hub again to aid our analysis. Figure 3.9 shows the comparisons of distribution of four main concerned properties. Figure 3.9a shows distribution of total pressure ratio. In general, all turbulence models underestimate the *Pr* of experimental data, although the variation of *Pr* along radial direction is well captured by all three methods. The largest discrepancy from experiment results is observed near tip region, but minor discrepancy is observed among the three numerical methods themselves. Figure 3.9b shows the distribution of total temperature ratio. The numerical results from all three methods capture the *Tr* distribution from experiment quite well. Figure 3.9c shows the distribution of adiabatic efficiency. In general, the Spallart-Allmaras model more closely captures the η_{ad} changes at different span locations, while the largest discrepancy is observed near tip and hub region for all three methods. Figure 3.9d shows the distribution of Mach number on compressor outlet surface. The Spallart-Allmaras model and Realizable $k-\epsilon$ model comparatively more closely capture the changes of Mach number obtained from experiment but underestimation of experimental value is also evident. Therefore, the Spallart-Allmaras turbulence model outstands itself for better prediction of compressor η_{ad} based current investigation, and further verification is conducted subsequently to ensure this conclusion.

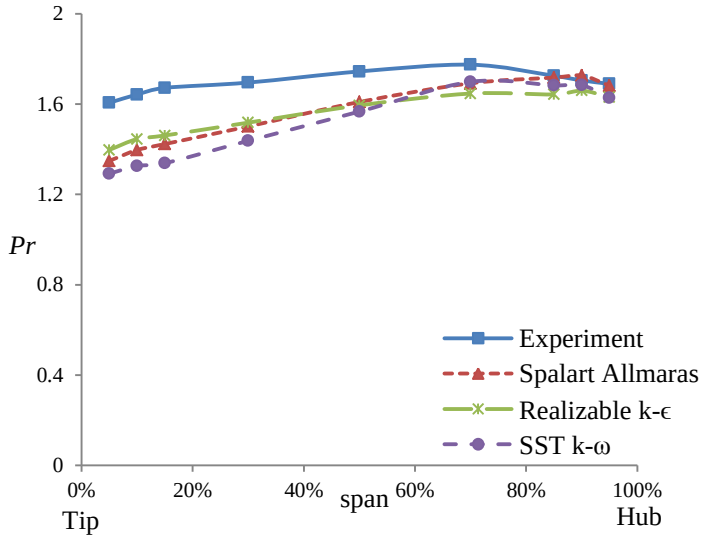

Fig 3.9a Distribution of *Pr* in radial direction for different turbulence models, with design Mfr at 100% design speed

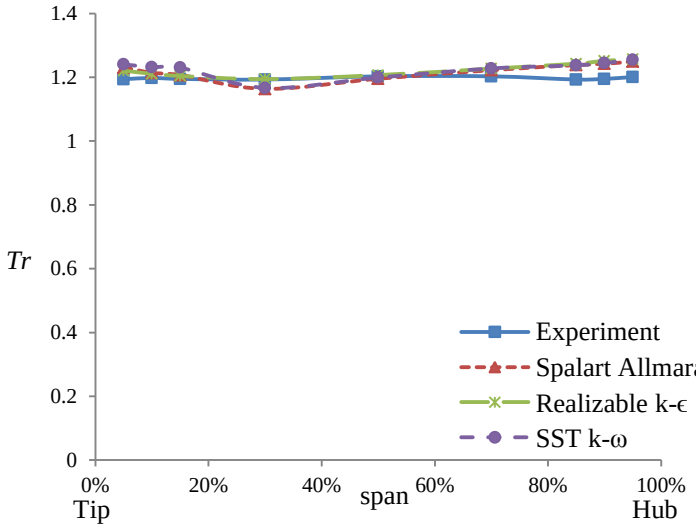

Fig 3.9b Distribution of *Tr* in radial direction for different turbulence models, with design Mfr at 100% design speed

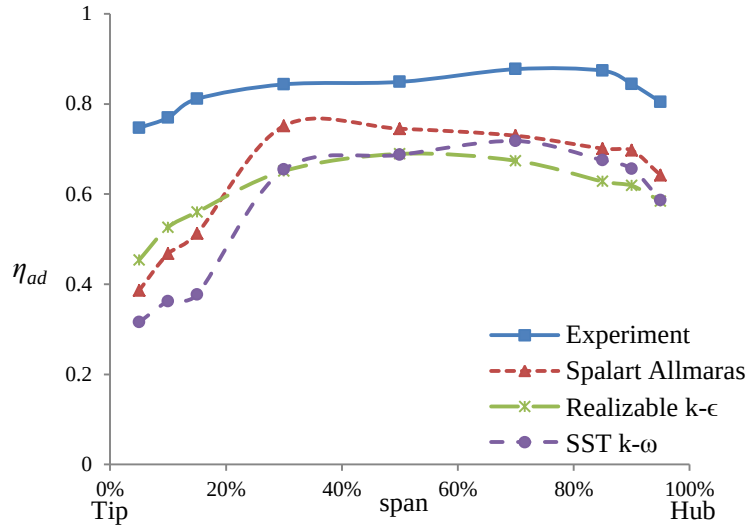

Fig 3.9c Distribution of η_{ad} in radial direction for different turbulence models, with design Mfr at 100% design speed

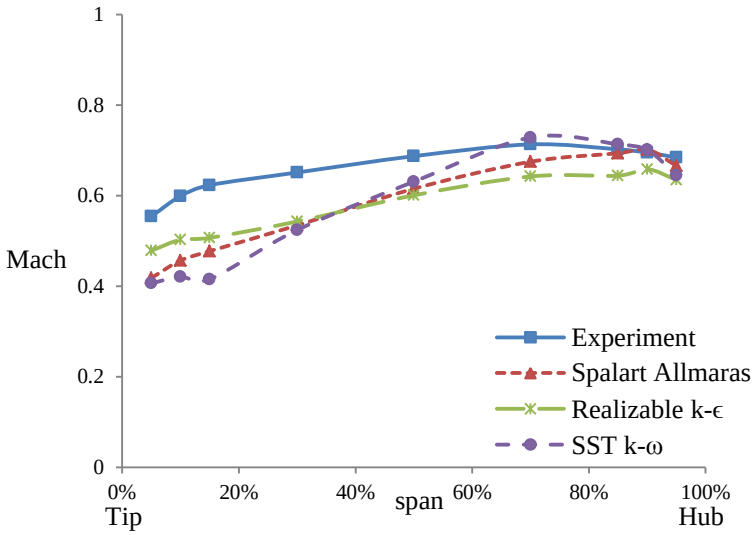

Fig 3.9d Distribution of Mach in radial direction on compressor outlet surface for different turbulence models, with design Mfr at 100% design speed

For the purpose of better understand the capability of different turbulence models in the prediction of compressor performance at high and relatively low operation speed situation, both 100% and 70% design speed are applied to all three turbulence model cases, respectively. Also, Mass flow rate is adjusted to measure the compressor operating range at different operating speed.

Figure 3.10 presents the comparison of numerical results and experimental data at 70% design speed. Figure 3.10a shows that *Pr* decreases with the increase of Mfr

after the optimum value, and numerical results quite well capture the changes of *Pr* measured from experiment. A slight underestimation of experimental data is observed. Figure 3.10b shows that numerical results almost perfectly capture the *Tr* changes from experiment. A slight decrease of *Tr* is observed with the increase of Mfr after its optimal value. Figure 3.10c shows that the stage η_{ad} slightly increases with the increase of Mfr until it reaches the optimal Mfr. Numerical results generally predict a smaller stage η_{ad} at all specified Mfr. In addition, the deviation between numerical results and experimental data amplifies with the increase of Mfr. The difference might be caused by the changing angle of attack at different Mfr for simulation, as the air enters the rotor perpendicularly to the inlet surface while the operation speed of rotor remains 70% speed. The effect of changing angle of attack is diminished in experiment, due to the inlet duct vane in front of the rotor which may induce pre-rotation of air before entering the compressor. In general, all the three turbulence models are capable in predicting compressor operation at 70% design speed.

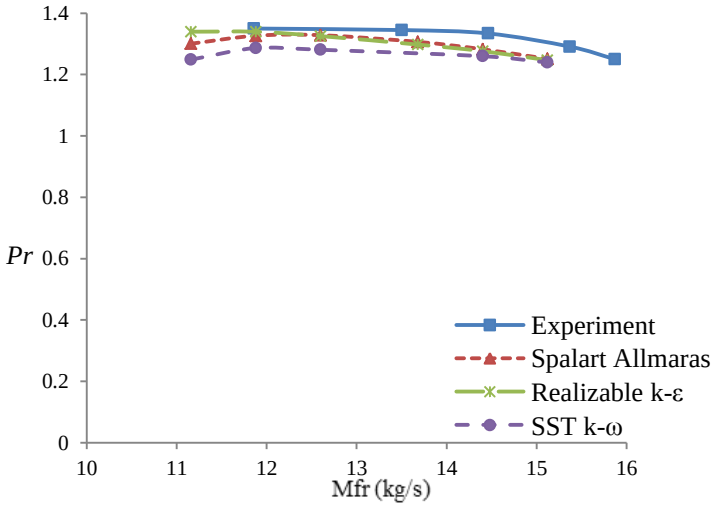

Fig 3.10a Distribution of *Pr* for different turbulence models, with varying Mfr at 70% design speed

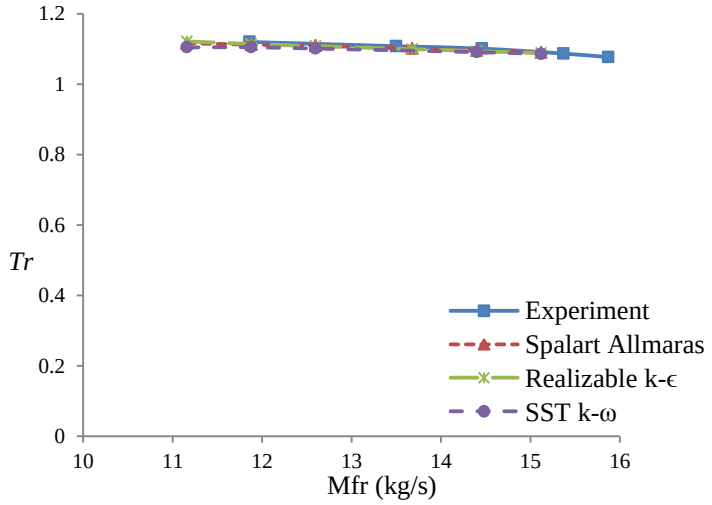

Fig 3.10b Distribution of *Tr* for different turbulence models, with varying Mfr at 70% design speed

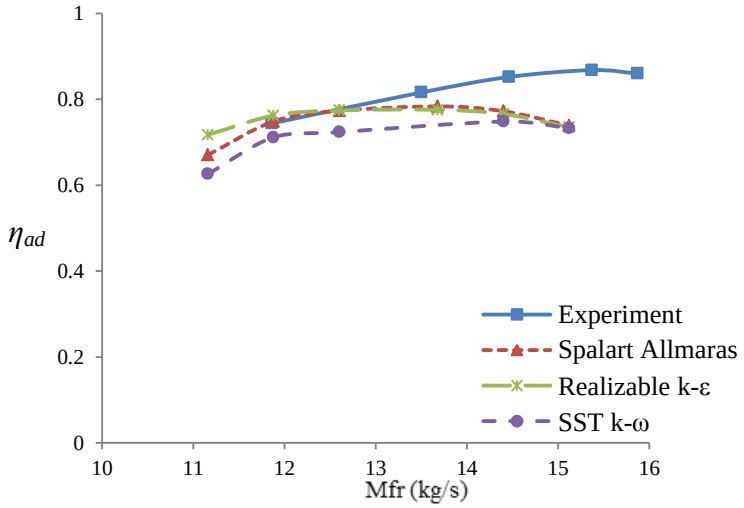

Fig 3.10c Distribution of η_{ad} for different turbulence models, with varying Mfr at 70% design speed

Figure 3.11 presents the comparison of numerical results and experimental data, with varying Mfr at 100% design speed. Figure 3.11a shows when compressor is operating at 100% design speed, numerical results for *Pr* from all three turbulence model tested underestimate experiment results. The *Pr* decreases with the increase of Mfr after its optimal value for the experimental data, similar results are observed for the 70% design speed test. However, only the Spallart-Allmaras and Realizable $k-\epsilon$ turbulence model correctly predict the changes as those from experiment, SST $k-\omega$ turbulence model results deviate that trend by showing an

increase of *Pr* with increased Mfr. Figure 3.11b shows numerical results underestimate experimental data, though all three models capture the experimental trend. The three turbulence models produce almost identical result for the *Tr* prediction. Figure 3.11c shows the numerical prediction of stage η_{ad} changes with the increase of Mfr. The Spallart-Allmaras and SST $k-\omega$ turbulence model generally follow the trend of η_{ad} change from experiment, showing a general increase of η_{ad} until the optimal Mfr is applied. The SST $k-\omega$ turbulence model generates better capture as improves the prediction of flow with adverse pressure gradient, but the Spalart-Allmaras turbulence model gives closer prediction of η_{ad} value, especially in the small flow rate region. In general, the Spallart-Allmaras model produces better prediction of compressor performance at high operation speed.

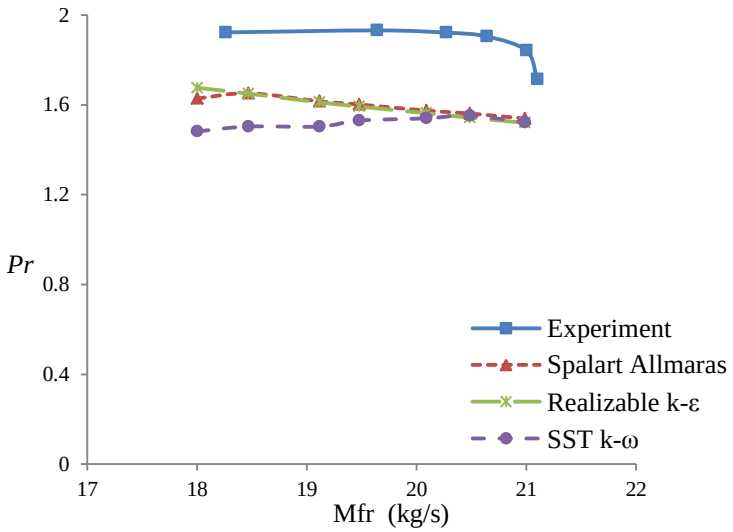

Fig 3.11a Distribution of *Pr* for different turbulence models, with varying Mfr at 100% design speed

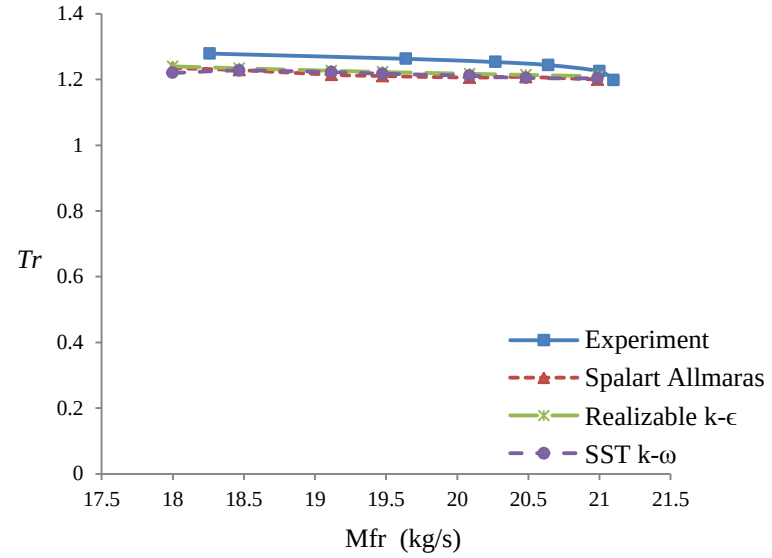

Fig 3.11b Distribution of *Tr* for different turbulence models, with varying Mfr at 100% design speed

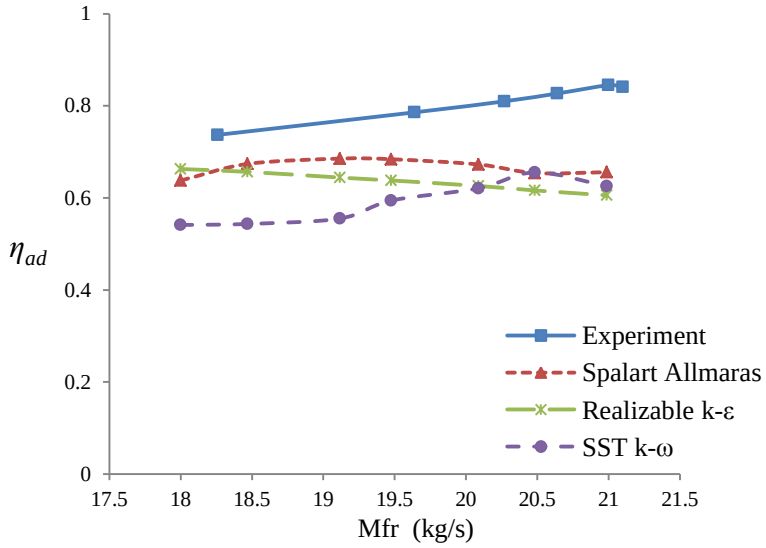

Fig 3.11c Distribution of η_{ad} for different turbulence models, with varying Mfr at 100% design speed

Based on the current numerical study, the Spallart-Allmaras turbulence model produces closer prediction of compressor performance at both high and low operation speed conditions. Furthermore, the Spallart-Allmaras turbulence model does not require as fine a grid resolution in wall-bounded flows as two-equation turbulence models[90], which is an advantage for turbomachinery application when the generation of very fine mesh is often difficult. As a one-equation model, it is simpler alternative to two-equation turbulence models and is well accepted

for turbo-machinery applications. The Spalart-Allmaras turbulence model also shows improvements in the prediction of flows with adverse pressure gradients, which is the applicable to the current study, though the improvements are not as much as the SST $k-\omega$ model[90]. In general, the Spalart-Allmaras turbulence model is a more reliable and suitable approach and it will be employed for further simulations throughout this work.

The current validation study has demonstrated the capability of CFD approach for the investigation of compressor performance. Section 3.1 to section 3.3 have illustrated the geometry and mesh generation in details, also, the reliability of mesh quality is verified to support further simulations. Section 3.4 gives the general boundary condition specification employed, referred to designed parameters and available experiment data. Section 3.5 describes the rotor-stator interaction treatment method and our comparison suggests mixing plane is more accurate to capture interactions between moving and stationary objects, in this case, the NASA 35 compressor. Section 3.6 compares the capability of turbulence models in the prediction of turbulence effect. Detailed analysis is provided for both high speed and relatively low speed operation conditions and our conclusion suggests that the Spalart-Allmaras turbulence model is more reliable and suitable for current study. This validation work laid the foundation of our confidence in adopting CFD as the primary tool for further investigation about compressor performance.

3.7 Flow Field Analysis

For the purpose of more thoroughly understand fluid property changes during compressor operation, the flow field analysis is conducted based on the simulation results obtained from the validation study as previously discussed. Results from the simulation with validated boundary and initial condition setup are utilized for the following discussions in this section. Results from both 100% and 70% design speed are discussed and compared, to support previous validation conclusions. This analysis will be adopted as the benchmark reference for follow up studies.

3.7.1 Flow Field Analysis at 100% Design Speed

In this section, the flow field analysis of the NASA 35 compressor operating at 100% design speed is conducted. Results from design Mfr test are utilized. The total pressure distribution in the rotor & stator fluid zone is presented in Figure 3.12. A gradual increase of Pt value along flow path is observed and peak Pt region is identified near rotor shroud. The simulation results indicate that the highest Pt reaches as high as over three times of atmosphere pressure in certain regions. High pressure gradient can be easily identified in the rotor fluid domain, especially near the region of R_{LE} on R_{ps}, and around half streamwise location on R_{ss}, when air coming from rotor frontal surface is quickly compressed by the rotating rotor blade. The compressed air leaves the rotor fluid domain and enters the stator, where the air is further compressed and decelerated by the diffuser, although the change of Pt is not prominent and tremendous as it behaves in the rotor domain.

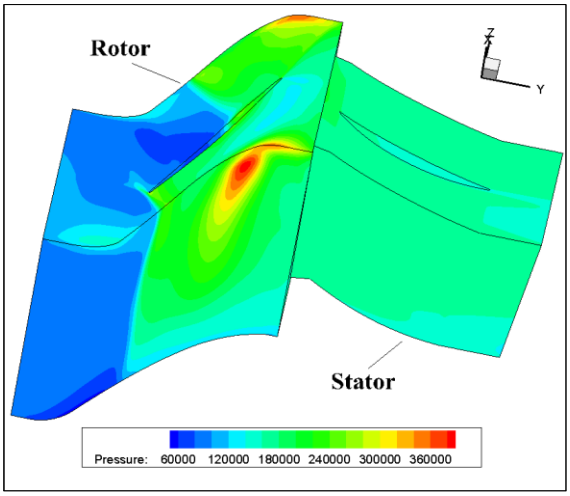

Fig 3.12 Distribution of Pt in the rotor & stator fluid zone, with design Mfr at 100% design speed

In order to understand the Pt variation in more details, cross sectional views of Pt distribution at 50% spanwise of rotor and stator are presented in Figure 3.13. The immediate Pt increase on the R_{ps} is easily understood, where fluid is abruptly compressed by the rotating rotor. However, a decrease of Pt on S_{ss} is actually observed. The extent of lower Pt region increases from S_{LE} towards S_{TE} on the S_{ss}.

The flow separation, which initiated from S_{LE}, may account for the Pt drop in that region.

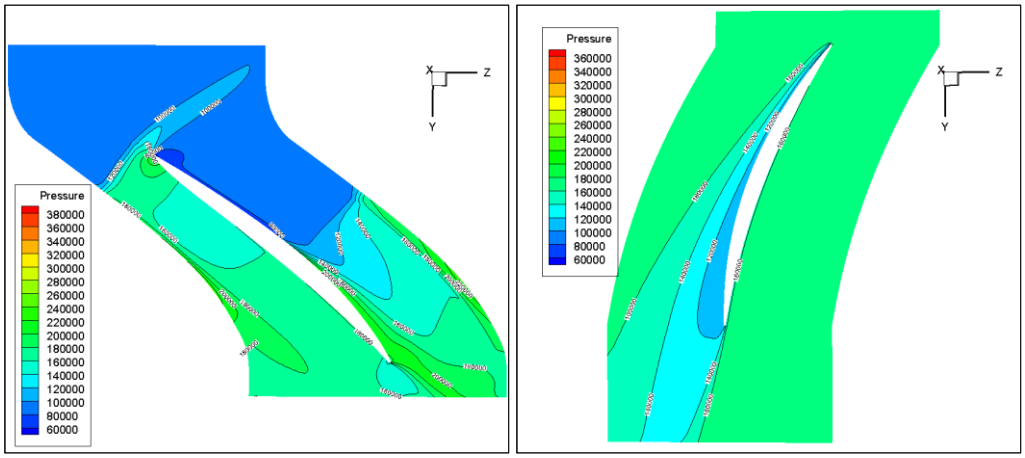

50% spanwise of rotor 50% spanwise of stator

Fig 3.13 Distribution of Pt at 50% spanwise, with design Mfr at 100% design speed

In Figure 3.14, the Mach number distribution at 50% spanwise of rotor and at R_{ss} is presented, to understand the Mach number variation along compressor flow path. A high Mach number region is observed near R_{TE} on R_{ss}. As further illustrated in the right figure, a high Mach number region is located in the vicinity of half spanwise of rotor. This could be due to the coupling of accelerated velocity components, while the boundary layer and friction on the wall delays the increase of the Mach number value near rotor hub and shroud areas.

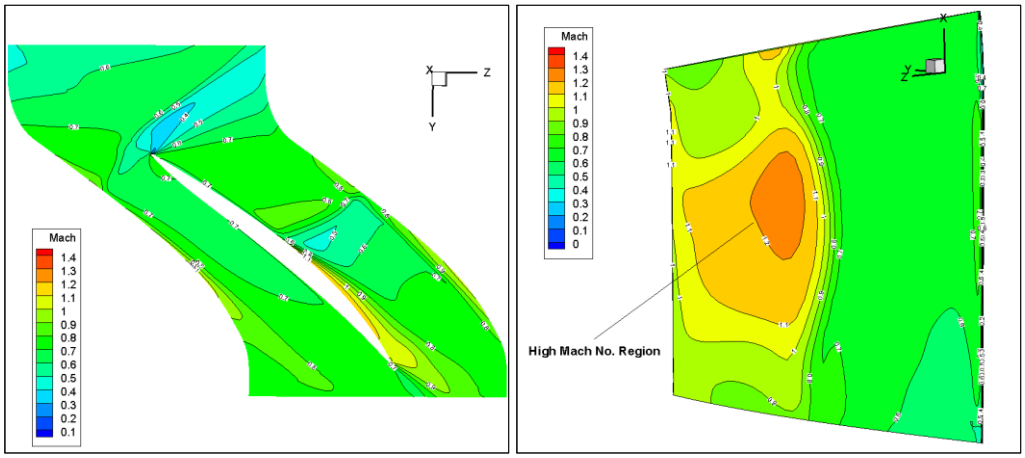

50% spanwise of rotor Rotor suction surface

Fig 3.14 Distribution of Mach at 50% spanwise of rotor and at $R_{ss,}$ with design Mfr at 100% design speed

The Mach number distribution at 50% spanwise of stator and at S_{ss} is presented in Figure 3.15. Low Mach number region is identified near S_{TE} on S_{ss}, indicating flow separation and it explains the low pressure value identified in that region as just described. High Mach number is observed at S_{LE}, while it deceases rapidly along the stator flow passage. The Mach number contour at S_{ss} shows fluid velocity decrease more prominently near stator hub and the lowest value is witnessed at S_{TE}, where the absolute Mach number is close to 0.1 as indicated in our results.

Figure 3.16 more explicitly shows the Mach number variation from stator hub towards the shroud. The 20%, 50% and 80% spanwise of stator are selected for this comparison. A decrease of the area with low Mach number is observed from stator hub towards its shroud.

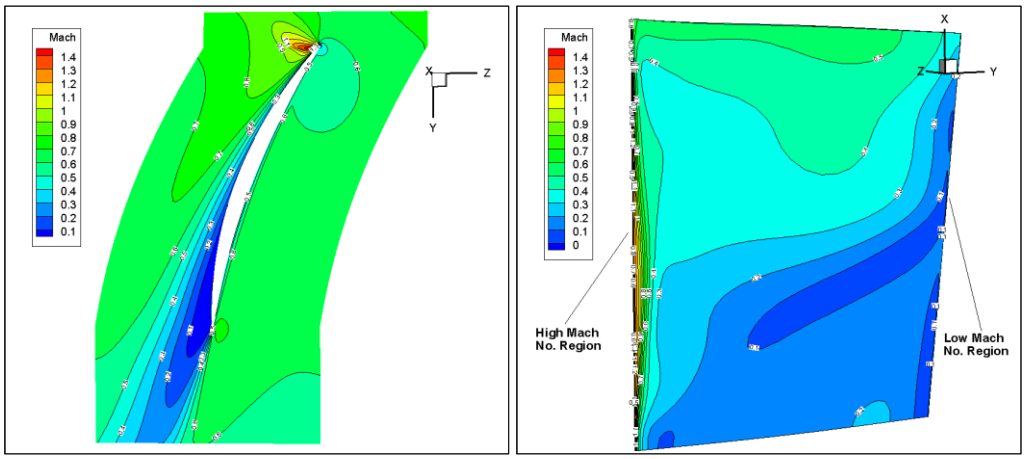

50% spanwise of stator Stator suction surface

Fig 3.15 Distribution of Mach at 50% spanwise of stator and at S_{ss}, with design Mfr at 100% design speed

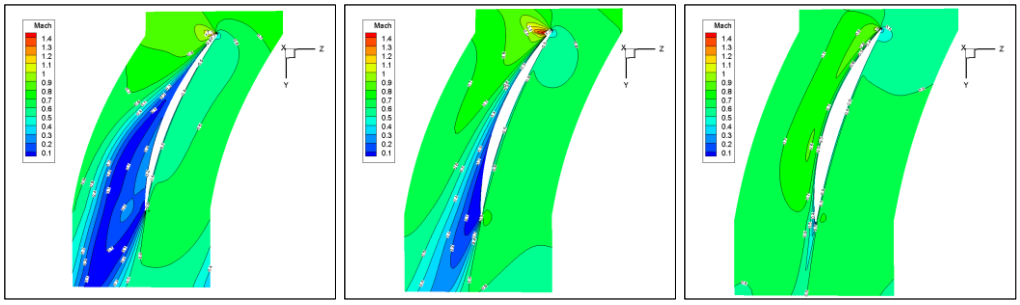

20% spanwise 50% spanwise 80% spanwise

Fig 3.16 Distribution of Mach on different spanwise of stator, with design Mfr at 100% design speed

In order to identify the intensity of turbulence, which is quantified by the Reynolds stress level, Figure 3.17a is presented for the distribution of turbulent viscosity, strain rate field and Reynolds stress at 30% spanwise of stator. Due to their correlation $\tau_{ij}^{R} = -\rho\overline{v_i' v_j'} = 2\tilde{\upsilon}\overline{S_{ij}} - \frac{2}{3}\rho k\delta_{ij}$, where $\tilde{\upsilon}$ is the turbulent viscosity, $\overline{S_{ij}}$ is the Reynolds-averaged strain-rate tensor, $-\frac{2}{3}\rho k\delta_{ij}$ is usually neglected, therefore $\tau_{ij}^{R} = 2\tilde{\upsilon}\overline{S_{ij}}$. The distribution shows that the high strain rate region is only identified at the leading/trailing edge region, while the rest of the strain rate field does not differ prominently. The identified high turbulent viscosity regions are almost identical with the high Reynolds stress regions, i.e., high turbulent intensity region. Therefore, in order to simplify our following analysis, the distribution of turbulent viscosity will be used to characterize turbulence in the future discussions unless specifically mentioned. It gives well-accepted prediction of turbulence, especially in the mainstream flow field. Figure 3.17b shows the distribution of turbulent viscosity at 20%, 50% and 80% spanwise of stator. It further demonstrates the intensity of turbulence in the radial direction in the stator zone. More intensive turbulence is observed in the lower half of stator zone, which explains the lower Mach number in that region.

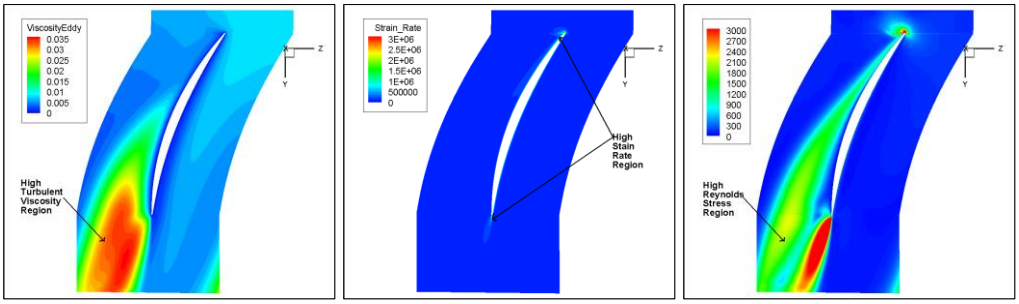

Turbulent Viscosity Strain Rate Reynolds Stress

Fig 3.17a Distribution of turbulent viscosity, Strain Rate and Reynolds Stress at 30% spanwise of stator, with design Mfr at 100% design speed

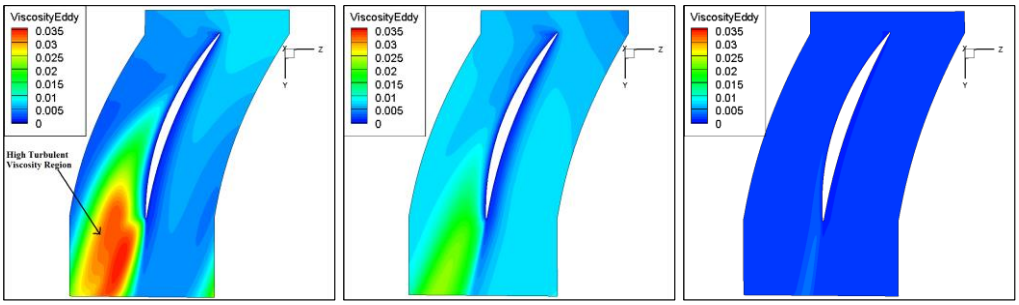

20% spanwise 50% spanwise 80% spanwise

Fig 3.17b Distribution of turbulent viscosity on different spanwise of stator, with design Mfr at 100% design speed

The value of η_{ad} is important for the evaluation of compressor performance. For compressor design, higher η_{ad} together with higher *Pr* is always desired. The change of entropy is usually used to indicate the η_{ad} change.

Figure 3.18 shows the distribution of entropy on R_{ss} and S_{ss}, to aid the understanding of η_{ad} loss during compressor operation. Values at rotor inlet are selected as reference. On R_{ss}, a high entropy region is identified near R_{TE}, which is approximately the corresponding area for high Mach numbers. More severe friction between fluid and rotor blade in this region may have contributed to the high entropy locations. A gradual increase of entropy value is also identified along the streamwise direction from R_{LE} towards R_{TE}, which is also in correspondence with the gradual increase of Mach number. On S_{ss}, the high entropy region is identified near S_{LE}, which also corresponds to the high Mach number region. The extent of relatively high entropy region along the S_{ss} towards S_{TE} is due to the occurrence of flow separation initiated shortly after the S_{LE}, where η_{ad} loss is high.

Figure 3.19 shows the distribution of entropy at 20%, 50% and 80% spanwise of rotor, to explain the changes of entropy in the rotor radial direction in more detail. The area of high entropy region increases from rotor hub towards 50% spanwise, and the area gradually decrease when it approaches the shroud. The high entropy region suggests more η_{ad} loss and a less isentropic process.

Figure 3.20 shows the distribution of entropy at 20%, 50% and 80% spanwise of stator. Lower value of entropy is observed compared with those in the rotor region,

which indicating less η_{ad} loss. The existence of comparatively high entropy region is aroused by the flow separation, where the interaction of fluid intensifies. High entropy is also identified at S_{LE}, indicating severe friction loss as discussed earlier.

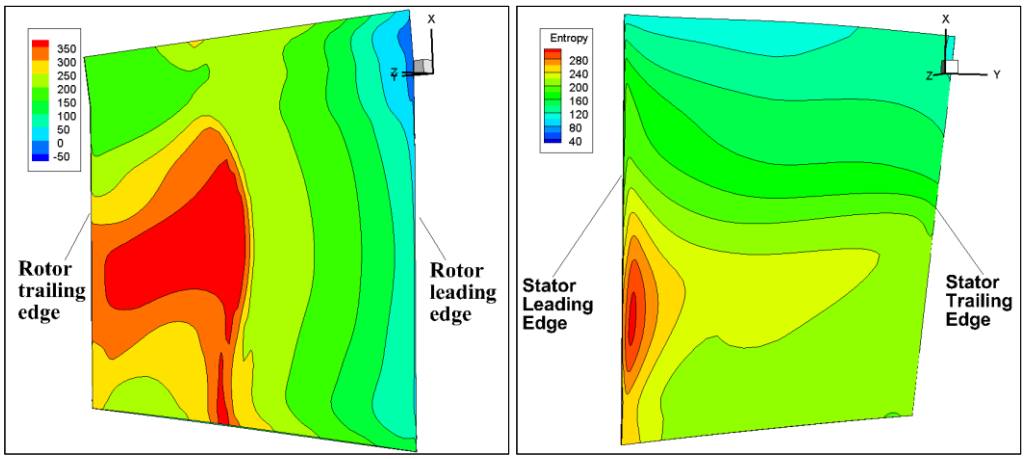

Rotor Suction Side Stator Suction Side

Fig 3.18 Distributions of entropy on R_{ss} and $S_{ss,}$ with design Mfr at 100% design speed

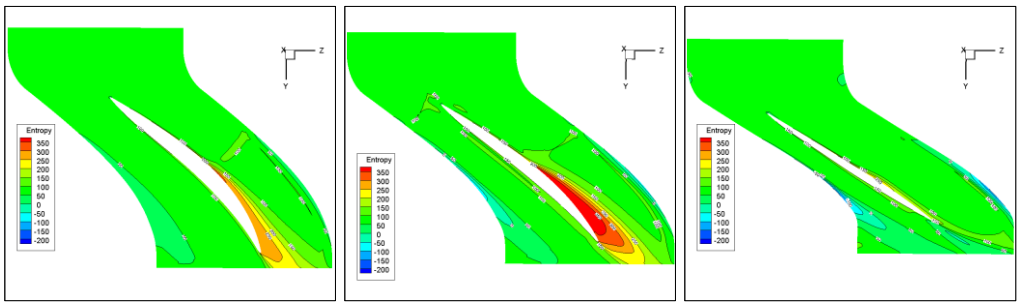

20% spanwise 50% spanwise 80% spanwise

Fig 3.19 Distribution of entropy on different spanwise of rotor, with design Mfr at 100% design speed

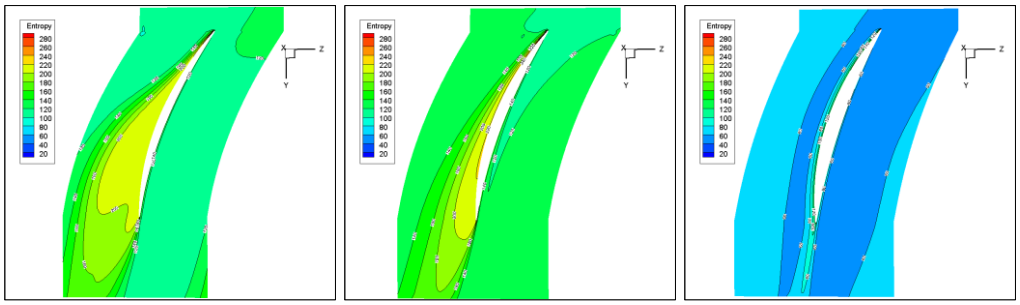

20% spanwise 50% spanwise 80% spanwise

Fig 3.20 Distribution of entropy on different spanwise of stator, with design Mfr at 100% design speed

3.7.2 Flow Field Analysis at 70% Design Speed

The flow field analysis of the NASA 35 compressor operating at 70% design speed is conducted. Results from the optimal Mfr (13.5kg/s) test are utilized. The distribution of Pt at 20%, 50% and 80% spanwise of rotor is shown in Fig 3.21. Different from the result from 100% design speed, result from 70% design speed presents less increase of Pt. Also, the high pressure region propagates less downstream in the flow path. This is probably because of the smaller tangential driving force at 70% design speed, which is less powerful to pressurize the air to the downstream.

Figure 3.22 shows the distribution of Mach number at 50% spanwise of rotor and at R_{ss}, with optimal Mfr at 70% design speed. As expected, the increase of Mach along flow path is less significant and the supersonic flow region near the R_{ss} disappears. In addition, the high Mach region locates close to R_{LE} at 70% design speed, which is different from that at 100% design speed where high Mach is close to R_{TE}. Smaller fluid momentum at 70% design speed is again the reason for this difference.

Figure 3.23 shows the distribution of entropy at 50% spanwise of rotor and at R_{ss}, with optimal Mfr at 70% design speed. Lower entropy is observed at 70% design speed, compared with that from 100% design speed simulation. Therefore, the flow is more isentropic at 70% design speed.

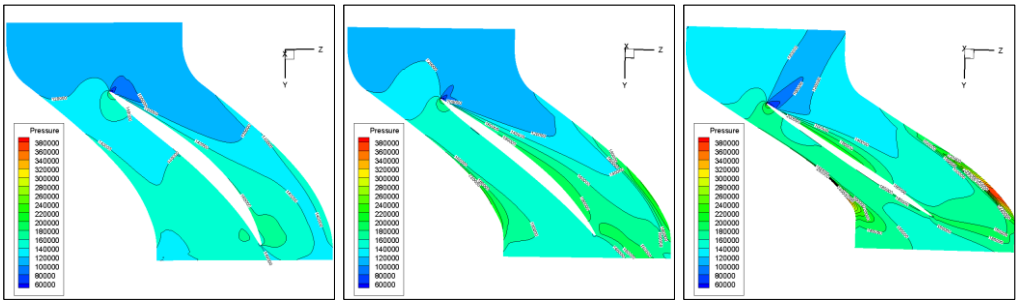

20% spanwise 50% spanwise 80% spanwise

Fig 3.21 Distribution of Pt on different spanwise of rotor, with optimal Mfr at 70% design speed

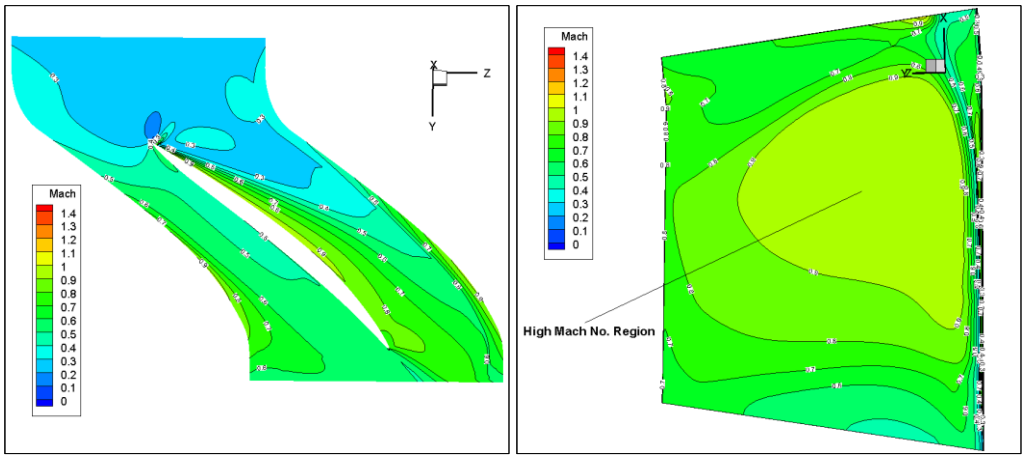

50% spanwise of rotor Rotor suction surface

Fig 3.22 Distribution of Mach at 50% spanwise of rotor and at $R_{ss,}$ with optimal Mfr at 70% design speed

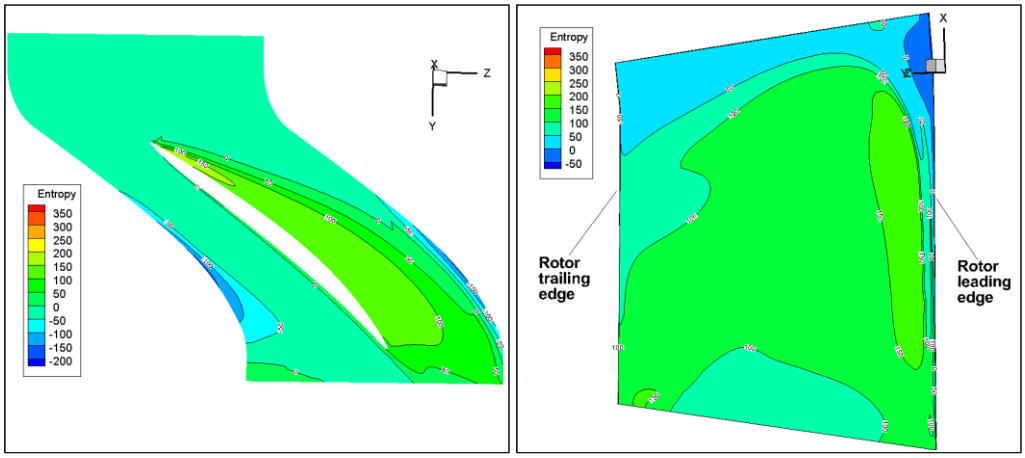

50% spanwise of rotor Rotor suction surface

Fig 3.23 Distribution of entropy at 50% spanwise of rotor and at $R_{ss,}$ with optimal Mfr at 70% design speed

Figure 3.24 shows the distribution of Mach at four streamwise locations in stator, with optimal Mfr at 70% design speed. The expansion of low Mach region on the S_{ss} starts from S_{LE} towards S_{TE}. It describes how flow separation develops along the flow path between stator blades. However, when the flow leaves the S_{TE}, the low Mach region gradually decreases, when high Mach fluid from the S_{ps} interacts with low Mach fluid from the S_{ss}. The interaction occurs immediately after the S_{TE}, and propagates downstream. The low Mach region at four different streamwise planes is pointed out, therefore the variation of separated flow is easy to identify. In addition, the high Mach region is also pointed out. High Mach is

observed near blade tip on S_{ss}. The high Mach region develops from the S_{LE} near shroud and gradually increases its area until it reaches around 50% streamwise in stator, after that, a slight decrease of the high Mach area is observed. A further decrease of high Mach area is identified after the S_{TE}, where high speed fluid gradually merges with low speed fluid from lower stator zone, and further suppresses the low speed fluid towards the stator hub.

Figure 3.25 shows the distribution of entropy at four streamwise locations in stator, with optimal Mfr at 70% design speed. The expansion of high entropy region is almost identical with the expansion of low Mach region as just shown. It further proves that increased fluid interaction as a result of flow separation, which induces entropy increase due to dissipative losses. The large entropy region is also pointed out at different locations. However, the absolute value of entropy in stator at 70% design speed is still much lower than that from the 100% design speed. The low entropy value region is identified and pointed out near the stator casing, which also indicates a higher loss of η_{ad} as the flow is less isentropic in those regions.

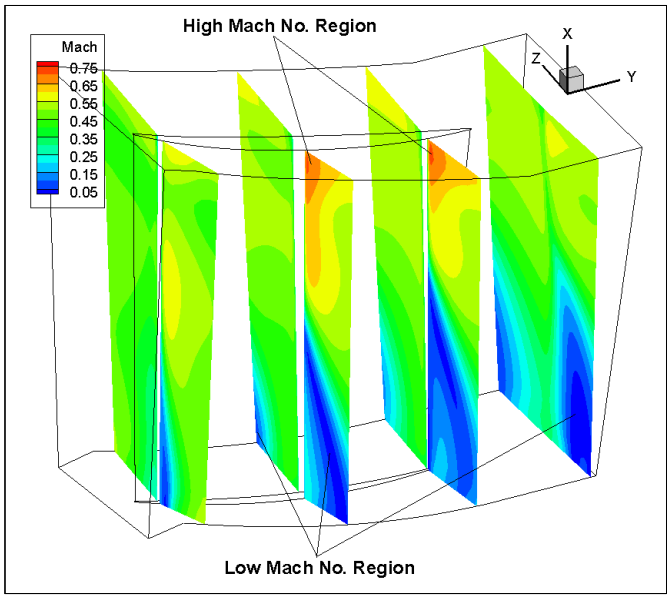

Fig 3.24 Distribution of Mach along the stator flow path, with optimal Mfr at 70% design speed

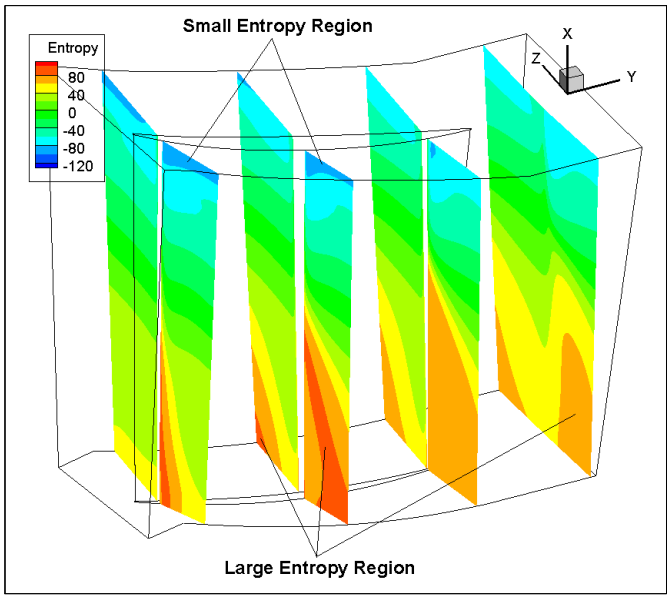

Fig 3.25 Distribution of entropy along the stator flow path, with optimal Mfr at 70% design speed

To understand the turbulence generation along stator flow path, the development of turbulent viscosity is shown in Figure 3.26. The turbulence intensifies, especially in the lower flow path, as flow propagates downstream. The creation of high turbulent viscosity region is observed near S_{TE} flow path and further develops downstream. A high turbulent viscosity layer, i.e., intensive turbulent layer, is then formed when the flow propagates downwards the vane exit, as illustrated in Figure 3.27. The turbulent layer almost stabilizes at the vane exit. Because only one stage of rotor and stator is considered in current study, the extension of the stator vane is built to aid the understanding of wake flow.

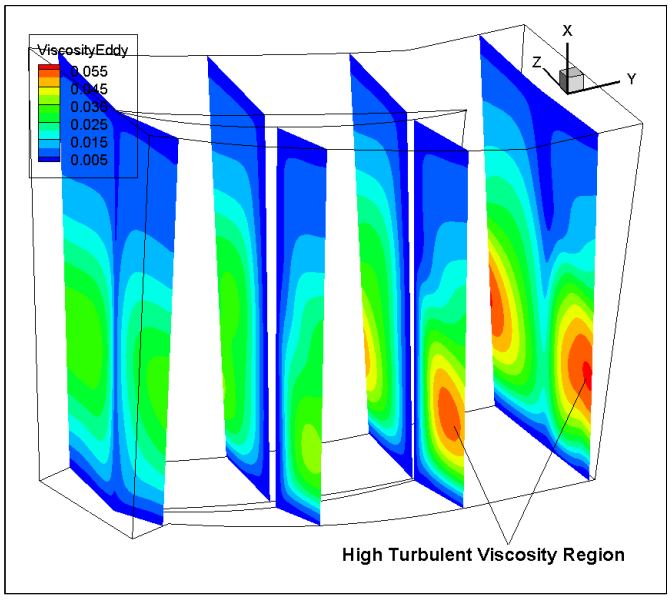

Fig 3.26 Development of turbulent viscosity in the stator fluid zone

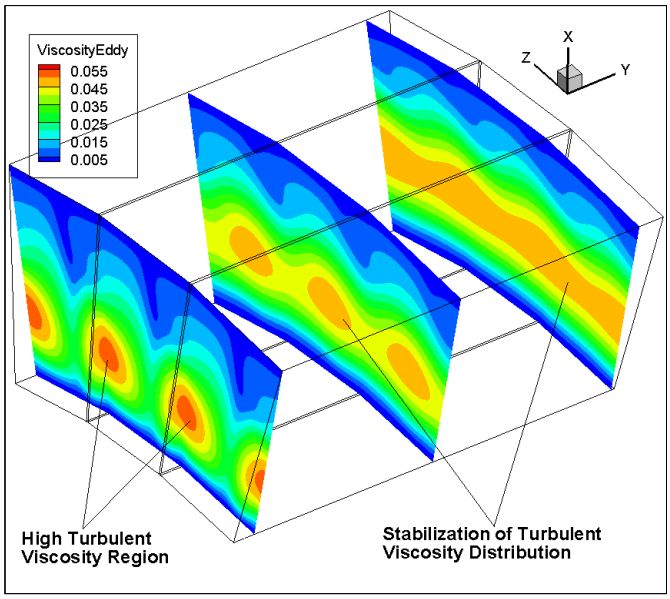

Fig 3.27 Development of turbulent viscosity in the outlet vane fluid zone

The streamline in the flow path at both 100% and 70% design speed is presented, to further explain flow property changes. In Figure 3.28, the sectional streamlines in rotor are presented. Our focus remains near the rotor tip regions, where slight difference of streamline is observed at two different operation speeds. As shown, the general streamline path on R_{ps} at both operating speeds is similar, while slight difference is identified in the low Mach region. The fluid coming from inlet is

driven by the rotating rotor blade and changes its trajectory, from R_{ps} towards the suction side of adjacent rotor blade. The streamline near blade tip has less curvature at 100% design speed, which is due to the higher rotating speed of rotor and thus a higher driving force, resulting in higher tangential speed for the fluid. The existence of low Mach region and generation of flow separation is more prominent at 70% design speed. This is because of the relatively lower Mach and thus a lower fluid momentum to suppress the flow separation initiated by the detachment of boundary layer on the R_{ps}. Although the development of streamline in rotor at two different speeds is not significantly different, this explanation still assists our understanding of the flow development in rotor and the influence of operating speed.

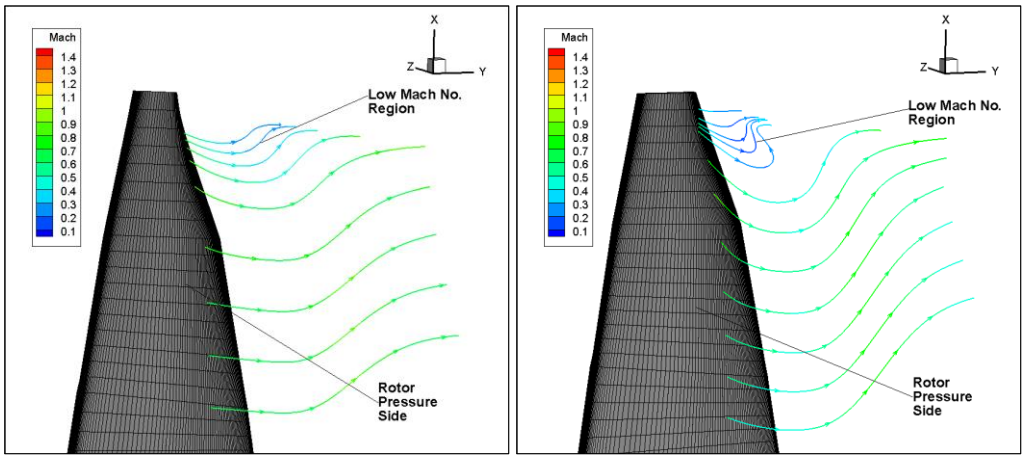

100% design speed 70% design speed

Fig 3.28 Streamline in rotor at 100% and 70% design speed respectively

The streamline (view from z axis) in the stator is also presented in Figure 3.29, at both 100% and 70% design speed. The streamline on S_{ss} is considered, where the main difference is identified. At 100% design speed, the streamline released from S_{LE} detaches from the S_{ss} and starts to propagate towards the stator shroud, until it is suppressed by the axial flow in the upper zone of stator at around 30% spanwise and reverses back towards stator hub. Similar phenomenon is also identified at 70% design speed. However, the fluid with lower momentum, i.e., with lower Mach number, travels further towards the stator shroud and only reverses back until it reaches around 60% spanwise. Lower Mach of fluid in the

upper zone is also identified at 70% design speed, compared with that at 100% design speed. This actually answers the difference of streamline pattern at 70% design speed, as upper zone fluid is with lower momentum, thus less powerful to maintain the reverse flow in the lower zone. It is not difficult to understand the difference, because the rotor located upstream of the stator has less driving force and thus smaller fluid momentum when it enters the stator zone, when 70% design speed is applied.

A more detailed illustration of the streamline pattern (view from x axis) in the stator is presented in Figure 3.30, at 100% and 70% design speed. At 100% design speed, the streamline on the S_{ps} follows the blade path reasonably well, while the streamline on the S_{ss} further explains the occurrence of reverse flow and it mainly locates in the downstream of stator flow path. However, at 70% design speed, the expansion of reverse flow region on the S_{ss} is much larger and propagates more upstream. It further demonstrates that fluid at upper zone has less momentum, compared with that at 100% design speed, to suppress reverse flow in the lower stator zone.

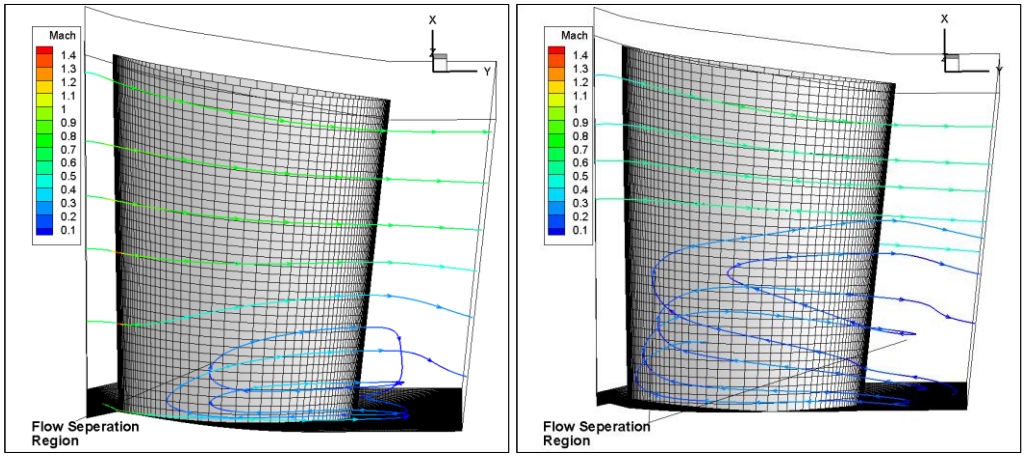

100% design speed 70% design speed

Fig 3.29 Streamline in stator at 100% and 70% design speeds respectively (View from Z axis)

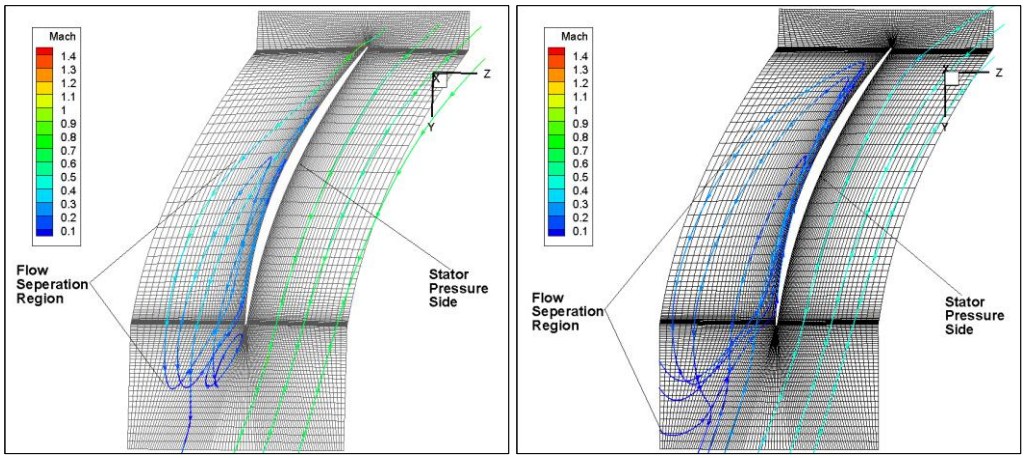

100% design speed 70% design speed

Fig 3.30 Streamline in stator at 100% and 70% design speeds respectively (View from X axis)

In summary, the validation of the computational tools and methods is conducted. Numerical results have captured the major trends from experiments, while details, especially for the adiabatic efficiency, are only approximately predicted. The performance characteristic of the NASA 35 compressor is analyzed, based on simulation results. Therefore, the proposed numerical approach can be used for follow-up study.

Chapter 4

Reynolds Number Effect

Next, the effect of Reynolds number on the performance of an axial compressor is studied. The compressor model built according to the design parameters is the benchmark case, where the scaling factor (SF) is defined as SF=1. Based on that, different SF specified as 1.6, 1.3, 0.7 and 0.4 respectively, are applied on the three dimensions of the original model. The scaling procedure is conducted in ANSYS Fluent. For the benchmark case, the radius of rotor is 25.2cm, therefore, the corresponding radius of rotor is around 40.4cm for SF=1.6 case and 10.1cm for SF=0.4 case. It is previously specified in Table 3.1, the hub-tip radius ratio is 0.7, and thus the height of rotor at different SF conditions can be computed accordingly. Figure 4.1 describes the variation of rotor blade height in more details. The stator blade height also changes at different SF conditions.

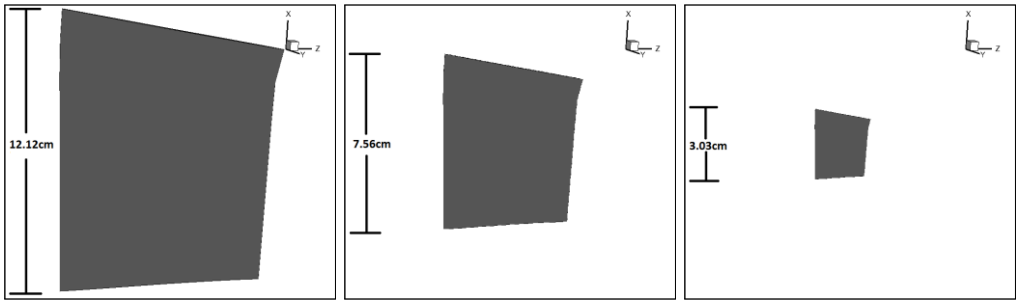

SF=1.6 SF=1 SF=0.4

Fig 4.1 Variation of rotor blade height for different SF applied

The operation speed of rotor is adjusted, according to the SF specified, to keep the tip speed constant. The maximum pressure ratio obtained by the compressor is determined by the blade-tip speed. In addition, this limit also impacts on the maximum power and efficiency that can be obtained by engine. This statement relies on the assumption that the non-dimensional parameters $\frac{m\sqrt{\gamma RT_{in}}}{D^2 p_{in}}$ and $\frac{\Omega D}{\sqrt{\gamma RT_{in}}}$ are kept constant. Throughout this section for all cases, the inlet total temperature T_{in} is kept as 288k and the inlet total pressure p_{in} is kept as 101325pa. Therefore, the values of $\frac{m}{D^2}$ and ΩD are also constant and the similarity is ensured. Apart

from that, during the testing of engineering models, the similitude concept should also be followed, where the angle of attack is kept unchanged for this problem. Figure 4.2 shows the specification of rotor operation speed at different SF conditions in more details.

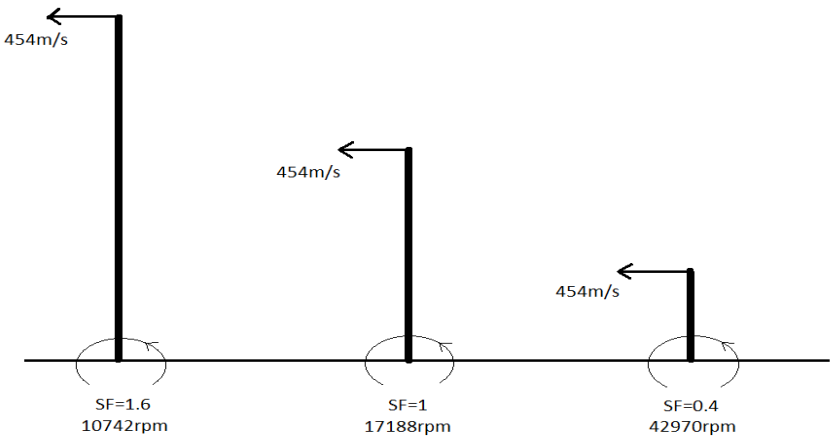

Fig 4.2 Adjustment of RPM at different SF conditions

The Reynolds number at rotor inlet is calculated to quantify the percentage of miniaturization of the compressor geometry. Therefore, for a constant specific mass flow rate (Mfr per unit area), the Reynolds number only changes with the variation of the hydraulic diameter (D_H), i.e., the rotor blade height. The resulting Reynolds number ranges from *Re* 2.14×10^5 to *Re* 8.54×10^5, at 100% design speed condition. Table 4.1 describes the variation of Reynolds number with the change of SF applied, i.e., the resulted D_H.

Table 4.1 Relations between Reynolds Number and SF Applied

Scaling Factor	D_H (m)	Specific Mass Flow Rate (kg/m^2×s)	Reynolds Number
1.6	8.86×10^{-2}	172.6	8.54×10^5
1.3	7.20×10^{-2}	172.6	6.94×10^5
1	5.54×10^{-2}	172.6	5.34×10^5
0.7	3.87×10^{-2}	172.6	3.74×10^5
0.4	2.21×10^{-2}	172.6	2.14×10^5

For cases with different SF, except the difference of operating rotating speed as just discussed, other boundary conditions are defined identical with the validated specifications described in Chapter 3. Simulation results are compared with the well-known empirical formula [91], which was developed for the correction of

efficiency for a compressor stage $\eta_{ad} = ((\overline{P_{out}}/\overline{P_{in}})^{(\gamma-1)/\gamma} - 1)/((\overline{T_{out}}/\overline{T_{in}}) - 1)$, for Reynolds number effects.

$$\frac{1-\eta_{ad}}{1-\eta_{ref}} = a + (1-a)[\frac{Re_{ref}}{Re}]^n \qquad \text{Eq 4.1}$$

where the empirical value for the Reynolds ratio exponent "n" is 0.2 and the Reynolds independent loss fraction "a" is 0 for axial compressors. However, our numerical result proposes a suggested Reynolds ratio exponent "n" of 0.1, to capture the variation of efficiency with Reynolds number. Figure 4.3 describes the comparison of adiabatic efficiency (η_{ad}) variations for results from CFD, empirical formula and our suggested correction. The conditions and results from Re=8.54×10^5 is taken as the Re_{ref} and η_{ref}.Within the scope of this study when Reynolds number increases from Re 2.14×10^5 to Re 8.54×10^5, an increase of 2.77% of η_{ad} is observed from CFD results and an increase of 10% η_{ad} is predicted using the empirical formula[91], while our suggested correction method achieved an increase of 4.42% of η_{ad} and deviates less from the simulation results. The discrepancy between CFD and empirical formula is much smaller than the discrepancy between CFD and experimental data as previously shown, which needs to be noted. The empirical formula generally quite well validates the reliability of the CFD method proposed.

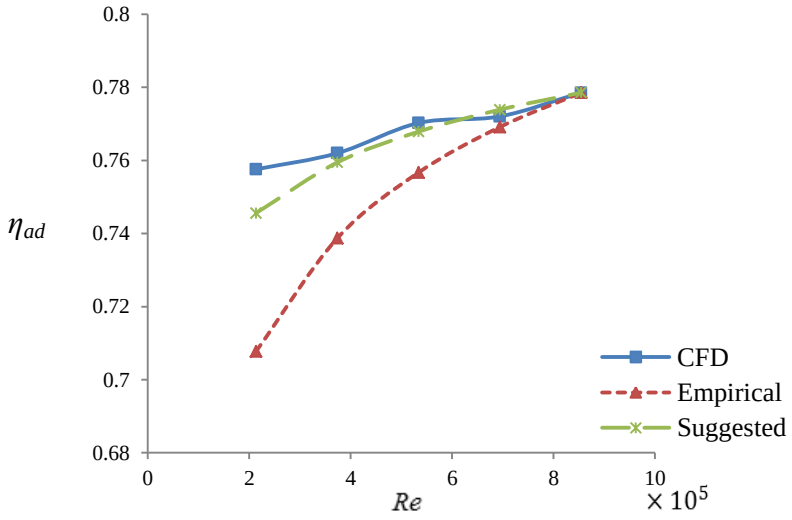

Fig 4.3 Comparison of η_{ad} at different Re condition, with design Mfr at 100% design speed

The distribution of total pressure ratio (*Pr*) from CFD is also shown in Figure 4.4. Gradual increase of *Pr* is observed with the increase of Reynolds number, and the total increase of 1.45% in *Pr* is achieved when Reynolds number ranges from *Re* 2.14×10^5 to *Re* 8.54×10^5. The highest *Pr* achieved is 1.76 at *Re* 8.54×10^5 condition.

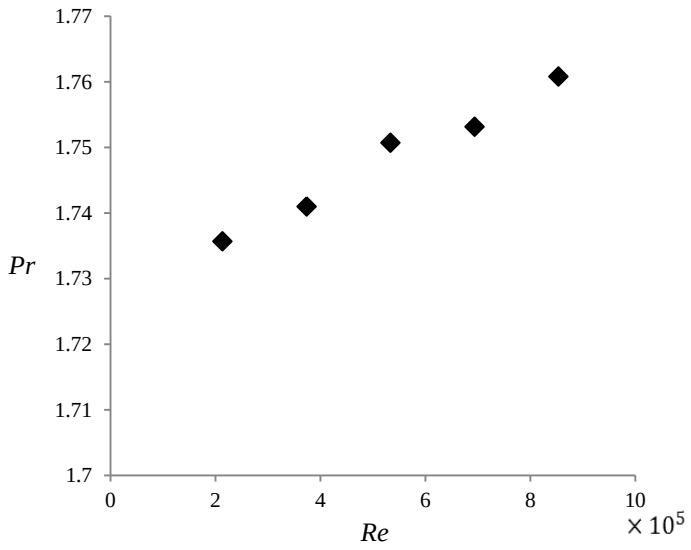

Fig 4.4 Distribution of *Pr* at different *Re* condition, with design Mfr at 100% design speed

The distribution of temperature ratio (*Tr*) from CFD is also shown in Figure 4.5. As can be identified from the distribution, within the scope of study when Reynolds number increases from *Re* 2.14×10^5 to *Re* 8.54×10^5, the change of *Tr* is negligible, less than 0.01% and much less than the numerical accuracy. This is not surprising, as according to Euler's work equation, $C_p \cdot (T_2 - T_1) = v_{tip2} r_2 \vec{w}_2 - v_{tip1} r_1 \vec{w}_1$, the temperature ratio is prescribed by the work input, which is an input to the problem by imposing the blade geometry and the rotational speed. The observed *Tr* falls in the vicinity of 1.2252.

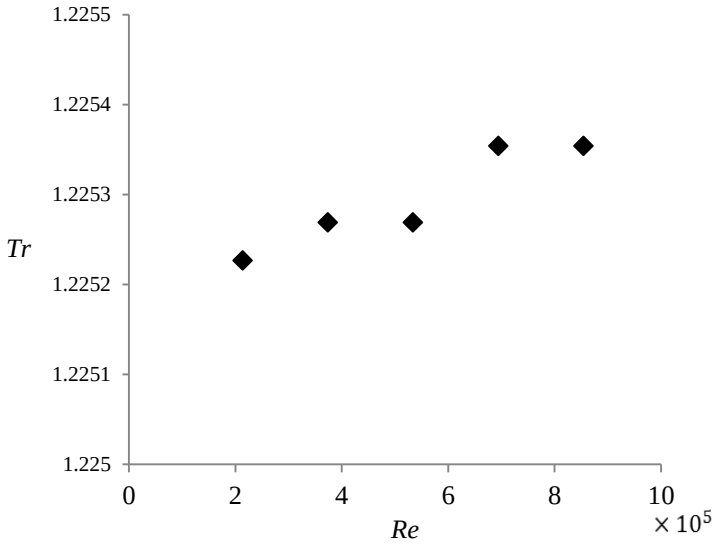

Fig 4.5 Distribution of *Tr* at different *Re* condition, with design Mfr at 100% design speed

Further comparison of compressor performance at different Reynolds number conditions is conducted. The cases with SF=1.6, SF=1 and SF=0.4 are selected. Variations of the specific Mfr, ranging from 142.6kg/m^2×s to 202kg/m^2×s, are applied. This is conducted for further understanding of the compressor operation map when it is miniaturized. The Mfr is normalized by the designed value, i.e., 172.6 kg/m^2×s, to simplify our analysis.

Figure 4.6 illustrates the variation of adiabatic efficiency with varying Mfr. Results from the three selected cases are considered. The η_{ad} generally increases from smaller Mfr until it reaches the optimal point, and it drops beyond that optimal value. When the normalized Mfr changes from 0.9 to 1, an increase of 11% in η_{ad} is observed for case with SF=1.6, indicating that the η_{ad} variation is relatively sensitive in the vicinity of designed Mfr. For all three cases, the optimal η_{ad} point is identified at the 111.2% design Mfr, where the highest η_{ad} is achieved as 0.803 for SF=1.6 case. At the optimal point, a drop of 1.3% in η_{ad} is observed when SF decreases from 1.6 to 0.4. The η_{ad} of SF=1.6 case is the highest among the three different Reynolds number cases, for all tested Mfr conditions, which is identical with analysis made from Figure 4.3 previously.

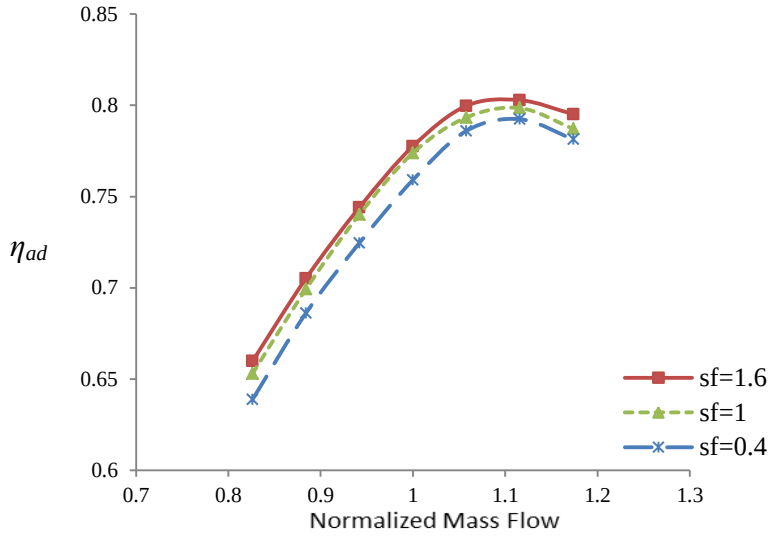

Fig 4.6 Variations of η_{ad} with varying Mfr, at 100% design speed

Figure 4.7 illustrates the variation of total pressure ratio with varying Mfr. Results from three selected cases are considered. Similar with the variation of η_{ad} discussed earlier, the *Pr* generally increases with the increase of Mfr, until it reaches the optimal point, and it drops rapidly beyond the optimal operation region. However, different from that of η_{ad} variation, when the normalized Mfr changes from 0.9 to 1, the increase of *Pr* is observed as 2% for case with SF=1.6, which is relatively less sensitive in the vicinity of design Mfr. For all three cases, the optimal *Pr* is identified at the design Mfr, where the highest *Pr* achieved is 1.76 for case with SF=1.6. At the optimal point, a drop of 1.39% in *Pr* is observed when SF decreases from 1.6 to 0.4. The *Pr* of SF=1.6 case is everywhere the highest among the three Reynolds number cases, though the difference is less apparent at high Mfr region. The change of *Pr* with Reynolds number is also identical with analysis made from Figure 4.4 previously.

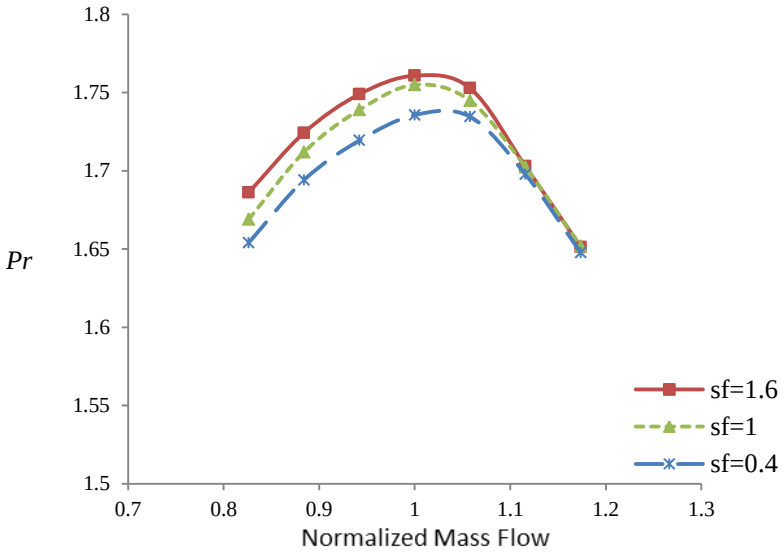

Fig 4.7 Variations of *Pr* with varying Mfr, at 100% design speed

Figure 4.8 illustrates the variation of total temperature ratio with varying Mfr. Within the applied range of Mfr, the *Tr* decreases with the increase of Mfr. In addition, the value of *Tr* is almost identical for all three cases, which is consistent with discussions for Figure 4.5, i.e., the Reynolds number has minor effects on the distribution of *Tr*.

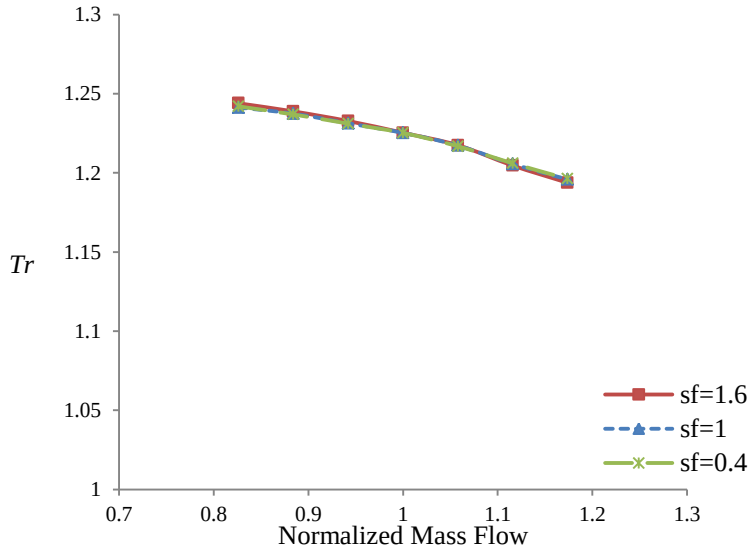

Fig 4.8 Variations of *Tr* with varying Mfr, at 100% design speed

4.1 Reynolds Number Effect in Rotor Zone

The comparison of entropy distribution on rotor suction side (R_{ss}), with reference value from airflow inlet area, is shown in Figure 4.9. For all three Reynolds number conditions, regions of high entropy are located close to the R_{TE}, indicating more energy loss in those areas. However, comparatively a larger area of high entropy is observed for SF=0.4 case, indicating more energy loss compared with the other two Reynolds number conditions. Results from design Mfr are used for this comparison analysis.

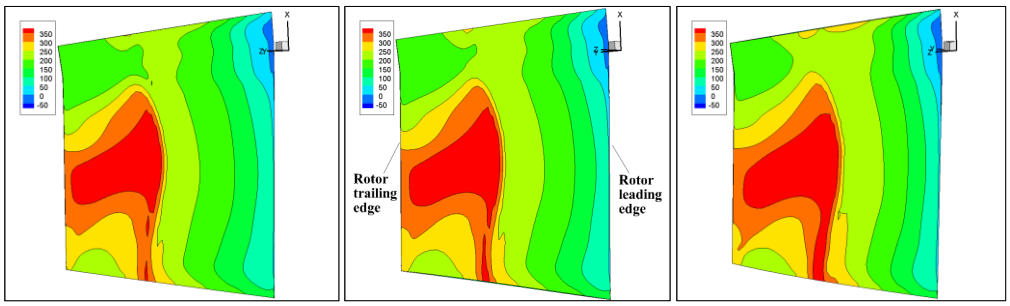

SF=1.6 SF=1 SF=0.4

Fig. 4.9 Comparison of entropy distributions on R_{ss} during its miniaturization process, with design Mfr at 100% design speed

The main difference of entropy distribution is located in the lower half of the rotor flow path, as identified from Figure 4.9. Therefore, the comparison of entropy distributions at three different Reynolds number conditions, at 30% spanwise of rotor, is shown in Figure 4.10. The location of high entropy is almost identical, near R_{TE} on R_{ss}. However, slightly larger area of high entropy is still identified at smaller Reynolds number condition. This is in consistence with discussions made for Figure 4.9 previously, indicating more energy loss at small Reynolds number condition.

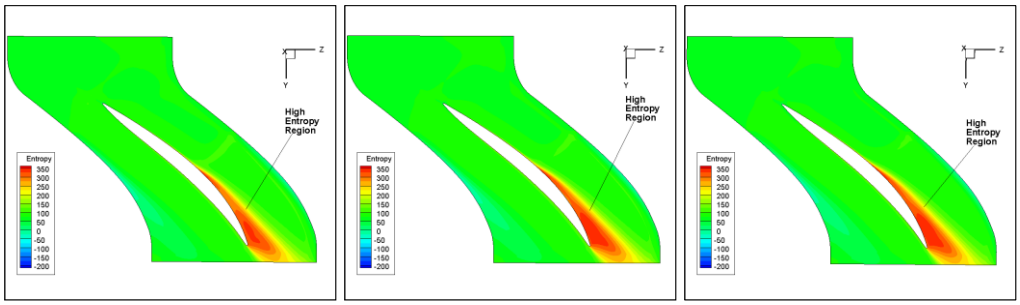

SF=1.6 SF=1 SF=0.4

Fig 4.10 Comparison of entropy distributions on 30% spanwise of rotor, with design Mfr at 100% design speed

For the purpose of more statistically describing the difference, values of entropy near R_{ss} are computed from the CFD results. Figure 4.11 shows the locations of data extraction points. As a 3D problem, the 30% spanwise of rotor is selected as the primary surface because more difference in entropy is observed in the lower half of flow path as previously discussed, values from 5%, 20% and 40% span from R_{ss} are extracted based on the primary surface. In total, 20 data points are specified for each span location, ranging from R_{LE} to R_{TE}.

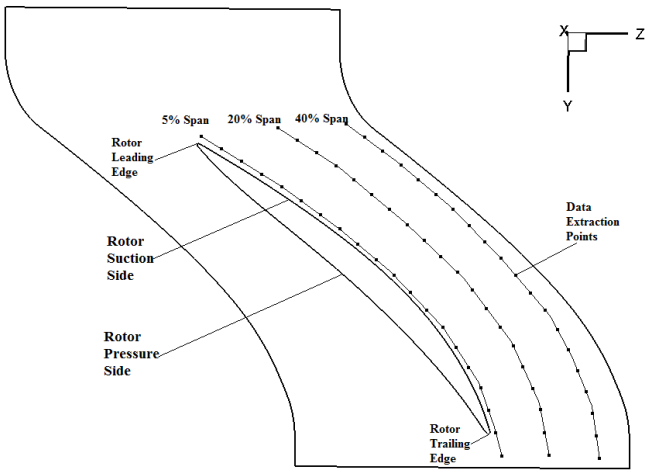

Fig 4.11 Locations of data extraction points on the primary surface in rotor zone

The distribution of entropy on primary surface at 5% span and 20% span from R_{ss} at different Reynolds number conditions is firstly shown in Figure 4.12, respectively. The nondimensionalized rotor length is used to identify the locations of data points along rotor flow path, and ΔS indicate the entropy value with reference to the entropy value at rotor inlet surface. At 5% span, the entropy remains unchanged until 40% chord length, where a sudden jump of entropy value is observed. After that, the entropy remains almost unchanged at the high value until around 90% chord length, where a sudden drop of entropy value is observed, suggesting the flow leaving the rotor trailing edge, as can be identified in the data locations shown in Figure 4.11 previously. At 20% span, the entropy remains almost unchanged until around 70% chord length, where a gradual increase of entropy value is observed. A slight drop of entropy is also observed at around 90% chord length, when the flow leaves the rotor trailing edge region. In general, slightly higher entropy is observed at small Reynolds number condition, i.e. SF=0.4, especially at 5% span location. This is consistent with observations made from Figure 4.10.

At 5% span, the sudden jump of entropy might be explained by the sudden change of flow, which intensifies the flow interaction. Figure 4.13 shows the Mach distribution at 5% span and 20% span from R_{ss}, respectively. At both 5% and 20% span, a sharp decrease of Mach is observed at 40% chord length, which is identical with the location of entropy jump. The interaction of flow in axial direction and flow quickly driven by the rotating rotor has contributed to the abrupt change in flow property at this location, though larger effect of sudden Mach change on entropy value is identified in near wall region, i.e. at 5% span. The Mach generally increases gradually along rotor flow path. However, at 5% span, a drop of Mach is observed again at 90% chord length, when flow leaves the rotor trailing edge; while at 20% span, the drop of Mach is not observed again at 90% chord length. This suggests that rotor blade has minor effect on flow structure in the free stream.

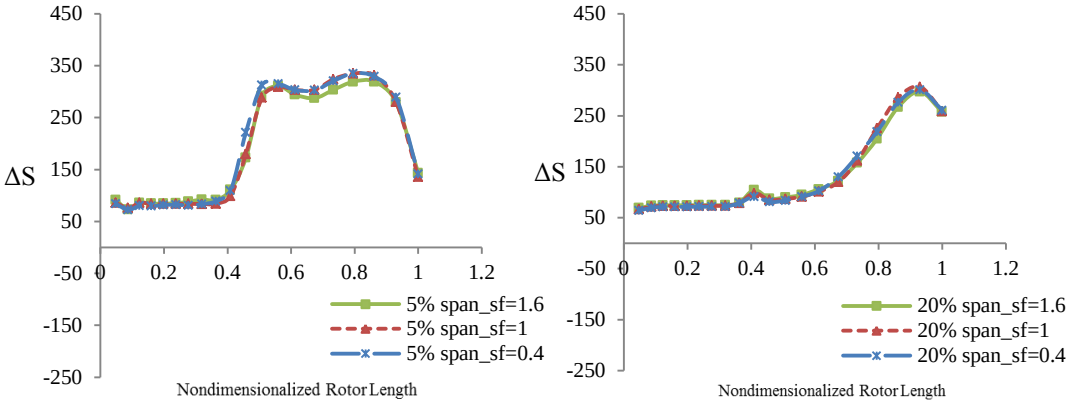

5% span 20% span

Fig 4.12 Distribution of entropy at 5% span and 20% span from R_{ss} based on the primary surface, with design Mfr at different *Re* condition

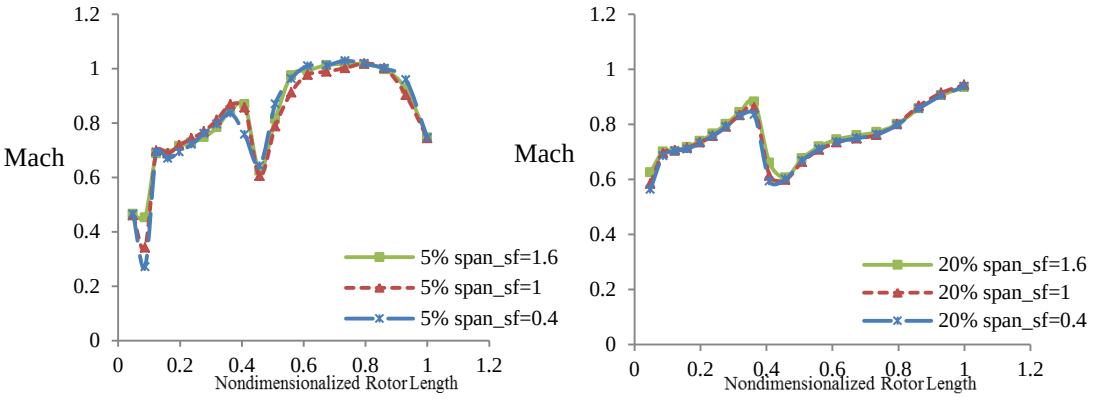

5% span 20% span

Fig 4.13 Distribution of Mach at 5% span and 20% span from R_{ss} based on the primary surface, with design Mfr at different *Re* condition

The observed higher entropy at small Reynolds number condition is probably induced by the more intensive viscous effect near boundary when the compressor is miniaturized, suggesting more energy loss. Another explanation could be drawn from the intensity of turbulence at different Reynolds number conditions. Figure 4.14 shows the distribution of turbulent viscosity ϑ(kg/m·s) based on the primary surface, to quantify the intensity of turbulence at 5% span and 20% span from R_{ss}, respectively. At 5% span, the turbulent viscosity remains zero during the first 40% chord length, indicating the flow is laminar in this region. However, the turbulent viscosity increases gradually after 40% chord length and jump dramatically at

around 90% chord length, i.e. when flow leaves the R_{TE}, indicating the flow becomes more turbulent in the wake region. At 20% span, the turbulent viscosity remains zero until 60% chord length, where a sudden jump is observed. In addition, the peak value of turbulent viscosity at 20% span is higher than that at 5% span. At both span locations, the turbulent viscosity is higher at larger Reynolds number condition, suggesting the flow is more turbulent with larger Reynolds number. The increase of turbulence actually intensifies the change of flow structure and weakens the effect of the boundary layer, resulting in reduced overall drag and skin friction. Therefore, the more intensified turbulence contributes to lower entropy values at large Reynolds number condition, especially in near wall regions.

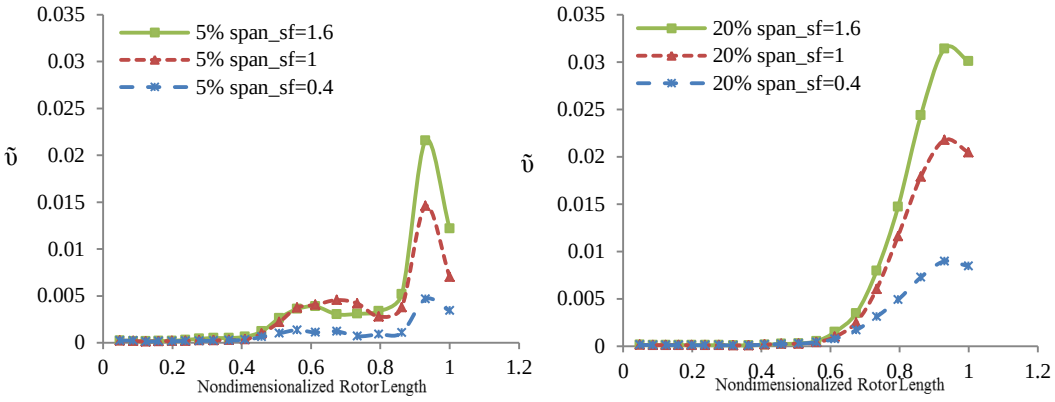

5% span 20% span

Fig 4.14 Distribution of turbulent viscosity at 5% span and 20% span from R_{ss} based on the primary surface, with design Mfr at different *Re* condition

In order to further understand the intensity of turbulence at different Reynolds number condition, the contours of turbulent viscosity at 50% span from rotor hub is shown in Figure 4.15, and at 80% span chord length is shown in Figure 4.16 respectively. Figure 4.15 clearly illustrates the development of turbulence along the flow path on R_{ss}, where the SF=1.6 case, i.e. at large Reynolds number condition, higher value of turbulent viscosity is observed, though the high turbulent viscosity region locates at almost the same area at three Reynolds number condition. In addition, the location of the peak turbulent viscosity explains the slightly drop of its value beyond 93% chord length, as shown in

Figure 4.14, for both near wall and free stream flow. Figure 4.16 also shows more intensive turbulence at large Reynolds number condition, though the extension of turbulent region is almost identical. In addition, at all three Reynolds number conditions, the existence of turbulence on R_{ps} are also identified, suggesting flow separation in that region.

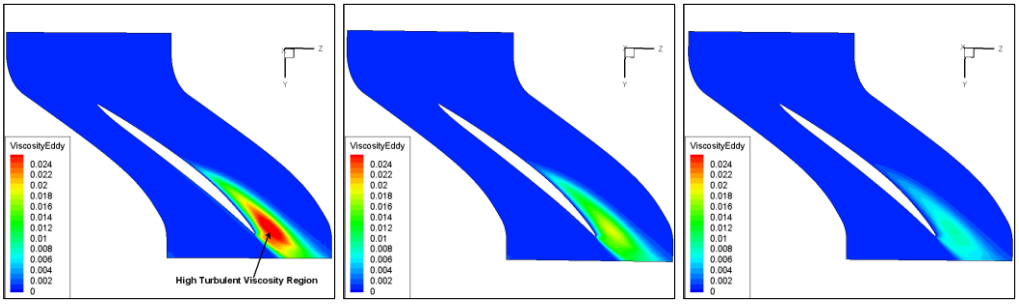

SF=1.6 SF=1 SF=0.4

Fig 4.15 Comparison of turbulent viscosity at 50% span from rotor hub, with design Mfr at different *Re* condition

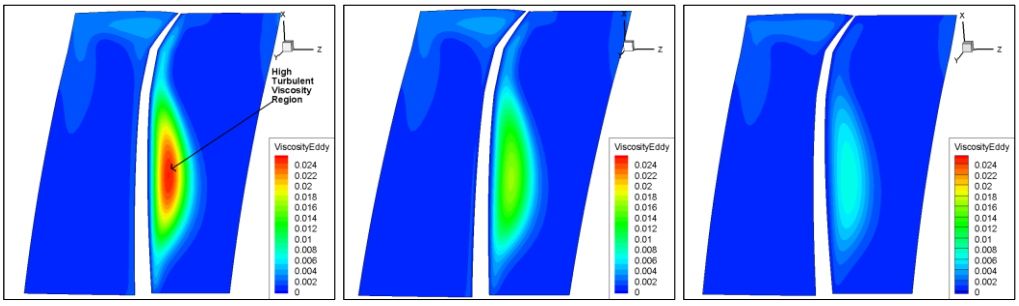

SF=1.6 SF=1 SF=0.4

Fig 4.16 Comparison of turbulent viscosity at 80% streamwise, with design Mfr at different *Re* condition

Figure 4.17 and Figure 4.18 further demonstrate the expansion of flow separation and development of wake right after the R_{TE}. For this comparison, only the values from *Re* 2.14×10^5 is considered, with 80%, 90% and 100% streawmise in rotor selected. In Figure 4.17, the expansion and transition of flow separation near R_{TE} is shown. The separated flow structure gradually merges with turbulent flow propagated from R_{ss}, forming the wake after leaving the R_{TE}. In Figure 4.18, the expansion of low Mach near rotor tip, further demonstrates the occurrence of flow separation and generation of wake. Fluid with low Mach from R_{ps} propagates downstream and interacts with fluid with high Mach from R_{ss}.

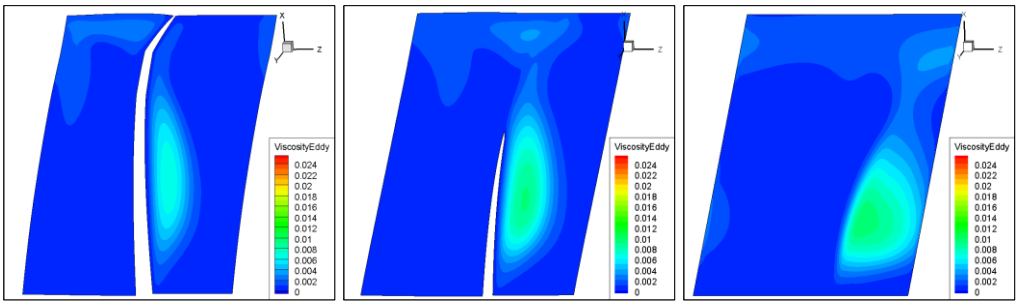

80% streamwise 90% streamwise 100% treamwise

Fig 4.17 Expansion of flow separation near R_{TE}, with design Mfr at *Re* 2.14×10^5 condition

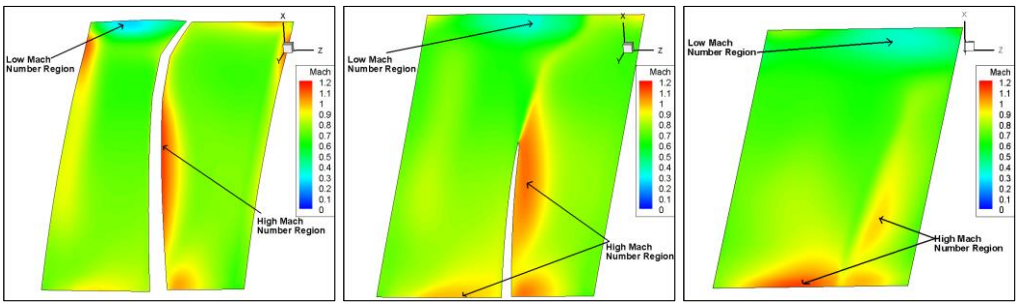

80% streamwise 90% streamwise 100% streamwise

Fig 4.18 Expansion of Mach contour near R_{TE}, with design Mfr at *Re* 2.14×10^5 condition

More statistical demonstration of the effect of flow separation on the η_{ad} loss, or the generation of entropy, is demonstrated. Figure 4.19 shows the locations of data points specified along flow path on R_{ps}, at 20%, 50%, 80%, 90% and 95% spanwise of rotor respectively, with 20 data points at each span location. The 90% and 95% spanwise are considered to better understand the flow separation near rotor tip. The case with designed Mfr at *Re* 5.34×10^5 condition is considered.

Figure 4.20 shows the distribution of entropy on R_{ps}, at different spanwise locations, respectively. At 20%, 50% and 80% span, the entropy increases from R_{LE}, after that, the entropy remains almost unchanged towards R_{TE}. A slightly higher entropy value is observed at upper span locations, as Mach is higher at upper span locations, resulting in more friction loss. At 90% and 95% span, the distribution of entropy is different from that at lower span locations. Although a slight increase of entropy is also observed at R_{LE}, the entropy value decreases rapidly at around 50% chord length, indicating the occurrence of flow separation.

The boundary layer near rotor tip detaches from the blade surface and interacts with free stream flow.

Figure 4.21 shows the distribution of Mach number on R_{ps}, at different span locations, respectively. At 20%, 50% and 80% spanwise, the Mach decreases slightly from R_{LE}, indicating the generation of boundary layer. After that, the Mach remains unchanged towards the R_{TE}. A slightly higher Mach is observed at upper spanwise locations, which is caused by the higher circumferential velocity at upper spanwise location. At 90% and 95% spanwise, the Mach increases from the R_{LE} towards around 60% chord length, where a decrease of Mach is observed towards the R_{TE}. This further identifies the occurrence of flow separation near rotor tip region.

Figure 4.22 shows the distribution of turbulent viscosity on R_{ps}, at different spanwise locations, respectively. At 20%, 50% and 80% spanwise, the turbulent viscosity increases gradually from R_{LE} towards R_{TE}, indicating the flow becomes more turbulent in the flow path. However, the turbulent viscosity value is higher at lower spanwise location, and the influence of compressor hub might contribute to this behavior. At 90% and 95% spanwise, the turbulent viscosity value remains almost zero from R_{LE} towards around 60% chord length, where a sudden jump of its value is observed. The jump of turbulent viscosity further demonstrates the occurrence of flow separation and the generation of turbulent flow. The smaller turbulent viscosity value near rotor tip on R_{ps} compared with that on R_{ss} suggests the flow is less turbulent on R_{ps}.

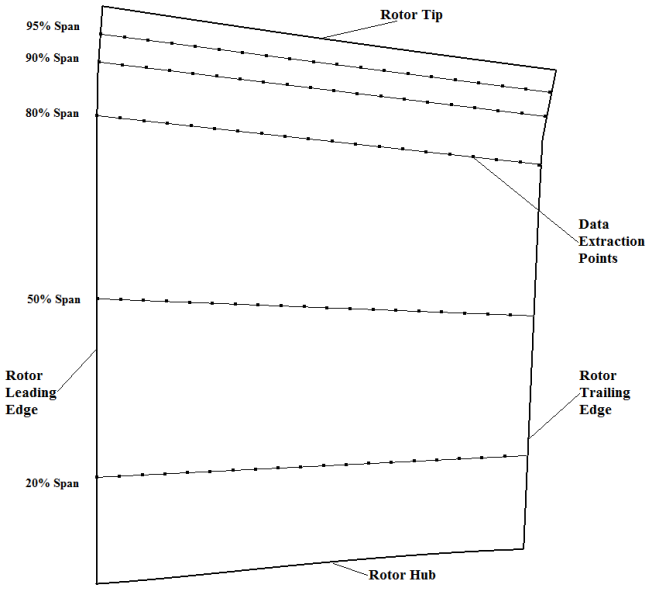

Fig 4.19 Locations of data extraction points on R_{ps}

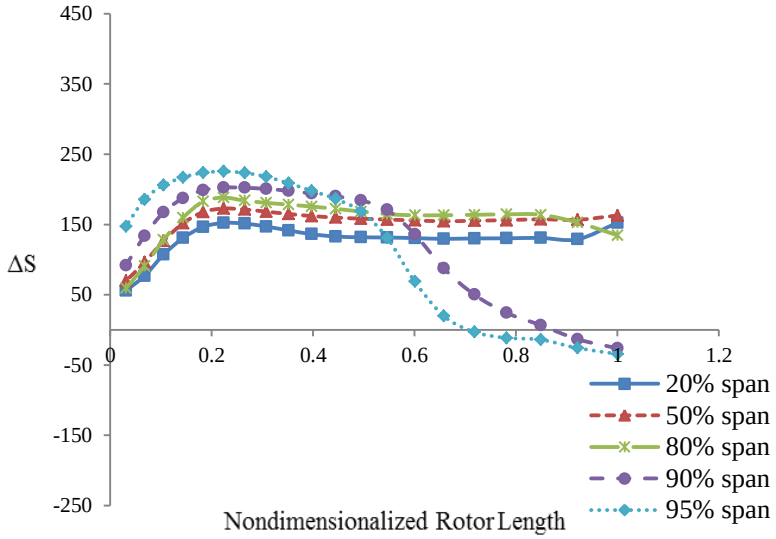

Fig 4.20 Distribution of entropy on R_{ps}, at 20%, 50%, 80%, 90% and 95% spanwise of rotor, with design Mfr at *Re* 5.34×10^5 condition

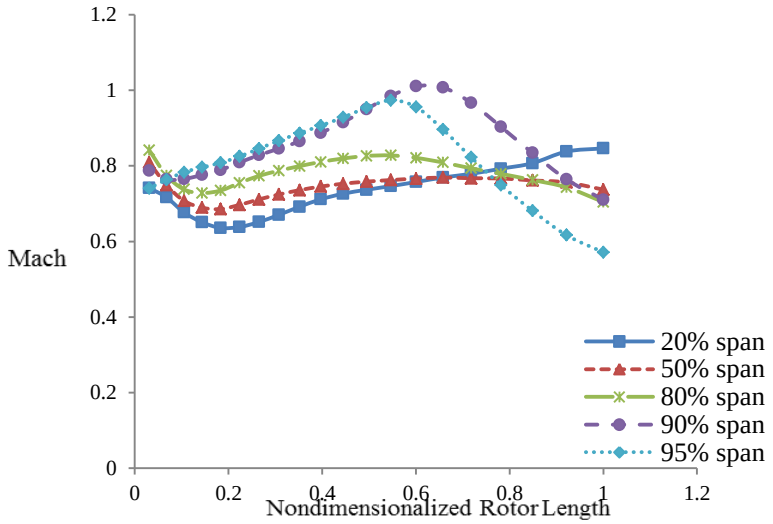

Fig 4.21 Distribution of Mach on R_{ps}, at 20%, 50%, 80%, 90% and 95% spanwise of rotor, with design Mfr at *Re* 5.34×10^5 condition

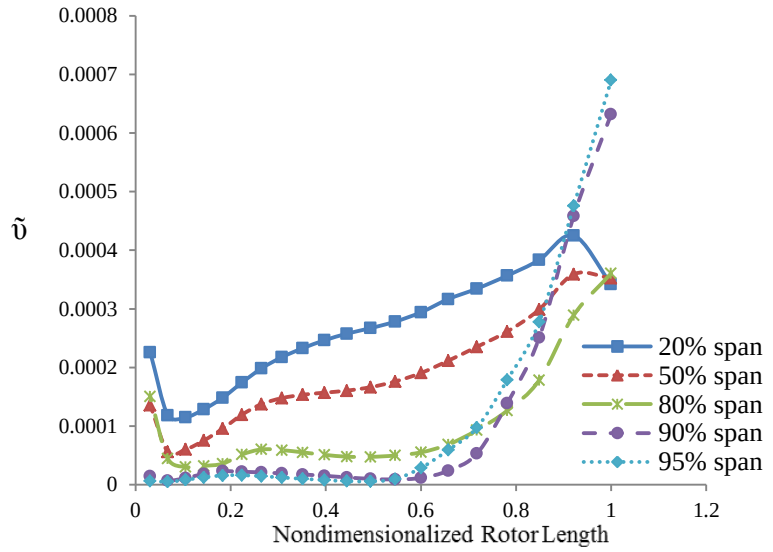

Fig 4.22 Distribution of turbulent viscosity on R_{ps}, at 20%, 50%, 80%, 90% and 95% spanwise of rotor, with design Mfr at *Re* 5.34×10^5 condition

As previously specified in Figure 4.11, based on the primary surface of 30% spanwise of rotor, the comparison of flow properties at 5%, 20% and 40% span from R_{ss} is also considered, to understand the effect of boundary layer and its interaction with induced turbulent flow. The case with designed Mfr at *Re* 5.34×10^5 condition is considered.

Figure 4.23 shows the distribution of entropy at different spans from R_{ss}. The entropy distribution at 5% span differs from the other two, as the effect of boundary layer is more prominent. The entropy distribution at 40% span is almost a flat line without any changes, indicating the free stream flow is nearly isentropic. In addition, the slight increase of entropy near the trailing edge plane shows the expansion of flow separation initiated from R_{ss}. Also, no further drop of entropy value is observed beyond 90% chord length at 40% span, which is different from the other two, suggesting effect of boundary layer has vanished in the free stream.

Figure 4.24 shows the distribution of Mach at different spans from R_{ss}. At all three span locations, a sudden drop of Mach is observed at around 40% chord length, though the location of abrupt Mach change delays when it is closer to R_{ss}. However, the Mach distribution at 5% span differs from the other two after the sudden drop. The Mach jumps to a relatively high value again and maintains until the R_{TE}. While at 20% and 40% spans, the Mach increases slightly towards rotor end after the dropping. This difference is caused by the boundary layer separation, which occurs right after the sudden drop of Mach on the R_{ss}.

Figure 4.25 shows the distribution of turbulent viscosity at different spans from R_{ss}. It further illustrates the location of boundary layer separation and the propagation of turbulence. At 5% span, the turbulent viscosity remains zero until 40% chord length, where slight increase is observed. It indicates the occurrence of boundary layer separation. At 20% span, the turbulent viscosity remains zero until 60% chord length, where a sharp increase is observed, indicating the propagation of turbulence induced by boundary layer separation at 40% chord length at 5% span. At 40% span, the turbulent viscosity behaves similar with that from 20% span, where a sharp increase is observed at a delayed location of 80% chord length. Therefore, the difference of turbulent viscosity at three spans indicates the transition of boundary layer separation and its interaction with core flow.

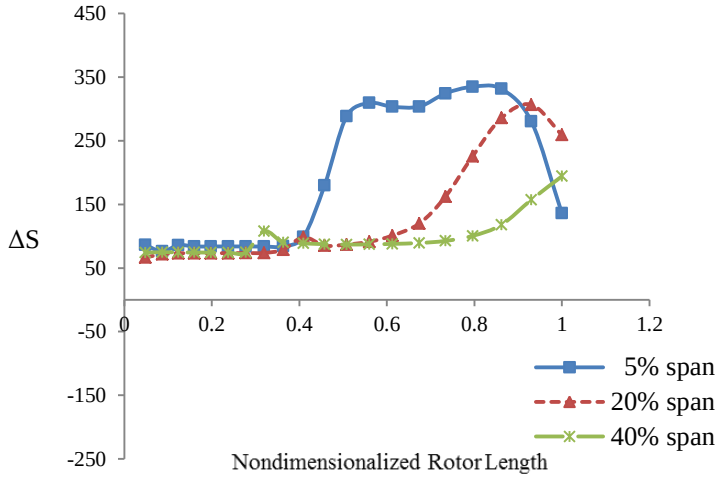

Fig 4.23 Distribution of entropy at 5%, 20% and 40% span from R_{ss}, with design Mfr at *Re* 5.34×10^5 condition

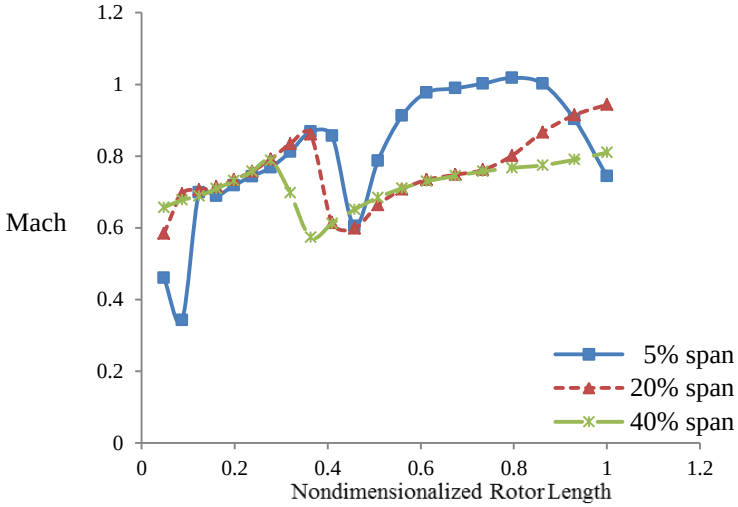

Fig 4.24 Distribution of Mach at 5%, 20% and 40% span from R_{ss}, with design Mfr at *Re* 5.34×10^5 condition

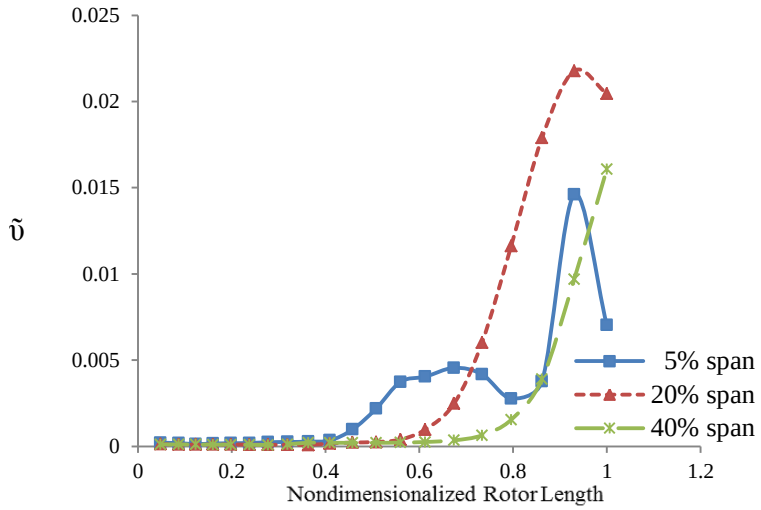

Fig 4.25 Distribution of turbulent viscosity at 5%, 20% and 40% span from R_{ss}, with design Mfr at *Re* 5.34×10^5 condition

4.2 Reynolds Number Effect in Stator Zone

The comparison of entropy distribution on S_{ss}, with reference value from airflow inlet area, is shown in Figure 4.26. The high entropy region is identified near the S_{LE} at all three Reynolds number conditions, indicating more friction loss in that region. Similar with observations made for Figure 4.9 previously, a comparative larger area of high entropy is also observed on S_{ss} for SF=0.4 case, suggesting more energy loss compared with the other two Reynolds number conditions. Results from designed Mfr are used for this comparison analysis.

As shown in Figure 4.26, the high entropy region mainly locates at the lower stator zone. Therefore, the entropy distribution on 30% spanwise of stator is considered, to investigate the difference of the extension of high entropy region, at different Reynolds number conditions. Figure 4.27 shows that the expansion of relative high entropy is almost identical at three Reynolds number conditions, locating at the S_{ss} flow path. This is caused by flow separation in that region, as previously discussed for Figure 3.19, and it coincide with the recirculation region as previously shown in Figure 3.29 and Figure 3.30 in Chapter 3. In addition, the high entropy which occurred by friction near S_{LE} only exists in a thin layer shortly

after the S_{LE}, as flow separation occurs right after the S_{LE}. The Reynolds number generally has minor effect on the overall distribution of entropy in the stator zone.

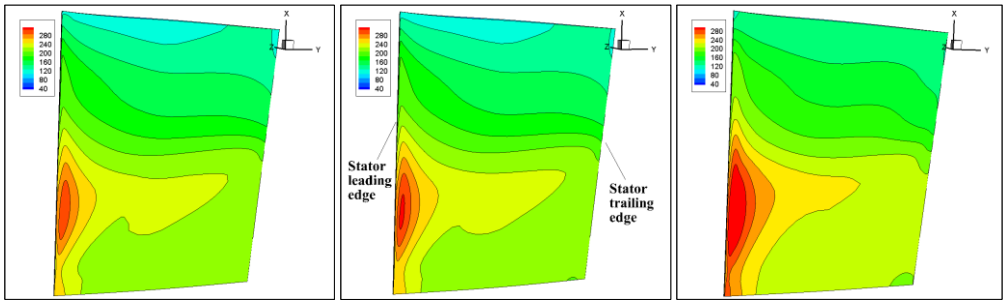

SF=1.6 SF=1 SF=0.4

Fig 4.26 Comparison of entropy distribution on S_{ss} at different *Re* condition, with design Mfr

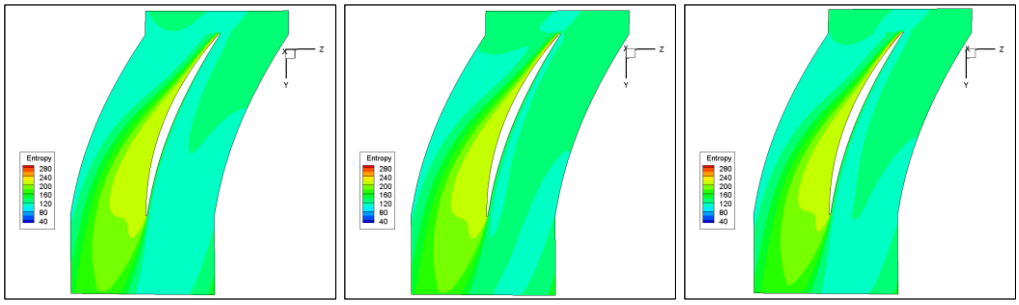

SF=1.6 SF=1 SF=0.4

Fig 4.27 Comparison of entropy distribution on 30% spanwise of stator at different *Re* condition, with design Mfr

In order to more statistically demonstrate the conclusion, a similar approach, which is used for the analysis of rotor zone, is adopted. As a 3D problem, the 30% spanwise of stator is selected as the primary surface because more variation of entropy is observed in the lower fluid zone as previously discussed, values from 5%, 20% and 40% span from S_{ss} are extracted based on the primary surface. In total, 20 data points are considered for each span location, ranging from S_{LE} to S_{TE}. Figure 4.28 shows the location of data extraction points.

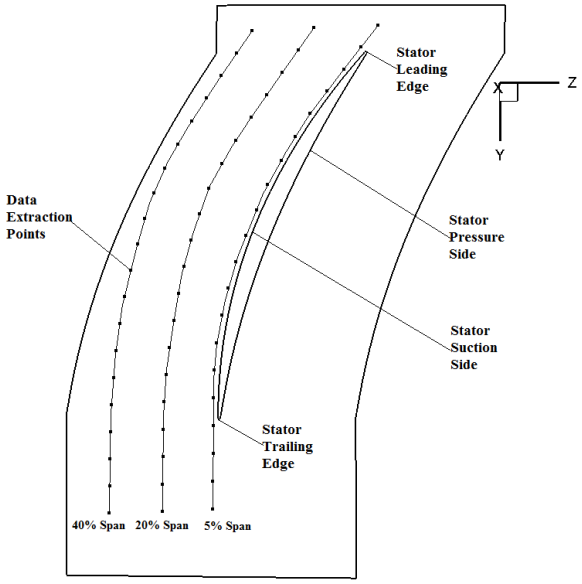

Fig 4.28 Locations of data extraction points on the primary surface in stator zone

The distribution of entropy on primary surface at 5% and 20% span from S_{ss} at different Reynolds number conditions is shown in Figure 4.29, respectively. The nondimensionalized stator length is used to identify the locations of data points along stator flow path, and ΔS indicate the entropy value with reference to the entropy value at rotor inlet surface. At 5% span, the entropy distributes similar along stator flow path at different Reynolds number conditions. The entropy starts from a low value at 0% chord length, which locates right before the stator blade. After that, the entropy climbs quickly when flow attacks the stator blade, where friction loss is high. From around 9% to 80% chord length, the entropy remains at the relative high value, indicating the flow is almost isentropic in the near wall region. After 80% chord length, a sudden drop of entropy is observed, indicating the flow leaving S_{TE}, which can be identified from data point locations shown previously. A slight higher entropy value is observed from around 9% to 18% chord length, which indicates S_{LE} region, at relative small Reynolds number condition, i.e. SF=0.4. This is identical with observations made in Figure 4.26 previously, where larger area of high entropy is identified at small Reynolds number condition. At 20% span, the entropy distribution at different Reynolds number condition is almost identical. However, distribution at 20% span is

dramatically different from that at 5% span. The entropy slightly decreases from 0% chord length till around 20% chord length, where a quick climb of entropy value is observed until 60% chord length. After 60% chord length, the entropy slightly decreases again towards 100% chord length. The sharp increase of entropy indicates the propagation of flow separation and the effect of turbulence, where fluid interaction is tremendous.

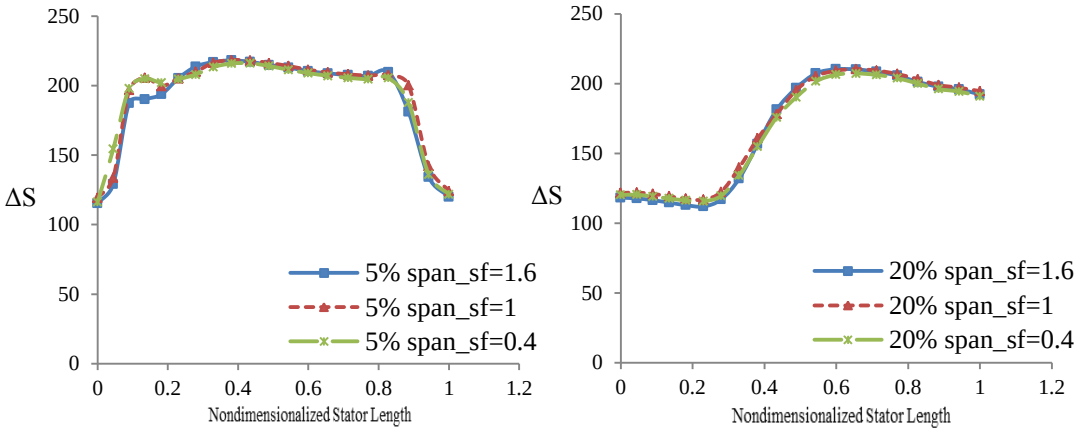

5% span 20% span

Fig 4.29 Distribution of entropy at 5% and 20% span from S_{ss} based on the primary surface, with design Mfr at different *Re* condition

Figure 4.30 shows the distribution of Mach on primary surface at 5% and 20% span from S_{ss} at different Reynolds number conditions. It further explains the entropy distribution as just discussed. At 5% span, a sudden jump of Mach is identified at S_{LE}, when flow impinges on stator blade. After that, the Mach decreases sharply to small value until around 40% chord length, indicating the development of flow separation induced right after the S_{LE}. The Mach remains relatively small until around 80% chord length, when flow leaves S_{TE}. A sudden jump of Mach is observed at 80% chord length, when fluid with low Mach from S_{ss} interacts with fluid with relative high Mach from S_{ps}. At 20% span, the Mach decreases gradually from 0% chord length until around 70% chord length, where a slight increase of Mach is observed. The decrease of Mach further describes the propagation of flow separation along stator flow path, while the slight increase of Mach indicates the expansion of interaction with high Mach fluid from S_{ps}. Again, the Mach presents similar distribution at different Reynolds number conditions.

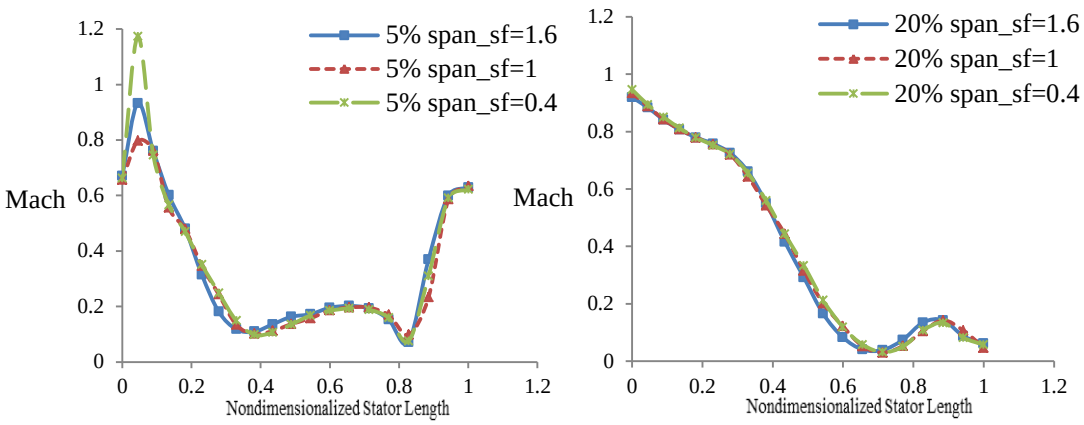

5% span 20% span

Fig 4.30 Distribution of Mach at 5% and 20% span from S_{ss} based on the primary surface, with design Mfr at different *Re* condition

Figure 4.31 shows the distribution of turbulent viscosity on primary surface at 5% and 20% span from S_{ss} at different Reynolds number condition. It more straightforwardly describes the generation and intensity of turbulence in the flow path. At 5% span, the turbulent intensity remains almost zero from 0% chord length until around 80% chord length, where an increase of its value is observed. This is caused by the interaction of flow with different velocity after S_{TE}. At 20% span, the turbulent viscosity remains at low value until around 30% chord length, where a gradual increase of its value is observed until 100% chord length. This is caused by the expansion of flow separation which induced near the S_{LE}. At both 5% and 20% span, more intensive turbulence is observed at the larger Reynolds number condition, as less viscous effect is expected. Figure 4.32 further illustrates the difference of turbulent viscosity at different Reynolds number condition. At large Reynolds number condition, higher turbulent viscosity value is identified, though the high turbulent viscosity region locates at almost the same area at all three Reynolds number conditions. The contour also shows the development of turbulence along stator flow path.

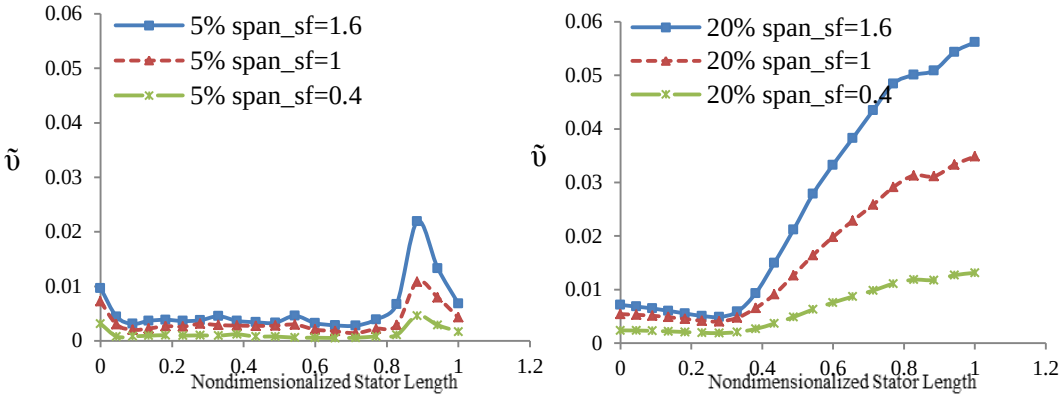

5% span 20% span

Fig 4.31 Distribution of turbulent viscosity at 5% and 20% span from S_{ss} based on the primary surface, with design Mfr at different *Re* condition

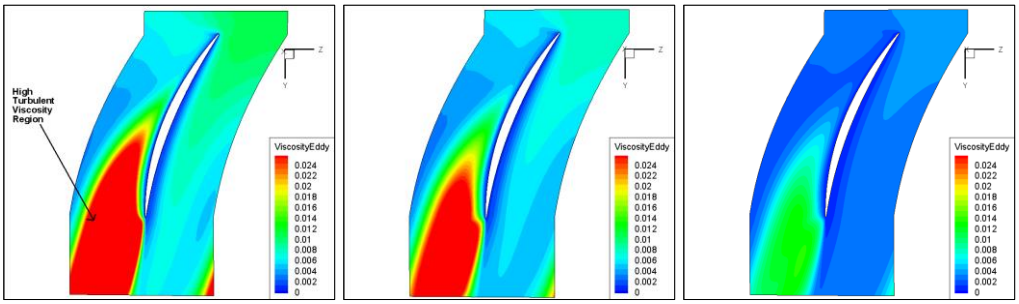

SF=1.6 SF=1 SF=0.4

Fig 4.32 Comparison of turbulent viscosity on 30% spanwise of stator, with design Mfr at different *Re* condition

As previously specified in Figure 4.28, based on the primary surface of 30% spanwise of stator, the comparison of flow properties at 5%, 20% and 40% span from S_{ss} is also considered, to further understand the effect of boundary layer separation and its interaction with free stream flow. The case with designed Mfr at *Re* 5.34×10^5 condition is considered.

Figure 4.33 shows the distribution of entropy at 5%, 20% and 40% span from S_{ss}, at *Re* 5.34×10^5. At the 5% span, the entropy distributes differently from the other two. A sudden jump of entropy is observed near S_{LE}, as previously discussed. Also, a sudden drop of entropy is observed near S_{TE}, indicating the flow interaction and wake region after stator blade. At 20% span and 40% span, the change of entropy is more gradual, as previously discussed, indicating the propagation of flow separation induced from S_{LE} region. In addition, the further

away from stator blade, the lower entropy value is observed, as well as smaller entropy gradient. This further shows the development of turbulence, as shown in Figure 4.32 previously.

Figure 4.34 shows the distribution of Mach at 5%, 20% and 40% span from S_{ss}, at *Re* 5.34×10^5 condition. The Mach distribution is different at each span. At 5% span, the Mach drops early due to the early occurrence of flow separation. Also, the interaction of low Mach fluid from S_{ss} with high Mach fluid from S_{ps} results the increase of Mach after the S_{TE}. At 20% span, the Mach decreases from 0% chord length, as the high Mach fluid at S_{LE} only impacts near wall regions. A slight increase of Mach is also observed at 70% chord length, due to the expansion of flow interaction in S_{TE} region. At 40% span, the Mach decreases gradually without any fluctuation, indicating that free stream flow is not affected by S_{TE} wake.

Figure 4.35 shows the distribution of turbulent viscosity at 5%, 20% and 40% span from S_{ss}, at *Re* 5.34×10^5 condition. At 5% span, the distribution behaves different from the other two. The Turbulent viscosity remains almost unchanged until 80% chord length, as previously discussed, when flow interaction happens in the wake region. At 20% span and 40% span, the distribution behaves similarly, where a gradual increase of turbulent viscosity is observed from 30% chord length at 20% span, while 40% chord length at 40% span. The delay of increase at 40% span illustrates the propagation of separated flow initiated from $S_{LE.}$

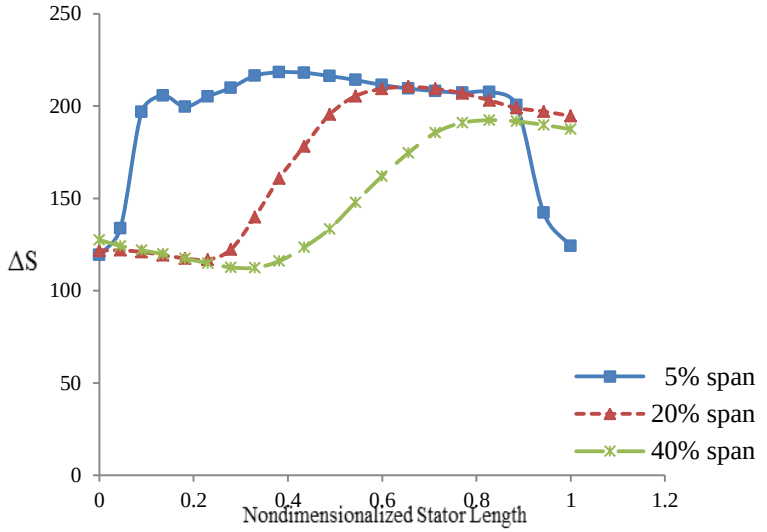

Fig 4.33 Distribution of entropy at 5%, 20% and 40% span from S_{ss}, with design Mfr at *Re* 5.34×10^5 condition

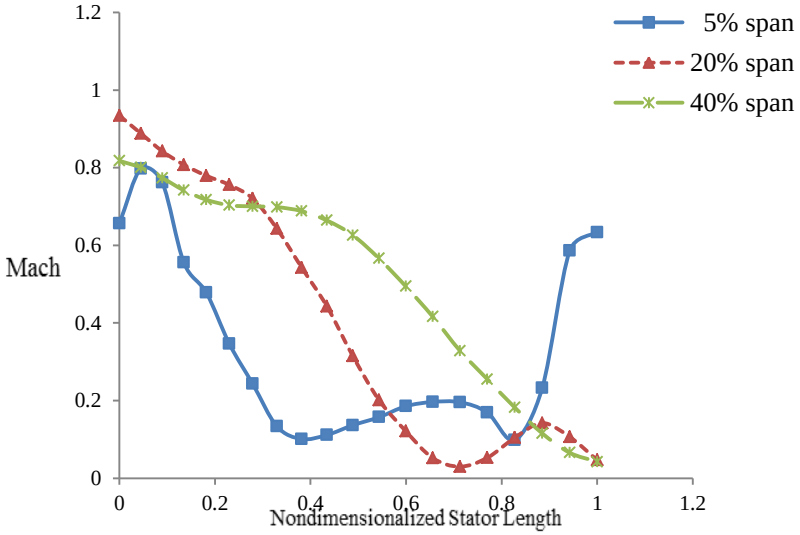

Fig 4.34 Distribution of Mach at 5%, 20% and 40% span from S_{ss}, with design Mfr at *Re* 5.34×10^5 condition

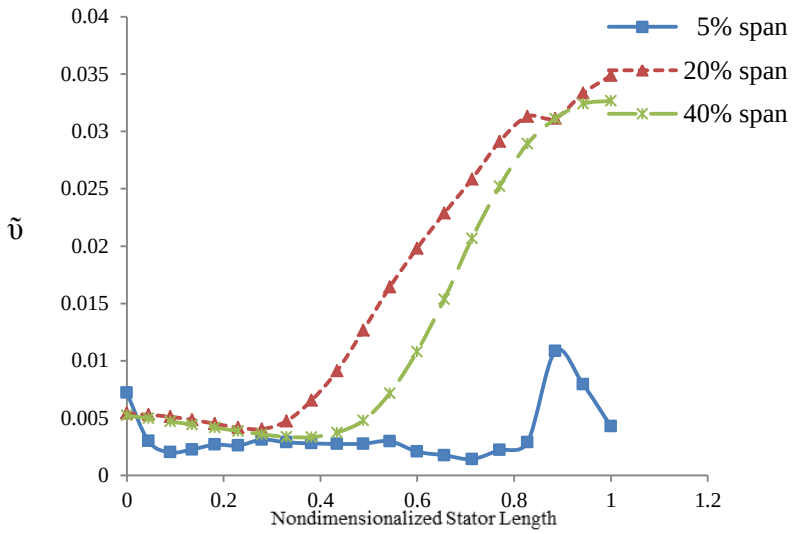

Fig 4.35 Distribution of turbulent viscosity at 5%, 20% and 40% span from S_{ss}, with design Mfr at *Re* 5.34×10^5 condition

In summary, the effect of Reynolds number during the miniaturization of an axial compressor is studied. Scaling factors ranging from 1.6 to 0.4 are applied on the original compressor geometry, resulting in operating Reynolds number ranges from *Re* 2.14×10^5 to *Re* 8.54×10^5, when designed Mfr and 100% design speed are applied. Numerical results indicate that the miniaturization has an adverse effect on compressor performance, due to increased viscous effect. Both the total pressure ratio and the overall adiabatic efficiency drop when Reynolds number decreases. Analysis of flow fields at varying Reynolds number conditions shows that the miniaturization process has minor effects on flow property changes except the generation of turbulence, where the decrease of turbulence intensity is prominent with the decrease of Reynolds number.

Chapter 5

Heat Transfer Effect

Thereafter, the heat transfer effect on the compressor performance is investigated. For miniaturized gas turbines, larger heat loss is expected due to the higher surface-to-volume ratio. In this study, three different thermal conditions are applied on the wall boundaries, to verify the difference of performances when wall thermal conditions are changed.

Table 5.1 presents the different thermal conditions applied. Case 1: Adiabatic wall condition is initially applied, where heat transfer through wall is not allowed. This is also the default wall thermal conditions for simulations discussed in previous chapters. Case 2: A constant heat transfer coefficient (h) is applied on wall boundaries, where heat exchange between internal flow and external air are enabled. Case 3: Isothermal wall condition is applied to approximate the thermal condition when the effect of combustion chamber is considered, which is mounted downstream of the compressor.

Table 5.1 Specifications of Wall Thermal Conditions

	Specification of Thermal Conditions	Specification of Values
Case 1	Adiabatic Wall Condition	Q=0
Case 2	Constant Heat Transfer Coefficient	h=200 (W/m^2·k)
Case 3	Isothermal Wall Condition	T=380 (k)

The default wall thermal condition was applied for simulations in previous chapters, where the system was considered adiabatic, i.e. without transfer of heat and matter between the system and its surroundings. In order to aid our analysis, 9 spanwise locations are specified in the blade radial direction, on rotor inlet and stator outlet surface. The spanwise location ranges from 5% to 95% is specified, corresponding to the locations of test points specified in experiment. Therefore, the 5% spanwise indicates data line adjacent to compressor hub, and the 95% spanwise indicates data line adjacent to compressor casing. At each spanwise, 20

data points are extracted which evenly distribute on each line and the average of data from these points are calculated for analysis. Figure 5.1 shows the specifications of data extraction points on rotor inlet surface and Figure 5.2 shows the specifications of data extraction points on stator outlet surface, respectively.

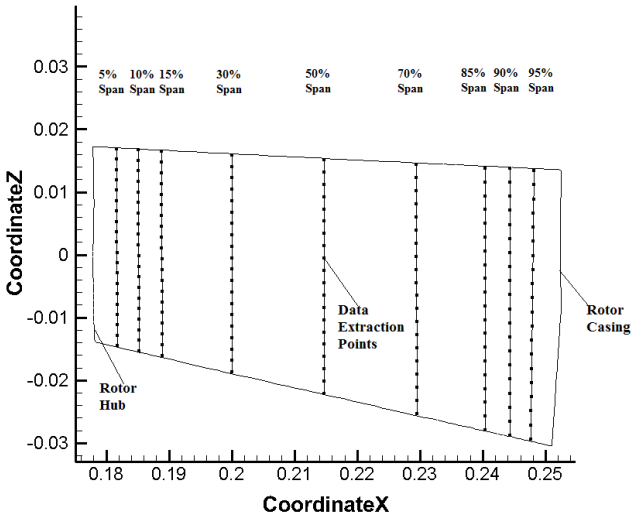

Fig 5.1 Locations of data extraction points on rotor inlet surface

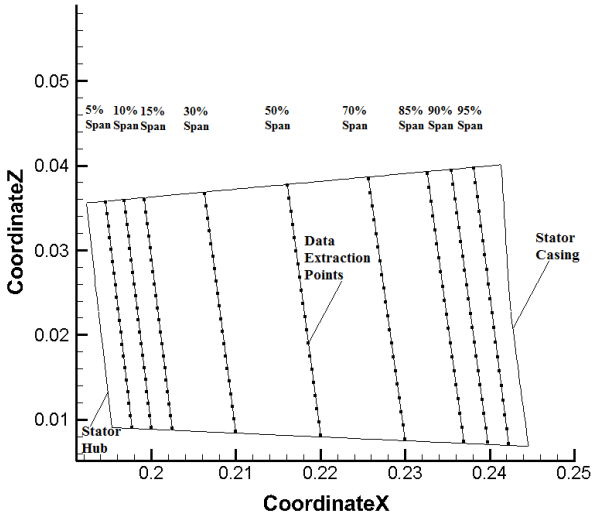

Fig 5.2 Locations of data extraction points on stator outlet surface

Boundary conditions validated in Chapter 3 are applied except for the wall thermal condition, which varies from case to case in this chapter. Only 100% design speed and design Mfr are considered in this study. Results from Case 1 are firstly compared with available experimental data, to understand the accuracy of CFD in predicting compressor performance at changed thermal conditions.

Figure 5.3 shows the distribution of total pressure ratio (*Pr*) at different blade radial spans. For the CFD results, the average value at each spanwise is calculated and used as mentioned. At adiabatic wall condition, i.e. wall Q=0, the CFD results generally captures the value of *Pr* from experiments. The value of *Pr* gradually drops from hub towards casing and the CFD results generally underestimate experimental data. The largest deviation is observed near casing and an underestimation of 10% is identified at 95% spanwise. The best consistence is observed near hub, where almost identical *Pr* value is achieved. Therefore, the CFD approach is considered reliable.

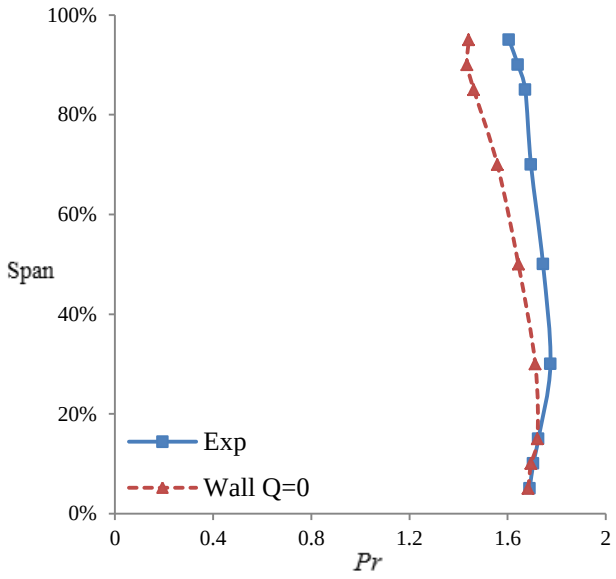

Fig 5.3 Distribution of *Pr* at different blade radial spans

Figure 5.4 shows the distribution of total temperature ratio (*Tr*) at different blade radial spans. At adiabatic wall condition, the CFD results satisfactorily capture the value of *Tr* from experiments. The value of *Tr* from experiments slightly fluctuate around 1.2 from hub towards casing. The CFD produces less than 5% difference

with experimental data at every span, and the area-averaged *Tr* from simulation is 1.225. Therefore, the prediction of *Tr* by CFD is considered reliable.

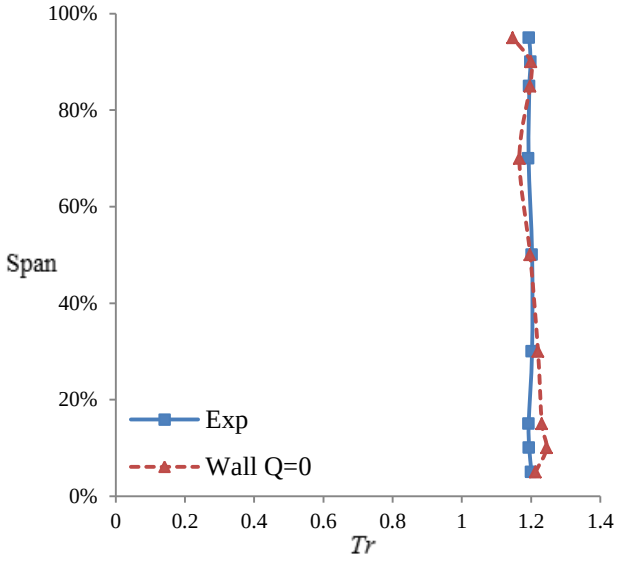

Fig 5.4 Distribution of *Tr* at different blade radial spans

Figure 5.5 shows the distribution of sectional adiabatic efficiency $\eta_{ad} = ((\overline{P_{out}}/\overline{P_{in}})^{(\gamma-1)/\gamma} - 1)/((\overline{T_{out}}/\overline{T_{in}}) - 1)$ at different blade radial spans. At adiabatic wall condition, the CFD results generally underestimate the value of η_{ad} compared with experiments. Especially at 90% spanwise, an underestimation of 27% is observed. The experimental data falls in the region between 0.74 and 0.88, from hub towards casing. While the CFD results fall in the region between 0.55 and 0.81, from hub towards casing, suggesting a larger fluctuation. However, large deviations are mainly identified near casing and hub regions, and the area-averaged η_{ad} from simulation is 0.77, which gives reasonable prediction of experimental data.

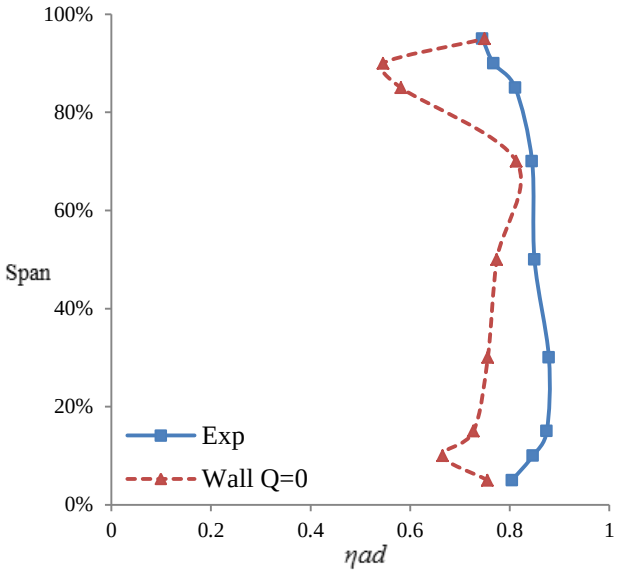

Fig 5.5 Distribution of η_{ad} at different blade radial spans

The comparison of simulation results for Case 1 and experimental data has demonstrated the capability of CFD in predicting compressor performance. Also, the drawbacks and inaccuracy of CFD in precisely capturing property distribution at different spanwise locations are also understood. The simulation solves time-averaged RANS equations, where the nonlinear Reynolds stress term is modelled by the proposed turbulence model. In addition, the mixing plane interface treatment method has enforced the circumferential averaging of flow data, where any unsteadiness is removed when fluid passes from rotor to stator. The reason mentioned might have contributed to the deviation of simulation results and experimental data.

5.1 Effect of Heat Flux

The heat transfer coefficient is then applied on wall boundaries, replacing the default adiabatic wall condition. Heat exchange is thus allowed between the system and its surroundings. The Chilton-Colburn Analogy $\frac{f}{2} = \frac{k_c}{U}\mathrm{Sc}^{2/3} = \frac{h}{\rho U C_p}\mathrm{Pr}^{2/3}$ is followed to describe the similarity between momentum, mass and energy. Based on experimental data, the turbulent Prandtl number ($\mathrm{Pr_t}$) ranges

from 0.7 to 0.9 depending on the Prandtl number ($\mathrm{Pr} = \frac{Viscous\ Diffusion\ Rate}{Thermal\ Diffusion\ Rate} = \frac{\mu C_p}{k}$) of the fluid, where μ is the dynamic viscosity, C_p is the specific heat and k is the thermal conductivity. When Pr is small, i.e., $\mathrm{Pr} \ll 0$, the thermal diffusivity (heat conduction) dominates and the heat diffuses quickly compared to momentum (convection). As an indication of heat transfer, the heat transfer coefficient calculates the proportionality of heat flux and temperature difference, which is defined in Equation 5.1.

$$h = \frac{q''}{\Delta T} \tag{5.1}$$

where q'' is the heat flux (W/m^2), i.e. thermal power per unit area, ΔT is the difference in temperature (k) between the solid surface and its surrounding fluid, and h is the heat transfer coefficient (W/m^2·k). Therefore, the predefined value of heat transfer coefficient partially determines the intensity of heat transfer, typically by convection or phase transition as ΔT is simultaneously calculated during simulation when internal flow temperature varies.

Boundary conditions are defined exactly the same as Case 1, except the wall thermal conditions. Different values of heat transfer coefficient, ranging from 100W/m^2·k to 600W/m^2·k, are firstly applied to understand its impact, although the physical value of certain fluid is limited within an empirical range. Figure 5.6a shows the distribution of *Pr* and η_{ad} (Stage adiabatic efficiency) with the increase of heat transfer coefficient. The value of heat transfer coefficient only has minor effect on the compressor overall performance. Less than 0.3% increase of *Pr* and less than 2% of η_{ad} are observed. Figure 5.6b further shows the distribution of *Tr* with the increase of heat transfer coefficient. Only 0.2% decrease of *Tr* is observed, indicating the heat loss through wall is not significant compared with the total work input. This could be explained by the total work input formula, $\dot{m}C_p(T_{o2} - T_{o1}) + Q$, where Q is the heat loss through wall. The value of $\dot{m}C_p(T_{o2} - T_{o1})$ is calculated as 36836.8 watt and Q is calculated as 293.8 watt with h=600W/m^2·k. Therefore, the total work input should be 0.79% higher, due

to heat loss. Since the heat loss is still small compared with the total work input, the observation of Pr and η_{ad} distribution will still remain reliable.

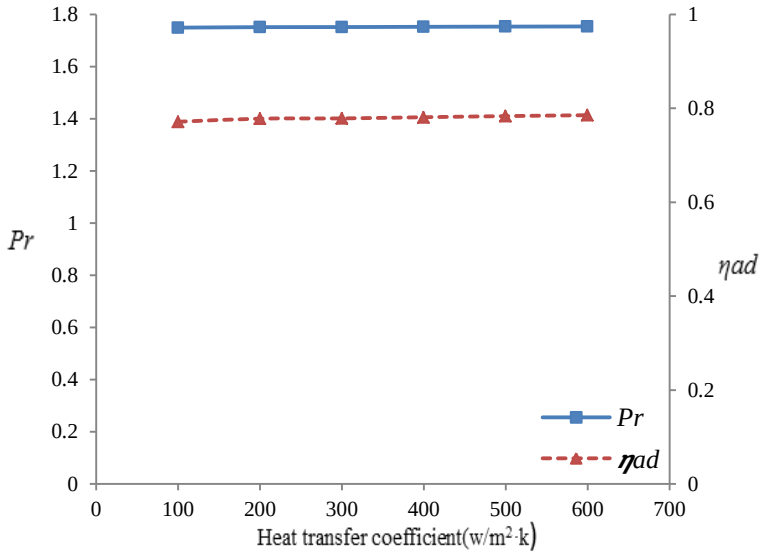

Fig 5.6a Distribution of Pr and η_{ad} with the increase of heat transfer coefficient

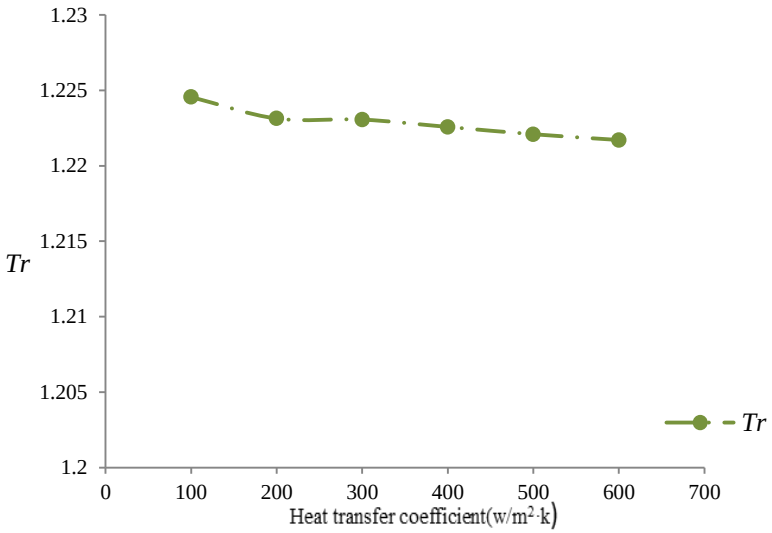

Fig 5.6b Distribution of Tr with the increase of heat transfer coefficient

The difference of performance with different values of heat transfer coefficient is minor as discussed. However, the difference of compressor performance w/ or w/o heat transfer through wall is not yet investigated. Therefore, a constant value of h =200 W/m^2·k is applied, i.e. Case 2, to further understand the problem. The

h =200 W/m^2·k is chosen referred to the empirical heat transfer coefficient of air, which ranges from -10 W/m^2·k to 100 W/m^2·k, but we use an amplified while still physically possible value (when outside cooling technique is applied) to aid our subsequent study. The constant value is also applied on SF=1.6 and SF=0.4, as discussed in Chapter 4, to understand the effect of heat transfer at varying Reynolds number conditions. Table 5.2 shows the specifications of thermal condition and comparison of numerical results.

The change of *Pr* is negligible at all three *Re* conditions, which is in consistence with previous discussions that the heat transfer coefficient has minor effect on overall *Pr*. However, a slight increase of η_{ad} is observed at all three *Re* conditions. The largest increase is observed for SF=0.4, where more than 1% increases is identified. At small *Re* condition, i.e. for miniaturized compressor, the increase of surface-to-volume ratio also contributes to an increased heat transfer through wall. The decrease of compressor internal temperature leads to lower entropy at small *Re* condition, indicating less η_{ad} loss. Figure 5.7 shows the comparison of *Pr* at two thermal conditions, suggesting minor effect of heat transfer on *Pr*. Figure 5.8 shows the comparison of η_{ad} at two thermal conditions, supporting discussions just made about the difference of heat transfer on η_{ad} at varied *Re* conditions. As mentioned previously, the small heat loss due to the applied heat transfer coefficient is not taken into account in the calculation of $\eta_{ad.}$ The heat loss at h =200 W/m^2·k is Q=137.72 watt for SF=1 case, i.e., 0.37% of the total work input.

Table 5.2 Comparison of Results from Different Thermal Conditions

Heat transfer coefficient (W/m^2·k)			200	
Free stream temperature (k)			288	
SF	*Pr*	Change of *Pr*	η_{ad}	Change of η_{ad}
1.6	1.760264	-0.03%	0.783879	+0.68%
1	1.751108	+0.02%	0.777988	+1.00%
0.4	1.734521	-0.06%	0.765332	+1.02%

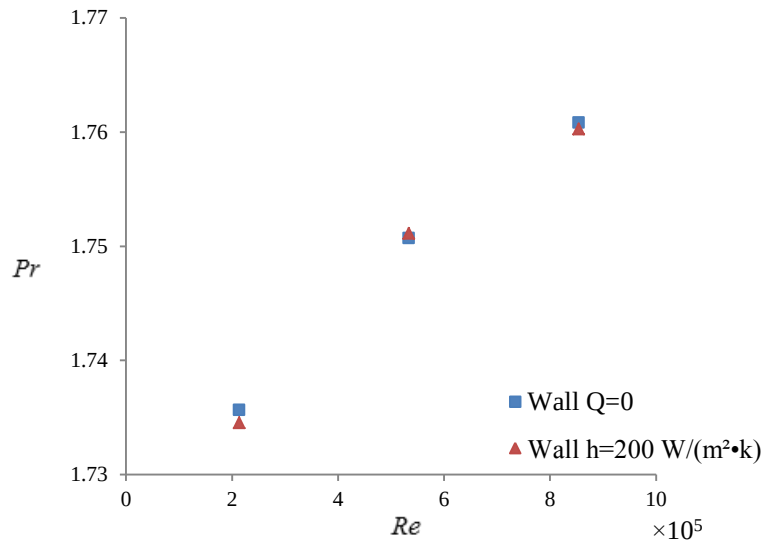

Fig 5.7 Comparison of *Pr* for Wall Q=0 & Wall *h*=200 W/m^2·k

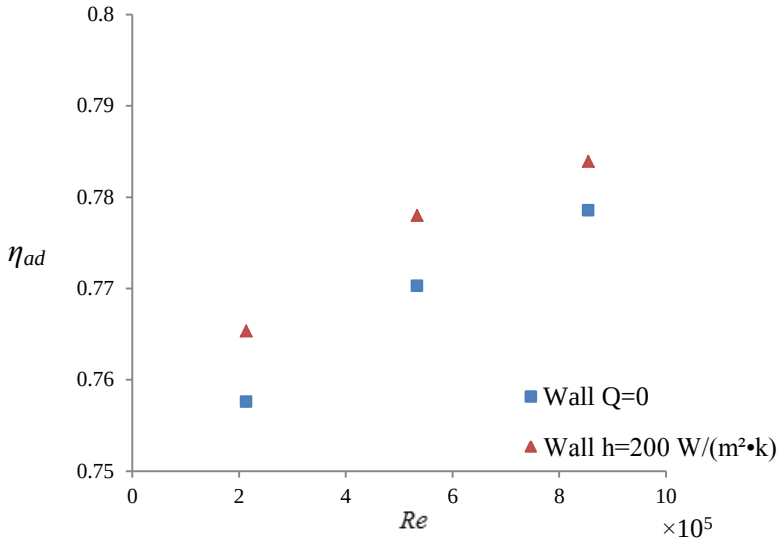

Fig 5.8 Comparison of η_{ad} for Wall Q=0 & Wall *h*=200 W/m^2·k

The comparison of entropy distribution on R_{ss} for Case 1 and Case 2 is also shown in Figure 5.9, and the results at *Re* 5.34×10^5 are used. The decrease of high entropy region is observed for Case 2, indicating less efficiency loss. In addition, the comparison of temperature distribution on R_{ss} for Case 1 and Case 2 is also shown in Figure 5.10. The decrease of high temperature region is also observed for Case 2, proving the effect of heat transfer through wall. The decreased loss of

efficiency can also be explained by the decrease of average T_o, as the heat loss is due to $T_o dS$.

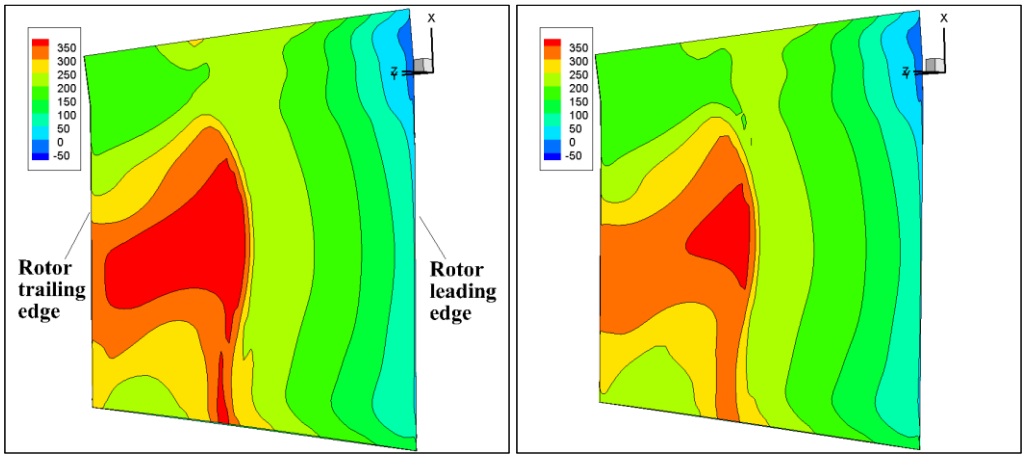

Case1 Case2

Fig 5.9 Comparison of entropy distribution on R_{ss} for Case1 & Case 2, with design Mfr at *Re* 5.34×10^5 condition

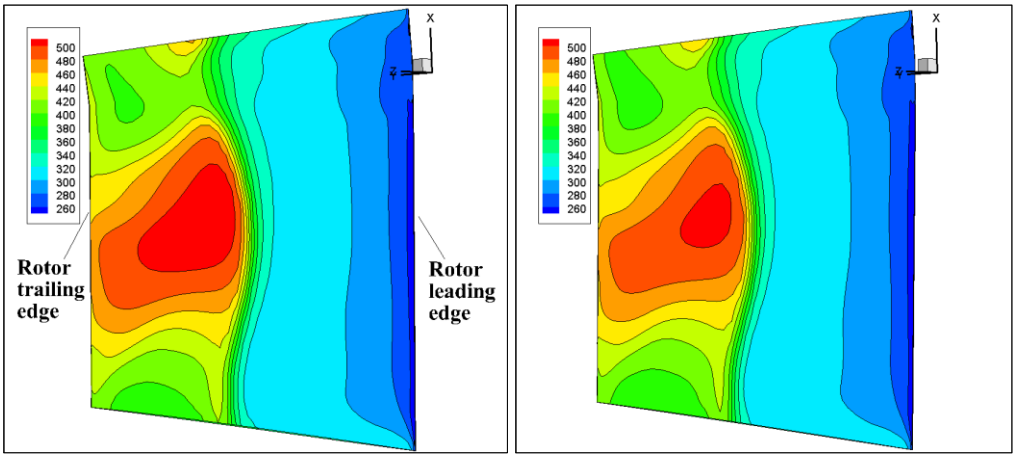

Case1 Case2

Fig 5.10 Comparison of temperature distribution on R_{ss} for Case 1 & Case 2, with design Mfr at *Re* 5.34×10^5 condition

Besides that, the comparison of entropy distribution on R_{ss} for Case 2 at three varied *Re* conditions is also shown in Figure 5.11, to further understand the difference of heat transfer effect when compressor is miniaturized. Relative smaller high entropy area is observed at SF=0.4, though the difference is not prominent. In addition, the comparison of temperature distribution on R_{ss} for Case

2 at three *Re* conditions is also shown in Figure 5.12. The high temperature region almost disappears at SF=0.4, showing more heat loss for miniaturized compressor.

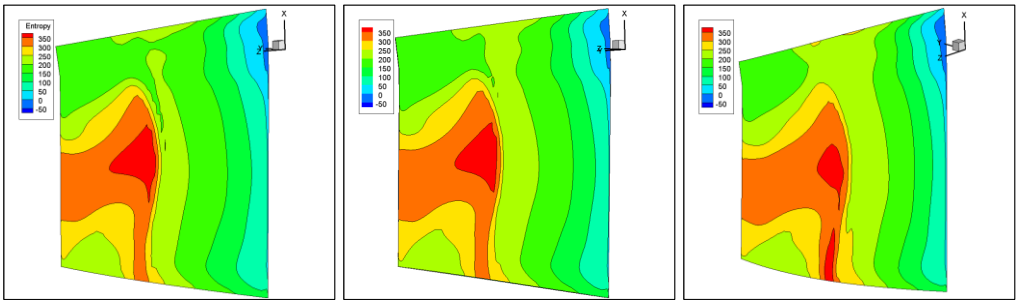

SF=1.6 SF=1 SF=0.4

Fig 5.11 Comparison of entropy distribution Variation on R_{ss} for Case2, with design Mfr at varying *Re* condition

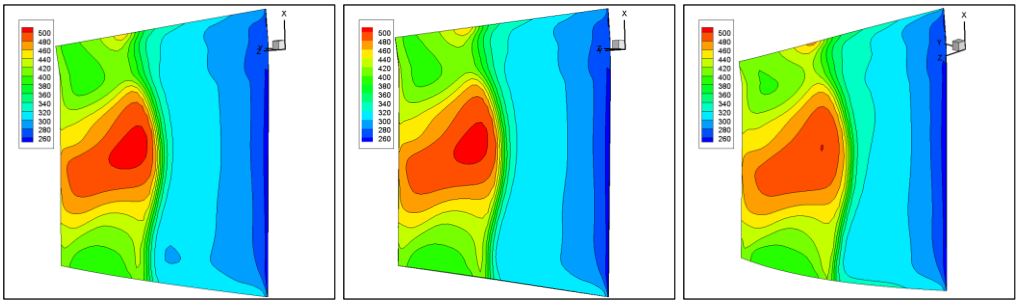

SF=1.6 SF=1 SF=0.4

Fig 5.12 Comparison of temperature distribution Variation on R_{ss} for Case2, with design Mfr at varying *Re* condition

5.2 Effect of Isothermal Wall

The metal temperature is tested, due to the effect of combustion chamber locates after the compressor. In Case 1 and Case 2, the effect of heat from combustor is not considered. In this study, different isothermal wall conditions are firstly applied to understand its effect on the overall performance. The result from isothermal wall temperature 380k, i.e. Case 3, is then utilized for comparison with Case 1 and Case 2, which will be discussed in details shortly.

This thermal conduction boundary condition is different from the previous convective boundary condition, as it is due to the collisions and diffusion of

molecules during their random motion. The Fourier's law is used to define the thermal conduction, where its differential form is given as,

$$\vec{q} = -\kappa\nabla T \tag{5.2}$$

$\vec{q}$ is the local heat flux density, and it equals to the product of thermal conductivity κ and the negative local temperature gradient $-\nabla T$. The heat flux density is the amount of energy that flows through a unit area per unit time.

Boundary conditions are defined exactly identical with Case 1, except the wall thermal conditions. Again, the *Re* 5.34×10^5 condition is considered. Five different isothermal conditions, from 300k to 460k with an interval of 40k between subsequent levels, are applied. This is specified according to available experimental data, as temperature at 5% span from stator casing is observed as 382k, when 100% design speed is applied.

Figure 5.13 shows the distribution of *Pr* with the change of isothermal wall temperature. The *Pr* almost declines linearly with the increase of isothermal wall temperature. In total, 2.2% drop of *Pr* is identified within the applied temperature range. This can be explained by the ideal gas law introduced previously. As the isothermal wall temperature increases, the air within the compressor is also heated up. The volume of air expands as it is proportionally related to temperature at ideal condition, while the pressure of air is inversely proportional to the volume occupied. Therefore, the overall *Pr* also decreases with the increase of temperature. Figure 5.14 shows the distribution of *Tr* with the change of isothermal wall temperature. The *Tr* increases by 1.8% within the applied wall temperature range, because of more heat added into the internal flow from wall. Figure 5.15 shows the distribution of η_{ad} with the change of isothermal wall temperature. A decrease of η_{ad} is observed, suggesting the heat from combustor deteriorates compressor efficiency. Similar to the discussions for Case 2, the total work input should be justified by the formula $\dot{m}C_p(T_{o2} - T_{o1}) + Q$, while Q will be of opposite sign. The value of $\dot{m}C_p(T_{o2} - T_{o1})$ is calculated as 37970.24 watt with T=380k, which is higher than Case 2 due to heat addition. The value of Q is

calculated as -341.94 watt at T=380k. Therefore the total work input should be 0.9% smaller, due to heat addition. This difference is not taken into our calculation due to its insignificance. In general, the isothermal wall, i.e. heat from downstream combustor and turbines, has an adverse effect on compressor overall performance.

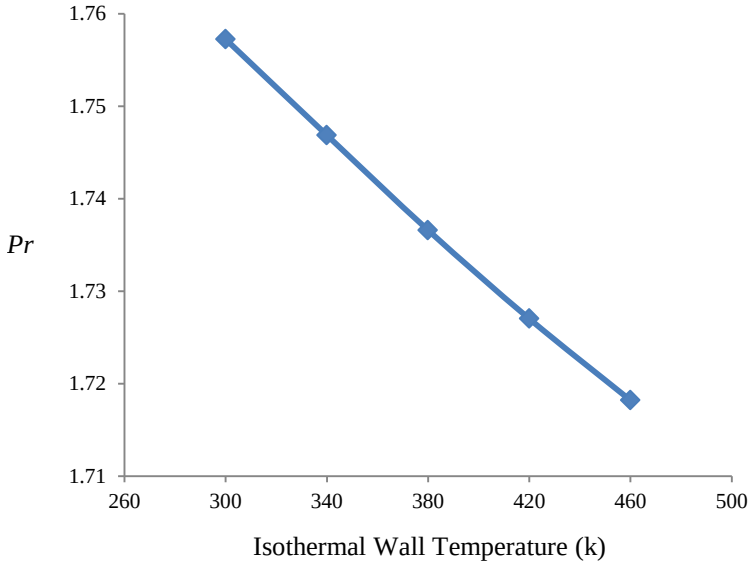

Fig 5.13 Distribution of *Pr* with the change of isothermal wall temperature, with design Mfr at *Re* 5.34×10^5 condition

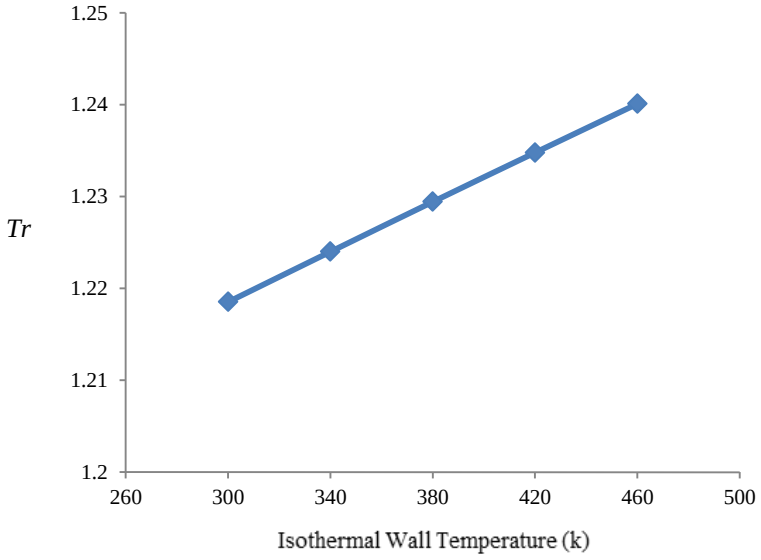

Fig 5.14 Distribution of *Tr* with the change of isothermal wall temperature, with design Mfr at *Re* 5.34×10^5 condition

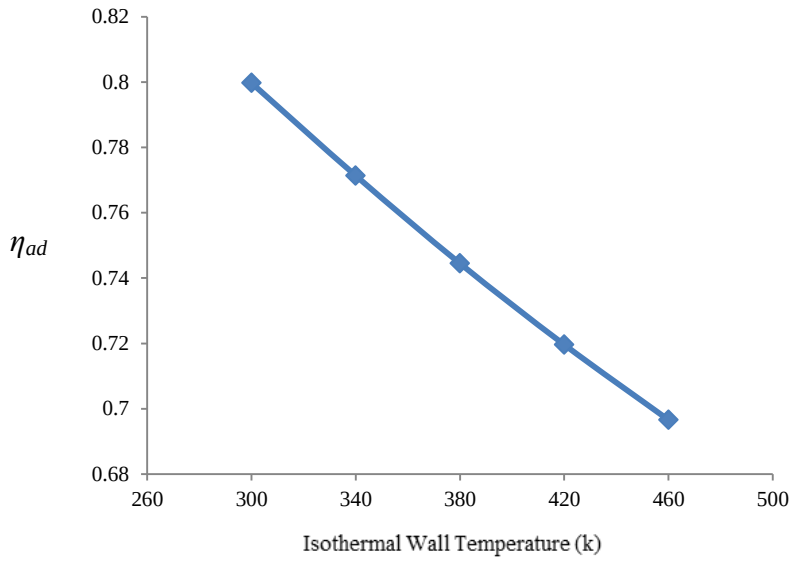

Fig 5.15 Distribution of η_{ad} with the change of isothermal wall temperature, with design Mfr at *Re* 5.34×10^5 condition

The increase of internal flow temperature with the increase of isothermal wall temperature can be easily identified. Figure 5.16 and Figure 5.17 shows the distribution of temperature and entropy on rotor suction surface with 300k, 380k and 460k isothermal wall conditions. The increase of high value region for both properties is observed when isothermal wall temperature increases. Figure 5.18 and Figure 5.19 shows the distribution of temperature and entropy at 30% spanwise of rotor with 300k, 380k and 460k isothermal wall conditions. Similar change of high value region for both properties is also observed. Therefore, more η_{ad} loss is expected at high isothermal wall temperature. In addition, Figure 5.20 shows the distribution of turbulent viscosity at 30% spanwise of rotor with 300k, 380k and 460k isothermal wall conditions. An increase of turbulence is observed near rotor end at high isothermal wall temperature, showing that isothermal wall conditions also impact on turbulence generation.

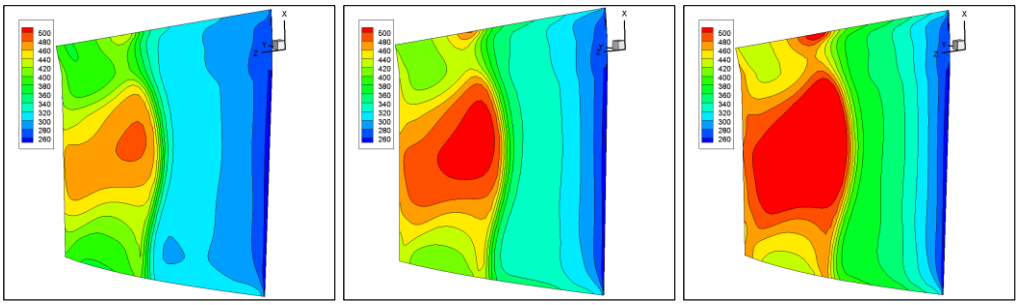

300k 380k 460k

Fig 5.16 Comparison of temperature distribution on R_{ss} with different isothermal wall conditions, with design Mfr at *Re* 5.34×10^5 condition

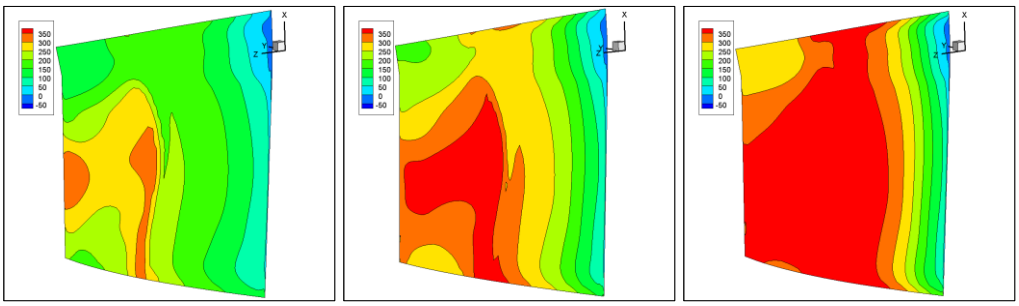

300k 380k 460k

Fig 5.17 Comparison of entropy distribution on R_{ss} with different isothermal wall conditions, with design Mfr at *Re* 5.34×10^5 condition

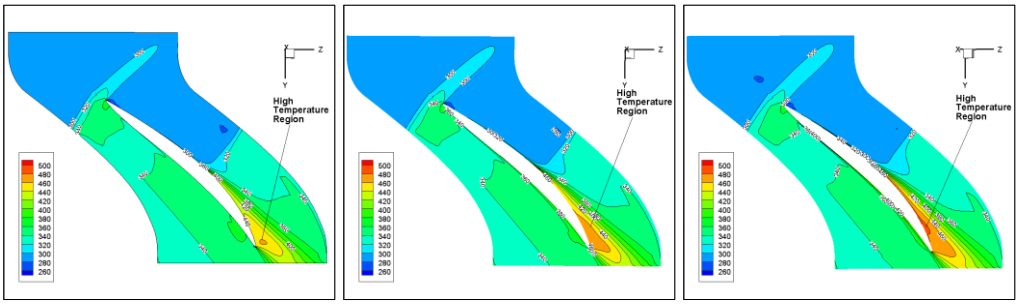

300k 380k 460k

Fig 5.18 Comparison of temperature distribution at 30% spanwise of rotor with different isothermal wall conditions, with design Mfr at *Re* 5.34×10^5 condition

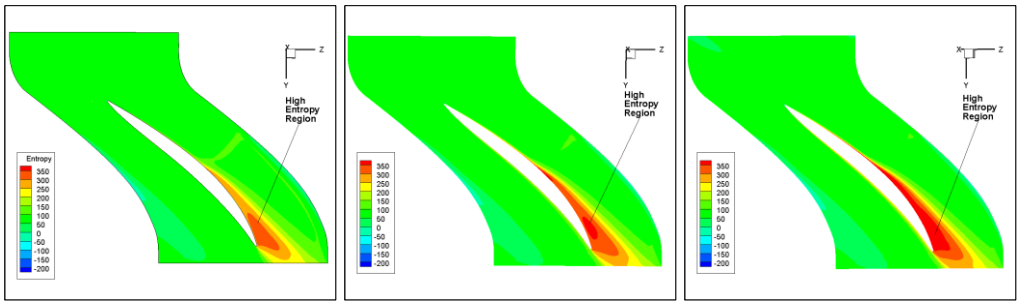

300k 380k 460k

Fig 5.19 Comparison of entropy distribution at 30% spanwise of rotor with different isothermal wall conditions, with design Mfr at *Re* 5.34×10^5 condition

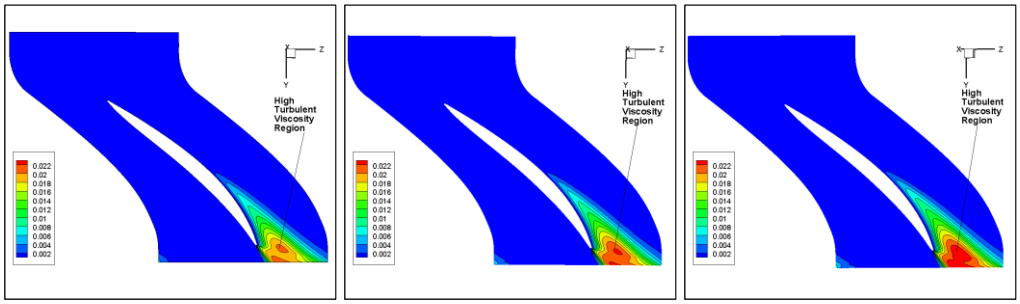

300k 380k 460k

Fig 5.20 Comparison of turbulent viscosity distribution at 30% spanwise of rotor with different isothermal wall conditions, with design Mfr at *Re* 5.34×10^5 condition

The comparison of heat transfer effect at the discussed three wall thermal conditions, i.e. Case1, Case 2 and Case 3, is then conducted to generate a comprehensive understanding of them. The *Re* 5.34×10^5 condition is applied. In total, 9 spanwise locations are specified as previously discussed, for Case 1, Case 2 and Case 3, respectively.

Figure 5.21 shows the spanwise *Pr* distribution at three wall thermal conditions. The length scale is adjusted to aid our analysis. The difference among them is not prominent, as the value of *Pr* gradually drops from hub towards casing. The highest *Pr* is identified at around 20% span. However, slight difference is still observable. At 5% span, deviation is more prominent, indicating that wall thermal conditions more significantly impact compressor performance at near wall regions. 1.24% decrease is observed at 5% span from Case 1 to Case 3, which is in

consistence with previous discussions that isothermal wall has an adverse effect on *Pr* produced.

Figure 5.22 shows the spanwise *Tr* distribution at three wall thermal conditions. The distributions are similar for all three cases, while the difference among them is also easy to tell. The value of *Tr* at Case 3 is almost everywhere higher than value from the other two cases. The largest deviation is identified at 10% span, where 1.45% increases is observed from Case 1 to Case 3. The difference between Case 1 and Case 2 is minor, because the heat loss at Case 2 is Q=137.72 watt at h=200 W/m^2·k, therefore the *Tr* at Case 2 should be slightly smaller than *Tr* at Case 1. The difference between Case 1 and Case 3 is larger, because the heat addition at Case 3 is Q=-341.94 watt at T=380k, therefore the *Tr* at Case 3 should be larger than *Tr* at Case 1 and Case 2. Therefore, it demonstrates that *Tr* is more sensitive to isothermal wall condition, i.e. heat transfer from combustor.

Figure 5.23 shows the spanwise η_{ad} distribution at three wall thermal conditions. The distributions are similar for all three cases, as large fluctuation of η_{ad} value is observed from 70% to 95% span and from 5% to 15% span. This is caused by the interaction between flow and wall boundary, where rapid flow structure and flow property change occurs. The value of η_{ad} at Case 3 is almost everywhere lower than value from the other two cases. The largest deviation is identified at 10% span, where 7.82% decreases is observed from Case 1 to Case 3. This is in consistence with the largest deviation of *Tr* also identified at 10% span, as heat from wall has an adverse effect on η_{ad}.

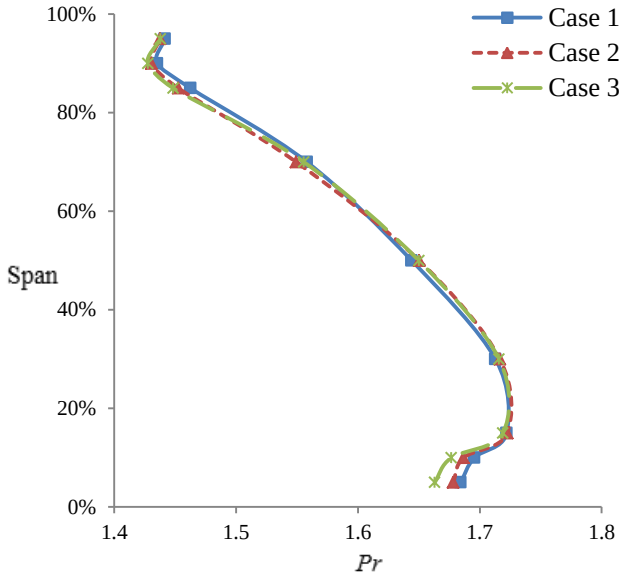

Fig 5.21 Comparison of spanwise *Pr* distribution at different wall thermal conditions, with design Mfr at *Re* 5.34×10^5 condition

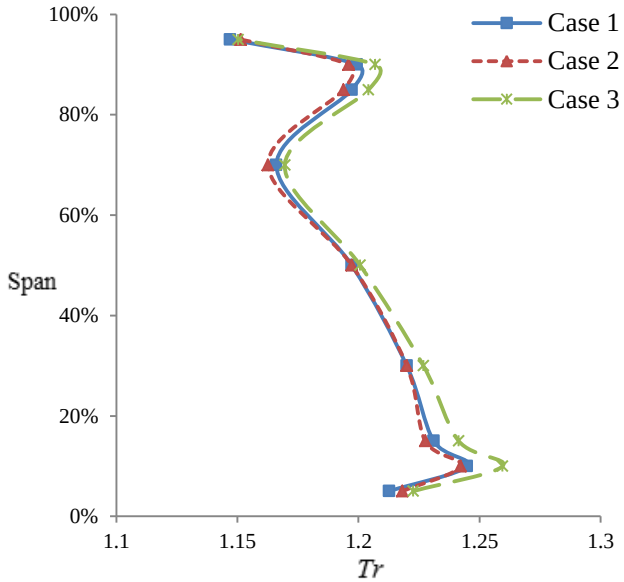

Fig 5.22 Comparison of spanwise *Tr* distribution at different wall thermal conditions, with design Mfr at *Re* 5.34×10^5 condition

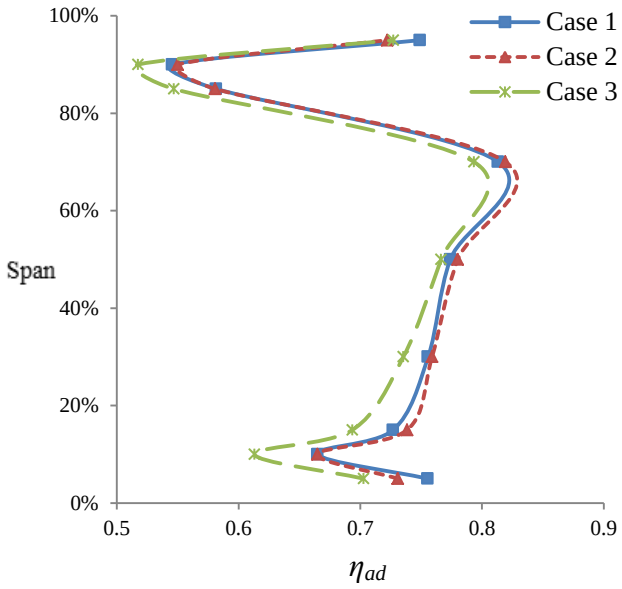

Fig 5.23 Comparison of spanwise η_{ad} distribution at different wall thermal conditions, with design Mfr at *Re* 5.34×10^5 condition

In summary, the effect of heat transfer on the performance of an axial compressor is studied. Three varying thermal conditions are applied to clarify the problem. Numerical results indicate that the increased heat transfer from compressor internal flow towards the ambient air will actually benefit compressor performance, as blades cooling are enhanced when compressor is miniaturized. However, when isothermal wall condition is applied, heat transfer from combustor is therefore allowed. Numerical results indicate that heat transfer from combustor has an adverse effect on compressor performance, especially on its adiabatic efficiency, as the compressor blades are heat up and more entropy change is observed. Therefore, blade cooling is proposed to enhance the overall performance and efficiency.

Chapter 6

Tip Clearance Effect

The effect of tip clearance (TC) on compressor performance is studied in this section. The leakage flow through the blade tip and compressor casing can induce many effects on free stream flows, thus influencing the overall performance. Due to manufacturing limitations, the TC is not avoidable. Therefore, it is essential to more profoundly understand its effects when the compressor geometry is changed. Especially for miniaturized gas turbines, the TC ratio may increase and become larger than for conventional gas turbines, as the clearance gap may not scale with the reduction of engine size due to manufacturing tolerances. In this study, three different approaches to investigate the TC effect are presented.

Table 6.1 shows the specifications of three different methods adopted. Case 1: A constant TC value of 0.5mm is applied for the *Re* 5.34×10^5 condition as defined in Chapter 4. It is then compared with results from previous study w/o TC, to understand its general effect on compressor performance. Case 2: TC values ranging from 0.3125mm to 1.25mm are applied, at the *Re* 5.34×10^5 condition. It is conducted to understand the effect of TC ratio. Case 3: A constant TC value of 0.5mm is applied, from *Re* 2.14×10^5 to *Re* 8.54×10^5condition, i.e. when compressor is miniaturized. It is supposed to understand the Reynolds number effect when constant TC value is considered.

Table 6.1 Specification of Three Tip Clearance (TC) Approaches

	Specification of TC & *Re* Condition	Specification of TC & *Re* Values
Case 1	Constant TC, Constant *Re*	TC 0.5mm, *Re* 5.34×10^5
Case 2	Varying TC, Constant *Re*	TC 0.3125mm, 0.5mm, 0.75mm, 1mm, 1.25mm, *Re* 5.34×10^5
Case 3	Constant TC, Varying *Re*	TC 0.5mm, *Re* $2.14\times10^5 \sim 8.54\times10^5$

The default boundary conditions discussed in Chapter 3 are implemented, with adiabatic wall condition applied. All cases in this study are conducted with the design Mfr, at 100% design speed. The previously validated mesh is adopted, with additional structured mesh built for the TC region, by an extension along the blade radial direction. Figure 6.1 shows the structured mesh built for the clearance gap, with TC value of 0.5mm for illustration purpose. In total, 10 cells are defined in the radial direction within the TC, to well capture rapid flow change across the tip and to guarantee simulation convergence. Cases with different TC values are built similarly for each specific study.

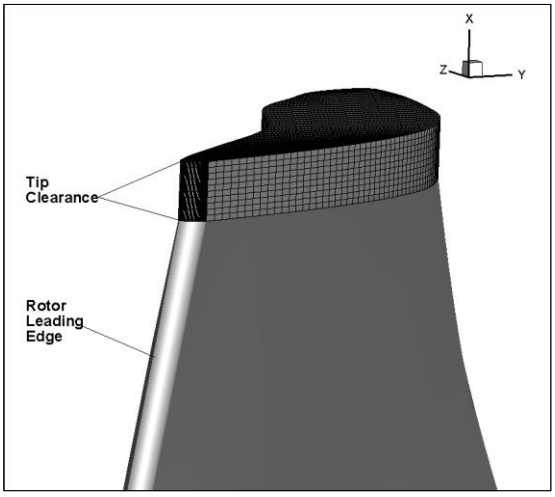

Fig 6.1 Tip clearance mesh

6.1 Effect of Constant Tip Clearance

A constant tip clearance value of 0.5mm is applied for the *Re* 5.34×10^5 condition. For comparison purpose, the 50% spanwise plane, i.e. mid-span of blade radial length, and 95% spanwise plane, i.e. cross-sections in the rotor zone near the blade tip are selected from validation results and Case 1 results in this study. In addition, 20 data extraction points are specified in the streamwise direction on each plane, at 30% span from R_{ss}.

Figure 6.2 shows the specification of spanwise data planes and specification of streamwise data points based on the 50% spanwise plane. The data points ranges from R_{LE} plane towards R_{TE} plane, and the coordinate of each point is normalized

by the rotor chord length to aid the analysis. Due to confidence obtained from the validation study in Chapter 3 and the limitations of good experimental data for varying tip clearance for the current test rig, numerical methods validated previously for the TC=0 is applied to this Tip Clearance study and comparisons are made for TC=0 and TC=0.5mm cases.

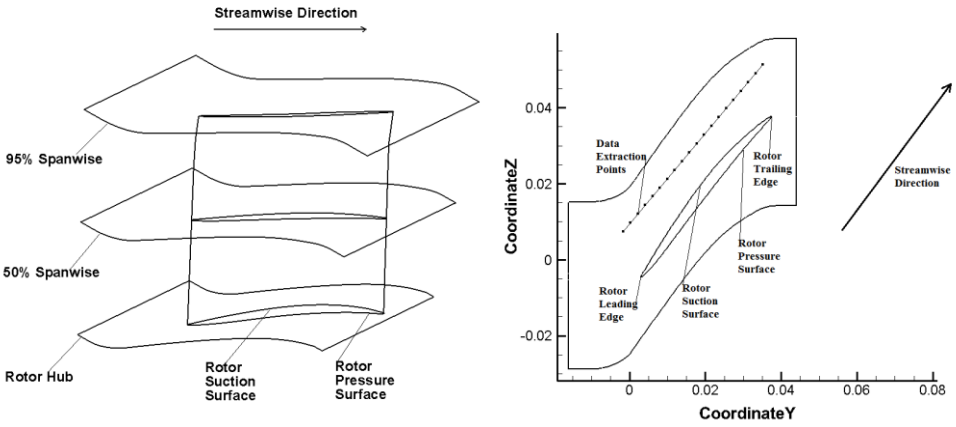

Fig 6.2 Specification of spanwise planes (Left) and streamwise data points (right)

For the purpose of understanding the effect of TC on flow property, the comparison of validation results, i.e. w/o TC or TC=0, and results from Case 1 in this study is conducted. The 95% spanwise plane is firstly studied. Figure 6.3 shows the comparison of Mach number distribution on 95% spanwise plane, with TC=0 and TC=0.5mm. With TC=0, the flow separation is identified on R_{ps} flow path. A relative high Mach region is also identified on the R_{ss} flow path, which is induced by the boundary layer separation from the blade surface. The wake region is identified after R_{TE}, where high and low Mach number flow merge and interact downstream of rotor flow path. With TC=0.5mm, a fluid jet is observed on the R_{ss} flow path. The fluid jet is initiated by the pressure difference at TC, where fluid is ejected across the blade tip from R_{ps} to R_{ss}. The fluid jet is with high Mach and high momentum, thus it displaces the flow separation primarily located on R_{ps} towards the blade surface and downstream. The development of boundary layer separation on R_{ss} also diminishes because of the impact of fluid jet. The wake region is also identified, although it is less developed and less expansive after R_{TE}.

Figure 6.4 shows a comparison of the total pressure (Pt) distribution in the 95% spanwise plane, with TC=0 and TC=0.5mm. With TC=0, a sudden Pt increase is observed at the stage entrance, where fluid is rapidly compressed. Further gradual increase of Pt is observed along the flow path, with the highest value achieved in the stage exit. Low Pt value is observed near R_{TE} on R_{ps}, indicating flow separation. With TC=0.5mm, the increase of Pt at stage entrance is relatively more gradual. However, a rapid increase of Pt is observed along the flow path, as the Pt levels are less flat. This is because of fluid jet initiated at TC, and the pressure difference between R_{ps} and R_{ss} is observable. The low Pt region is reduced and shifted downstream, due to the shifted flow separation as a result of propagated fluid jet.

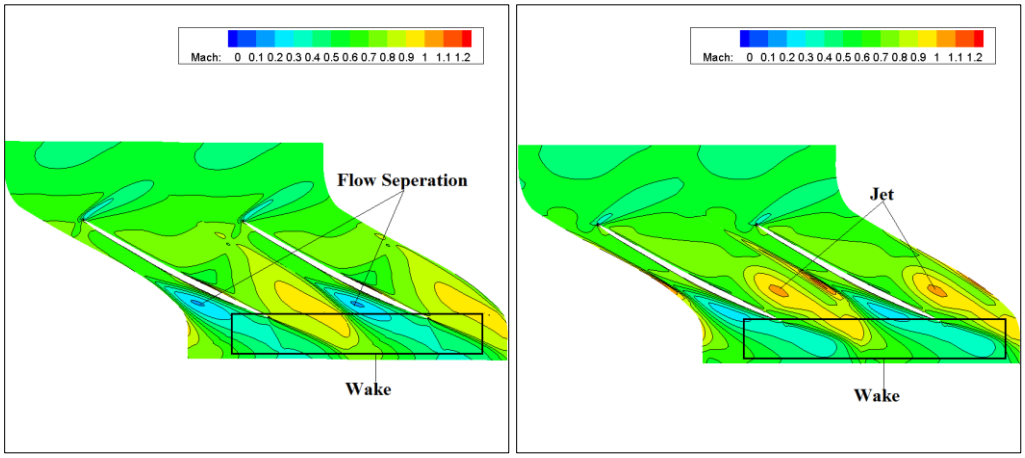

TC=0 TC=0.5mm

Fig 6.3 Comparison of Mach distribution on 95% spanwise plane

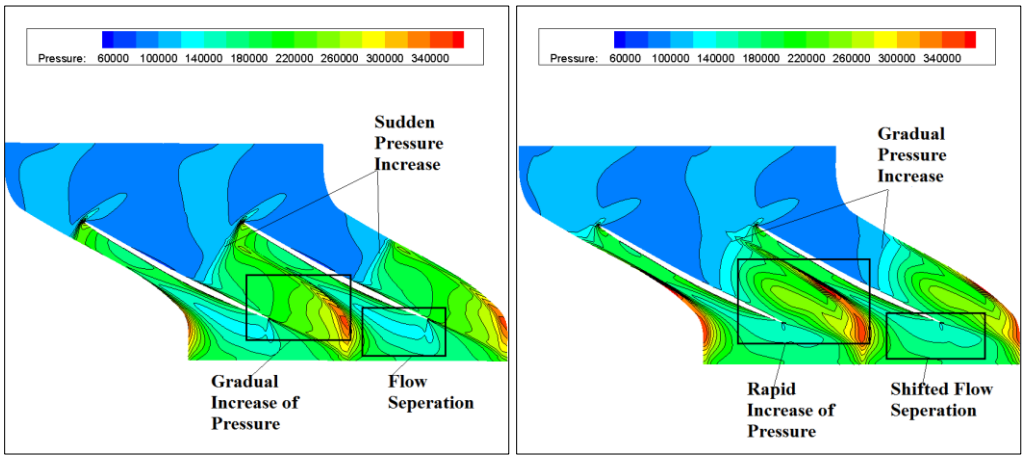

TC=0 TC=0.5mm

Fig 6.4 Comparison of Pt distribution on 95% spanwise plane

The structure of the fluid jet is also of interest. The fluid jet is believed to contribute to the generation of turbulence after its interaction with the main flow. Therefore, the value of turbulent viscosity (ῡ) is adopted to illustrate turbulence effects. Again, the 95% spanwise plane is studied. Figure 6.5 shows a comparison of turbulent viscosity distribution on the 95% spanwise plane, with TC=0 and TC=0.5mm. With TC=0, the turbulent viscosity only slightly increases at the end of rotor zone, and its value is small and insignificant. With TC=0.5mm, relative large turbulence is observed on the R_{ss} flow path, clearly shows the intensity of turbulence and the fierce interaction of fluid jet and mean flow.

In order to better understand the turbulence structure, Figure 6.6a further shows the comparison of turbulent viscosity distribution at stage exit plane, i.e. 100% streamwise span, with TC=0 and TC=0.5mm. With TC=0, relative large turbulence caused by boundary layer separation adjacent to R_{ss} is observed. With TC=0.5mm, however, the jet-induced turbulence is observed near rotor tip on R_{ss}, showing that fluid jet propagates downstream and slightly shifted away from R_{ss}. In addition, the extension of turbulence caused by boundary layer separation adjacent to R_{ss} has decreased and the turbulence cores moves downwards. The upper-zone turbulence possibly suppresses the development of boundary layer separation, thus results the decrease of turbulence intensity in the lower-zone. Besides that, turbulence induced by flow separation near rotor tip on R_{ps} is also identified larger with TC=0.5mm. As mentioned previously in Figure 3.17a, the turbulent viscosity values and distribution give well-accepted prediction of the intensity of turbulence. In order to understand the validity of simplification when TC is applied, Figure 6.6b shows the distribution of turbulent viscosity, strain rate field and Reynolds stress at rotor exit plane, with TC=0.5mm. High strain rate region is identified only near the shroud region and close to the rotor tip, which could be a result of fluid jet. The strain rate in the mean stream is relatively low and the difference is not prominent to tell. Therefore, the distribution of turbulent viscosity is still a reliable way to identify turbulence intensity, especially in the main stream. It will be further used as a good characterization of turbulence.

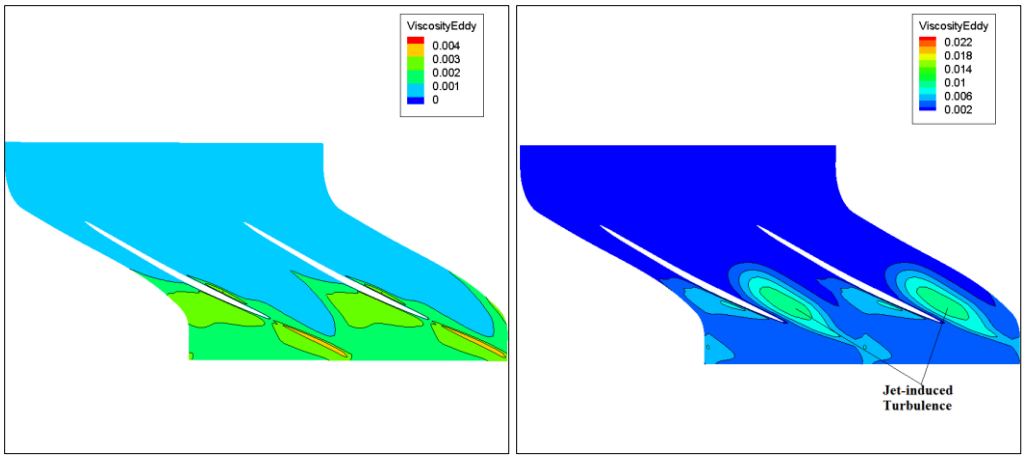

TC=0 TC=0.5mm

Fig 6.5 Comparison of turbulent viscosity distribution on 95% spanwise plane

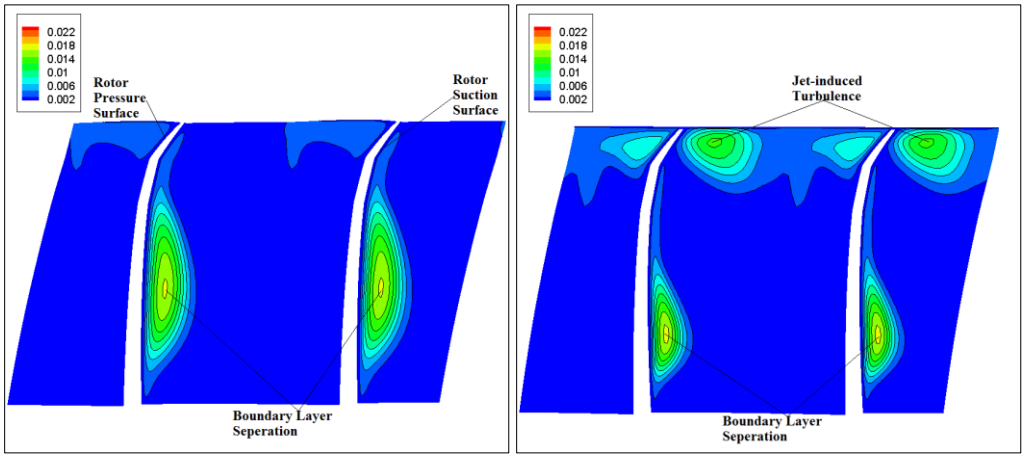

TC=0 TC=0.5mm

Fig 6.6a Comparison of turbulent viscosity distribution on 100% streamwise span

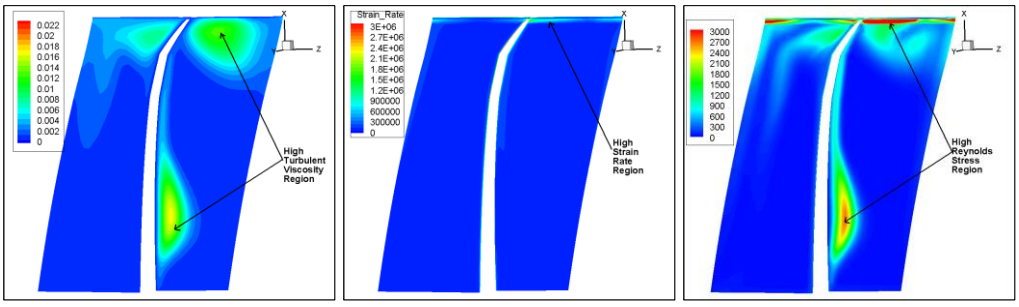

Turbulent Viscosity Strain Rate Reynolds Stress

Fig 6.6b Distribution of turbulent viscosity, strain rate field and Reynolds stress at rotor exit plane, with TC=0.5mm

The TC flow also impacts on the compressor efficiency. The value of entropy is usually adopted to explain η_{ad} loss. Therefore, Figure 6.7 shows the comparison of entropy distribution on 95% spanwise plane, with TC=0 and TC=0.5mm. The entropy is calculated with reference to the value at rotor inlet surface. With TC=0.5mm, a shift of high entropy region is observed, as it locates more into the core flow path rather than adjacent to R_{ss} with TC=0. Also, an increased area of peak entropy is identified, which is due to the interaction of fluid jet with low momentum separated flow initiated from R_{ps}. The higher entropy suggests more η_{ad} loss w/ TC.

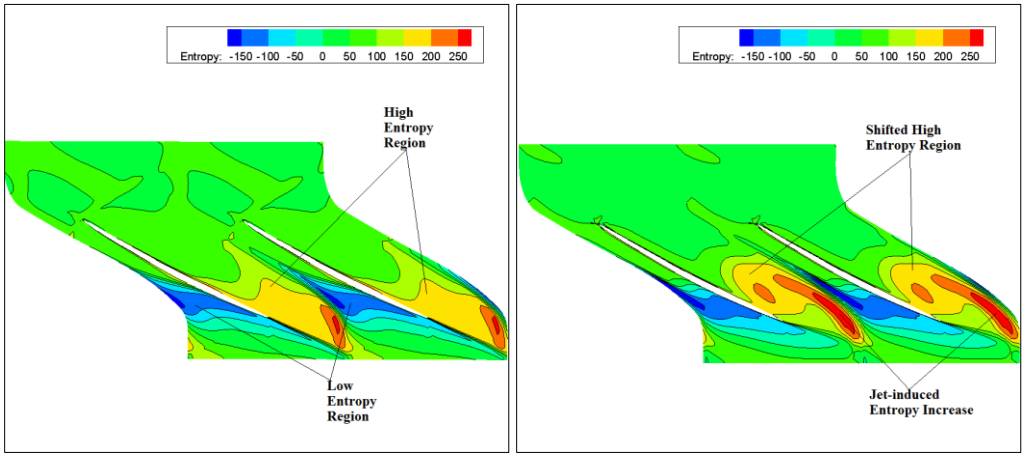

TC=0 TC=0.5mm

Fig 6.7 Comparison of entropy distribution on 95% spanwise plane

More quantitative analysis is required to better illustrate the effect of TC. Both 95% spanwise and 50% spanwise planes are studied. The streamwise data points are specified as previously discussed. The 50% spanwise is adopted to investigate the effect of TC flow along the lower-zone flow path. The data line at 30% span from R_{ss} is selected, because more pronounced flow property changes are identified in the core flow, as previous analysis suggests.

Figure 6.8 shows the comparison of Mach number distribution along rotor streamwise direction, with TC=0 and TC=0.5mm, on 95% spanwise plane and 50% spanwise plane. At 95% spanwise, the Mach gradually increases along rotor streamwise direction for both w/ and w/o tip clearance cases. However, with TC=0.5mm, a larger Mach gradient is observed from 52.6% chord length towards

73.7% chord length, indicating the rapid increase of Mach due to effect of fluid jet initiated from TC. This can also be identified in the Mach contour presented previously. At 50% spanwise, a sudden drop of Mach is observed at 36.8% chord length, as a result of sudden redirection of fluid at stage entrance. Slight larger Mach numbers are observed w/ TC, from 36.8% chord length towards the stage exit, as a result of the expansion of high momentum fluid due to fluid jet. The Mach distribution clearly suggests the effect of fluid jet is more prominent in the upper-zone flow path. Also, the propagation of fluid jet at 30% span from R_{ss} is identified at around 52.6% chord length location, indicating the fluid jet is initiated from the first half chord length at blade tip.

Figure 6.9 shows the comparison of total pressure distribution along rotor streamwise direction, with TC=0 and TC=0.5mm, on 95% spanwise plane and 50% spanwise plane. At 95% spanwise, high pressure gradients are observed from around 20% to 80% chord length for w/ TC case, which can also be identified in the pressure distribution contour presented previously. However, a sudden jump of Pt is observed at 47.4% chord length for w/o TC case, showing the abrupt redirection and compression of fluid at stage entrance. At 50% spanwise, a gradual increase but lower value of Pt along rotor streamwise direction is observed, with a sudden jump of Pt at around 36.8% chord length for both w/ and w/o TC cases. This shows the fluid jet has minor effect on Pt at lower-zone flow path, although slightly larger value of Pt is still observed from 52.6% chord length towards rotor end, proving the expansion of fluid jet.

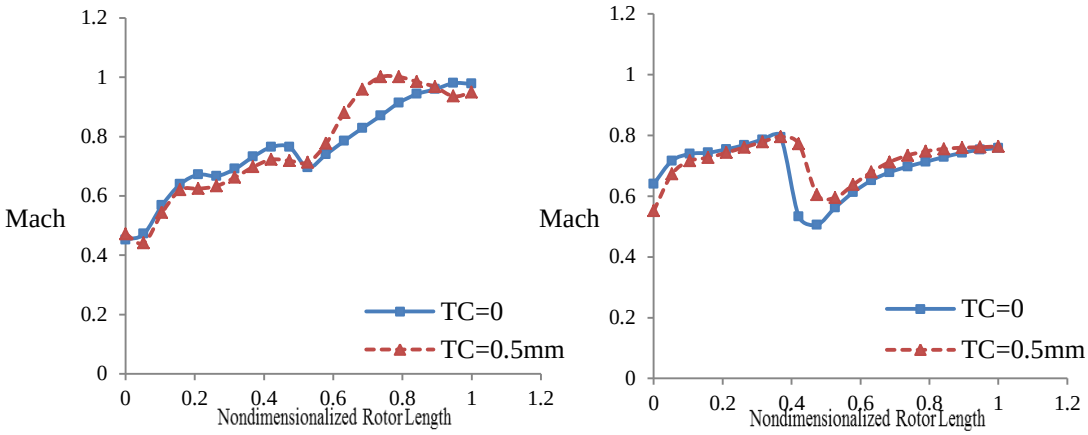

95% spanwise 50% spanwise

Fig 6.8 Comparison of Mach distribution along rotor streamwise direction, with TC=0 and TC=0.5mm

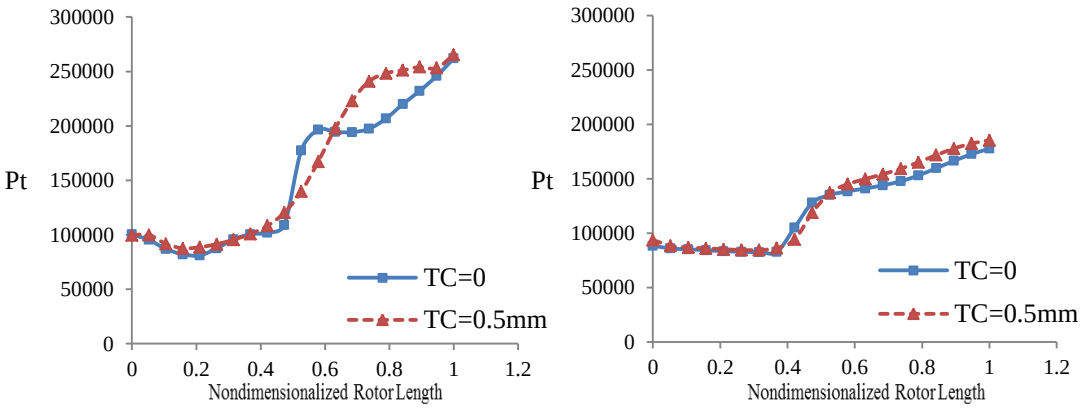

95% spanwise 50% spanwise

Fig 6.9 Comparison of Pt distribution along rotor streamwise direction, with TC=0 and TC=0.5mm

Figure 6.10 shows the comparison of turbulent viscosity distribution along rotor streamwise direction, with TC=0 and TC=0.5mm, on 95% spanwise plane and 50% spanwise plane. At 95% spanwise, high gradient of turbulent viscosity is observed from 42.1% to 84.2% chord length for w/ TC case. After the peak value, the turbulent viscosity drops rapidly towards rotor end. This clearly shows the generation of turbulence near blade tip due to fluid jet, as high momentum fluid interacts with relatively low momentum fluid in the mean flow. The turbulent viscosity contour presented previously also demonstrates the generation of turbulence adjacent to R_{ss} due to fluid jet. The turbulent viscosity for w/o TC case

remains almost zero until around 47.4% chord length, where a slight increase is observed. The slight increase is caused by the expansion of flow separation initiated from R_{ss} as previously shown. At 50% spanwise, turbulent viscosity remains unchanged at a small value until 36.8% chord length, where a sudden jump is observed for both w/ and w/o TC cases. In addition, after the sudden jump of turbulent viscosity, the value from w/o TC case is everywhere larger than the value from w/ TC case, and the deviation further increases towards the rotor end. This could be explained by the turbulent viscosity contour at 100% streamwise span shown previously, where the expansion of boundary layer separation with TC=0 is larger than that with TC=0.5mm, due to less suppression from fluid jet in the upper-zone flow path. However, compared with the value of turbulent viscosity due to fluid jet, the intensity of turbulence induced by boundary layer separation on R_{ss} is insignificant.

Figure 6.11 shows the comparison of the entropy distribution in the rotor streamwise direction, with TC=0 and TC=0.5mm, on 95% spanwise plane and 50% spanwise plane. At 95% spanwise, high entropy gradients are observed from 42.1% to 73.7% chord length for w/ TC case. This is almost identical with that of turbulent viscosity value, where a high gradient is also observed due to fluid jet. After 73.7% chord length, the entropy decreases rapidly, showing the decrease of turbulence and less fluid interaction. This can also be identified from previously presented entropy contour, where a shifted high entropy region is pointed out and with higher gradient. In contrast, the entropy value for w/o TC case increases gradually from 42.1% chord length towards rotor end, which is with a smaller gradient. This is due to the increased fluid momentum and thus increased fluid interaction with compressor casing, resulting in more efficiency loss. At 50% spanwise, the entropy remains at small value and only slightly increases along rotor streamwise direction. However, the entropy value from TC=0 is still relatively higher than that from TC=0.5mm, due to higher turbulence contributed by larger expansion of boundary layer separation on R_{ss} for w/o TC case, as just discussed.

Figure 6.12 shows the comparison of total temperature distribution along rotor streamwise direction, with TC=0and TC=0.5mm, on 95% spanwise plane and 50% spanwise plane. Similar observation with the distribution of entropy is obtained. At 95% spanwise, higher Tt value for w/ TC case is identified from 57.9% to 89.5% chord length, due to increased friction with compressor shroud as a result of fluid jet. At 50% spanwise, the difference of Tt between w/ TC case and w/o TC case is not evident, showing that the effect of smaller turbulence on Tt is insignificant.

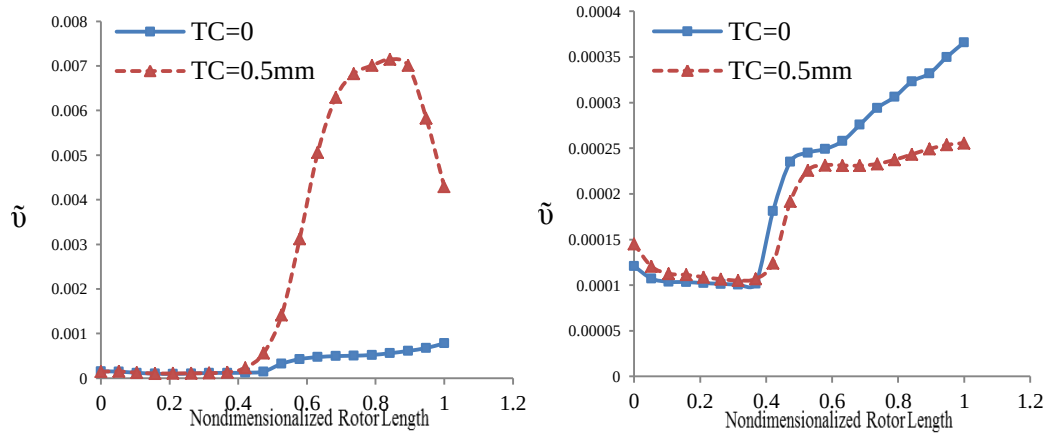

95% spanwise 50% spanwise

Fig 6.10 Comparison of turbulent visocisty distribution along rotor streamwise direction, with TC=0 and TC=0.5mm

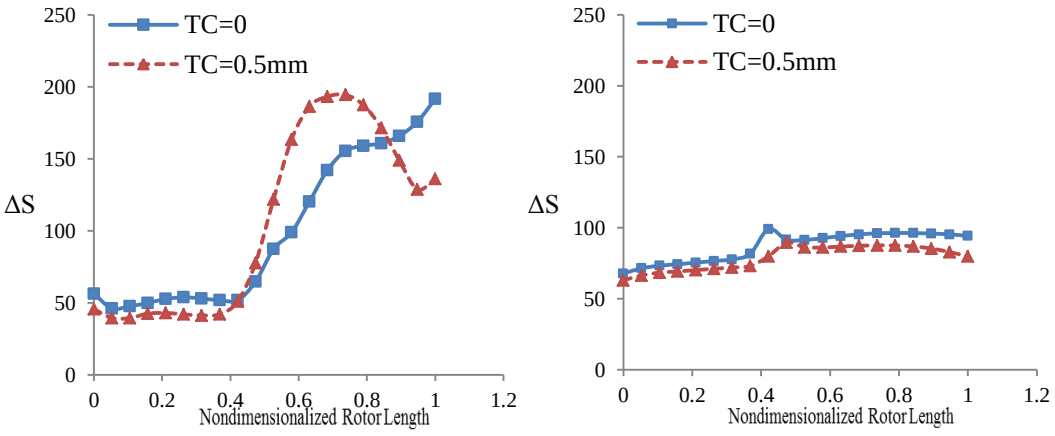

95% spanwise 50% spanwise

Fig 6.11 Comparison of entropy distribution along rotor streamwise direction, with TC=0 and TC=0.5mm

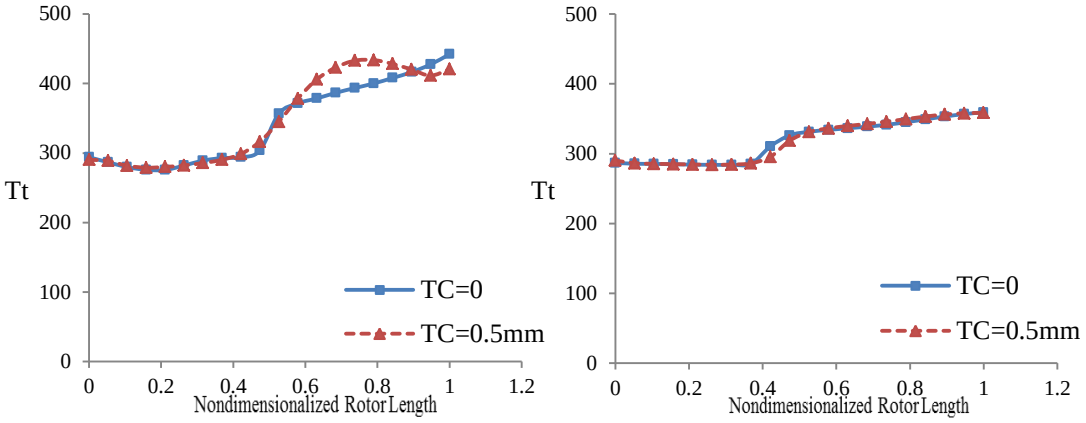

95% spanwise 50% spanwise

Fig 6.12 Comparison of Tt distribution along rotor streamwise direction, with TC=0 and TC=0.5mm

6.2 Effect of Varying Tip Clearance

Varying TC values, ranging from 0.3125mm to 1.25mm are applied, with design Mfr at a constant *Re* 5.34×10^5 condition. This is conducted to understand the effect of varying TC on compressor performance. Boundary conditions and TC mesh are specified as discussed in Case 1, with varying TC value applied. To aid our analysis, 5 streamwise spans in rotor zone are defined, which are located mainly in the downstream of rotor flow path.

Figure 6.13 shows the specification of five data planes, i.e. at 60%, 80%, 100%, 120% and 140% streamwise. The 100% streamwise span corresponds to stage exit plane and 140% streamwise corresponds to rotor outlet surface. To quantitatively present the results, three data lines are defined on each streamwise plane, at 90%, 50% and 10% spanwise respectively. In addition, at each spanwise line, 30 data extraction points are specified in the span width direction, i.e. from R_{ss} towards R_{ps}. The length of each span line is defined as span width and each data point location is normalized by the span width to simplify analysis, where the point on R_{ss} is considered 0% span width and the point on R_{ps} is 100% span width. Figure 6.13 also shows the specification of span width data points, based on 100% streamwise plane. The TC location is also pointed out, showing that TC value is comparatively small compared with blade height. Table 6.2 describes the details

of specified TC value and its corresponding TC ratio, at constant *Re* 5.34×10^5 condition. The height of rotor blade is 75mm according to the design parameters presented previously, therefore the TC ratio changes only with the variation of TC value.

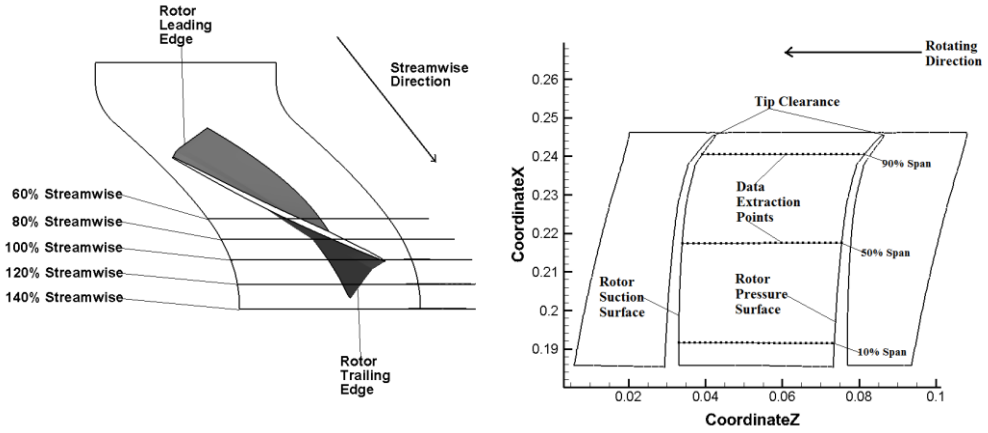

Fig 6.13 Specification of streamwise data planes (Left) and span width data points (right)

Table 6.2 Specification of TC Value and TC Ratio

TC Value (mm)	Rotor Blade Height (mm)	TC Ratio	Reynolds number
0.3125	75	0.42%	5.34×10^5
0.5	75	0.67%	5.34×10^5
0.75	75	1.00%	5.34×10^5
1	75	1.33%	5.34×10^5
1.25	75	1.67%	5.34×10^5

The effect of varying TC on compressor overall performance is firstly discussed. Area-averaged value of total pressure and total temperature at rotor inlet surface and stator outlet surface are calculated for performance evaluation. The 100% design speed and *Re* 5.34×10^5 condition is considered. Figure 6.14 shows the change of *Pr* and change of η_{ad} with varying TC ratio. Both *Pr* and η_{ad} drop with the increase of TC ratio, indicating the increased loss due to TC flow. Figure 6.15 further shows the percentage of loss with varying TC ratio, for both *Pr* and η_{ad} value. The value of loss is calculated with reference value from TC=0 case as

previously introduced. In total, when TC increases from 0.3125mm to 1.25mm with blade height unchanged, the loss of both properties increases. The percentage of loss of *Pr* increases from 1.34% to 3.02%, and the percentage of loss of η_{ad} increases from 5.08% to 6.62%. The results suggest that the existence of TC has larger effect on compressor η_{ad}. In addition, the loss of *Pr* and η_{ad} increases with the increase of TC, within the scope of this study.

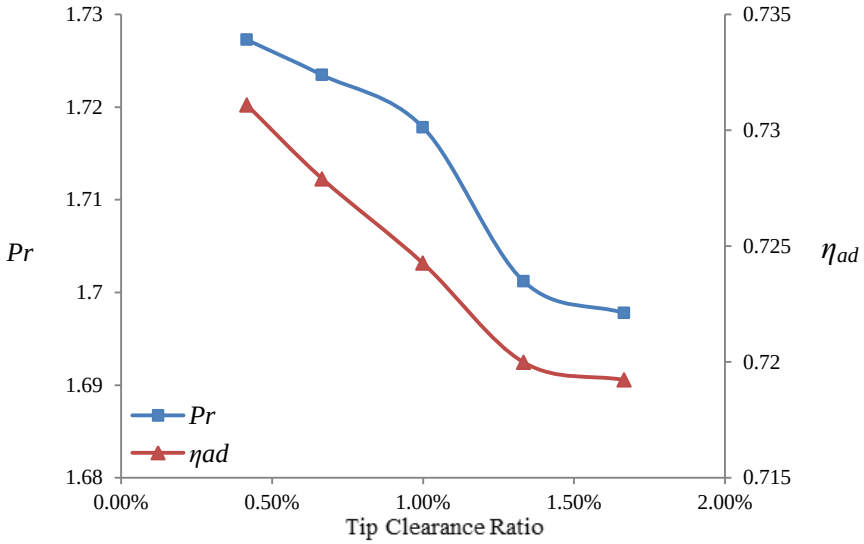

Fig 6.14 Change of *Pr* and η_{ad} with varying TC ratio

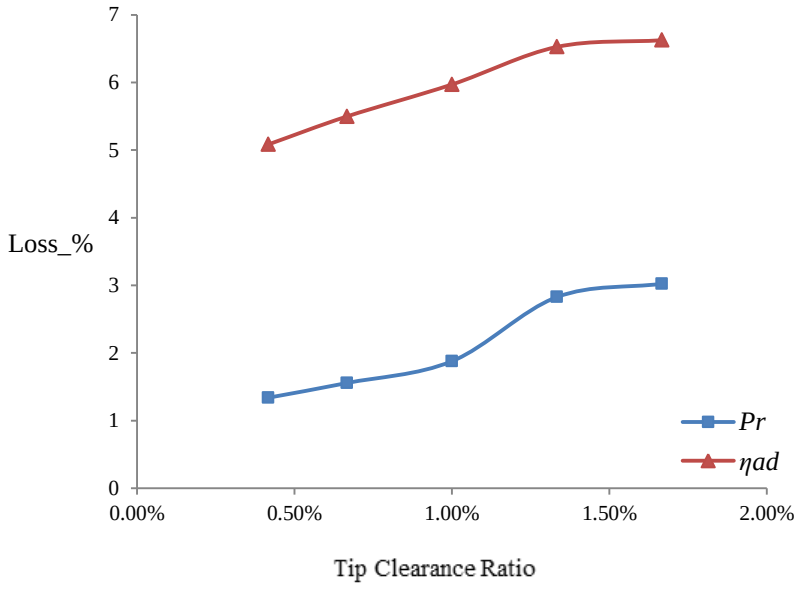

Fig 6.15 Percentage of loss of *Pr* and η_{ad} with varying TC ratio

Before the comparison of results from varying TC value, the TC=1.25mm case is selected to further understand flow property variation due to TC flow. As specified earlier, only data points locate at 95% span line are utilized. Three streamwise planes, i.e. at 60%, 80% and 100% streamwise, are selected for this comparison analysis.

Figure 6.16 shows the variation of Mach number at 95% span line. Mach increases from R_{ss}, i.e. at 0% span width, until a peak value is identified. On 60% streamwise plane, the peak Mach is observed at 45.7% span width, indicating the impact of fluid jet. However, the peak Mach is observed at 30.9% span width on 80% streamwise plane and at 28.1% span width on 100% streamwise plane, showing a transition of fluid jet towards the downstream. This might due to the twisted and tilt blade geometry, compressing fluid jet approach back to R_{ss} in the downstream. In addition, the peak value at 80% and 100% streamwise is larger than that at 60% streamwise, indicating the further increase of Mach due to further acceleration of fluid in the downstream. The lowest Mach is observed at around 80.1% span width, suggesting flow separation near blade tip on R_{ps}. Also, at 80.1% span width, the value of Mach decreases when flow propagates downstream, i.e. from 60% to 100% streamwise, showing the intensification of flow separation towards R_{TE} on R_{ps}.

Figure 6.17 shows the variation of turbulent viscosity at 95% span line. The turbulent viscosity increases from R_{ss}, until the peak value is achieved. The transition of peak turbulent viscosity is also observed from 60% to 100% streamwise, showing the fluid jet approaching back towards R_{ss} again. In addition, the peak value also increases from 60% to 100% streamwise, indicating the turbulence becomes more intensive in the downstream as a result of fluid interaction. The turbulent viscosity value drops rapidly after the peak location, suggesting that the expansion of turbulent core is limited. Slight increase of turbulent viscosity is observed near R_{ps} due to flow separation in that region, but its impact on the mean flow is insignificant.

Figure 6.18 shows the variation of mean field vorticity ($\vec{\omega}$) at 95% span line. As a quantity to describe the local rotational motion, vorticity determines the tendency of fluid rotation near some point. Therefore, regions of large vorticity should reflect zones of large gradients, usually referring to the boundary layer, recirculation zones and zones where vertical motion is strong. In the current plot, the data points on R_{ss} and R_{ps} are not included, due to their extremely large values, which may undermine the observation of vorticity variation in the main flow path. At 60% and 80% streamwise, peak vorticity is observed at 76.7% span width, indicating fluid is more prone to rotate due to flow separation. Fluctuation of vorticity is also observed at 60% and 80% streamwise. However, at 100% streamwise, the vorticity varies in a sinusoid pattern from R_{ss} towards R_{ps}. This is the interaction result of fluid jet from TC, flow in the mean stream and spinning flow due to flow separation. Figure 6.19 shows the distribution of mean field vorticity at 100% streamwise for further illustration. Extremely large vorticity is identified at near wall regions due to boundary layer effect. In addition, extremely large vorticity is also identified near TC region, where fluid is more prone to rotation due to ejection of fluid from R_{ps} to R_{ss} at blade tip. The fluctuation of vorticity in the upper-zone flow path is observed, explains the sinusoid pattern of vorticity variation at 95% span on 100% streamwise plane.

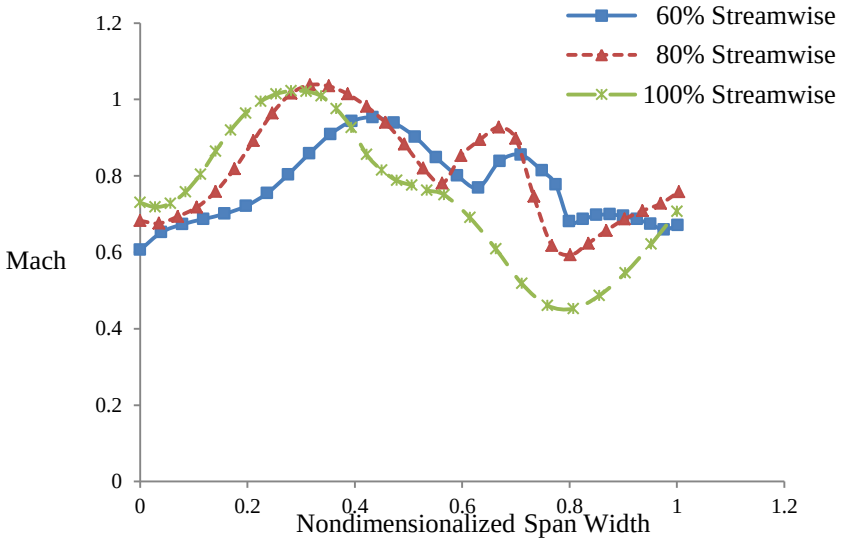

Fig 6.16 Variation of Mach at 95% span line, on 60%, 80% and 100% streamline planes, with TC=1.25mm

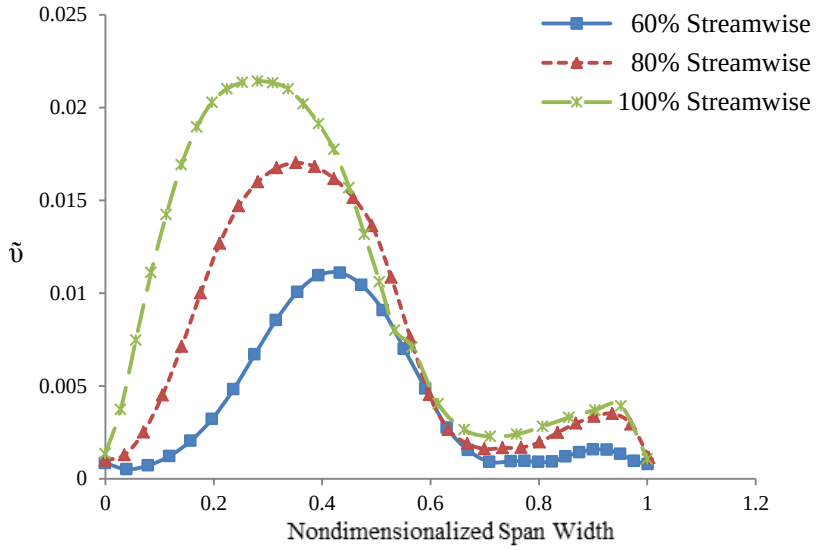

Fig 6.17 Variation of turbulent viscosity at 95% span line, on 60%, 80% and 100% streamline planes, with TC=1.25mm

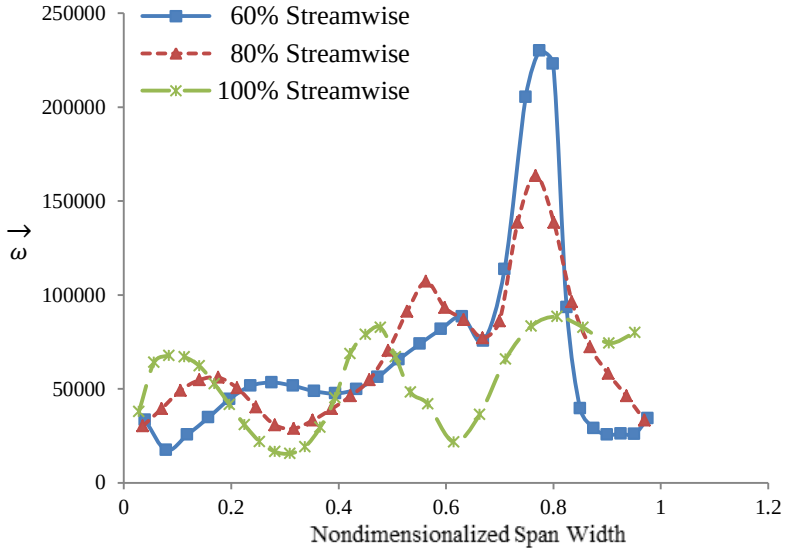

Fig 6.18 Variation of vorticity at 95% span line, on 60%, 80% and 100% streamline planes, with TC=1.25mm

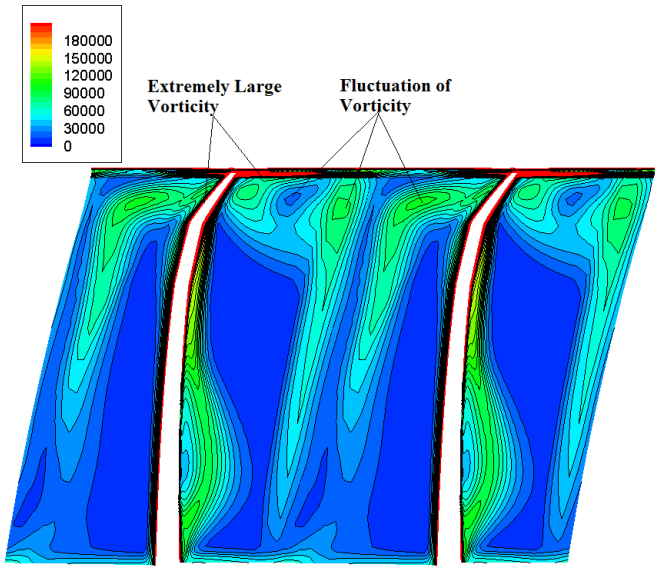

Fig 6.19 Distribution of vorticity on 100% streamwise plane, with TC=1.25mm

The comparison of flow property change with varying TC value is then conducted. To simplify the analysis, three TC value cases are selected for discussion. TC values of 0.3125mm, 0.75mm and 1.25mm are considered, representing small, medium and large TC within the scope of this study.

Figure 6.20 shows the distribution of Mach number on 100% streamwise plane, with TC=0.3125mm, TC=0.75mm and TC=1.25mm, respectively. With the increase of TC value, the shift of high Mach region, i.e. fluid jet, is identified. The fluid jet shifts from TC region near R_{ss} towards the middle span width, when TC value changes from 0.3125mm to 1.25mm, showing fluid jet from large TC case travels further away from the ejection location. In addition, the extension of low Mach region is slightly larger on R_{ss} near shroud for large TC case, as more low momentum fluid travels from R_{ps} to R_{ss} in the R_{TE} region. The extension of high Mach region at middle spanwise on R_{ss} decreases due to the increased suppression of fluid jet, with the increase of TC value.

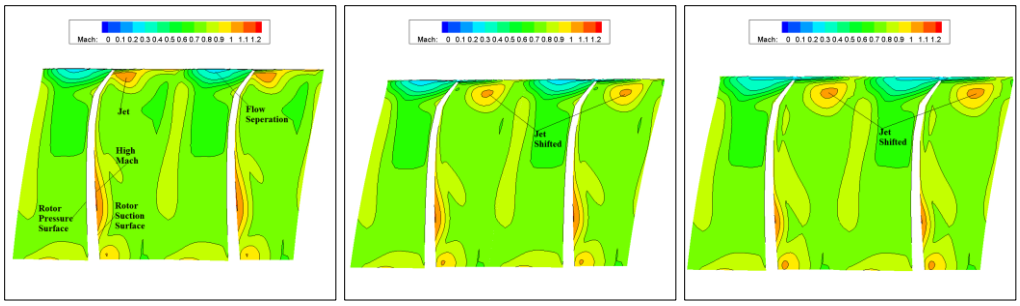

TC=0.3125mm TC=0.75mm TC=1.25mm

Fig 6.20 Distribution of Mach on 100% streamwise plane, at TC=0.3125mm, TC=0.75mm and TC=1.25mm

Figure 6.21 shows the distribution of turbulent viscosity on 100%, 120% and 140% streamwise planes, respectively. The shift of distribution of high turbulent viscosity region clearly illustrates the shift of fluid jet, either in streamwise direction or in spanwise direction, with the increase of TC value. Consider Figure 6.21a for instance, with the increase of TC value, the intensity of turbulence near blade tip region also increases, with a shift of turbulence core observed. The intensity and extension of turbulence near R_{ss} decrease with the increase of TC value due to larger suppression by fluid jet, which is in consistence with previously discussion. The turbulence further develops towards rotor end and shifts towards the R_{ps}, which can be identified in Figure 6.21b. The high turbulent viscosity region near tip expands for all three TC value cases. In addition, the high turbulent viscosity region is further suppressed due to the expansion of turbulence region in upper-zone, but the value of turbulence viscosity near R_{ss} increases when fluid propagates towards downstream. The turbulence core near rotor shroud almost merge together to form a continuous turbulence layer on 140% streamwise plane, as identified in Figure 6.21c. In addition, the value of turbulence core drops with the expansion of turbulence in the wake region, for all TC value cases.

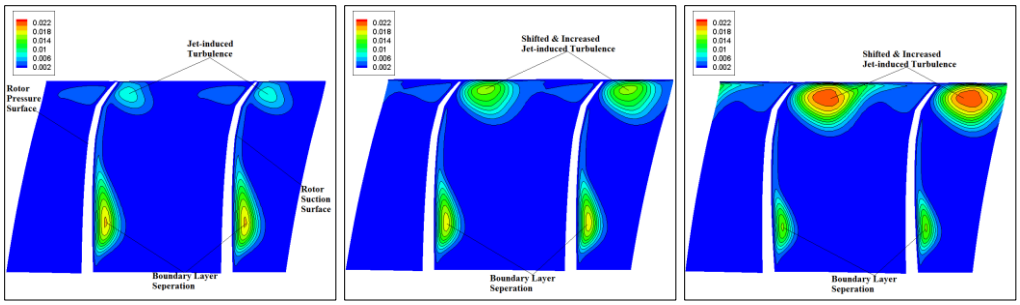

TC=0.3125mm TC=0.75mm TC=1.25mm

Fig 6.21a Distribution of turbulent viscosity on 100% streamwise plane, with TC=0.3125mm, TC=0.75mm and TC=1.25mm

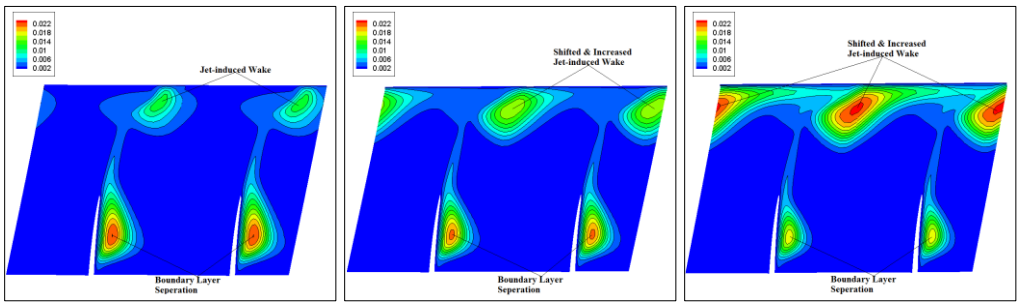

TC=0.3125mm TC=0.75mm TC=1.25mm

Fig 6.21b Distribution of turbulent viscosity on 120% streamwise plane, with TC=0.3125mm, TC=0.75mm and TC=1.25mm

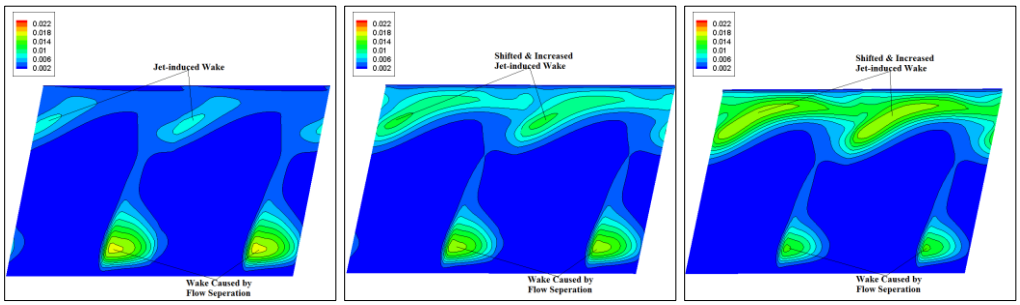

TC=0.3125mm TC=0.75mm TC=1.25mm

Fig 6.21c Distribution of turbulent viscosity on 140% streamwise plane, with TC=0.3125mm, TC=0.75mm and TC=1.25mm

More quantitative comparison of fluid property change with varying TC value is conducted. Based on 100% streamwise plane, the comparison of TC=0.3125mm, TC=0.75mm and TC=1.25mm is conducted, with data points specified as mentioned earlier. Figure 6.22 shows the distribution of Mach number at 90% span line on 100% streamwise plane. As explained earlier, the peak of Mach distribution is due to fluid jet from TC and the valley of Mach distribution is due

to flow separation near tip on R_{ps}. The shift of peak Mach location is observed again with the increase of TC value. The value of Mach at the valley location for TC=0.3125mm case is slightly larger than the other two, as fluid jet initiated from TC has less suppression effect on the flow separation initiated from R_{ps} for smaller TC case. Figure 6.23 shows the distribution of total pressure at 90% span line on 100% streamwise plane. The Pt distribution presents similar pattern with the Mach distribution, showing the impact of fluid jet and flow separation on the pressure generation and pressure loss. The shift of peak Pt location is also identified, further demonstrates the shift of fluid jet with varying TC value.

Figure 6.24 shows the distribution of turbulent viscosity at 90% span line on 100% streamwise plane. The peak value increases by 200% from TC=0.3125mm case to TC=1.25mm case, with a shift of peak location from 14.5% to 28.1% span width. This proves that with the increase of TC value, fluid jet intensifies and the intensity of turbulence increases on R_{ss} flow path. At large TC value, more fluid is ejected from R_{ps} towards R_{ss}, resulting in more fluid momentum for fluid jet, which makes it less likely to be compressed back towards blade surface by the mean stream fluid. Thus the fluid jet for large TC case travels further away from blade surface after the ejection from blade tip.

Figure 6.25 shows the distribution of mean field vorticity at 90% span line on 100% streamwise plane. The sinusoidal pattern of distribution along the span width is observed for all three TC value cases. However, the Magnitude of fluctuation with TC=0.75mm and TC=1.25mm is generally larger than that with TC=0.3125mm, from R_{ss} to around 60% span width, showing that fluid is more prone to rotate with large TC value. This is due to larger effect of TC flow at large TC value. The magnitude of vorticity fluctuation amplifies from R_{ss} towards R_{ps}, due to more effect of flow separation near R_{ps}. From 60% span width to R_{ps}, the magnitude of vorticity fluctuation does not present evident difference for three TC value cases, showing the difference of impact of flow separation near R_{ps} on the spinning motion of fluid is insignificant.

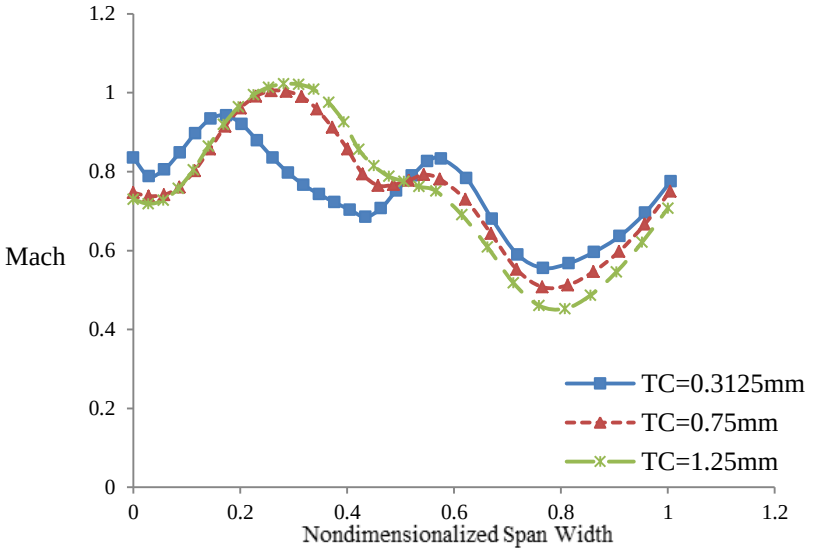

Fig 6.22 Distribution of Mach at 90% span line on 100% streamwise plane, with TC=0.3125mm, TC=0.75mm and TC=1.25mm

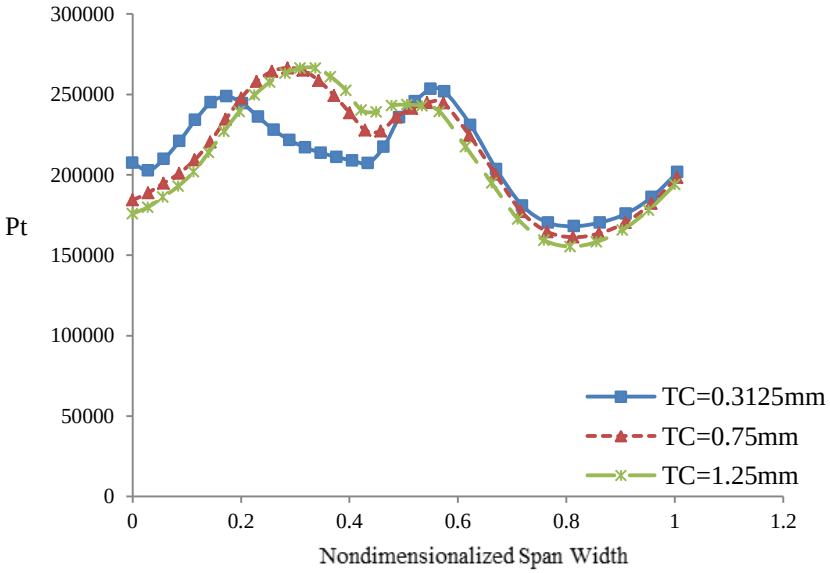

Fig 6.23 Distribution of Pt at 90% span line on 100% streamwise plane, with TC=0.3125mm, TC=0.75mm and TC=1.25mm

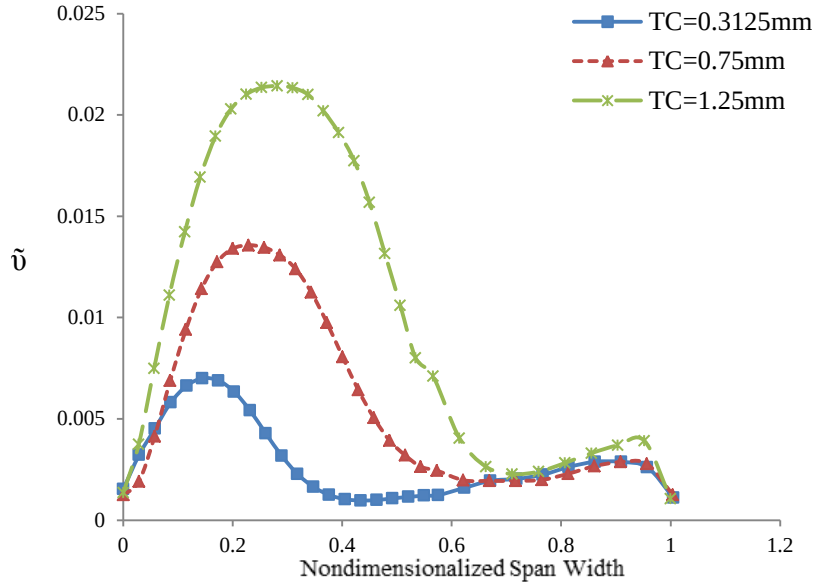

Fig 6.24 Distribution of turbulent viscosity at 90% span line on 100% streamwise plane, with TC=0.3125mm, TC=0.75mm and TC=1.25mm

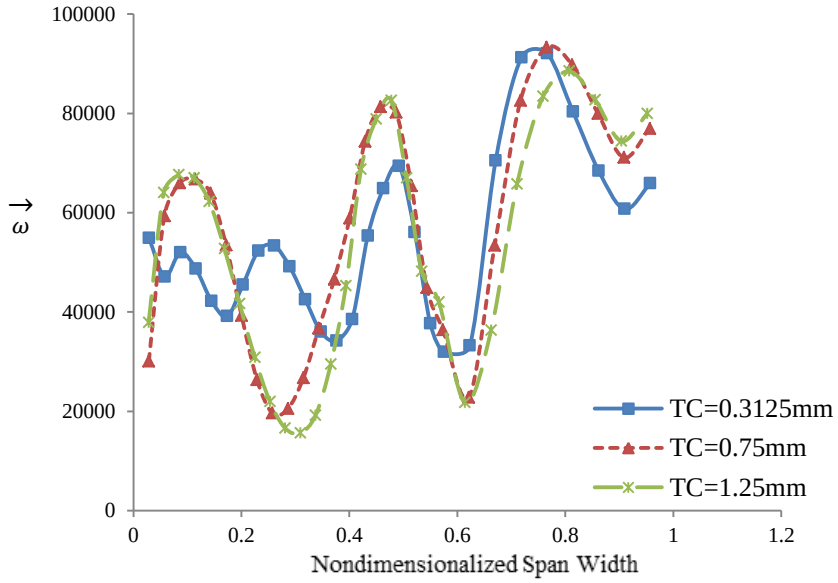

Fig 6.25 Distribution of vorticity at 90% span line on 100% streamwise plane, with TC=0.3125mm, TC=0.75mm and TC=1.25mm

The comparison of fluid property change with varying TC value, at 50% span line on 100% streamwise plane, is also considered. This is conducted to understand the effect of extension of fluid jet towards the lower-zone flow path and the effect of boundary layer separation on $R_{ss,}$ when TC value is changed. Again, three

different TC values are considered, i.e. TC=0.3125mm, TC=0.75mm and TC=1.25mm.

Figure 6.26 shows the distribution of Mach number at 50% span line on 100% streamwise plane. The Mach generally slightly decreases from R_{ss} towards R_{ps}, but the variation of Mach is insignificant. The Mach fluctuates slightly from 41.1% to 75.9% span width, suggesting the blocking of core flow due to TC vortex initiated from blade tip and flow separation initiated from R_{ps}, which squeezes the core flow to propagate through a narrow path near the middle span width. This can also be identified from the Mach contour on 100% streamwise plane, which is presented earlier. In addition, the Mach at near R_{ss} region for small TC case is relatively larger than that for large TC cases, which is in consistence with observations made from the Mach contour. In general, the variation of Mach at 50% span line is insignificant. Figure 6.27 shows the distribution of total pressure at 50% span line on 100% streamwise plane. The distribution of Pt presents similar pattern with the distribution of Mach, which further demonstrates the effect of Mach on Pt generation and Pt loss.

Figure 6.28 shows the distribution of turbulent viscosity at 50% span line on 100% streamwise plane. The peak value is identified at near R_{ss} regions, indicating the effect of boundary layer separation. However, the peak value point shifts from 5.6% span width with TC=0.3125mm to 2.7% spanwidth with TC=1.25mm, with a decrease of turbulent viscosity value by 57.1%. This observation is identical with discussions made for the turbulent viscosity contour on 100% streamwise plane, where both the value and the extension of high turbulent viscosity region near R_{ss} decreases with the increase of TC value, due to the increased suppression by fluid jet. The variation of turbulent viscosity from around 13.7% span width towards the R_{ps} is insignificant, as the flow is less turbulent.

Figure 6.29 shows the distribution of mean field vorticity at 50% span line on 100% streamwise plane. Again, the data points on blade surface are not included to avoid extremely large value. Large vorticity value is observed near R_{ss} due to boundary layer effect, as discussed earlier. However, a fluctuation region is

identified from 35.6% span width towards the R_{ps}, showing that fluid is more prone to rotate. This can be explained by the relative high Mach region identified from 41.1% to 75.9% span width as previously shown, which stimulates relative motion of fluid in adjacent low Mach region and forces fluid to spin. The variation of vorticity can also be observed from previously shown vorticity contour on 100% streamwise plane, which more intuitively explains the fluctuation of vorticity at 50% span line.

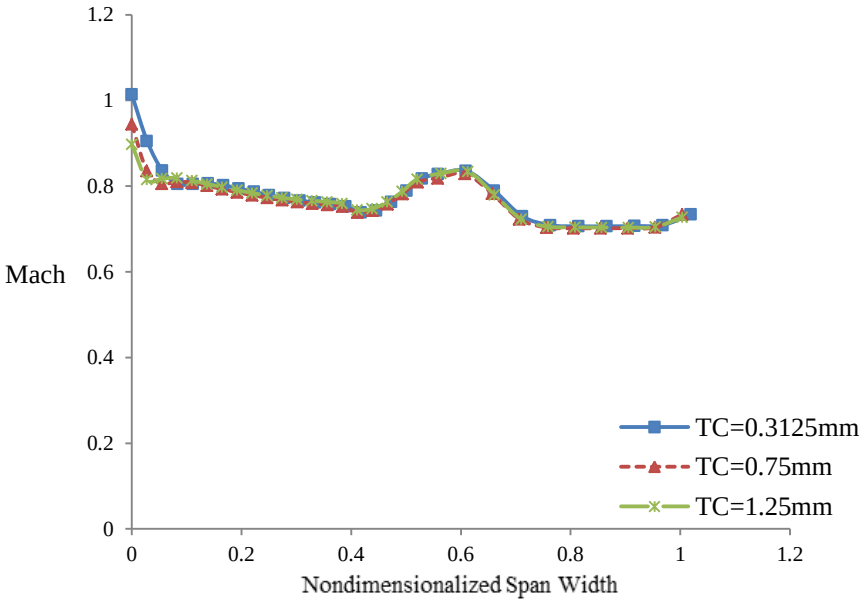

Fig 6.26 Distribution of Mach at 50% span line on 100% streamwise plane, with TC=0.3125mm, TC=0.75mm and TC=1.25mm

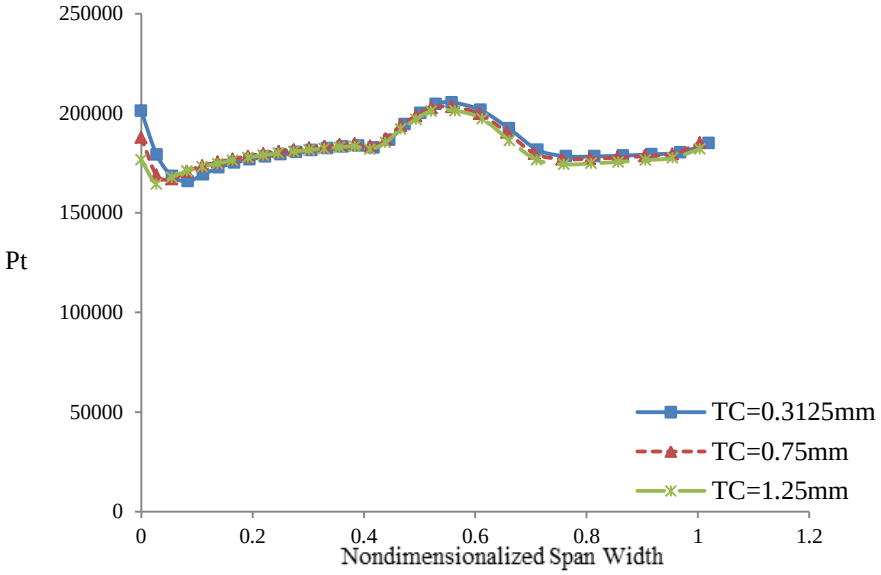

Fig 6.27 Distribution of Pt at 50% span line on 100% streamwise plane, with TC=0.3125mm, TC=0.75mm and TC=1.25mm

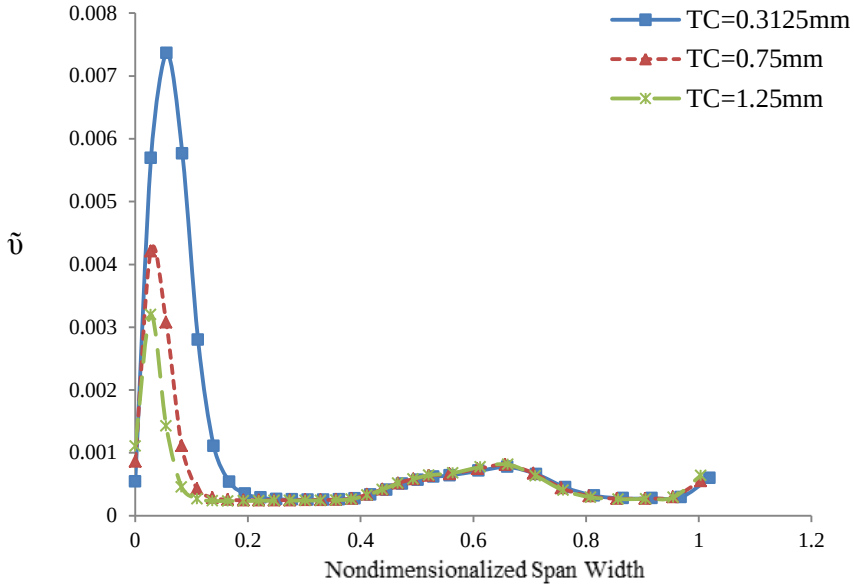

Fig 6.28 Distribution of turbulent viscosity at 50% span line on 100% streamwise plane, with TC=0.3125mm, TC=0.75mm and TC=1.25mm

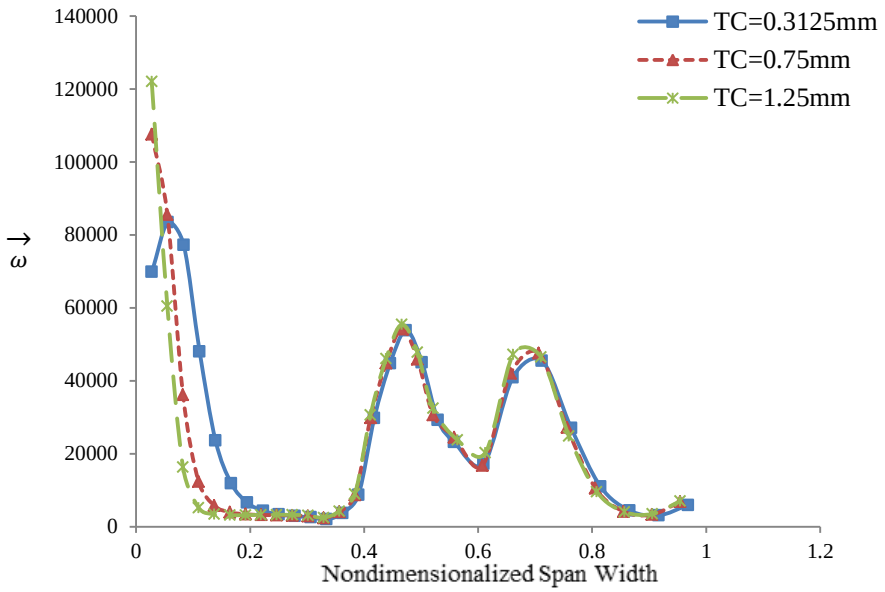

Fig 6.29 Distribution of vorticity at 50% span line on 100% streamwise plane, with TC=0.3125mm, TC=0.75mm and TC=1.25mm

The comparison of fluid property change with varying TC value, at 10% span line, is also briefly discussed. This is conducted to understand the change of expansion of boundary layer separation on R_{ss} when TC value is changed. Again, three different TC values are studied, i.e. TC=0.3125mm, TC=0.75mm and TC=1.25mm. The data line is based on 100% streamwise plane as well.

Figure 6.30 shows the distribution of Mach number at 10% span line on 100% streamwise plane. High Mach is observed at around 8.9% span width for all three TC value cases. This can also be identified from the previously shown Mach contour on 100% streamwise plane, where small region of high Mach is identified at the left-bottom corner near R_{ss}. The lowest Mach is identified at 32.9% span width, locating outside the rim of high Mach corner. The difference of Mach distribution with varying TC value is not prominent to tell. Figure 6.31 shows the distribution of mean field vorticity at 10% span line on 100% streamwise plane. Similar distribution is observed with that at 50% span line as just discussed, although the value of vorticity is smaller at 10% span line, showing fluid is less prone to rotate as the effect of boundary layer weakens towards the rotor hub. Therefore, the effect of tip clearance has minor effect on flow in the lower-zone.

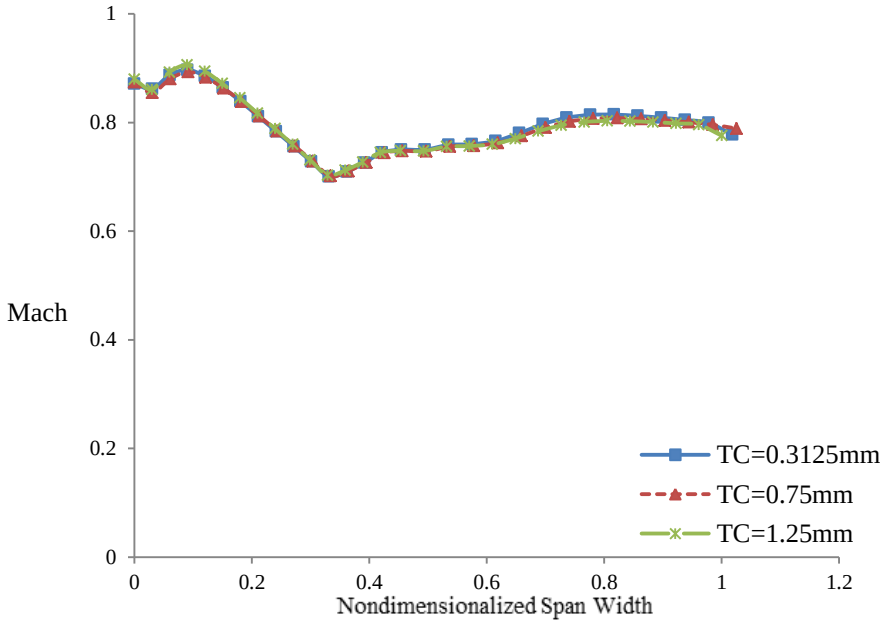

Fig 6.30 Distribution of Mach at 10% span line on 100% streamwise plane, with TC=0.3125mm, TC=0.75mm and TC=1.25mm

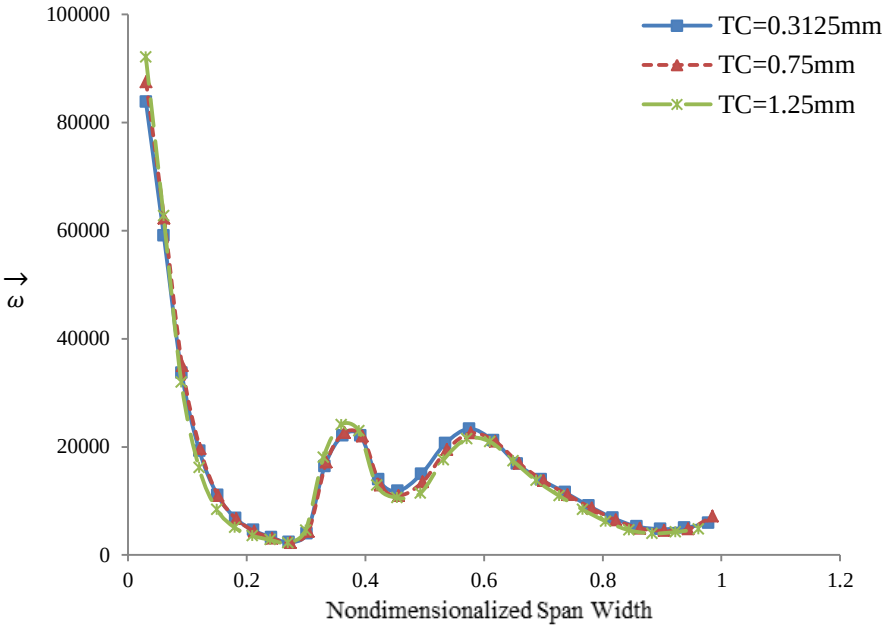

Fig 6.31 Distribution of vorticity at 10% span line on 100% streamwise plane, with TC=0.3125mm, TC=0.75mm and TC=1.25mm

6.3 Effect of Reynolds Number with Constant TC

With a constant TC=0.5mm, the effect of Reynolds number on compressor performance is studied. This is in contrast with previous *Re* effect study in Chapter 4, when TC is not included. This study is conducted due to concerns about limitation of manufacturing when compressor is miniaturized, as the TC may not be feasible to be further contracted due to manufacture tolerance. Table 6.3 shows the specification of TC and *Re*. Different scaling factors are applied, resulting in variation of Reynolds number from *Re* 2.14×10^5 to *Re* 8.54×10^5. The compressor RPM and rotor blade height are adjusted accordingly, as previously introduced in Chapter 4. Constant TC=0.5mm is applied at varied *Re* conditions, resulting in the TC ratio variation from 0.42% to 1.67%.

Table 6.3 Specification of Tip Clearance and Reynolds Number

Scaling Factor	RPM	Reynolds Number	Blade Height (mm)	Constant TC (mm)	TC Ratio
1.6	10742	8.54×10^5	120	0.5	0.42%
1	17188	5.34×10^5	75	0.5	0.67%
0.7	25784	3.74×10^5	52.5	0.5	0.95%
0.4	42970	2.14×10^5	30	0.5	1.67%

The boundary conditions are applied identical with that in Case 1, with design Mfr at 100% design speeds. Results from w/ TC case are compared with w/o TC case, at different *Re* conditions, to understand the effect of *Re* with constant TC. Figure 6.32 shows the comparison of compressor *Pr* for w/ and w/o TC cases, at varying *Re* condition. As discussed before, for w/o TC case, the *Pr* decreases with the decrease of *Re*. However, at constant TC=0.5mm, the drop of *Pr* with small *Re* is more prominent, and the distribution of *Pr* becomes almost a flat line at large *Re* condition. This can be explained by the relatively large change of TC ratio at small *Re* condition, which can be identified from Table 6.3 just presented.

Figure 6.33 shows the comparison of the compressor η_{ad} for w/ and w/o TC cases, at varying *Re* condition. A drop of η_{ad} from w/o TC case to w/ TC case is also

observed. The decrease of η_{ad} value at different *Re* conditions is almost identical, although at small *Re* condition, i.e. *Re* 2.14×10^5, the drop of value is still slightly larger, with a decrease of η_{ad} by 6.65%. Figure 6.34 further shows the distribution of *Pr* and η_{ad} with varying TC ratio. Both properties decrease with the increase of TC ratio, which is identical with previous discussions. In general, the results show that at constant TC value, the loss of compressor performance amplifies with the decrease of *Re*, i.e. with the miniaturization of compressor.

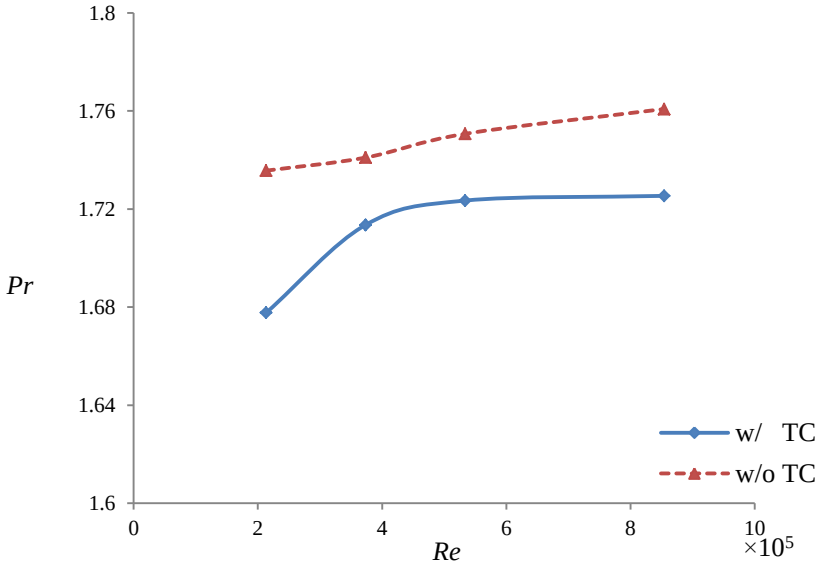

Fig 6.32 Comparison of *Pr* for w/ and w/o TC cases, at varying *Re* condition

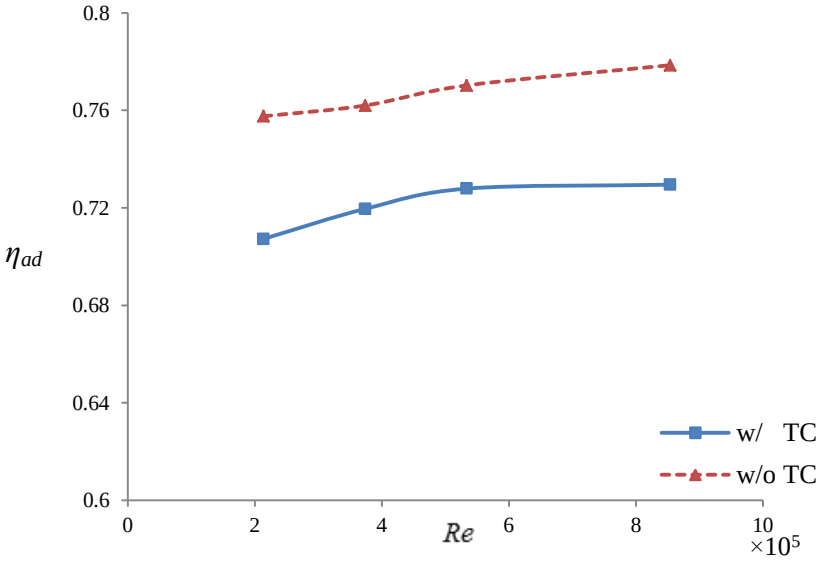

Fig 6.33 Comparison of η_{ad} for w/ and w/o TC cases, at varying *Re* condition

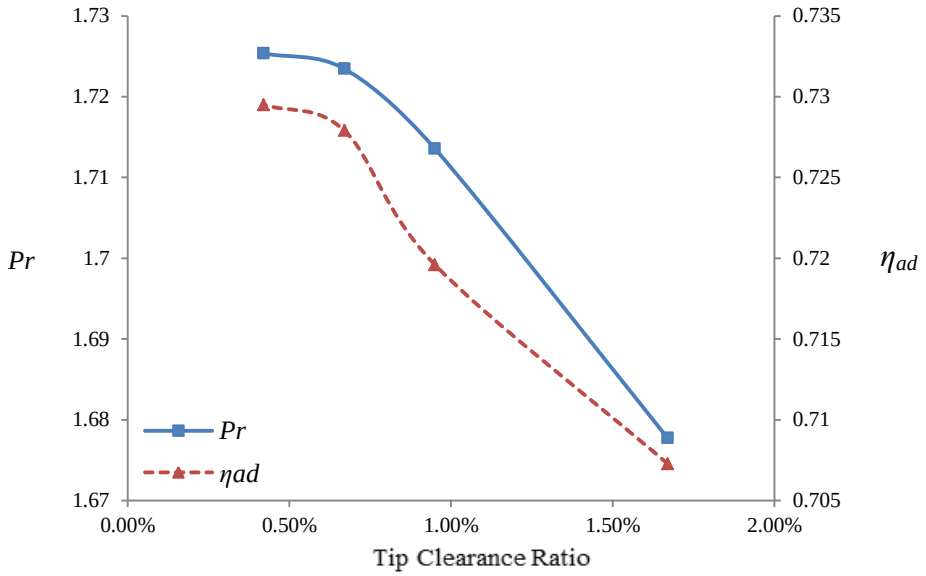

Fig 6.34 Distribution of *Pr* and η_{ad} with varying TC ratio

To better understand the change of compressor performance, the flow field analysis at TC region is conducted. Two Reynolds number conditions are applied, i.e. *Re* 8.54×10^5 and *Re* 2.14×10^5, representing large and miniaturized compressor, respectively.

Figure 6.35 shows the streamline at rotor TC with top view, at large and small *Re* conditions. Relative velocity components are used because of rotor rotation, to better present the fluid traces in rotor zone. At both *Re* conditions, the generation of TC vortex initiates from the tip region near R_{LE}. Fluid is ejected from R_{ps} to R_{ss} along the chord of rotor tip, forming a vortex zone on R_{ss} and propagates towards downstream of the flow path. However, at *Re* 8.54×10^5, the expansion of TC vortex is comparatively smaller than that at *Re* 2.14×10^5, which is attributed to the smaller momentum of fluid jet when smaller TC ratio is resulted at large *Re* condition. In addition, the strongest fluid ejection is observed at around mid-span chord length at *Re* 8.54×10^5, which is slightly earlier than the strongest fluid ejection at *Re* 2.14×10^5 at around 60% chord. Also, the fluid jet propagates less distance away from R_{ss} at *Re* 8.54×10^5 than that at *Re* 2.14×10^5.

Figure 6.36 shows the streamline at rotor TC with front view, at large and small *Re* condition. The generation of TC vortex is clearly identified from R_{LE}.

However, the TC vortex is more pronounced at *Re* 2.14×10^5, presenting a more rotating pattern than that at *Re* 8.54×10^5. Also, the expansion of TC vortex away from shroud is more evident at small *Re* condition, which is attributed to the larger fluid jet momentum with larger TC ratio.

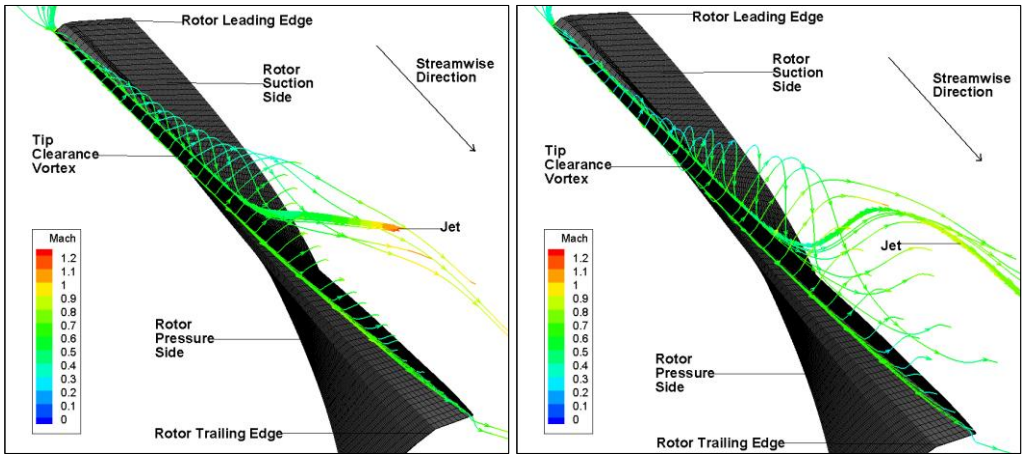

Re 8.54×10^5 *Re* 2.14×10^5

Fig 6.35 Streamline at rotor TC with top view, at large and small *Re* condition

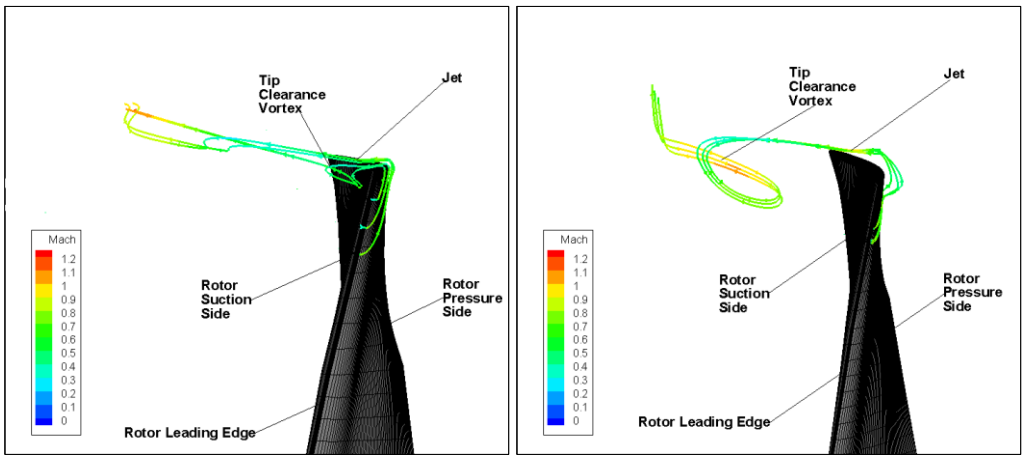

Re 8.54×10^5 *Re* 2.14×10^5

Fig 6.36 Streamline at rotor TC with front view, at large and small *Re* condition

Figure 6.37 shows the streamline at stator TC with downstream view, at large and small *Re* condition. Absolute velocity components are used, with no relative motion considered in stationary stator zone. The streamlines travel from S_{ps} towards S_{ss}, crossing the TC region. The difference at two *Re* conditions is

evident to tell. At *Re* 2.14×10^5, the expansion of streamlines is less suppressed, i.e. the TC flow region is wider, compared with that at *Re* 8.54×10^5. This is attributed to the smaller TC ratio at *Re* 8.54×10^5. Figure 6.38 shows the streamline at stator TC with top view, at large and small *Re* condition. At *Re* 2.14×10^5, the streamlines travel slight further away from S_{ss} due to larger TC ratio, compared with that at *Re* 8.54×10^5.

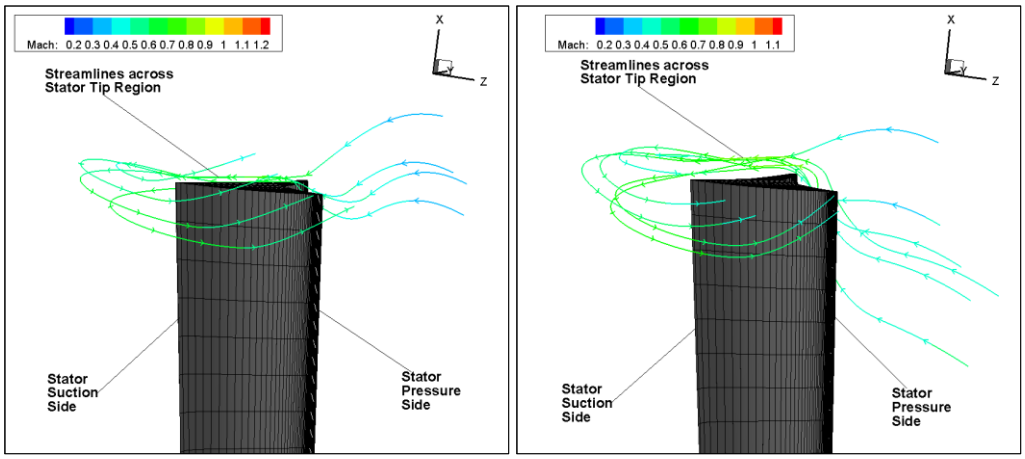

Re 8.54×10^5 *Re* 2.14×10^5

Fig 6.37 Streamline at stator TC with downstream view, at large and small *Re* condition

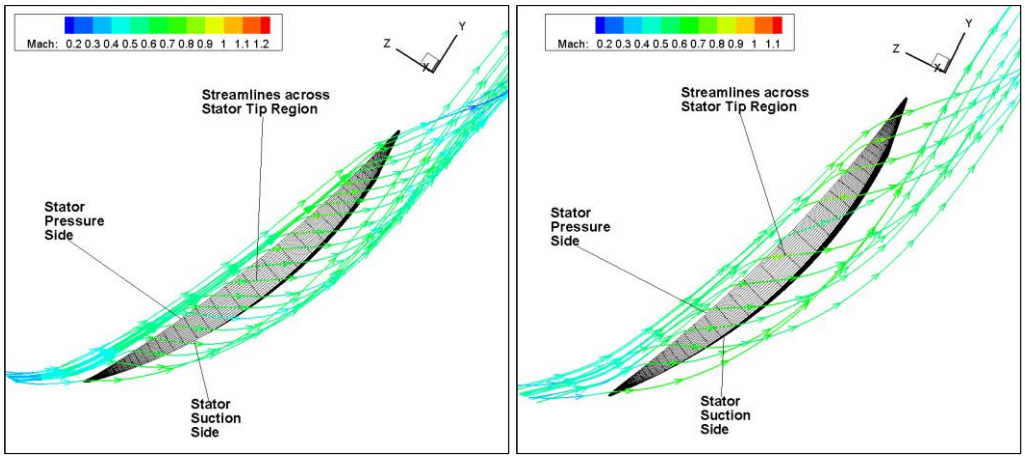

Re 8.54×10^5 *Re* 2.14×10^5

Fig 6.38 Streamline at stator TC with top view, at large and small *Re* condition

In summary, the effect of tip clearance on the performance of an axial compressor is studied. Both varying TC value and varying Reynolds number are applied, to investigate compressor performance and flow structure at different TC conditions. Numerical results indicate the existence of TC has an adverse effect on compressor performance, and the loss of performance amplifies during the miniaturization. Besides that, analysis of flow structure shows that the existence of TC dramatically impacts flow structure, especially near blade tip region. Fluid jet is observed at TC, ejecting from blade pressure side towards its suction side. The generation of turbulence and change of flow properties are evident near the blade tip region, but the TC impact on flow structure gradually diminishes away from the tip region.

Chapter 7

Conclusions and Recommendations

7.1 Conclusions

The present numerical investigation aims to elucidate the effects of miniaturization on the performance of a gas turbine compressor. Based on the CFD validation study of the NASA Stage35 compressor [47, 48], three parametric studies are numerically conducted regarding their effects on compressor performance during the miniaturization process.

Firstly, the effect of Reynolds number is studied, as an indication of the extent of miniaturization. Scaling factors ranging from 1.6 to 0.4 are applied on the original compressor geometry, resulting in operating Reynolds number ranges from *Re* 8.54×10^5 to *Re* 2.14×10^5, when design Mfr and 100% design speed are applied. Numerical results indicate that the miniaturization has an adverse effect on compressor performance, due to increased viscous effect. At the optimal Mfr (111.2% of design Mfr), the total pressure ratio drops 1.39% and the overall adiabatic efficiency drops 1.3%, when scaling factor decreases from 1.6 to 0.4. Analysis of flow fields at varying Reynolds number conditions shows that the miniaturization process has minor effects on fluid property changes except the generation of turbulence, where the decrease of turbulence intensity is prominent with the decrease of Reynolds number.

Secondly, the effect of heat transfer is studied, with three varying thermal conditions applied. Numerical results indicate that the heat loss from compressor to the ambient air will benefit the compressor performance, about 1.0% increase of adiabatic efficiency is observed when a constant heat transfer coefficient $h = 200$ W/m^2·k is applied at *Re*=5.34 × 10^5. The heat loss amplifies with the miniaturization of compressor, due to the increased surface to volume ratio. Therefore, the increase of adiabatic efficiency ranges from 0.68% to 1.02%, when scaling factor decreases from 1.6 to 0.4. The total pressure ratio does not present

observable changes due to the applied heat loss. However, when isothermal wall condition is applied, heat transfer from downstream combustor is therefore allowed. At wall temperature T=380k, the overall adiabatic efficiency drops 3.37% and the overall pressure ratio drops 0.8% at design Mfr at Re=5.34 × 10^5. Numerical results indicate that heat transfer from combustor has an adverse effect on the compressor performance, especially on its adiabatic efficiency, due to heat addition into compressor. Therefore, blade cooling is proposed to enhance the overall performance and efficiency.

Thirdly, the effect of tip clearance is studied, with both varying TC value and varying Reynolds number applied. Numerical results indicate the existence of TC deteriorates compressor performance. When TC value ranges from 0.3125mm to 1.25mm, i.e., TC ratio ranges from 0.42% to 1.67% at Re=5.34×10^5, the drop of total pressure ranges from 1.34% to 3.02% and the drop of overall adiabatic efficiency ranges from 5.08% to 6.62%, indicating the amplification of loss of performance with the increased TC ratio. For miniaturized gas turbines, the loss of compressor performance amplifies due to the increased TC ratio, when a constant TC=0.5mm is applied in the current study. In addition, at Re=2.14× 10^5, with a corresponding TC ratio of 1.67%, the total pressure drops 3.37% and the overall adiabatic efficiency drops 6.65%, indicating that the loss of performance is even higher than the conventional ones, though the same TC ratio is applied. Besides that, analysis of flow structure shows that the existence of TC also impacts flow structure, especially near blade tip region. Fluid jet is observed at TC, ejecting from blade pressure side towards its suction side and further propagating downstream towards the adjacent blade. The generation of turbulence and change of fluid properties are evident near the blade tip region, but the TC impact on flow structure gradually diminishes away from the tip region.

In summary, the effects of miniaturization of gas turbine compressor are further elaborated in this study. The tip clearance loss is considered the most critical loss among the parameters investigated, and the miniaturization impairs the overall performance. In addition, heat addition from combustor undermines compressor

efficiency thus compressor cooling is essential to enhance the overall performance. This numerical investigation shed more light on the performance characteristic and fluid property behaviors during compressor operation, meanwhile, the numerical approach adopted is demonstrated to be reliable for MGT investigation.

7.2 Recommendations

The current research focuses on the investigation of the effects of miniaturization on compressor performance, based on parametric studies of Reynolds number, heat transfer and tip clearance. Although these parameters are considered important impact factors during compressor operation, the investigation of additional parameters is still required, such as effect of pre-rotating flow, effect of wall roughness, impact of blade geometry, effect of splitter implement, etc. In addition, experiments are also required for the validation of CFD proposed miniaturized gas turbine design.

Although the current numerical results are valid and valuable to clarify the issues enclosed in this thesis, the proposed numerical method still requires additional adjustment. The discrepancy of efficiency distribution should draw special attention, as the numerical results capture the trend of efficiency distribution while details are only approximately predicted. This might be due to several reasons, among which the insufficient capability of SA turbulence model in predicting adverse pressure gradient should be specially noticed. More powerful and suitable turbulence models should be developed and used.

The current numerical results are from 3D steady-state simulations, and the time-averaged solution reasonably predicts the compressor performance. However, transient simulations should be used if more accurate results are required. Also, transient simulations should be considered when the operation conditions and output on time basis are concerned. In addition, although the current numerical approach produces well acceptable results, special treatment or models may be proposed for near wall region.

APPENDIX I

KJ-66 Micro Gas Turbines Compressor Test

The KJ-66 micro gas turbines (MGT) compressor is numerically simulated, to deepen the understanding of performance of miniaturized gas turbines. Initial and boundary conditions including interface method, turbulence models, adiabatic wall condition, inlet and outlet boundary types, periodic boundary technique, and operation condition, etc., are specified referring to previous validation study. Operational speed, mass flow rate, inlet and outlet temperature and pressure values and etc., which are specially mentioned in this chapter for KJ-66 compressor are defined differently from the previous validation study. Although the configuration of radial compressor is different from previous axial compressor, the previous validated setup is still a valuable reference for the current study, as both compressor present adverse pressure gradients.

For the clarification of applying previous validated setup to this MGT compressor, the limitations are discussed. For MGT radial compressor, the tip loss is expected to be more significant, the surface area for heat transfer is much greater and the friction on the shroud is a major source of loss. In the current MGT radial compressor study, the tip clearance is not considered, the heat transfer through wall is also not considered as adiabatic wall boundary condition is specified.

A-I.1 Design Details of KJ-66 MGT Compressor

The KJ-66 MGT is chosen, because it is a reliable and robust engine and it is well tested. The combination of extreme conditions in terms of rotational speed with elevated gas temperatures, making MGT among the most advanced and complicated systems.

Figure A-i.1 shows the layout of KJ-66 MGT and identification of each component. The single stage centrifugal compressor is mounted at the engine entrance and colored in purple. The combustion chamber is located immediately

after the compressor, followed by the turbine at the engine exit. More compact assembly is identified as smaller internal space is available, compared with conventional large gas turbines.

Table A-i.1 presents the design parameters and performance characteristics of KJ-66 MGT. The designed diameter and length demonstrate the small scale of MGT. In total, 10 rotor blades and 15 stator blades are built, with a designed maximum rotational speed of 117,000 rpm, which is 7 times larger than that of NASA Stage35 previously introduced. With a design thrust of 75N, the KJ-66 engine is widely recognized as an efficient model for MGT study. The compressor pressure ratio is design as 2.2 for the KJ-66 engine with only one compressor stage, which demonstrates the requirement of MGT for high performance compressor, as few compressor stages are available.

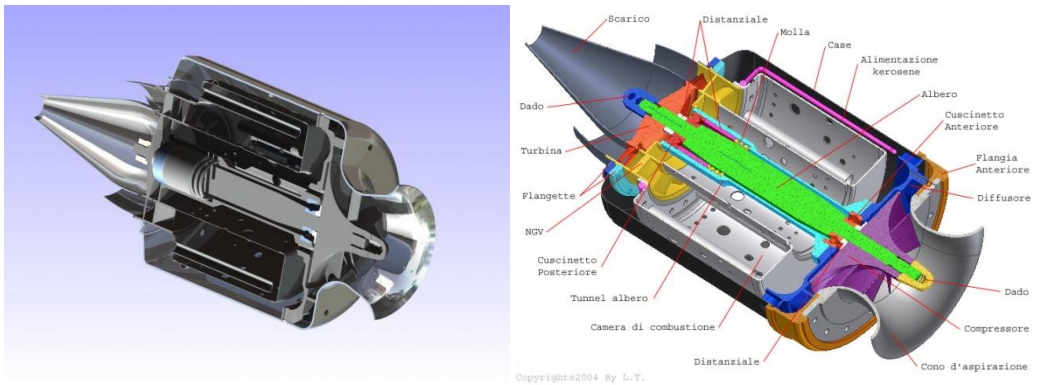

Fig A-i.1 Layout of KJ-66 micro gas turbine

Table A-i.1 Design Parameters and Performance Characteristics of KJ-66 MGT

Diameter	110 mm
Length	240 mm
Weight	0.93 kg
Number of Compressor Rotors	10
Number of Compressor Stators	15
Thrust	75 N
Maximum Wheel Speed	117,000 rpm
Compressor Pressure Ratio	2.2
Mass Flow Rate	0.22 kg/s
Maximum Exhaust Temperature	843 K

The centrifugal configuration of KJ-66 compressor differs from the previous NASA Stage35 compressor, where axial configuration of compressor is presented. Nevertheless, all basic flow features studied in the previous sections are relevant for centrifugal compressor as well. Flow is accelerated and redirected towards the radial direction when it reaches the diffusor. Figure A-i.2 shows the 3D model of KJ-66 MGT centrifugal compressor, w/ and w/o shroud, respectively. The twisting geometry of rotor blades is identified and the assembly of impeller and diffusor is also illustrated. The impeller has a tip radius of R_{tip}=33mm, with inlet hub and inlet shroud radius of R_{ih}=6.25mm and R_{is}=22.5mm, respectively. The inner diameter of the whole shroud is D_{shroud}=107.4mm. The splitter blades mounted after the compressor are also presented in the w/ shroud description, showing fluid is further redirected into axial direction before it enters the combustor.

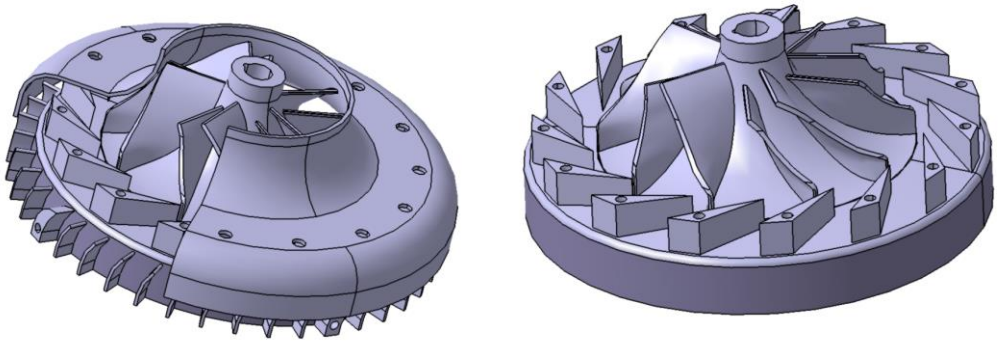

w/ shroud w/o shroud

Fig A-i.2 3D model of KJ-66 MGT compressor, w/ and w/o shroud

A-I.2 Numerical Approach Setup

Similar approach for model generation with NASA Stage35 compressor is utilized. For KJ-66 MGT compressor, 1/5 of compressor is simulated with 72 degrees azimuthally, consists of two rotor blades and three stator blades. Periodic boundary conditions are also applied in the azimuthally direction to represent the full circular. Tip clearance is not considered in this study. Figure A-i.3 shows the 3D view of the computational domain.

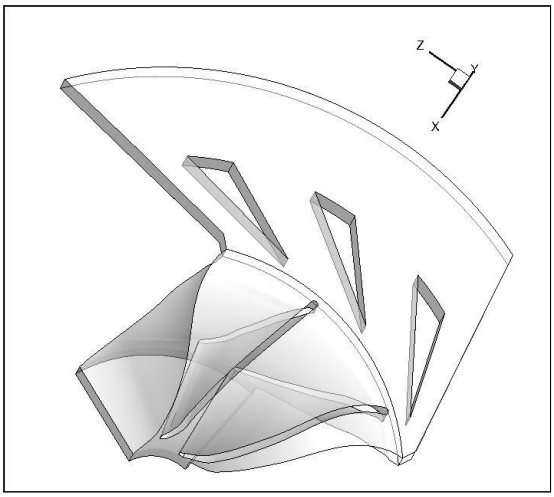

Fig A-i.3 3D view of the computational domain

The computational domain is further subdivided into rotating impeller zone and stationary diffuser zone. Structured hexahedral meshes are generated for each zone separately, dividing at interface surface. Each computational zone is further subdivided into sub-blocks, to aid mesh refinement based on block geometry. Identical with the NASA Stage35 compressor meshing approach, mesh refinement is considered near blade edge and near wall regions. Figure A-i.4 shows the structured mesh built for KJ-66 MGT compressor. Local refinement of mesh generated can be identified. The grid independence study suggests that 1.3 million meshes are sufficient in producing sufficiently accurate results.

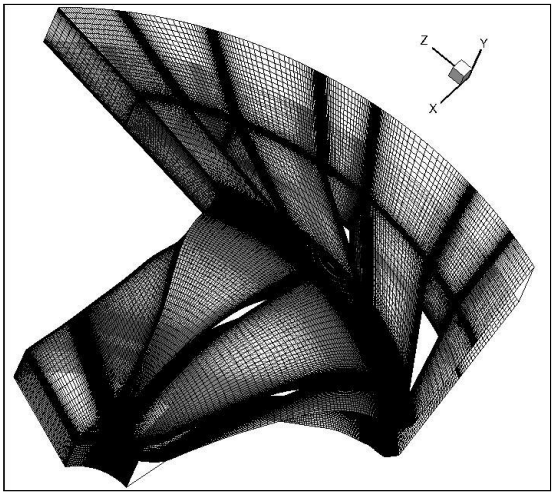

Fig A-i.4 Structured mesh for KJ-66 MGT compressor

Boundary conditions are specified referred to previous validation study, with adjustment made according to KJ-66 MGT compressor design parameters. Figure A-i.5 shows the specification of boundary conditions and each boundary type it highlighted in different colors. Impeller entrance is defined as mass flow inlet boundary and diffuser exit is defined as pressure outlet boundary. The impeller-diffuser interface is highlighted in purple and periodic boundary is applied in the azimuthally direction and highlighted in green. Wall boundary is defined as viscous surface, assuming fluid velocity is zero at wall.

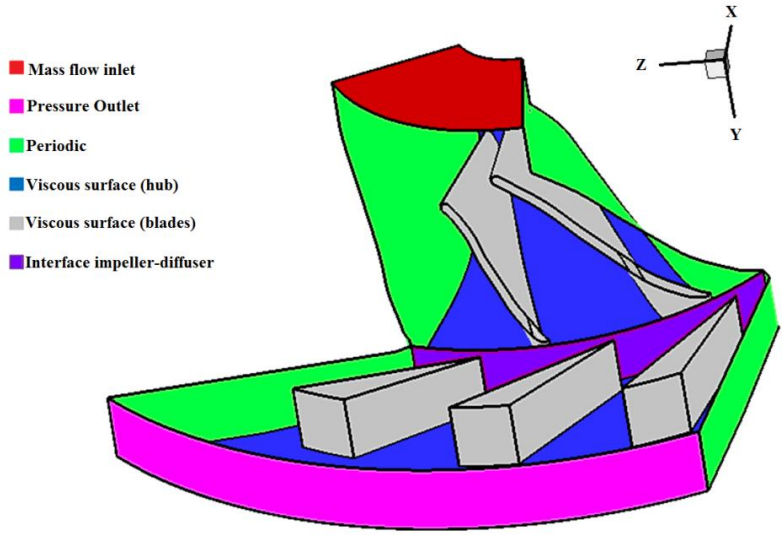

Fig A-i.5 Specification of boundary conditions for KJ-66 MGT compressor

The steady state simulation is considered. The Spalart-Allmaras turbulence model and mixing plane interface method are applied, which are identical with validation case. The adiabatic wall condition is applied throughout this MGT study. The operation speed is defined at 80k, 100k and 117k rpm, with varying mass flow rate applied. Table A-i.2 presents the details of boundary conditions and Mfr and at varying operation speed. The applied Mfr is 1/5 of the real Mfr for the full compressor circular.

Table A-i.2 Details of Boundary Conditions and Mfr at Various Operation Speed

	Operation Speed (rpm)		
	80k rpm	**100k rpm**	**117k rpm**
Inlet Temperature (k)	**288**		
Outlet Temperature (k)	**288**		
Operating Pressure (Pa)	**0**		
Inlet Pressure (Pa)	**101325**		
Outlet Pressure (Pa)	**131325**	**161325**	**202325**

Operation Speed (rpm)					
80k rpm		**100k rpm**		**117k rpm**	
Mass Flow Rate (kg/s)		Mass Flow Rate (kg/s)		Mass Flow Rate (kg/s)	
Input Value	Real Value	Input Value	Real Value	Input Value	Real Value
0.022	0.11	0.034	0.17	0.044	0.22
0.024	0.12	0.036	0.18	0.046	0.23
0.026	0.13	0.038	0.19	0.048	0.24
0.028	0.14	0.040	0.20	0.050	0.25
0.030	0.15	0.042	0.21	0.052	0.26
0.032	0.16	0.044	0.22	0.054	0.27
0.034	0.17	0.046	0.23	0.056	0.28
0.038	0.19	0.048	0.24	0.058	0.29

The first order accuracy is initially enabled to accelerate the convergence and is switched to second order when a relatively low and stabilized residual is achieved. It takes approximately 10,000 iterations to reach the initial convergence, and a total of around 40,000 iterations to gain the confidence that final convergence is achieved.

A-I.3 Numerical Results for KJ-66 MGT Compressor

For the purpose of understanding the operation of MGT compressor and determining the optimal operation point of the KJ-66 engine, simulation results are analyzed. The compressor performance is mainly indicated by the overall pressure ratio achieved and the efficiency loss.

Figure A-i.6 shows the distribution of total pressure ratio with varying Mfr, at different operation speed. Peak *Pr* value is observed for each operation speed, respectively. According to the designed performance table, a *Pr* of 2.2 is achieved

with Mfr of 0.22 kg/s at 117k rpm. However, simulation results produce peak *Pr* of 1.96 with Mfr of 0.24 kg/s at 117k rpm. The *Pr* drops away from the optimal Mfr point. Result from simulations at 80k rpm and 100k rpm presents similar distribution, but smaller total pressure ratio is achieved with the decrease of operation speed. The peak *Pr* of 1.54 is achieved with Mfr of 0.13 kg/s at 80k rpm, and peak *Pr* of 1.76 is achieved with Mfr of 0.19 kg/s at 100k rpm, respectively. Generally, the higher the operation speed, the higher *Pr* is achieved. This is in consistence with experimental results shown in Figure A-i.7 [92].

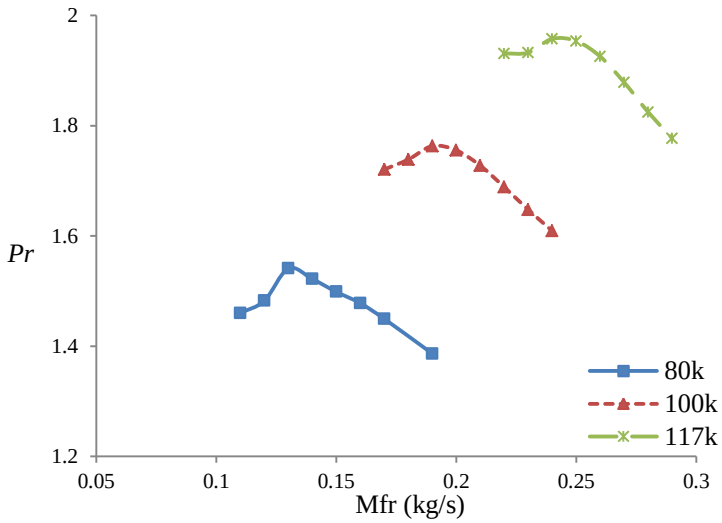

Fig A-i.6 Distribution of *Pr* with varying Mfr, at different operation speed

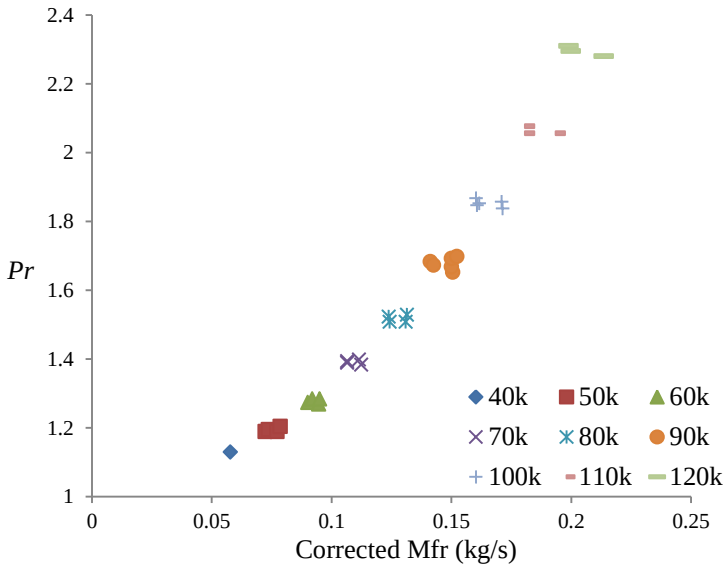

Fig A-i.7 Distribution of experiment *Pr* with varying Mfr at different operation speed

Figure A-i.8 shows the distribution of adiabatic efficiency with varying Mfr, at different operation speed. Peak η_{ad} value is observed for each operation speed, respectively. However, value of η_{ad} generally decreases with the increase of operation speed, and it is in contrast with the *Pr* distribution. At each operation speed, the η_{ad} drops away from the optimal Mfr point. The simulation results produce peak η_{ad} of 0.73 with Mfr of 0.13 kg/s at 80k rpm, peak η_{ad} value of 0.63 with Mfr of 0.2 kg/s at 100k rpm, and peak η_{ad} value of 0.55 with Mfr of 0.25 kg/s at 117k rpm, respectively. Regarding each operation speed, the peak η_{ad} and peak *Pr* is identified with almost identical Mfr, suggesting it the optimal operation Mfr. Figure A-i.9 [92] shows the experimental results of η_{ad} distribution at different operational speeds. The experimental results present identical distribution with simulation results from 80k rpm to 120k rpm, where a decrease of η_{ad} is observed with the increase of operation speed. However, the η_{ad} slightly drops with the decrease of operation speed smaller than 80k rpm, which is not investigated in our simulations.

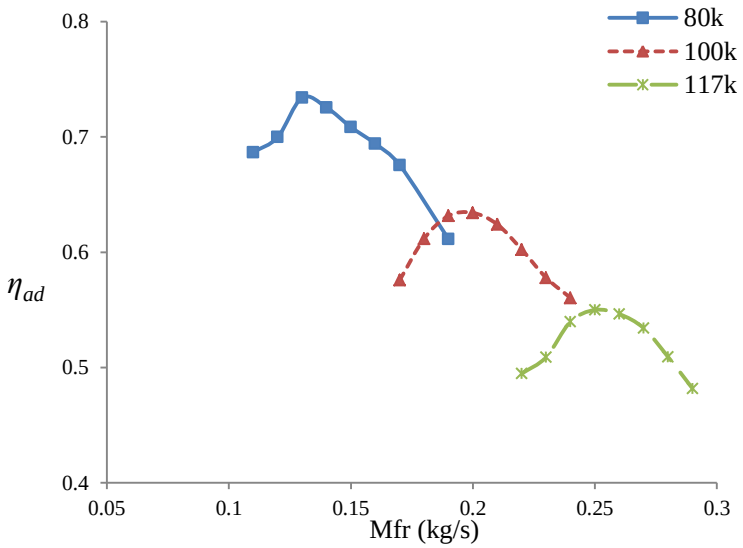

Fig A-i.8 Distribution of η_{ad} with varying Mfr, at different operation speed

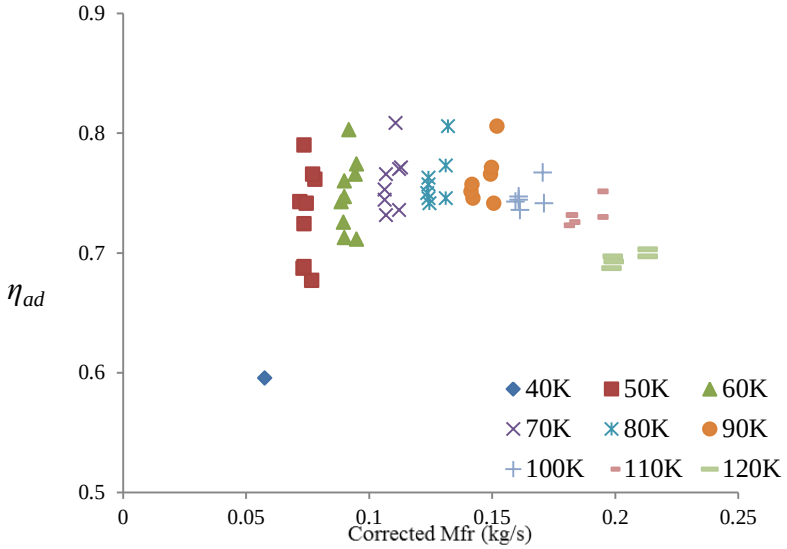

Fig A-i.9 Distribution of experiment[92] η_{ad} with varying Mfr at different operation speed

The simulation results are further analyzed regarding flow structure within compressor. Figure A-i.10 shows the distribution of total pressure within compressor and on rotor blade, with designed Mfr at 117k rpm. The gradual increase of total pressure along impeller streamwise is observed, with high total pressure region identified on the R_{ps} near R_{TE}.

Figure A-i.11 further demonstrates the increase of total pressure along impeller streamwise, with designed Mfr at 80k, 100k and 117k rpm respectively. The total pressure at 10 meridional spans is presented, on both R_{ss} and R_{ps}. The total pressure value is normalized by the reference value at impeller inlets. At 117k rpm, the observed *Pr* between R_{LE} and R_{TE} is around 2, and it is the highest *Pr* achieved among the three operation speed cases. This indicates that the *Pr* increases with the increase of operation speed. In addition, the theoretical blade work can also be obtained from the integral of total pressure difference between R_{ps} and R_{ss}. Therefore, the blade work also increases with the increase of operation speed, as the difference of total pressure between R_{ps} and R_{ss} increases.

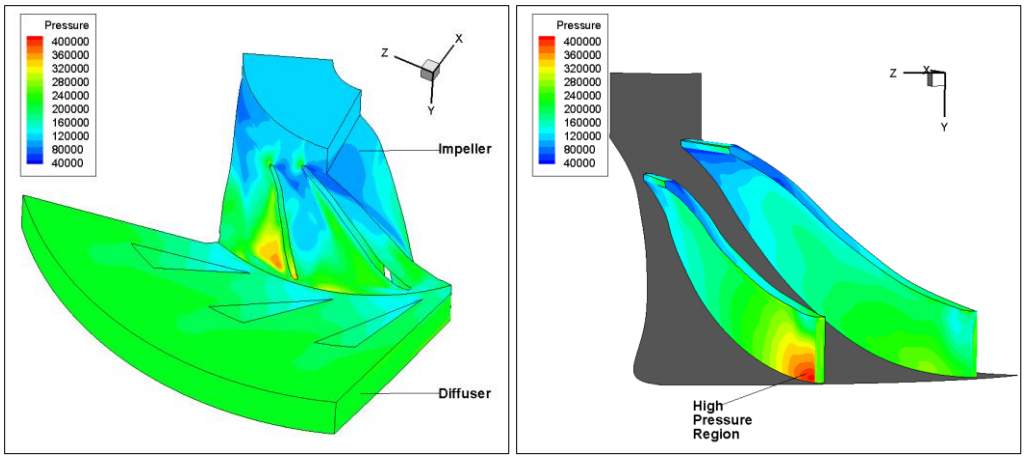

Fig A-i.10 Distribution of Pt within compressor (Left) and on rotor blade (Right)

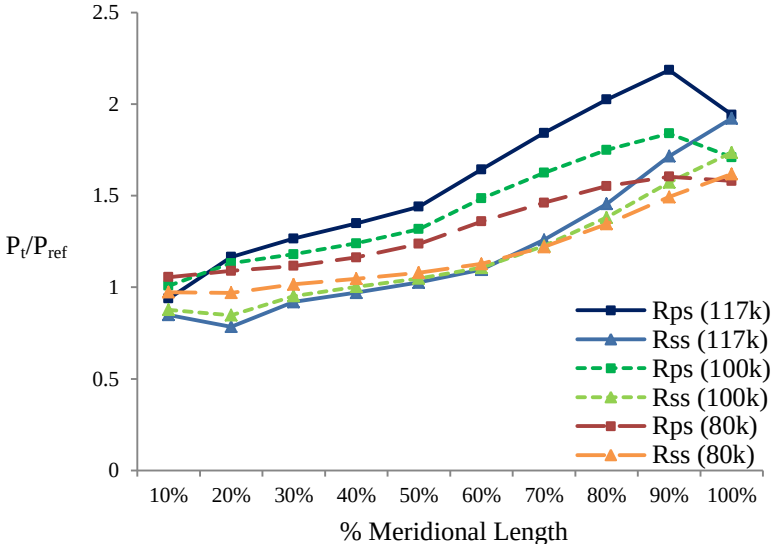

Fig A-i.11 Distribution of Pt on R_{ps} and R_{ss} along rotor meridional length, at different operation speed

The irreversibility within the KJ-66 MGT compressor is also considered. Figure A-i.12 shows the distribution of radial velocity and entropy along impeller streamwise, with design Mfr at 117k rpm. At the impeller entrance, the radial velocity is almost uniform, corresponding to nearly isentropic entropy distribution. However, small radial velocity is initially observed near R_{ss} close to the shroud when fluid enters the in-between blade path. This indicates occurrence of reversible flow due to false incidence angle, when incoming fluid attacks on R_{LE}. The generation of high entropy is also identified near R_{ss} close to shroud,

indicating the incidence loss. As fluid further propagates downstream, the small radial velocity region dissipates and expands towards $R_{ps,}$ still mainly locating near the shroud. This indicates the secondary flow region and reversible flow, due to the streamwise and corner vortex. The high entropy region expands in similar pattern, suggesting the increase of η_{ad} loss along impeller streamwise.

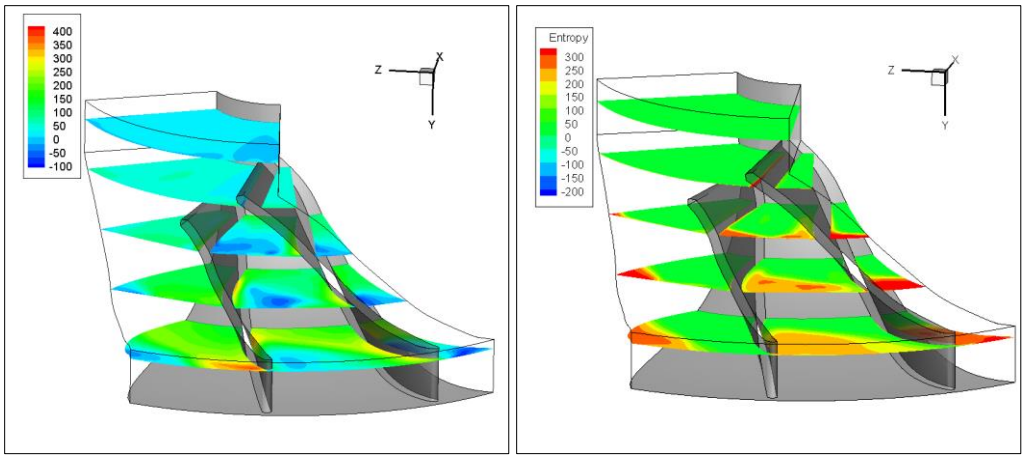

Fig A-i.12 Distribution of radial velocity (Left) and Entropy (Right) along impeller streamwise, with design Mfr at 117k rpm

The entropy distribution along impeller streamwise is further illustrated in Figure A-i.13, where the entropy distribution on rotor blade with design Mfr at 117k rpm and entropy distribution over impeller meridional length at three operation speeds are presented, respectively. The increase of entropy is observed along blade meridional length and high entropy is identified mainly near impeller shroud, which is identical with discussion made earlier. The normalized entropy rise curve further illustrates the increase of entropy from R_{LE} to R_{TE}. In addition, the larger the operation speed, more entropy rise is identified, indicating more efficiency loss.

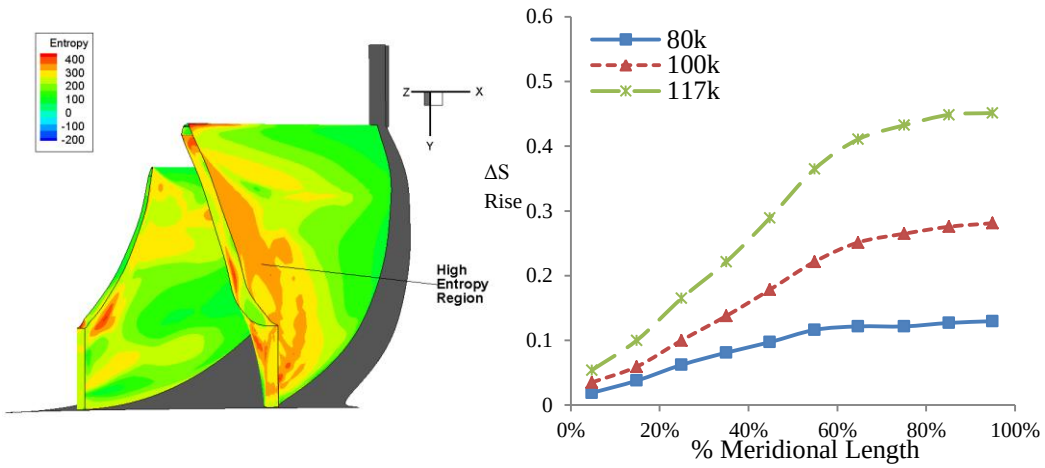

Fig A-i.13 Distribution of entropy on rotor blade with design Mfr at 117k rpm and over impeller meridional length at different operation speed

Figure A-i.14 shows the streamline along impeller streamwise and diffuser streamwise, with design Mfr at 117k rpm. The streamline in impeller is plotted in relative frame to counteract the effect of rotating rotor, while the streamline in diffuser is plotted in absolute frame. The reversible flow identified close to R_{ss} demonstrates the development of small radial velocity in the same region, due to streamwise and corner vortex. In the diffuser, vortex is also observed after the splitter blade, and the vortex moves from hub towards shroud. Further observation is presented in Figure A-i.15, where the velocity vectors on 50% spanwise in diffuser is shown. Strong vortex in the diffuser wake region can be identified and a zoom-in view shows the vortex behaves in clockwise pattern. In addition, as the vectors are colored by Mach value, a gradual decrease of fluid Mach is observed along the diffuser streamwise and small Mach region initiates near the S_{TE} on S_{ps}.

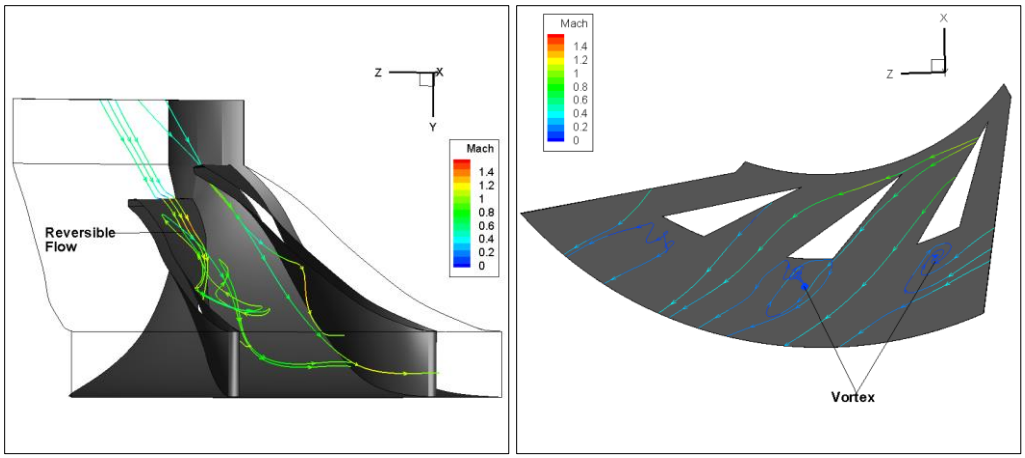

Fig A-i.14 Streamline along impeller streamwise (Left) and diffuser streamwise (right), with design Mfr at 117k rpm

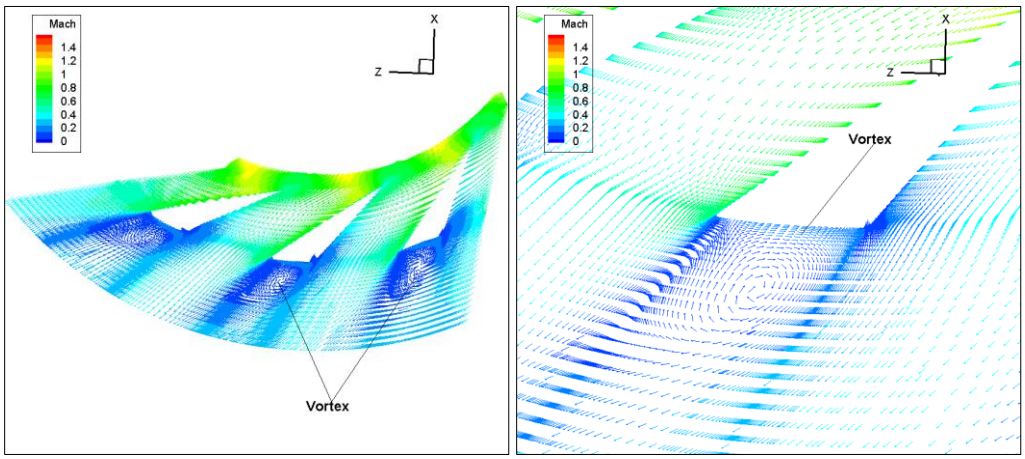

Fig A-i.15 Velocity vectors on 50% spanwise in diffuser, normal view (Left) and zoom-in view, with design Mfr at 117k rpm

In summary, the KJ-66 MGT compressor is computationally studied. It further demonstrates the reliability of the computational tools and methods applied on MGT investigation. The operation range at different operation speeds is predicted and analysis of flow field is also carried out. It deepens the understanding of performance of miniature gas turbines.

For future work of this MGT study, more detailed analysis should be enclosed. Specific parametric study regarding the MGT is required. The small size of MGT increased the difficulty of engine cooling, which may result in engine overheating, and further deteriorate its endurance time. Therefore, techniques preventing overheating should also be considered.

APPENDIX II
Experiments Uncertainty

According to the NASA Technical Paper 1338 (1978)[47, 48], the estimated errors in the data, based in inherent accuracies of the instrumentation and the recording system, are as follows:

Mass Flow (kg/s) ---------- $\pm$0.3

Rotate Speed (rpm) ---------- $\pm$30

Flow Angle (deg) ---------- $\pm$1.0

Temperature (k) ---------- $\pm$0.6

Rotor Inlet Total Pressure (N/cm^2) ---------- $\pm$0.01

Rotor Inlet Static Pressure (N/cm^2) ---------- $\pm$0.03

Stator Outlet Total Pressure (N/cm^2) ---------- $\pm$0.17

Stator Outlet Static Pressure (N/cm^2) ---------- $\pm$0.10

Overall Performance for Stage 35

(a) 100 Percent of design speed

Parameters	Reading					
	4004	3978	3977	3974	3976	3975
ROTOR TOTAL PRESSURE RATIO	1.738	1.875	1.955	1.985	2.036	2.014
STATOR TOTAL PRESSURE RATIO	0.986	0.982	0.974	0.968	0.945	0.959
ROTOR TOTAL TEMPERATURE RATIO	1.198	1.226	1.245	1.254	1.277	1.263
STATOR TOTAL TEMPERATURE RATIO	1.000	1.000	1.000	1.000	1.001	1.000
ROTOR ADIABATIC EFFICIENCY	0.865	0.872	0.863	0.853	0.812	0.841
ROTOR MOMENTUM-RISE EFFICIENCY	0.861	0.869	0.859	0.853	0.808	0.836
ROTOR HEAD-RISE COEFFICIENT	0.286	0.341	0.371	0.380	0.402	0.391
FLOW COEFFICIENT	0.412	0.412	0.402	0.390	0.340	0.373
AIRFLOW PER UNIT FRONTAL AREA	101.42	100.77	99.15	97.42	88.08	94.57
AIRFLOW PER UNIT ANNULUS AREA	190.55	189.33	186.28	183.03	165.49	177.67
AIRFLOW AT ORIFICE	20.95	20.82	20.48	20.13	18.20	19.54
AIRFLOW AT ROTOR INLET	21.10	21.00	20.64	20.27	18.26	19.64
AIRFLOW AT ROTOR OUTLET	20.97	20.83	20.50	20.14	18.21	19.55
AIRFLOW AT STATOR OUTLET	20.08	19.92	19.49	19.11	16.98	18.41
ROTATIVE SPEED	17220.2	17119.1	17125.1	17196.8	17218.5	17224.5
PERCENT OF DESIGN SPEED	100.2	99.6	99.6	100.0	100.2	100.2
Compressor performance						
STAGE TOTAL PRESSURE RATIO	1.714	1.842	1.905	1.922	1.923	1.932
STAGE TOTAL TEMPERATURE RATIO	1.198	1.225	1.244	1.253	1.279	1.263
STAGE ADIABATIC EFFICIENCY	0.841	0.845	0.827	0.810	0.737	0.786

(d) 70 Percent of design speed

Parameters	Reading				
	3995	3994	3993	3990	3989
ROTOR TOTAL PRESSURE RATIO	1.264	1.300	1.343	1.356	1.375
STATOR TOTAL PRESSURE RATIO	0.989	0.993	0.993	0.992	0.982
ROTOR TOTAL TEMPERATURE RATIO	1.076	1.087	1.101	1.108	1.120
STATOR TOTAL TEMPERATURE RATIO	1.000	1.000	1.000	1.000	1.000
ROTOR ADIABATIC EFFICIENCY	0.905	0.893	0.873	0.840	0.793
ROTOR MOMENTUM-RISE EFFICIENCY	0.899	0.895	0.871	0.842	0.794
ROTOR HEAD-RISE COEFFICIENT	0.212	0.240	0.275	0.288	0.306
FLOW COEFFICIENT	0.407	0.393	0.366	0.340	0.296
AIRFLOW PER UNIT FRONTAL AREA	76.53	74.11	69.63	64.93	57.06
AIRFLOW PER UNIT ANNULUS AREA	143.78	139.23	130.82	121.99	107.19
AIRFLOW AT ORIFICE	15.81	15.31	14.38	13.41	11.79
AIRFLOW AT ROTOR INLET	15.87	15.37	14.46	13.50	11.86
AIRFLOW AT ROTOR OUTLET	15.81	15.31	14.39	13.42	11.79
AIRFLOW AT STATOR OUTLET	15.12	14.60	13.74	12.78	11.15
ROTATIVE SPEED	12074.9	12074.5	12073.2	12040.8	12022.9
PERCENT OF DESIGN SPEED	70.2	70.2	70.2	70.1	69.9
Compressor performance					
STAGE TOTAL PRESSURE RATIO	1.250	1.291	1.334	1.345	1.350
STAGE TOTAL TEMPERATURE RATIO	1.077	1.087	1.101	1.108	1.120
STAGE ADIABATIC EFFICIENCY	0.860	0.868	0.852	0.816	0.744

Blade Element Data at Blade Edges for Rotor 35

(a) 100 Percent of design speed; reading 4004

RP	RADII IN	RADII OUT	ABS BETAM IN	ABS BETAM OUT	REL BETAM IN	REL BETAM OUT	TOTAL TEMP IN	TOTAL TEMP RATIO	TOTAL PRESS IN	TOTAL PRESS RATIO
1	24.915	24.221	-0.1	35.4	67.0	59.4	288.9	1.194	9.92	1.657
2	24.572	23.932	-0.0	34.8	64.4	57.3	288.1	1.198	10.13	1.669
3	24.224	23.642	-0.0	34.3	63.5	56.2	288.1	1.195	10.14	1.692
4	[illegible]	22.771	-0.0	34.5	61.3	54.1	288.5	1.193	10.13	1.710
5	21.[illegible]	21.613	-0.1	36.3	59.2	49.5	287.9	1.203	10.15	1.767
6	20.2[illegible]	20.455	-0.0	37.0	57.6	45.0	288.1	1.203	10.15	1.798
7	19.0[illegible]	19.583	-0.0	37.3	56.5	42.5	288.2	1.193	10.15	1.751
8	18.[illegible]	19.294	-0.0	37.8	56.4	41.7	287.9	1.195	10.15	1.737
9	18.158	19.004	-0.1	38.9	56.3	39.2	288.0	1.201	10.12	1.743

RP	ABS VEL IN	ABS VEL OUT	REL VEL IN	REL VEL OUT	MERID VEL IN	MERID VEL OUT	TANG VEL IN	TANG VEL OUT	WHEEL SPEED IN	WHEEL SPEED OUT
1	190.9	223.9	489.5	358.1	190.9	182.5	-0.3	129.7	450.4	437.9
2	211.0	232.2	489.0	353.2	211.0	190.8	-0.1	132.4	441.1	429.6
3	216.7	236.4	486.1	350.7	216.7	195.2	-0.0	133.4	435.2	424.7
4	229.1	241.7	477.5	339.7	229.1	199.3	-0.0	136.7	418.9	411.8
5	234.5	254.6	458.2	316.0	234.5	205.1	-0.4	150.8	393.2	391.1
6	231.8	264.3	433.1	298.5	231.8	211.1	-0.0	159.0	365.8	370.0
7	226.2	263.7	409.8	284.6	226.2	209.9	-0.1	159.6	341.7	351.8
8	223.6	265.1	404.1	280.8	223.6	209.6	-0.1	162.3	336.6	349.2
9	218.2	270.6	392.8	271.5	218.2	210.5	-0.4	170.0	326.2	341.4

RP	ABS MACH NO IN	ABS MACH NO OUT	REL MACH NO IN	REL MACH NO OUT	MERID MACH NO IN	MERID MACH NO OUT	MERID PEAK SS VEL R	MERID PEAK SS MACH NO
1	0.579	0.624	1.484	0.998	0.579	0.509	0.956	1.653
2	0.645	0.649	1.496	0.987	0.645	0.533	0.904	1.616
3	0.664	0.663	1.490	0.983	0.664	0.547	0.901	1.609
4	0.706	0.679	1.470	0.955	0.706	0.560	0.870	1.569
5	0.725	0.717	1.416	0.889	0.725	0.577	0.875	1.546
6	0.715	0.747	1.336	0.843	0.715	0.596	0.911	1.571
7	0.696	0.748	1.261	0.807	0.696	0.596	0.928	1.539
8	0.688	0.752	1.243	0.797	0.688	0.595	0.937	1.527
9	0.670	0.767	1.205	0.770	0.670	0.597	0.965	1.494

RP	PERCENT SPAN	INCIDENCE MEAN	INCIDENCE SS	DEV	D FACT	EFF	LOSS COEFF TOT	LOSS COEFF PROF	LOSS PARAM TOT	LOSS PARAM PROF
1	5.00	5.4	3.0	6.6	0.369	0.799	0.145	0.016	0.028	0.003
2	10.00	3.8	1.1	5.3	0.379	0.794	0.151	0.028	0.031	0.006
3	15.00	3.7	0.7	4.8	0.380	0.831	0.123	0.004	0.026	0.001
4	30.00	3.0	-0.4	5.5	0.391	0.859	0.105	-.002	0.022	-.000
5	50.00	3.1	-1.2	5.2	0.422	0.872	0.105	0.013	0.023	0.003
6	70.00	3.9	-1.6	5.8	0.428	0.900	0.090	0.004	0.020	0.001
7	85.00	4.2	-2.4	9.1	0.425	0.899	0.093	0.026	0.021	0.006
8	90.00	4.3	-2.5	10.6	0.426	0.878	0.116	0.053	0.025	0.012
9	95.00	4.3	-2.9	10.5	0.437	0.855	0.147	0.095	0.033	0.021

(m) 70 Percent of design speed; reading 3995

RP	RADII IN	RADII OUT	ABS BETAM IN	ABS BETAM OUT	REL BETAM IN	REL BETAM OUT	TOTAL TEMP IN	TOTAL TEMP RATIO	TOTAL PRESS IN	TOTAL PRESS RATIO
1	24.915	24.221	-0.0	23.2	68.5	58.0	289.0	1.068	10.01	1.195
2	24.572	23.932	-0.1	22.9	65.8	55.8	288.4	1.071	10.14	1.208
3	24.224	23.642	-0.0	22.0	64.9	54.6	288.5	1.069	10.14	1.227
4	23.162	22.771	-0.1	23.0	62.8	51.5	288.3	1.072	10.14	1.248
5	21.725	21.613	-0.1	25.1	60.8	47.9	288.0	1.076	10.14	1.268
6	20.221	20.455	-0.1	26.8	59.2	43.2	287.9	1.080	10.14	1.289
7	19.020	19.583	-0.0	27.8	58.3	39.0	288.0	1.083	10.14	1.299
8	18.595	19.294	-0.0	28.4	57.9	37.6	287.9	1.085	10.14	1.308
9	18.158	19.004	-0.0	29.3	57.9	34.7	288.0	1.089	10.12	1.316

RP	ABS VEL IN	ABS VEL OUT	REL VEL IN	REL VEL OUT	MERID VEL IN	MERID VEL OUT	TANG VEL IN	TANG VEL OUT	WHEEL SPEED IN	WHEEL SPEED OUT
1	124.0	164.5	338.9	285.2	124.0	151.2	-0.0	64.7	315.3	306.5
2	140.0	173.3	340.9	284.3	140.0	159.6	-0.3	67.3	310.6	302.5
3	143.6	178.2	338.3	284.9	143.6	165.2	-0.0	66.8	306.3	298.9
4	150.8	185.8	329.7	274.9	150.8	171.0	-0.3	72.7	292.9	287.9
5	153.9	191.7	315.1	258.8	153.9	173.6	-0.3	81.3	274.6	273.2
6	152.7	200.3	297.9	245.3	152.7	178.7	-0.3	90.4	255.5	258.5
7	148.9	209.2	283.0	238.2	148.9	185.0	-0.0	97.7	240.6	247.7
8	147.6	214.3	277.8	236.2	147.6	188.5	-0.0	101.9	235.3	244.1
9	144.1	219.9	271.0	233.1	144.1	191.8	-0.0	107.6	229.5	240.2

RP	ABS MACH NO IN	ABS MACH NO OUT	REL MACH NO IN	REL MACH NO OUT	MERID MACH NO IN	MERID MACH NO OUT	MERID PEAK SS VEL R	MERID PEAK SS MACH NO
1	0.369	0.477	1.008	0.828	0.369	0.439	1.219	1.312
2	0.418	0.504	1.019	0.827	0.418	0.465	1.141	1.256
3	0.429	0.520	1.012	0.831	0.429	0.482	1.151	1.253
4	0.452	0.542	0.988	0.803	0.452	0.499	1.134	1.217
5	0.462	0.560	0.946	0.756	0.462	0.507	1.128	1.201
6	0.458	0.586	0.894	0.717	0.458	0.523	1.170	1.232
7	0.446	0.613	0.848	0.698	0.446	0.542	1.243	1.208
8	0.442	0.628	0.832	0.692	0.442	0.553	1.277	1.181
9	0.431	0.644	0.811	0.683	0.431	0.562	1.331	1.155

RP	PERCENT SPAN	INCIDENCE MEAN	INCIDENCE SS	DEV	D FACT	EFF	LOSS COEFF TOT	LOSS COEFF PROF	LOSS PARAM TOT	LOSS PARAM PROF
1	5.00	6.9	4.5	5.3	0.230	0.768	0.103	0.095	0.021	0.019
2	10.00	5.1	2.4	3.8	0.240	0.784	0.099	0.094	0.021	0.020
3	15.00	5.0	2.1	3.2	0.231	0.865	0.062	0.057	0.013	0.012
4	30.00	4.4	1.0	2.9	0.245	0.903	0.048	0.046	0.011	0.010
5	50.00	4.6	0.4	3.6	0.266	0.922	0.044	0.043	0.010	0.010
6	70.00	5.4	-0.1	4.1	0.274	0.937	0.040	0.040	0.009	0.009
7	85.00	5.9	-0.6	5.6	0.264	0.941	0.043	0.043	0.010	0.010
8	90.00	5.8	-1.1	5.9	0.260	0.935	0.049	0.049	0.012	0.012
9	95.00	5.9	-1.2	6.0	0.257	0.913	0.073	0.073	0.017	0.017

Blade Element Data at Blade Edges for Stator 35

(a) 100 Percent of design speed; reading 4004

RP	RADII IN	RADII OUT	ABS BETAM IN	ABS BETAM OUT	REL BETAM IN	REL BETAM OUT	TOTAL TEMP IN	TOTAL TEMP RATIO	TOTAL PRESS IN	TOTAL PRESS RATIO
1	23.993	23.752	32.1	11.1	32.1	11.1	345.1	1.000	16.44	0.969
2	23.736	23.523	31.6	10.4	31.6	10.4	345.3	1.000	16.91	0.984
3	23.480	23.294	31.3	10.2	31.3	10.2	344.3	1.000	17.16	0.988
4	22.685	22.593	31.6	9.7	31.6	9.7	344.1	1.000	17.33	0.991
5	21.608	21.656	33.7	10.9	33.7	10.9	346.3	1.000	17.94	0.987
6	20.505	20.709	34.8	11.6	34.8	11.6	346.5	1.000	18.25	0.987
7	19.670	19.990	35.7	10.7	35.7	10.7	343.8	1.000	17.78	0.985
8	19.388	19.746	36.6	9.5	36.6	9.5	343.9	1.000	17.64	0.981
9	19.103	19.505	38.3	9.3	38.3	9.3	345.9	1.000	17.63	0.970

RP	ABS VEL IN	ABS VEL OUT	REL VEL IN	REL VEL OUT	MERID VEL IN	MERID VEL OUT	TANG VEL IN	TANG VEL OUT	WHEEL SPEED IN	WHEEL SPEED OUT
1	246.6	200.2	246.6	200.2	209.0	196.4	131.0	38.4	0.0	0.0
2	254.9	215.6	254.9	215.6	217.2	212.0	133.5	38.8	0.0	0.0
3	258.5	223.2	258.5	223.2	220.9	219.6	134.3	39.5	0.0	0.0
4	261.6	232.6	261.6	232.6	222.7	229.3	137.3	39.1	0.0	0.0
5	271.9	245.1	271.9	245.1	226.2	240.7	150.8	46.5	0.0	0.0
6	278.0	253.7	278.0	253.7	228.3	248.5	158.6	51.0	0.0	0.0
7	272.5	249.1	272.5	249.1	221.3	244.7	158.9	46.2	0.0	0.0
8	271.1	246.8	271.1	246.8	217.7	243.4	161.6	40.7	0.0	0.0
9	272.8	244.0	272.8	244.0	214.1	240.8	169.1	39.5	0.0	0.0

RP	ABS MACH NO IN	ABS MACH NO OUT	REL MACH NO IN	REL MACH NO OUT	MERID MACH NO IN	MERID MACH NO OUT	MERID PEAK SS VEL R	MERID PEAK SS MACH NO
1	0.693	0.554	0.693	0.554	0.587	0.543	0.940	0.900
2	0.719	0.599	0.719	0.599	0.612	0.589	0.976	0.917
3	0.731	0.623	0.731	0.623	0.625	0.613	0.994	0.921
4	0.741	0.651	0.741	0.651	0.631	0.642	1.029	0.935
5	0.771	0.687	0.771	0.687	0.641	0.675	1.064	1.019
6	0.790	0.713	0.790	0.713	0.649	0.699	1.088	1.060
7	0.776	0.702	0.776	0.702	0.630	0.690	1.106	1.045
8	0.771	0.695	0.771	0.695	0.619	0.686	1.118	1.054
9	0.774	0.684	0.774	0.684	0.608	0.675	1.125	1.094

RP	PERCENT SPAN	INCIDENCE MEAN	INCIDENCE SS	DEV	D FACT	EFF	LOSS COEFF TOT	LOSS COEFF PROF	LOSS PARAM TOT	LOSS PARAM PROF
1	5.00	-2.3	-10.0	8.5	0.334	0.000	0.113	0.113	0.042	0.042
2	10.00	-3.0	-10.3	7.8	0.297	0.000	0.054	0.054	0.020	0.020
3	15.00	-3.4	-10.6	7.6	0.277	0.000	0.042	0.042	0.016	0.016
4	30.00	-3.4	-9.8	6.9	0.252	0.000	0.029	0.029	0.011	0.011
5	50.00	-2.0	-7.5	7.8	0.238	0.000	0.040	0.040	0.014	0.014
6	70.00	-1.6	-6.3	8.1	0.224	0.000	0.037	0.037	0.013	0.013
7	85.00	-1.8	-5.8	7.1	0.227	0.000	0.047	0.047	0.016	0.016
8	90.00	-1.2	-5.0	5.9	0.241	0.000	0.059	0.059	0.020	0.020
9	95.00	0.1	-3.5	5.7	0.265	0.000	0.091	0.091	0.031	0.031

(m) 70 Percent of design speed; reading 3995

RP	RADII IN	RADII OUT	ABS BETAM IN	ABS BETAM OUT	REL BETAM IN	REL BETAM OUT	TOTAL TEMP IN	TOTAL TEMP RATIO	TOTAL PRESS IN	TOTAL PRESS RATIO
1	23.993	23.752	21.0	11.4	21.0	11.4	308.6	1.000	11.95	0.980
2	23.736	23.523	20.8	9.6	20.8	9.6	308.8	1.000	12.25	0.990
3	23.480	23.294	20.1	8.9	20.1	8.9	308.5	1.000	12.44	0.988
4	22.685	22.593	21.1	8.0	21.1	8.0	309.1	1.000	12.65	0.987
5	21.608	21.656	23.3	9.1	23.3	9.1	310.0	1.000	12.86	0.990
6	20.505	20.709	25.2	10.0	25.2	10.0	311.0	1.000	13.07	0.989
7	19.670	19.990	26.6	10.5	26.6	10.5	311.8	1.000	13.17	0.991
8	19.388	19.746	27.4	10.9	27.4	10.9	312.5	1.000	13.26	0.990
9	19.103	19.505	28.8	11.3	28.8	11.3	313.8	1.000	13.31	0.984

RP	ABS VEL IN	ABS VEL OUT	REL VEL IN	REL VEL OUT	MERID VEL IN	MERID VEL OUT	TANG VEL IN	TANG VEL OUT	WHEEL SPEED IN	WHEEL SPEED OUT
1	182.6	177.1	182.6	177.1	170.5	173.6	65.3	35.0	0.0	0.0
2	191.4	191.9	191.4	191.9	178.9	189.3	67.9	31.9	0.0	0.0
3	196.2	199.3	196.2	199.3	184.3	196.9	67.3	30.9	0.0	0.0
4	202.4	209.1	202.4	209.1	188.8	207.1	72.9	29.0	0.0	0.0
5	205.8	221.3	205.8	221.3	189.1	218.5	81.3	35.2	0.0	0.0
6	211.6	229.9	211.6	229.9	191.4	226.5	90.2	39.7	0.0	0.0
7	217.2	233.9	217.2	233.9	194.3	230.0	97.3	42.6	0.0	0.0
8	220.2	236.0	220.2	236.0	195.5	231.8	101.4	44.4	0.0	0.0
9	222.5	235.6	222.5	235.6	195.0	231.0	107.1	46.0	0.0	0.0

RP	ABS MACH NO IN	ABS MACH NO OUT	REL MACH NO IN	REL MACH NO OUT	MERID MACH NO IN	MERID MACH NO OUT	MERID PEAK SS VEL R	MERID PEAK SS MACH NO
1	0.533	0.516	0.533	0.516	0.498	0.506	1.018	0.533
2	0.560	0.562	0.560	0.562	0.524	0.554	1.058	0.560
3	0.575	0.585	0.575	0.585	0.540	0.578	1.069	0.575
4	0.594	0.615	0.594	0.615	0.554	0.609	1.097	0.594
5	0.604	0.653	0.604	0.653	0.555	0.645	1.155	0.604
6	0.621	0.680	0.621	0.680	0.562	0.669	1.183	0.621
7	0.638	0.692	0.638	0.692	0.571	0.680	1.184	0.638
8	0.647	0.698	0.647	0.698	0.574	0.685	1.186	0.647
9	0.653	0.695	0.653	0.695	0.572	0.681	1.185	0.653

RP	PERCENT SPAN	INCIDENCE MEAN	INCIDENCE SS	DEV	D FACT	EFF	LOSS COEFF TOT	LOSS COEFF PROF	LOSS PARAM TOT	LOSS PARAM PROF
1	5.00	-13.5	-21.1	8.8	0.095	0.000	0.114	0.114	0.043	0.043
2	10.00	-13.8	-21.2	7.0	0.070	0.000	0.050	0.050	0.019	0.019
3	15.00	-14.7	-21.8	6.3	0.055	0.000	0.057	0.057	0.022	0.022
4	30.00	-13.9	-20.3	5.2	0.048	0.000	0.059	0.059	0.022	0.022
5	50.00	-12.5	-18.0	6.0	0.006	0.000	0.045	0.045	0.016	0.016
6	70.00	-11.2	-15.8	6.5	-.003	0.000	0.048	0.048	0.017	0.017
7	85.00	-10.9	-14.8	6.9	0.009	0.000	0.038	0.038	0.013	0.013
8	90.00	-10.4	-14.2	7.3	0.015	0.000	0.043	0.043	0.014	0.014
9	95.00	-9.4	-13.0	7.7	0.032	0.000	0.065	0.065	0.022	0.022

Bibliography

1. Taylor, J.W.R. and Munson, K., *Jane's pocket book of remotely piloted vehicles : robot aircraft today*. 1st Ameican ed. 1977, New York: Collier Books.
2. Wagner, W., *Lightning Bugs and other Reconnaissance Drones; The can-do story of Ryan's unmanned spy planes*. Armed Forces Journal International. 1982: Aero Publishers.
3. Defence, U.D.o., *FY2009–2034 unmanned systems integrated roadmap*. 2009.
4. *MQ-9Reaper*. http://en.wikipedia.org/wiki/General_Atomics_MQ-9_Reaper [cited 2015 09-Apr].
5. Guillory, M. *RQ-11Raven*. http://en.wikipedia.org/wiki/RQ-11_Raven 2006 [cited 2015 09-Apr].
6. *Massachusetts Institute of Technology Gas Turbine Lab*. http://web.mit.edu/aeroastro/labs/gtl/ [cited 2015 09-Apr].
7. Richard E. Sonntag, C.B., *Introduction to Engineering Thermodynamics.* 2006.
8. Genuth, I. *The Future of Things*. http://thefutureofthings.com/3063-engine-on-a-chip/ 2007 [cited 2015 09-Apr].
9. Dohmen, F. *The future of energy: a power station in your basement*. http://www.spiegel.de/international/business/the-future-of-energy-a-power-station-in-your-basement-a-647435.html 2009 [cited 2015 09-Apr].
10. Peirs, J. *Ultra micro gas turbine generator*. http://www.powermems.be/gasturbine.html 2008 [cited 2015 09-Apr].
11. Zürich, E. *Model-based control of micro gas gurbines*. http://www.idsc.ethz.ch/research-guzzella-onder/research-projects/ProjectArchive/micro-gas-turbine.html [cited 2015 09-Apr].
12. Guo, S., et al., *Numerical investigation of centrifugal compressor performance in a miniturbojet engine.* Journal of Aerospace Engineering, 2014. **27**(6): p. 04014036.
13. Guo, S., Duan, F., Tang, H, *Multi-objective optimization for centrifugal compressor of mini turbojet engine.* Aerospace Science and Technology, 2014. **39**: p. 414–425.
14. Xiang, J., J.U. Schlüter, and F. Duan, *CFD validation and analysis of a single-stage axial compressor.* Applied Mechanics and Materials, 2014. **629**(2014): p. 109-118.
15. Xiang, J., J.U. Schlüter, and F. Duan, *Miniature gas turbines: Numerical study of the effects of heat transfer and Reynolds number on the performance of an axial compressor.* International Journal of Computational Materials Science and Engineering, 2014. **03**(02): p. 1450008.
16. Wang, Y.-F. and J. Hu, *Effects of Reynolds number on performance and stability of axial fans/compressors.* Journal of Nanjing University of Aeronautics and Astronautics, 2004. **36**(2): p. 145-149.
17. Hobson, G.V., et al., *Effect of Reynolds number on separation bubbles on compressor blades in cascade.* Journal of Propulsion and Power, 2001. **17**(1): p. 154-162.
18. Zhao, S., et al., *Effects of low Reynolds number on flow stability of a transonic compressor.* Proceedings of the Institution of Mechanical Engineers, Part G: Journal of Aerospace Engineering, 2015. **229**(4): p. 601-611.
19. Choi, M., et al., *Effects of the low Reynolds number on the loss characteristics in an axial compressor.* Proceedings of the Institution of Mechanical Engineers, Part A: Journal of Power and Energy, 2008. **222**(2): p. 209-218.

20. Back, S.C., et al., *Effect of surface roughness location and reynolds number on compressor cascade performance.* Proceedings of the ASME Turbo Expo, 2010. **7**: p. 121-128.
21. Casey, M.V. and C.J. Robinson, *A unified correction method for Reynolds number, size, and roughness effects on the performance of compressors.* Proceedings of the Institution of Mechanical Engineers, Part A: Journal of Power and Energy, 2011. **225**: p. 864-876.
22. Dietmann, F. and M. Casey, *The effects of reynolds number and roughness on compressor performance.* 10th European Conference on Turbomachinery Fluid Dynamics and Thermodynamics, ETC 2013, 2014: p. 532-542.
23. Zheng, X., et al., *Effects of Reynolds number on the performance of a high pressure-ratio turbocharger compressor.* Science China. Technological Sciences, 2013. **56**(6): p. 1361-9.
24. Schiele, R. and S. Wittig, *Gas Turbine Heat Transfer: Past and Future Challenges.* Journal of Propulsion and Power, 2000. **16**(4): p. 583-589.
25. Romagnoli, A. and R. Martinez-Botas, *Heat transfer analysis in a turbocharger turbine: an experimental and computational evaluation.* Applied Thermal Engineering, 2012. **38**: p. 58-77.
26. Chen, L., F. Sun, and C. Wu, *Effect of heat resistance on the performance of closed gas turbine regenerative cycles.* International Journal of Power and Energy Systems, 1999. **19**(2): p. 141-145.
27. Maffulli, R. and L. He, *Wall Temperature Effects on Heat Transfer Coefficient for High-Pressure Turbines.* Journal of Propulsion and Power, 2014. **30**(4): p. 1080-1090.
28. Ma, Y. and G. Xi, *Effects of reynolds number and heat transfer on scaling of a centrifugal compressor impeller.* Proceedings of the ASME Turbo Expo, 2010. **5**: p. 565-572.
29. Domercq, O. and J.F. Escuret, *Tip clearance effect on high-pressure compressor stage matching.* Proceedings of the Institution of Mechanical Engineers, Part A (Journal of Power and Energy), 2007. **221**(A6): p. 759-67.
30. Puterbaugh, S.I. and M. Brende, *Tip clearance flow-shock interaction in a transonic compressor rotor.* Journal of Propulsion and Power, 1997. **13**(1): p. 24-30.
31. Williams, R., et al., *Experiments and computations on large tip clearance effects in a linear cascade.* Journal of Turbomachinery, 2010. **132**(2).
32. Van Zante, D.E., et al., *Recommendations for Achieving Accurate Numerical Simulation of Tip Clearance Flows in Transonic Compressor Rotors.* Journal of Turbomachinery, 1999. **122**(4): p. 733-742.
33. Chen, G.T., et al., *Similarity analysis of compressor tip clearance flow structure.* Journal of Turbomachinery, 1991. **113**(2): p. 260-269.
34. Wang, H.L., et al., Proceedings of the Institution of Mechanical Engineers, Part A: Journal of Power and Energy, 2011. **225**: p. 1143-1155.
35. Kunte, R., et al., *Experimental and Numerical Investigation of Tip Clearance and Bleed Effects in a Centrifugal Compressor Stage With Pipe Diffuser.* Journal of Turbomachinery, 2013. **135**(1): p. 011005 (12 pp.).
36. Ciorciari, R., et al., *Numerical investigation of tip clearance effects in an axial transonic compressor.* Journal of Thermal Science, 2012. **21**(2): p. 109-19.
37. Zhang, H., et al., *Unsteady tip clearance flow in an isolated axial compressor rotor.* Journal of Thermal Science, 2005. **14**(3): p. 211-219.

38. Jae Su, K. and H. Je-Chin, *Heat-Transfer Coefficients of a Turbine Blade-Tip and Near-Tip Regions.* Journal of Thermophysics and Heat Transfer, 2003(3): p. 297-303.
39. Kato, H., et al., *Experimental and numerical investigation on compressor cascade flows with tip clearance at a low Reynolds number condition.* Journal of Thermal Science, 2011. **20**(6): p. 481-485.
40. Gong, Y., et al., *Aerothermodynamics of micro-turbomachinery.* Proceedings of the ASME Turbo Expo, 2004. **6**: p. 95-102.
41. Ferrari, M.L., et al., *A micro gas turbine based test rig for educational purposes.* Journal of Engineering for Gas Turbines and Power, 2010. **132**(2): p. 024502 (5 pp.).
42. Mizuki, S., *Development of compressor for ultra micro gas turbine*. Journal of Thermal Science, 2007. **16**(1): p. 19-27.
43. Zanger, J., A. Widenhorn, and M. Aigner, *Experimental investigations of pressure losses on the performance of a micro gas turbine system.* Journal of Engineering for Gas Turbines and Power, 2011. **133**(8).
44. Verstraete, T., Z. Alsalihi, and R.A. Van den Braembussche, *Numerical study of the heat transfer in micro gas turbines.* Transactions of the ASME. The Journal of Turbomachinery, 2007. **129**(4): p. 835-41.
45. Steele, R., P. Baldwin, and J. Kesseli, *Insertion of shock wave compression technology into micro turbines for increased efficiency and reduced costs.* Proceedings of the ASME Turbo Expo, 2005. **1**: p. 857-862.
46. Chen, L., W. Zhang, and F. Sun, *Thermodynamic optimization for an open cycle of an externally fired micro gas turbine (EFmGT). part 1: Thermodynamic modelling.* International Journal of Sustainable Energy, 2011. **30**(4): p. 246-256.
47. Reid, L. and R.D. Moore, *Performance of single-stage axial-flow transonic compressor with rotor and stator aspect ratio of 1.19 and 1.26, respectively, and with design pressure ratio of 1.82.* NASA Technical Paper, 1978. **1338**.
48. Reid, L. and R.D. Moore, *Design and performance of four highly loaded, high speed inlet stages for an advanced high pressure ratio core compressor.* NASA Technical Paper, 1978. **1337**.
49. Anderson, J.D., *Fundamentals of Aerodynamics.* McGraw–Hill, 2007(4th Ed).
50. Blazek, J., *Computational fluid dynamics: principles and applications*. 2nd ed. 2005, Amsterdam: Elsevier.
51. Pijush K. Kundu, I.M.C., *Fluid Mechanics* 3ed. 2004, Amsterdam ; Boston: Elsevier Academic Press. 759.
52. Batchelor, G.K., *An Introduction to Fluid Dynamics.* Cambridge University Press, 2000: p. 131-173.
53. Stokes, G., *On the Effect of the Internal Friction of Fluids on the Motion of Pendulums.* Transactions of the Cambridge Philosophical Society, 1851. **9**: p. 8–106.
54. Reynolds, O., *An experimental investigation of the circumstances which determine whether the motion of water shall be direct or sinuous, and of the law of resistance in parallel channels.* Philosophical Transactions of the Royal Society, 1883. **174**(0): p. 935–982.
55. Avila, K.D.M.A.d.L.M.A.D.B.B.H., *The Onset of Turbulence in Pipe Flow.* Science 2011. **333**(6039): p. 192–196.
56. Moin, P. and J. Kim. *Tackling Turbulence with Supercomputers*. https://ctr.stanford.edu/articles/tackle.html [cited 2015 09-Apr].

57. Changgu, L., S. Arslan, and L.G. Frechette, *Design principles and measured performance of multistage radial flow microturbomachinery at low Reynolds numbers.* Journal of Fluids Engineering, 2008. **130**(11): p. 111103-1.
58. Ryzhov, O.S., *Transition length in turbine/compressor blade flows.* Proceedings of the Royal Society of London, Series A (Mathematical, Physical and Engineering Sciences), 2006. **462**(2072): p. 2281-98.
59. Epstein, A.H., *Millimeter-scale, micro-electro-mechanical systems gas turbine engines.* Transactions of the ASME. Journal of Engineering for Gas Turbines and Power, 2004. **126**(2): p. 205-26.
60. Isomura, K., et al., *Development of microturbocharger and microcombustor for a three-dimensional gas turbine at microscale*, in *Proceedings of the ASME Turbo Expo*. 2002, American Society of Mechanical Engineers: Amsterdam, Netherlands. p. 1127-1134.
61. Deardorff, J., *A numerical study of three-dimensional turbulent channel flow at large Reynolds numbers.* Journal of Fluid Mechanics, 1970. **41**(2): p. 453–480.
62. Schlichting, H. and K. Gersten, *Boundary Layer Theory*. 8th ed. 1999, Berlin: Springer.
63. Clapeyron, E., *Mémoire sur la puissance motrice de la chaleur.* Journal de l'École Polytechnique, 1834. **XIV**: p. 153–90.
64. Library, P.W.I. *PW6000 Engine*. http://www.pw.utc.com 2015 [cited 2015 09-Apr].
65. *IdealizedBraytonCycle*. http://upload.wikimedia.org/wikipedia/commons/3/3c/Brayton_cycle.svg [cited 2015 09-Apr].
66. Cohen, H., G.F.C. Rogers, and H.I.H. Saravanamuttoo, *Gas turbine theory (SI Unit)*. 2 ed. 1972, London: Longman Group Limited.
67. Lichty, L.C., *Combustion Engine Processes.* Lib.of Congress 67-10876, 1967.
68. Engware. *Brayton cycle*. http://en.wikipedia.org/wiki/Brayton_cycle [cited 2015 09-Apr].
69. LeVeque and R. J., *Finite Volume Methods for Hyperbolic Problems*. Cambridge Texts in Applied Mathematics; no. 31. 2002: Cambridge University Press.
70. Toro, E.F., *Riemann Solvers and Numerical Methods for Fluid Dynamics.* 2009(978-3-540-25202-3).
71. Sen, B.A., et al., *Pratt whitney gas turbine combustor design using ansys fluent and user defined functions.* Proceedings of the ASME Turbo Expo, 2012. **2**: p. 1547-1556.
72. Malael, I. and H. Dumitrescu, *Numerical Simulation of VAWT Flow Using Fluent.* University Politehnica of Bucharest, Scientific Bulletin, Series D (Mechanical Engineering), 2014. **76**(1): p. 109-22.
73. Nourbakshnia, N., et al., *Numerical simulation and experimental investigation of the failure of a gas turbine compressor blade.* Key Engineering Materials, 2008. **385-387**: p. 401-404.
74. ANSYS, I. *ANSYS 14.0 capability brochure*. http://www.cadit.com.sg/imagestore/userfiles/file/PDF14136.pdf 2011 [cited 2015 09-Apr].
75. University, C. *Introductory Fluent Training*. http://www.engr.uconn.edu/~barbertj/CFD%20Training/Fluent/4%20Solver%20Settings.pdf 2006 [cited 2015 09-Apr].
76. *Finite difference method*. http://en.wikipedia.org/wiki/Finite_difference_method [cited 2015 09-Apr].

77. Morkovin, M.V., *Effects of compressibility on turbulent flow. The mechanics of turbulence*, ed. F. A. 1964, New York.
78. Schluter, J.U., et al., *Integrated RANS-LES computations in gas turbine compressor-diffusor coupling.* AIAA, 2004. **0369**.
79. Gourdain, N., *Prediction of the unsteady turbulent flow in an axial compressor stage. Part 1: Comparison of unsteady RANS and LES with experiments.* Computers and Fluids, 2015. **106**: p. 119-129.
80. Gourdain, N., *Prediction of the unsteady turbulent flow in an axial compressor stage. Part 2: Analysis of unsteady RANS and LES data.* Computers and Fluids, 2015. **106**: p. 67-78.
81. P, S. and A. S, *A one-equation turbulence model for aerodynamic flows.* 30th Aerospace Sciences Meeting and Exhibit, 1992(AIAA-92-0439).
82. Spalding, D.B., *A single formula for the "Law of the wall".* ASME J. Applied Mechanics, Sept. 1961. **No. 28**: p. 455-458.
83. Viegas, J.R. and M.W. Rubesin, *Wall-function boundary conditions in the solution of the Navier-Stokes equations for complex compressible flows.* AIAA Paper 83-1694, 1983.
84. Abdol-Hamid, K.S., B. Lashmanan, and J.R. Carlson, *Application of Navier-Stokes Code PAB3D with k-ϵ turbulence models to attached and seperated flows.* NASA TR-3480, 1995.
85. Frink, N., *Assessment of an unstructured-grid method for predicting 3-D turbulent viscous flows.* AIAA Paper 96-0292, 1996.
86. Mohammadi, B. and O. Pironneau, *Unsteady seperated turbulent flows computation with wall-laws and k-ϵ model.* Comput. Meth. Appl. Eng,, 1997(148): p. 393-405.
87. Menter, F.R., *Two-Equation Eddy-Viscosity Turbulence Models for Engineering Applications.* AIAA Journal, 1994. **32**(8): p. 1598-1605.
88. Schluter, J.U., et al., *Integrated RANSLES computations of turbomachinery components: generic compress/diffuser*. 2003: p. 357-368.
89. Schluter, J.U., et al., *A framework for coupling reynolds-averaged with large-eddy simulations for gas turbine applications.* Journal of Fluids Engineering, 2005. **127**: p. 806-815.
90. Bardina, J.E., Huang, P.G. and Coakley, T.J., *Turbulence Modeling Validation, Tesing, and Development.* NASA TM-110446, 1997.
91. Wiesner, F.J., *New appraisal of Reynolds number effects on centrifugal compressor performance*. American Society of Mechanical Engineers, 1978(78 - GT-149).
92. Murray, P.W., *Microturbine for micro-cogeneration application.* URI: http://hdl.handle.net/1974/5237, Queen's University Master Thesis, 2009.